

***In vivo* Relevant Drug Product Evaluation by Using the Biphasic Dissolution Assay (BiPHa+)**

Dissertation

zur Erlangung des akademischen Grades

doctor rerum naturalium (Dr. rer. nat.)

der

Mathematisch-Naturwissenschaftlichen Fakultät

der

Rheinischen Friedrich-Wilhelms-Universität Bonn

vorgelegt von

ALEXANDER PETER DENNINGER

aus Karlsruhe

Bonn 2021

Angefertigt mit Genehmigung der Mathematisch-Naturwissenschaftlichen Fakultät der Rheinischen Friedrich-Wilhelms-Universität Bonn

Die folgende Arbeit wurde von 2016 – 2019 unter Leitung von Prof. Dr. Karl G. Wagner, Pharmazeutisches Institut der Universität Bonn, in Kooperation mit der Firma AbbVie Deutschland GmbH & Co. KG erstellt.

Erstgutachter: Prof. Dr. Karl G. Wagner

Zweitgutachter: Prof. Dr. Alf Lamprecht

Fachnaher Gutachter: Prof. Dr. Ulrich Jaehde

Fachferner Gutachter: Prof. Dr. Andreas Schieber

Tag der Promotion: 21. 03. 2022

Erscheinungsjahr: 2022

Abstract

An increasing number of new chemical entities (NCE) struggled with a very poor solubility in aqueous, intestinal media. Solubility or the ability to dissolve in aqueous, intestinal media is obligatory for oral bioavailability. The reasons for the low bioavailability are attributed to the dissolution rate limited absorption, permeability limited absorption or solubility – permeability limited absorption. Dealing with this challenge, advanced formulation technologies (e.g. amorphous solid dispersion) have been developed to increase the solubility of drug substances effectively. Followed by this formulation approaches, new *in vitro* characterisation methods became obligatory to sufficiently characterize the potential *in vivo* performance (e.g. biorelevant dissolution assay) and to guide formulation development effectively. There are already numerous improved *in vitro* test systems, which either offer limited predictive power with regard to the *in vivo* performance of drug formulations or are more complex and error-prone to perform in a laboratory environment.

The aim of the present study was to develop an efficiently performable biphasic dissolution assay having a high predictive power in terms of *in vivo* performance. The assay is intended to characterize bioavailability enhancing formulations with regard to their *in vivo* performance in a meaningful manner, and enable a greater mechanistic understanding of drug dissolution. In the present work, biphasic dissolution data in combination with the modelling approaches were proposed to provide valuable predictions of the *in vivo* performance of drug formulations.

First, a biphasic dissolution assay (BiPHA+) was designed as a fully automated small scale screening tool to achieve a high degree of biorelevance. A Labview® application was developed to execute the experimental sequence automatically (medium addition, pH-control and sampling) and, to enable dissolved drug quantification by UV-Vis spectroscopy. A spectra correction algorithm was designed for UV-Vis quantification because scattering in the aqueous phase caused by precipitated drug substance or overlapping of spectra occurred. Additional focus was put on the simulation of the gastrointestinal passage in the aqueous phase based on physiological data, hydrodynamics and geometrical parameters of the vessels. In a first feasibility trail, the assay design was able to generate highly biorelevant *in vitro* results (section 3.1).

Second, it was demonstrated that the distribution rate between the two phases was not majorly influenced by the interfacial properties between the decanol and the aqueous phase by using biorelevant aqueous media components (bile salt, lecithin) and formulation components (e.g. Soluplus®). In contrast, formulation components prove a

significant influence on drug distribution. This finding is important to assess the BiPHa+ data in terms of the discriminatory power of the assay with regard to formulation performance (section 3.2).

Third, an advanced kinetic model for amorphous solid dispersion formulations was established to describe the kinetic and mechanistic processes taking place during dissolution, precipitation and re-dissolution of an amorphous solid dispersion (ASD) in the BiPHa+ assay. The kinetic model described a sigmoidal partitioning profile resulting from a copovidone based ritonavir ASD. The processes included disintegration, dissolution, precipitation as nanodroplets, re-dissolution and partitioning in the organic phase. Ostwald ripening and a dynamic behaviour of nanodroplets were proposed as new effects, which possibly influence bioavailability (section 3.3).

Forth, the capability of the BiPHa+ assay to generate predictive dissolution results for various enabling formulations and drug substances was evaluated by using a single set of experimental settings. For this purpose, the influence of varying *in vitro* drug quantities of six different model drugs, formulated by different formulation approaches, was investigated. An *in vitro* dose of 10 mg drug substance containing formulation demonstrated high accordance to passively *in vivo* fraction absorbed, drug and formulation type independently. Further, a level A *in vivo* / *in vitro* relationship (IVIVR) for all model formulation was established. The convolutional based prediction approach demonstrated a high predictive power with regard to the formulation's *in vivo* performance, which facilitates the BiPHa+ assay as a meaningful tool for early stage formulation characterisation and lead formulation selection (section 3.4).

Fifth, a new workflow for the integration of BiPHa+ results into physiological based pharmacokinetic (PBPK) modelling tools was developed. The six model enabling formulations were chosen from section 3.4, because they prove already biorelevance by a level A IVIVR. For this purpose, the organic partitioning profiles obtained by the BiPHa+ assay were implemented in the PBPK software, PK-Sim® and GastroPlus® in the same way as modified release dissolution concentration time profiles. This procedure offers the advantage, that no complex mechanistic model of precipitation and dissolution was necessary for the simulations. The prediction demonstrated a high accuracy compared to the *in vivo* data even if a high first pass effect occurred, or the investigated drug represented a prodrug (section 3.5).

Finally, the rationally developed workflows from section 3.1 to 3.5 were applied to a specific case study. Different ABT-102 model amorphous solid dispersions administered to beagle dogs were investigated and assessed based on the BiPHa+ assay. The high predictive power of the BiPHa+ data were confirmed by a level A IVIVR, the convolutional

based pharmacokinetic prediction and PBPK modelling using PK-Sim® and GastroPlus®. All predictions of maximum plasma concentration (C_{max}) and area under the plasma concentration time profile (AUC) were within a 2-fold prediction range. Thus, the BiPHa+ assay and the presented prediction method delivered valuable *in vitro* data supporting a lead formulation selection during pharmaceutical development and, the assay proved to be suitable for the dissolution simulation in beagle dogs (section 3.6).

To conclude, the BiPHa+ assay was successfully validated by human and animal *in vivo* data and exhibited a remarkable power in terms of predicting the extent of passive drug absorption *in vivo*. The presented prediction workflows can be a valuable tool in the formulation development process to assess the dissolution behaviour towards the probable *in vivo* pharmacokinetic. Furthermore, the study results demonstrated the BiPHa+ assay as a powerful screening tool for different types of enabling formulation approaches. The BiPHa+ assay can guide formulation development and is potentially able to decrease the number of animal experiment during early stages of drug product development (section 5.1).

List of Publications

Parts of this thesis are published in the following publications:

Research articles

A. Denninger, U. Westedt, J. Rosenberg, K.G. Wagner, A Rational Design of a Biphasic Dissolution Setup—Modelling of Biorelevant Kinetics for a Ritonavir Hot-Melt Extruded Amorphous Solid Dispersion, *Pharmaceutics*. 12 (2020) 237, <https://doi.org/10.3390/pharmaceutics12030237>

A. Denninger, U. Westedt, K.G. Wagner, Shared IVIVR for Five Commercial Enabling Formulations Using the BiPha+ Biphasic Dissolution Assay, *Pharmaceutics*. 13 (2021) 285, <https://doi.org/10.3390/pharmaceutics13020285>

A. L. Marmol, A. Denninger, A Touzet, K Dauer, T Becker, F. Pöstges, A. Y. Pellequer, A. Lamprecht, K.G. Wagner, The relevance of supersaturation and solubilization in the gastrointestinal tract for oral bioavailability: an *in vitro* vs. *in vivo* approach, *International Journal of Pharmaceutics* (2021), 120648, <https://doi.org/10.1016/j.ijpharm.2021.120648> (no content of the thesis)

Conference abstracts including poster presentations

A. Denninger, J. Rosenberg, Karin Rosenblatt, K.G. Wagner, Biphasic dissolution model: comparing biorelevant medium and complex buffer; 11th Worldmeeting on Pharmaceutics, Biopharmaceutics and Pharmaceutical Technology 2018, Granada, Spain (no content of the thesis)

Patent

Liquid-solid pharmaceutical formulation and process for manufacturing of Corallopyronin A, 20172440.8-1109; 2020 (no content of the thesis)

Acknowledgments

First of all, I would like to express my deepest gratitude to *Prof. Dr. Karl G. Wagner* for giving me the opportunity to work in his research group, for his great support and his continuous encouragement and confidence. I also appreciate the given opportunity for participating scientific meetings.

I would especially like to thank *Dr. Ulrich Westedt* and *Dr. Jörg Rosenberg* from AbbVie for funding the research work. I would also like to express my gratitude to *Dr. Ulrich Westedt*, who has tirelessly supported the review process and contributed his scientific knowledge.

Many thanks to *Tim Lillotte* for deep scientific discussions, review of the manuscript, and always fun hours after a research workday.

A special thank you to *Dr. Marius Monschke* for the time spent together in the office, in the lab and the associated scientific discussions as well as funny conversations.

At *Barbara Schönfeld*, I would like to thank for the support and communication with AbbVie. Every visit to Bonn was always a pleasure.

I would like to express my gratitude to *Dr. Kathrin Schlanser* for scientific discussions, support for the manuscript and your great visits to Bonn.

Thank you *Dr. Álvaro López Mármol* and *Anna Krome* for the valuable collaboration and for the nice hours together.

I am very grateful to the working group, especially, *Christina, Anna, Alvaro, Tim B., Marius, Fabian, Jan, Barbara, Esther, Veronika, Bashar, Ozan, Roman, Dnyaneshwar, Mert, Tim L., Raphael, Liana, Kathrin, Martina, Alex, Jürgen* and *Birgit* for the wonderful time together and the introduction to the fantastic Bonner Karneval.

Personally, I would like to thank my *friends* and *family*, especially my parents and my siblings. Thank you for keeping me motivated all the time.

Very special thanks to my wife *Isabel* and my son *Johann*, who often had to spare me. In addition, you have given me limitless motivation and have always supported me throughout the years.

Table of Content

3.1.9	Comparison of BiPHa+ Assay with Established USP II/IV Biphasic Methods	28
3.2	Investigation of Organic / Aqueous Interfaces with Regard on Its Impact on Partitioning Rate	31
3.2.1	Interface Assessment	31
3.2.2	Influence of Interface Tension to Partitioning Rate.....	35
3.3	Modelling of Biorelevant Kinetics for a Ritonavir Hot-Melt Extruded Amorphous Solid Dispersion.....	38
3.3.1	Physical Explanations of the Complex <i>in vitro</i> Dissolution Kinetics for Ritonavir	38
3.3.2	Light Scattering Measurement as an Indicator of the Dynamic Behaviour of Small Nano-Droplets.....	41
3.3.3	<i>In silico</i> Model Fitting of Ritonavir <i>in vitro</i> Dissolution and Partitioning Kinetics	43
3.4	BiPHa+ Biphasic Dissolution Assay to assess <i>in vivo</i> Performance for poorly Soluble Drugs in six commercial enabling Formulations	53
3.4.1	Drug Properties	54
3.4.2	Dose Assessment.....	55
3.4.3	Drug Product Evaluation Using BiPHa+ Dissolution Assay	58
3.4.4	Pharmacokinetics and Compartment Analysis of <i>in vivo</i> Data	63
3.4.5	IVIVR: Compare Drug Partitioning during Dissolution and <i>in vivo</i> Absorption.....	65
3.4.6	<i>In vivo</i> Prediction from Biphasic <i>in vitro</i> Data and Prediction Error	67
3.5	Implementation of biphasic Dissolution Profiles in PBPK Models	75
3.5.1	Principals of Model Building and Evaluation.....	75
3.5.2	Model Building	77
3.5.3	IVIVE Using Organic Biphasic Partitioning Profiles.....	82
3.5.4	Predictive Performance of PBPK Models	87
3.5.5	Discussion	88
3.6	Systematic Evaluation and <i>in vivo</i> Prediction of ABT-102 Drug Products by using the BiPHa+ Assay	91
3.6.1	Assessing <i>in vivo</i> Relevance and Prediction Performance	91

Table of Content

3.6.2	ABT-102 Properties.....	92
3.6.3	Drug Product Evaluation by Using Biphasic Dissolution Assay	93
3.6.4	Compartment Analysis and IVIVR.....	96
3.6.5	Elimination and Distribution Model of Compartment Analysis and PBPK Modelling	97
3.6.6	Predicting of the <i>in vivo</i> Performance by Convolution and PBPK Modelling	98
4	Material and Methods	105
4.1	Materials.....	105
4.1.1	Drug Substances	105
4.2	BiPHa+ Setup	107
4.2.1	BiPHa+ Hardware.....	108
4.2.2	BiPHa+ Labview® Application	110
4.3	Rational Design of the Biphasic Dissolution Setup (BiPHa+).....	115
4.3.1	Hydrodynamic assessment.....	115
4.3.2	HPLC Method of Ritonavir	115
4.3.3	Equilibrium Solubility of Ritonavir	115
4.3.4	pKa Determination of Ritonavir	116
4.3.5	Comparison of the BiPHa+ Assay with Established USP II/IV Biphasic Methods	116
4.4	Investigation of Organic / Aqueous Interfaces with Regard on Its Impact on Partitioning Rate	118
4.4.1	Interface Assessment (Spinning Drop)	118
4.4.2	Influence of Interface Tension to Partitioning Rate	119
4.5	Modelling of Biorelevant Kinetics for a Ritonavir Hot-Melt Extruded Amorphous Solid Dispersion.....	121
4.5.1	Development of an Advanced Kinetic Model.....	121
4.6	BiPHa+ Biphasic Dissolution Assay to Assess <i>in vivo</i> Performance for Poorly Soluble Drugs in Six Commercial Enabling Formulations	122
4.6.1	Dose Assessment.....	122
4.6.2	Pharmacokinetics and Compartment Analysis of <i>in vivo</i> Data	122

Table of Content

4.6.3	Verification of <i>in vivo</i> Relevance and Predictive Power.....	125
4.7	Implementation of Biphasic Dissolution Profiles in PBPK Models.....	128
4.7.1	Methods.....	128
4.7.2	Drug Dossiers for Developing PBPK Models.....	128
4.8	Systematic evaluation and <i>in vivo</i> prediction of ABT-102 drug products by using the biphasic dissolution model.....	130
4.8.1	Materials.....	130
4.8.2	Physicochemical Characterisation.....	130
4.8.3	Extrudate Preparation.....	130
4.8.4	BiPHa+ Assay.....	131
4.8.5	<i>In vivo</i> Study.....	131
4.8.6	Compartment Analysis and IVIVR.....	131
4.8.7	Predicting of the <i>in vivo</i> Performance by Compartment Analysis.....	132
4.8.8	Predicting <i>in vivo</i> Performance by PBPK Modelling.....	132
5	Conclusion and Outlook.....	134
5.1	Conclusion.....	134
5.2	Outlook.....	137
	References.....	139

1 Introduction

1.1 New Chemical Entities: Classification and Challenges

Early drug candidates are chosen by high-throughput screening and rational drug design to generate a sufficient potency, selectivity and ADME properties [1,2]. During the optimization of a lead compound, molecules increase in their lipophilicity and respectively decrease in their aqueous solubility [3]. The percentage of poorly drug candidates (Figure 1, Class 2) having a micromolar and nanomolar activity is higher than 60 % (Figure 1). In the course of clinical investigation from phase 1 to 3, the number of drug candidates struggling with solubility issues decrease and reach < 30 % for approved drugs (Figure 1). In short, one important reason for a clinical failure represents limited solubility [4].

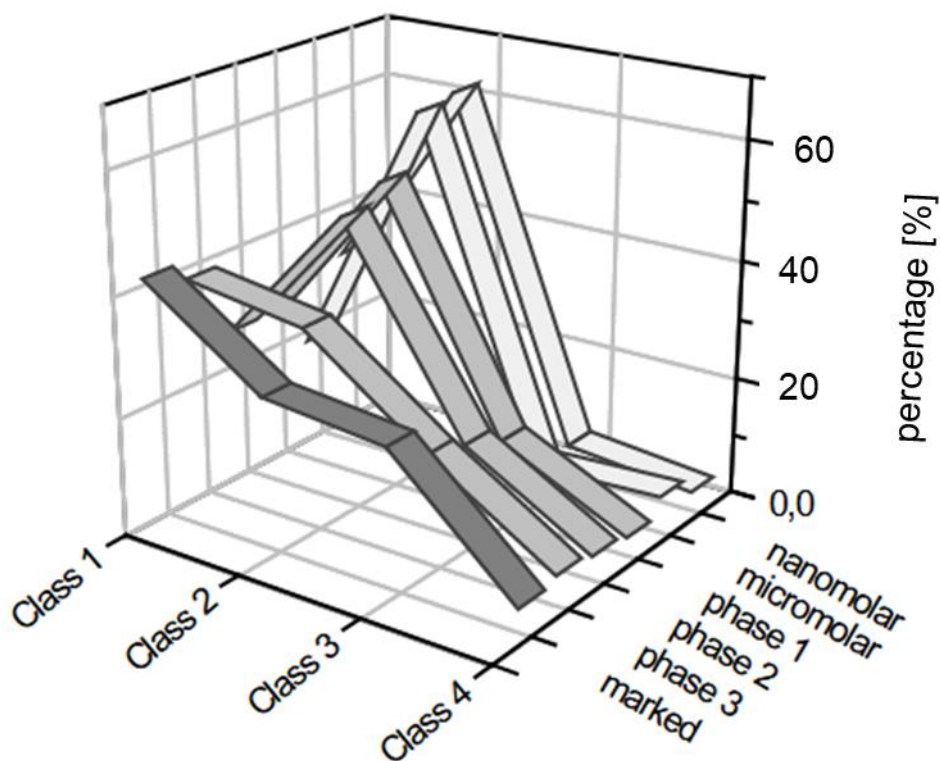


Figure 1: Categorization of drugs in a BCS-based (Class 1-4) provisional classification system: preclinical highly active compounds (nanomolar, micromoles), clinical development (Phase 1 - 3) and marked drugs.[4]

The biopharmaceutical classification system (BCS) was developed to categorize newly developed drugs with regard to their biopharmaceutical and physiological properties [5]. The BCS defines four categories depending on lowest solubility in 250 ml or less of aqueous media over the pH range of 1.2 – 6.8 at 37°C and intestinal permeability based on absorption extent [6]:

- (1) Class 1: high solubility, high permeability (absolute bioavailability > 85 %)
- (2) Class 2: low solubility, high permeability (absolute bioavailability > 85 %)
- (3) Class 3: high solubility, low permeability (absolute bioavailability < 85 %)
- (4) Class 4: low solubility, low permeability (absolute bioavailability < 85 %)

The BCS system represent a simple and effective framework to consider key factors affecting *in vivo* performance [7]. However, the classification system has some limitations in formulation development: Solubility in buffer media, unknown dose during early stage development and permeability requires human *in vivo* data [8].

Some modifications of the BCS have been proposed to improve the suitability in formulation development. The quantitative biopharmaceutical classification system (QBCS) categorizes drugs using P_{app} of CaCo-2 cells and dose / solubility ration [9]. In the Biopharmaceutics Drug Disposition Classification System (BDDCS) metabolism of a compound is assumed as an indicator for high permeability [10]. Tsume et al. expand the BCS system of low soluble drugs Class 2 and 4 in acids (a), bases (b) and neutral compounds (c) [11]. The f_{abs} classification system categorizes low soluble drugs in three classes: dissolution rate limited absorption, permeability limited absorption and solubility – permeability limited absorption [12].

A further developed BCS system for a more pragmatic applicability in early stage formulation development, the Developability Classification System (DCS, Figure 2) was proposed [7]. The intestinal solubility is estimated in 500 ml FaSSIF (Fasted state intestinal simulating fluid) and predicted permeabilities are used for the categorization. Compared the BCS class 2, the compensatory power of permeability towards poorly soluble drug is considered (2a, dissolution rate limited), which can be improved by particle size reduction approaches. Class 2b are very poorly soluble (solubility limited) so that an improved solubility using enabling formulation approaches is obligatory to enable sufficient bioavailability. The refined Developability Classification System (rDCS) is suggested to additionally consider the unknown dose of a NCE by investigating a dose range and advanced characterization methods leading a risk assessment of the respective drug [8,13].

DCS class 1 and class 3 are developed by conventional formulation. Poorly soluble drugs are formulated as enabling formulation. The aim of enabling formulations is to enhance solubility (2B, 4) or dissolution rate (2a) and respectively absorption. Optimally, a Class 2b compound become a class 2a or class 1 compound and a class 4 become a class 3 compound by using a suitable formulation approach (Figure 2). An increased apparent permeability is often observed as a result of the increase in solubility [13].

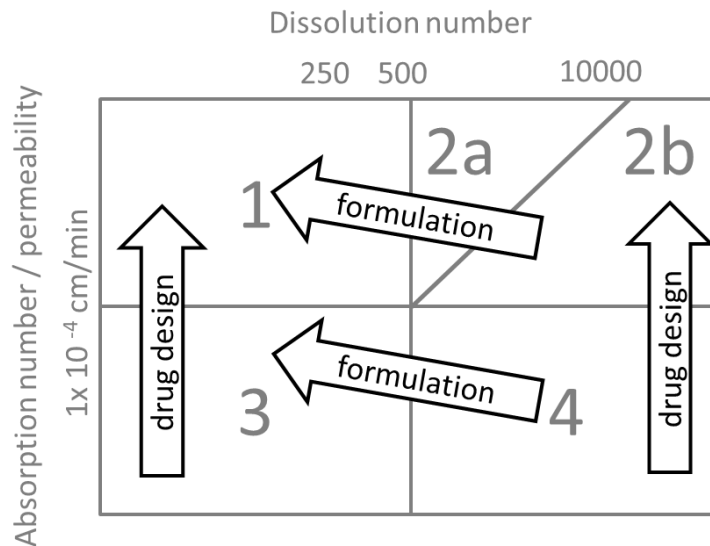


Figure 2: Developability classification system including class 2a (dissolution rate limited) and 2b (solubility limited) and possible optimisations by formulation and drug design (black arrow).

1.2 Enabling Formulations

Various approaches have been developed to enhance oral bioavailability of poorly soluble drugs (DCS class 2a, 2b and 4). These approaches aim to enhance solubility or dissolution rate into the gastrointestinal tract [3]. Figure 3 displays commonly used formulation approaches including a categorisation of the solid state drug characteristics.

Introduction

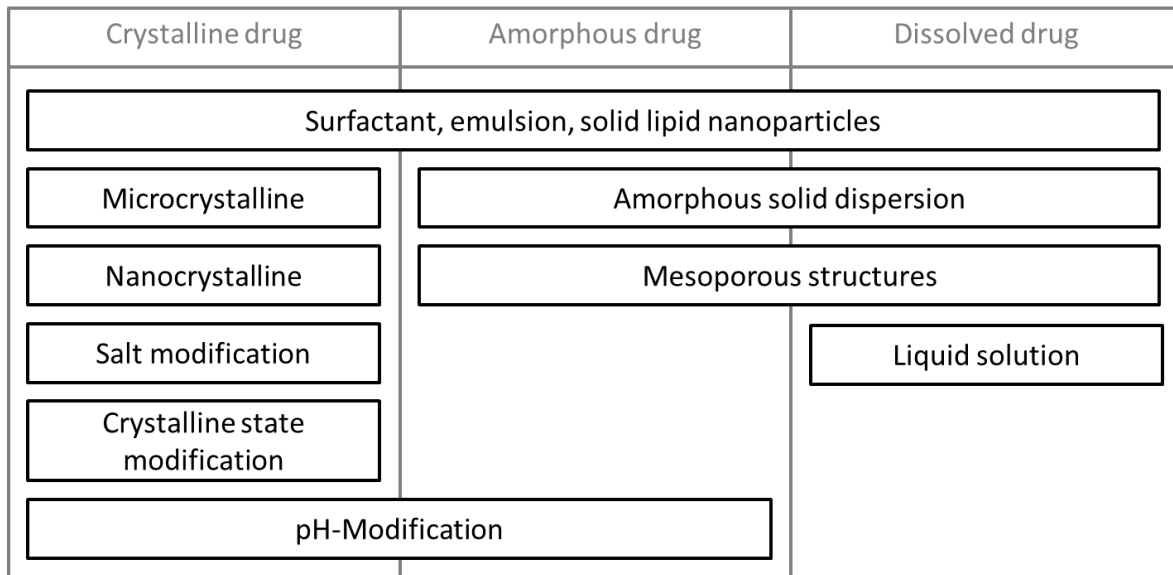


Figure 3: Formulation principles to improve solubility of poorly soluble drugs. Each formulation approach is categorized with regard to its solid state.

Crystal state can be modified to enhance the solubility of a drug. The solubility of a metastable polymorph is higher than the solubility of the thermodynamically stable polymorph [14]. Salt forming can lead to improved biopharmaceutical properties compared to the free drug [15]. Some co-crystals and solvates demonstrate improved dissolution behaviour [16,17].

Particle size reduction of $< 5 \mu\text{m}$ leads to an increased dissolution rate and particles $< 1 \mu\text{m}$ accelerate their dissolution rate and increase their solubility [18,19]. Microparticle ($< 5 \mu\text{m}$) formulations are produced by dry milling. Nanoparticles ($< 1 \mu\text{m}$) are formulated including surfactant and polymeric colloids for stabilization by wet milling, controlled precipitation or high pressure homogenization. To immobilize the nano-suspension and to decrease Ostwald ripening, the liquid suspension is often spray-dried, coated on pellets or lyophilized forming a crystalline solid dispersion [20].

The solubility of an amorphous drug is higher compared to the corresponding crystal form [21]. To this end, the amorphous drug is molecularly dispersed or dissolved in a water-soluble polymer matrix. This formulation is in the most cases kinetically stabilized [22].

Solid or liquid solutions can achieve an increase in solubility and dissolution rate [23]. Liquid solution consist of co-solvents which are directly formulated as oral liquid or are immobilized on mesoporous structures [24,25]. The most common way of formulating poorly soluble drugs is the amorphous solid dispersion (solution), using a polymeric matrix. If the drug is dissolved below the drug solubility in the polymer, the formulation will be stable. A supersaturated solid polymer solution is kinetically

stabilized since phase separation or crystallization can occur [22]. Amorphous solid dispersion are prepared by melting methods (hot melt extrusion) or solvent evaporation methods (spray drying, super critical fluid extraction in organic solutions) [26].

Surfactant can act as a surface-active agent increasing the drug substance dissolution rate and solubility. When a surfactant concentration is above the critical micellar concentration, micelles or liposomes arise which solubilize the drug in the nonpolar region [23]. Dispersed systems of two immiscible phases stabilized by surfactant are successfully applied for bioavailability enhancement. These surfactant related formulation approaches are often designed as emulsion, self-emulsifying drug delivery system or solid lipid nanoparticles [27,28].

Cyclodextrins increase the apparent solubility by complexation of a lipophilic drug [29]. Microenvironmental pH modulation can improve bioavailability of weak bases [30].

Dissolution assays strongly guide formulation and process development because it potentially serves as surrogate parameters for *in vivo* performance. All described enabling formulation approaches demonstrated a remarkable complexity. High complexity of formulations and low solubility of the drugs make it difficult to predictively characterise the formulations by *in vitro* approaches.

1.3 Biopharmaceutics – Gastrointestinal Physiology

The LADME-model [31] summarizes the drug compound behaviour in the human body and the body's respective responses. Liberation (L) is the disintegration and dissolution of a formulation, which can be actively influenced, resulting in an absorbable composition. Absorption (A) is a passive or active membrane passage. Then, the absorbed drug distributes (D) in various body compartments. Metabolism (M) or biotransformation describes an irreversible process of the original NCEs into an active or inactive metabolite. Excretion (E) is the irreversible removal of a drug from the body. The combination of all pharmacokinetics and pharmacodynamics results in a therapeutic effect [32].

Oral application of NCEs is the most common route of application. Drug absorption through oral administration into the blood stream involves a highly complex process and is mostly influenced by four main factors [31,33,34]:

- a) Gastrointestinal anatomy
- b) Intraluminal environment
- c) Physiochemical properties of the NCE
- d) Formulation design

The human gastrointestinal tract is a tube from mouth, oesophagus, stomach small intestine, colon to rectum. Liver, gall bladder and pancreas are directly associated to the gastrointestinal tract. An overview of gastrointestinal absorption area, pH, volume and transition time are presented in Figure 4 and Table 1.

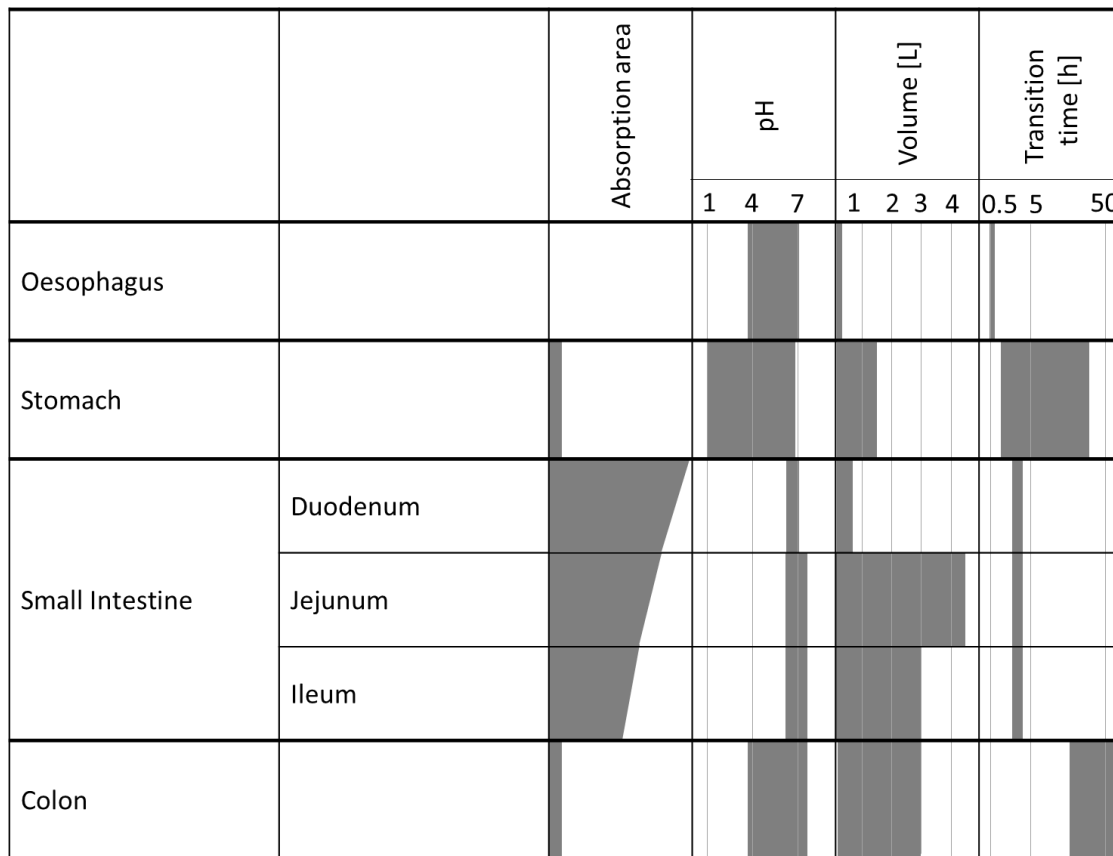


Figure 4: Schematic overview of gastrointestinal absorption area, pH, volume and transition time

Absorption in the stomach is neglectable for the most drugs. The small resorption area and the adherent mucus layer, which protects the stomach from self-digestion prevents absorption [35]. Gastric pH, transition time and chyme composition play an important role for the small intestine passage and absorption of the drug in the small intestine [31]. In the fasted state, the gastric pH is reported between 1.5 and 3.3 having a buffer capacity of $14.3 \text{ mmol L}^{-1} \text{ pH}^{-1}$ [35,36]. The duration of gastric

emptying is a period of 0.5h in the fasted state [37]. In the postprandial state, pH (elevated up to pH 7) and buffer capacity are initially similar to a previously ingested meal. Reacidification and gastric emptying strongly varies and a pH of < 2 is reached in average after 3 - 6 h [38]. Gastric content volume in fed state is 650ml and 30 ml in the fasted state [38,39].

The small intestine is divided in three sections: Duodenum, Jejunum and Ileum. Pancreatic digestive juice and bile is secreted in the Duodenum. Due to the high surface of 60 - 200 m², the duodenum represents the main absorption area [32,34]. This maximisation of absorption area is caused by the so-called villi shape and the micro-villi of the enterocytes. The complete small intestine transition time of 4 – 5 h is similar in the fasted and fed state [37,38]. While reaching the duodenum, bile and pancreatic juice elevates the pH to 6.1 in the fasted state and to 4.8 – 6.5, depending on the ingested meal, in the fed state [40]. pH increased steadily in both fasted and fed state to 7. The upper intestine fasted state liquid volume is reported between 50 - 100 ml. In the postprandial period comparable liquid volume is found [39,41]. Generally, absorption and secretion are a dynamic turnover, which explains these findings. Total bile salt content is highly variable. Bile salt content is higher in the fed state; ranging from 3.7 mM to 7.7 mM, whereas a median value of bile salts, one hour after a meal, is 18.2 mM [34]. Bile salt / phospholipids ratios have been reported to be 11.5 in the fasted state and a value of about 3.4 for the fed state. Buffer capacity in fasted state (10 mmol L⁻¹ pH⁻¹) is significantly smaller than in the fed state (25 mmol L⁻¹ pH⁻¹) [34,42].

Orally administered drugs are hardly absorbed in the Colon [34]. In this region only water and electrolytes are absorbed. pH range of 6 to 8, filling level and luminal composition depend strongly on the ingested meal [33].

Before a drug reaches the systemic blood stream, metabolism by CYP- and other enzymes can occur in intestine enterocytes and during the liver passage. The so called first pass metabolism eliminates drug compounds via phase 1 and phase 2 metabolism. The distribution of CYP-enzymes along the intestine differs. Hepatic enzyme distribution is strongly different compared to the intestine and the hepatic metabolism is dominant for the total drug metabolism [43]. CYP 3A4, CYP 2D6 and CYP 2D9 are the most frequent metabolizing enzymes. Both, hepatic and intestinal metabolism play an important role for bioavailability of a drug [44].

In the preclinical evaluation of enabling formulations for the selection of the most promising formulation approaches, the dog model is widely used [45]. The pH-profile of dogs and human are highly comparable, if the dog is pre-treated with gastrin

(Table 1). Small intestinal transition time and gastric emptying time slightly differ (Table 1). However, absolute bioavailability do frequently not correlate with human data, which is likely associated to differences in species specific metabolism [46,47]

Table 1: Overview of pH value in the stomach and in the small intestine; gastric emptying time (GET) and small intestine transition time (SITT) in human and dog [34,37,46]

	Human		Dog	
	Fasted	Fed	Fasted	Fed
GET [h]	0.5	6	0.6 0.9 (gastrin)	2.9
pH stomach	1.5 – 1.9	2 – 6.5 (2 h)	2.0 - 8.0 1.0 (gastrin)	2.0 - 6.0 (2h)
SITT [min]	4.1	5.0	1.4 1.7 (gastrin)	1.9
pH small intestine	6.1 – 7.0	4.8 – 7.0	6.5 – 8.0	6.0 – 8.0

1.4 Biopharmaceutics – Mechanism of Drug Absorption

Orally administered drug substances must pass the gastrointestinal membrane of enterocytes to enter the systemic blood stream. The enterocytes cell membrane is a phospholipid bilayer, which is highly permeable for rather lipophilic and not ionized drugs. This phospholipid bilayer is associated with membrane proteins, which form channels, transporters or carriers and pumps (p-gP) [32,48]. This membrane proteins enable an absorption of rather hydrophilic molecules [49].

Passive diffusion is the major mechanism of drug absorption of lipophilic unionized drugs. The driving force of this mechanism is the concentration gradient across the phospholipid bilayer between a donor (lumen) and an acceptor phase (cytosol) (Figure 5). The mass transport (dM) across the membrane depends on the thickness of the membrane (x), the absorption area (A), the diffusion coefficient (D), the distribution coefficient (K) and the concentration gradient between donor and acceptor phase ($C_d - C_a$). The permeability (P) of a drug is compound specific and recognizes diffusion, distribution and thickness of the membrane [48]. Based on this mathematical expression, the drug absorption rate will be high, if the drug is highly soluble and highly lipophilic. These properties are complementary and must be concerned in drug and formulation development.

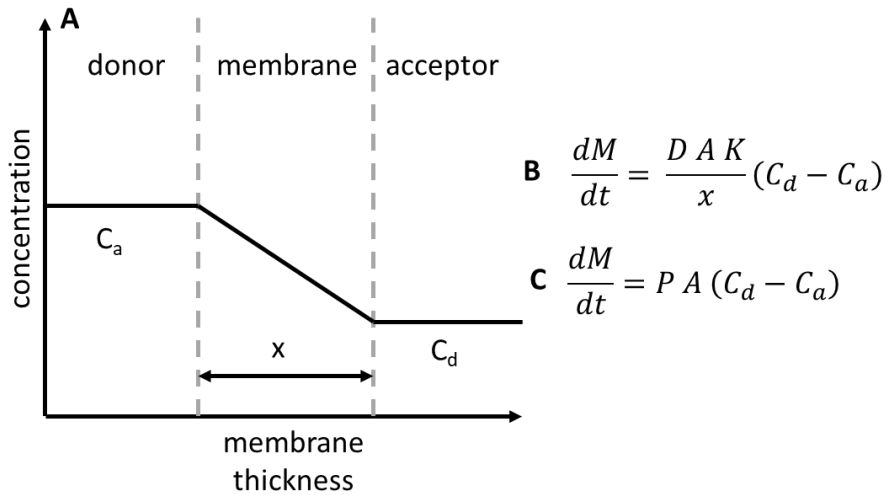


Figure 5: (A) Concentration gradient across a membrane (x) with drug concentration of donor (C_d) and acceptor (C_a) phase; (B) mass flow (dM) over time (dt). D is the diffusion coefficient. A is the absorption area and K is the distribution coefficient; (C) mass flow (dM) over time (dt) expressed by using the permeability (P) coefficient [48].

Some drug substances have higher or lower absorption rates as expected from simple passive diffusion. This behaviour is caused by active or passive transport proteins or first pass metabolism.

Physiochemical properties of a drug substance affect the oral absorption, which are categorized in the developability classification system (section 1.1). A higher solubility increases the absorption rate by increasing the concentration gradient. Solubility depends on pK_a values, salt type, solid state, particle size, lipophilicity (LogP) and composition of the chyme. A higher absorption rate is associated with a high permeability. Permeability is influenced by the chemical structure, lipophilicity (LogP) and of being a substrate of any transport protein [31,32].

The poor solubility of NCEs requires advanced technologies to enhance solubility and subsequently bioavailability [3], because molecularly dissolved drug is mostly the only species permeating through the intestinal membrane [50]. The generation of a drug solution depends on the enabling formulation type (section 1.2). Figure 6 presents an overview of different drug species appearing in the gastrointestinal dissolution process. These mechanisms can be classified in three categories:

- (1) Disintegration and Dissolution: If an oral formulation gets in contact with aqueous intestinal media, it will disintegrate in fine particles [31]. The fine crystalline or dispersed (drug) particles dissolve subsequently. If the formulation is an ASD, the formulation will dissolve simultaneously with the drug leading sometimes in a supersaturated solution or disperses in undissolved drug particles [51]. Particle size reduced formulations dissolve faster caused by an increased surface area. Carrier systems (cyclodextrins) and the complexed drug dissolve simultaneously [29,52]. The kinetic of these dissolution behaviours is majorly influence by formulation principal as well as by the gastrointestinal environment.
- (2) Apparently dissolved drug consists of molecularly dissolved drug and solubilized drug (micelles, complex cyclodextrins) [21,50,53]. Most likely truly dissolved drug contributes to the majority of bioavailable drug [50,54].
- (3) Supersaturated solutions of drugs are thermodynamically unstable and precipitate as undissolved drug particles [21,53]. Gastrointestinal composition and pH can additionally cause precipitation (weak base) or dissolution (acid) during the gastrointestinal passage. There are different types of precipitate species: drug rich nanoparticles or amorphous and crystalline drug particles, which can transform in thermodynamically more stable states over time. All these species can have different solid state properties and re-dissolution kinetics, which in turn plays an important role for oral bioavailability [21].

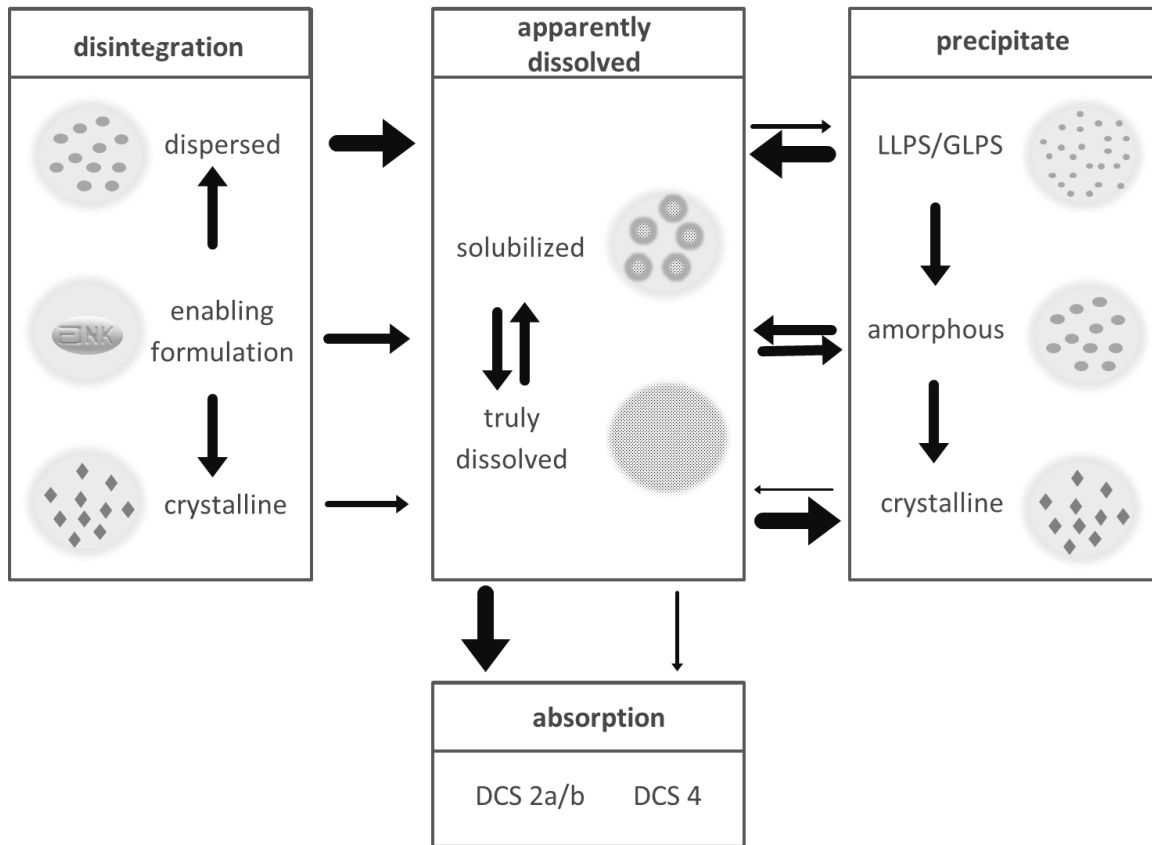


Figure 6: Processes taking place during gastrointestinal dissolution of drugs formulated as various enabling formulations. The thick arrows illustrate a favourable process. Disintegration: depending on the formulation type, the formulation disintegrates or disperses and dissolves in aqueous media. Apparently dissolved: The dissolved drug is either truly dissolved in aqueous media or is solubilized by complexes, surfactant or cyclodextrins. Precipitate: As the drug was prior in solution, the precipitate has different physical properties compared to the origin formulation. The morphology and solid state can change over time. Absorption: Depending on drug permeability, the drug is mostly absorbed in the intestine.

1.5 Dissolution Assay

Dissolution of a standard oral solid dosage form consists of two mechanisms:

- (1) Drug Release: An immediate release dosage form disintegrates in small particles. A modified release dosage form releases drug through erosion or diffusion [55,56].
- (2) Drug Dissolution: The drug rapidly dissolves in the aqueous medium.

The original idea of quality control dissolution testing was to demonstrate batch to batch consistency of drug release in aqueous media, which is characterized as rate limiting step [57]. Additionally, dissolution provides a surrogate parameter for *in vivo* performance for formulation and process development [57]. To characterize a drug

product meaningfully, sink conditions, where the saturation solubility of a drug is three to five times higher than the final drug concentration in the dissolution medium, are obligatory [57,58]. DCS 2 drugs are limited in their aqueous solubility, which led to a challenging dissolution method development because dissolution and not drug release is might evolve artificially to the rate limiting step. Additionally, modern enabling formulation technologies are more complex in their dissolution behaviour, so that compendia methods do not sufficiently reflect drug product performance. By using standard methods several modifications are applied to prevent this sink limitation: Adding surfactant, using large volumes of dissolution media, cosolvents or pH-adjustment [58].

Compendia dissolution apparatus for oral dosage forms are basketed apparatus, paddle apparatus reciprocating cylinder and flow-through cell (Figure 7). Temperature is kept constant in all apparatuses at 37° Celsius [59,60]. Paddle, basket, flow through and reciprocating cylinder apparatus are described in the following:

Paddle (apparatus 2, USP and PhEur) and basket (apparatus 1, USP and PhEur) apparatus consists of a vessel with a volume of 500 – 2000 ml. The paddle of apparatus 2 is the stirring element and the formulation is placed under the stirrer (Figure 7A). In the basket apparatus, the formulation is placed in the rotating basket, which causes hydrodynamics (Figure 7B). Apparatuses 1 and 2 are the most frequently used methods in the pharmaceutical industry [32,59,60].

The flow through assay (apparatus 4, USP and PhEur) consists of a pump with standard flow rates between 4 and 16 ml/min (Figure 7C). The drug product is placed into the cell and the assay can be run in an open or closed loop (Figure 7C). Poor solubility of a drug can be compensated by an increased dissolution volume. [32,59,60].

The reciprocating cylinder (apparatus 3, USP and PhEur) consists of a set of cylindrical, flat-bottomed glass vessels with 250 ml dissolution media, and glass reciprocating cylinders moving 10 cm up and down (Figure 7D). Major advantages of this method are the mechanical stress of the reciprocating cylinders movement and the easy media change [32,59,60].

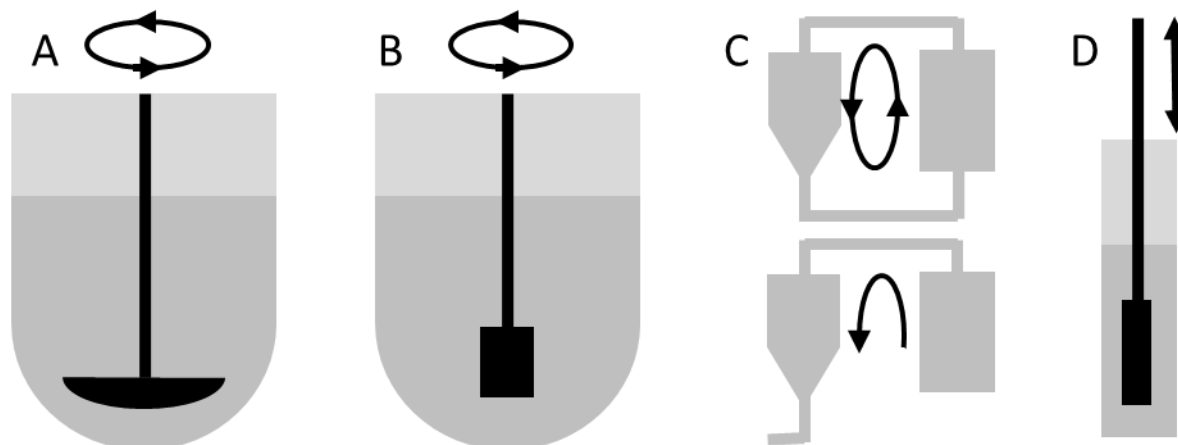


Figure 7: Overview of standard dissolution apparatus described in various pharmacopoeias for oral solid dosage forms (A) Paddle apparatus, (B) basketed apparatus, (C) Flow through cell, (D) Reciprocating cylinder apparatus.

The complexity and composition of aqueous dissolution media strongly depends on the requirements of the assay. A quality control method focuses on discriminatory power towards critical quality attributes [57]. To achieve this requirement the pH of any media has to be between pH = 1.0 to 6.8 (7.4). During earlier formulation development phases there are more *in vivo* relevant dissolution media necessary. Clinically relevant dissolution methods link *in vivo* data to *in vitro* data by any appropriate media [57]. Biorelevant dissolution media simulated gastrointestinal environment to guide formulation selection and optimisation [57]. Choosing an appropriate media during formulation development depends on drug properties. The degree of biorelevance of a certain dissolution medium is categorized in level 0 – 3. Level 0 media just have the pH range of the GI tract and is suitable for highly soluble DCS 1 and 3 compounds [61]. Level 1 considers pH and buffer capacity to evaluate pH dependant food effects of a DCS 1 and 3 compounds [62]. Additionally, to pH and buffer capacity, Level 2 media consists of bile components, lipids and considers osmolality (e.g.: FaSSIF, FeSSIF). Level 2 media are useful to characterize DCS 2 and 4 compounds [61]. Level 2 media dissolution results can be integrated into *in silico* tools to estimate *in vivo* performance [63]. Level 3 media consider additionally the intestinal enzymes and viscosity to simulate digestive processes, which is important for the characterisation of lipid based formulations and drugs degradation (e.g. peptides) [61].

The dissolution apparatus type used in quality control and clinically relevant dissolution methods typically consist of standard apparatuses. Contrary, biorelevant apparatuses are sometimes more complex to imitate the GI passage [64]. These advanced assays are necessary, because traditional assays have not led to the desired success of *in vivo* predictivity. Many biorelevant dissolution apparatuses are

customized and no standardized methods are currently available [64]. Basically, biorelevant dissolution assays can be categorized in single phase aqueous models and absorption sink models [32]. Single phase aqueous model simulate the GI passage with pH changes, transfer models and biorelevant media [64]. These assays are conducted under non-Sink conditions to evaluate enabling formulations of DCS 2 and 4 compounds. A major disadvantage of single phase aqueous assays are the established equilibrium of undissolved and dissolved drug species, which lead sometimes to an insufficient performance characterisation [58]. Dealing with this limitation, absorption assays are proposed [58]. Absorption assays consist of an aqueous donor phase, where the drug is allowed to dissolve under non-Sink conditions and an acceptor compartment, where the drug is allowed to partition in an absorption Sink media. The aqueous phase simulates the GI passage. The acceptor compartment either is an organic solvent (Figure 8A) or an aqueous media (Figure 8B). The aqueous acceptor phase is separated with a membrane from the donor phase [65,66]. The advantage of absorption (Sink) assay is the dynamic characterisation of enabling formulation leading to a more biorelevant surrogate parameter for oral drug absorption.

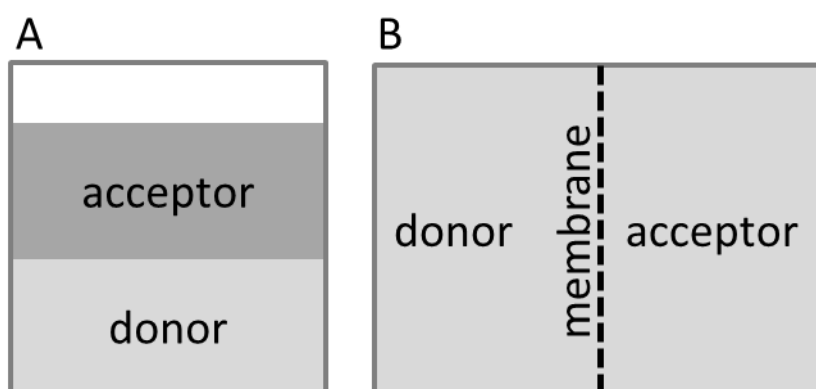


Figure 8: Dissolution absorption model: (A) Absorption model with an aqueous donor and organic acceptor medium; (B) Absorption assays with a membrane and two aqueous compartments.

1.6 Biphasic Dissolution Assay

The biphasic dissolution assay is a absorption assay with an organic acceptor medium and an aqueous dissolution donor medium (Figure 7A), which provide a high discriminatory power of enabling formulations with regard to their *in vivo* performance [67–69]. The assay combines a relatively simple *in vitro* assay with a high degree of biorelevance, because the flux through the interface is comparable to the flux through the gastrointestinal membrane (Figure 5) [58]. To achieve the high discriminatory power of the biphasic assay, some key parameters have to be controlled: hydrodynamics, media compositions, pH-profile and geometrical design of

the vessels [70,71]. The experimental setup reported in literature consists of various standard dissolution paddle apparatus, a combination of paddle and flow through apparatus or customized apparatus [65]. Dissolved drug is quantified either by HPLC or in line UV-Vis spectroscopy.

For the experimental procedure, the formulation of a poorly soluble drug is allowed to dissolve in an aqueous Non-Sink media. The aqueous media can be a simple buffer medium or a GI-passage simulating complex mixture [67,72]. Octanol is the commonly used organic acceptor medium of choice because of its desirable physical chemical properties and many poorly soluble drugs are acceptable soluble to maintain Sink conditions [73]. To assess the performance of the biphasic dissolution assay, either the organic layer or the sum of organic and aqueous layer is used as *in vivo* surrogate.

1.7 Pharmacokinetics

Pharmacokinetic describes mathematically the kinetic behaviour of a drug in the human body. For this, several processes such as absorption or elimination can be described by differential equations. The theoretical or physiological based body segments such as plasma or liver are described by so called compartments.

Compartment models describe and parameterize plasma concentration time profiles of a drug in the body. A kinetic first order is commonly assumed to describe each sub-process. A differential equation (Equation 1) describes the change of plasma concentration (dC_p) in a certain time (dt), which is proportional to the rate constant (k_e) and the plasma concentration (dC_p) [33]. Equation 1 represents the elimination for a bolus intravenous injection for an one-compartment model.

$$\frac{dC_p}{dt} = -k_e \cdot C_p \quad \text{Equation 1}$$

After the integration of Equation 1, the plasma concentration at every time can be calculated by an exponential function (Equation 2).

$$C_p(t) = C_0 \cdot e^{-k_e \cdot t} \quad \text{Equation 2}$$

After an oral administration, the drug substance has to pass the intestinal membrane. An additional first order absorption process has to be considered. The differential equation of the oral one compartment model includes the absorption process with the rate constant (k_a) and the plasma concentration (C_p). Elimination is equal to Equation 1 [31,32,48].

$$\frac{dC_p}{dt} = k_a \cdot C_p - k_e \cdot C_p \quad \text{Equation 3}$$

The integration of Equation 3 leads to the Bateman function, which describes the time depending plasma concentration profile of an orally administered drug. The Bateman function considers bioavailability (F), dose (D) and distribution volume (V_d) [31,32,48].

$$C_p(t) = \frac{F \cdot D}{V_d} \cdot \frac{k_a}{k_e - k_a} \cdot (e^{-k_e \cdot t} - e^{-k_a \cdot t}) \quad \text{Equation 4}$$

The oral two compartment model considers additional to Equation 4 and distribution step of a drug in a peripheral, additional compartment such as fat tissue or plasma protein binding (Equation 5), which is described in the derivative function by the disposition rate constant k_λ and the plasma concentration. Distribution occurs especially with hydrophobic drugs [33].

$$\frac{dC_p}{dt} = k_a \cdot C_p - k_\lambda \cdot C_p - k_e \cdot C_p \quad \text{Equation 5}$$

The area under the curve (AUC) is the integral of plasma concentration time profile ($C_p(t)$) and can be interpreted as drug exposure over a time period, which is proportional to absorbed drug quantity, which is also called fraction absorbed (f_a) [31,32,48].

$$AUC = \int_0^{\infty} C_p(t) dt \quad \text{Equation 6}$$

The volume of distribution (V_d) is defined as theoretical volume that would be necessary to dissolve the total absorbed drug quantity (D) in the observed plasma concentration (C_0) with $t = 0$ [31,32,48].

$$V_d = \frac{D}{C_0} \quad \text{Equation 7}$$

The absolute bioavailability of an oral administered compound is defined as ratio of the AUC of the oral administered compound and the AUC of intravenously administered drug compound. The absolute bioavailability comprises administered dose (D), fraction absorbed (f_a) and fraction which is not metabolized by first pass (f_{fp}) [31,32,48]:

$$F = \frac{AUC_{oral}}{AUC_{iv}} = D \cdot f_a \cdot f_{fp} \quad \text{Equation 8}$$

1.8 *In vitro* / *in vivo* Correlation

To assess dissolution profiles with regard to their *in vivo* performance, *in vivo* absorption profiles are necessary to perform this comparison. There are different methods to calculate the *in vivo* absorption time profiles from *in vivo* plasma concentration time data.

- (1) Based on compartmental models, the absorption profile is calculated by residual method.
- (2) Wagner Nelson (one compartment, Equation 9), and Loo-Riegelmann (two compartment) considered the total mass balance in the body:

Absorption (X_a) = Quantity in body (C_p) + eliminated quantity ($k_e \cdot \int_0^t C_p dt$)

$$X_a = \frac{C_p + k_e \cdot \int_0^t C_p dt}{k_e \cdot \int_0^\infty C_p dt} \quad \text{Equation 9}$$

- (3) Numerical deconvolution (Equation 10): $C\delta(t)$ is the impulse response which are figured by an oral or intravenous solution and $I_Q(t)$ are the arbitrary impulses which can be interpreted as the rate of released/absorbed drug [37]. The calculated *in vivo* dissolution is the sum of all unit impulse responses ($Q(t)$ vs. t). Each impulse $I_Q(t)$ decreases following the single impulse function $C\delta(t)$. The single impulse function $C\delta(t)$ can be expressed by one, two or n compartment models.

$$Q(t) = I_Q(t) * C\delta(t) \quad \text{Equation 10}$$

$$= \sum I_Q(t - t_n) - C(t - t_n)_{elimination}$$

In vivo in vitro correlation (IVIVC) is a predictive mathematical model describing the relationship between an *in vitro* performance of a dosage form and an *in vivo* response [74]. This model correlates the *in vivo* absorption and the *in vitro* dissolution directly to each other. In the case of the biphasic dissolution assay the IVIVC is sometimes called *in vivo in vitro* relationship (IVIVR). Three main levels of an IVIVC are defined:

- (1) Level 1: Correlation of dissolution profiles and absorption profile
- (2) Level 2: Correlation of mean dissolution time and mean absorption time
- (3) Level 3: Correlation of two single values of dissolution (dissolution rate, C_{max} , $C(90 \text{ min})$, etc.) and absorption (C_{max} , AUC, t_{max} , etc.)

1.9 *In silico* Approaches

Physiological based pharmacokinetic modelling (PBPK) software are *in silico* tools, which try to simulate *in vivo* performance of a drug based on physiological, anatomical structures and the biochemistry of the body combined with drug and formulation properties. These structures are simulated by multi compartmental models. The aim of these PBPK software are the prediction of pharmacokinetics of drug candidates to support formulation development [75–77]. Currently there are various PBPK software packages available such as PK-Sim[®], GastroPlus[®] or Simcyp[™] [78].

1.10 Pharmacokinetic Prediction of *in vivo* Performance Based on Dissolution Data

The pharmacokinetic of drug formulations can be predicted based on *in vitro* dissolution data. There are two approaches to perform a prediction: either pharmacokinetics can be calculated based on an previously established IVIVC / IVIVR [79] or experimental *in vitro* data can be implemented into PBPK tools [78].

Based on IVIVCs, retro-IVIVCs can be used to predict the *in vivo* pharmacokinetic using dissolution profiles. By using observed *in vivo* data of a certain number of formulations containing the same drug and their dissolution data, an IVIVC can be established. In order to make a prediction of a unknown formulation not tested *in vivo*, the pharmacokinetics can be calculated by applying the IVIVC retrospectively and then convolute the data [80].

Linking PBPK models with dissolution results is an additional approach to estimate *in vivo* performance of the investigated formulation. To enable a pharmacokinetic prediction, properties of the respective drug, an intravenous elimination model and an absorption model are necessary. The dissolution data can be implemented either directly or as a mathematical dissolution model of the drug [75–77].

2 Scope and Objectives

During early formulation development of oral solid dosage forms reliable screening assays are needed to develop enabling formulations which provide suitable biopharmaceutical performance. State of the art screening tools focus on supersaturation, which do not cover the entire dynamic dissolution process of complex enabling formulations. Many animal studies are currently obligatory to evaluate and to select suitable formulations. The present thesis investigates the biphasic dissolution assay as a formulation screening tool, which is able to guide formulation development even for small formulation quantities and potentially to reduce animal studies. To develop and evaluate the performance of the assay the following work packages were investigated:

- (1) Developing a small scale and, fully automated biphasic assay, which is able to quantify dissolved drug in aqueous and organic media *in line*. The development is guided by literature data to fulfil requirements of high degree of *in vivo* predictive power (3.1)
- (2) Investigation of organic / aqueous phase interfaces with regard on its impact on partitioning rate (3.2)
- (3) Enhancing mechanistic and kinetic understanding of enabling formulation approaches to provide superior bioavailability (3.3)
- (4) Evaluation and validation of the biphasic dissolution assay by means of various poorly soluble drugs formulated by different enabling formulation approaches with regard to *in vivo* performance (3.4)
- (5) Integration of biphasic dissolution results into *in silico* tools to enable rapid estimation of the resultant pharmacokinetics (3.5)
- (6) Systematic formulation screening based on the developed workflows to predict *in vivo* performance and enable a meaningful prototype selection (3.6)

3 Results and Discussion

3.1 Rational Design of the Biphasic Dissolution Setup (BiPHa+)

A general purpose of the present study was to combine the advantages of a small scale one vessel method as a useful tool in formulation screening [67,72,81] and the proven biorelevance of the USP apparatus II and USP apparatus IV model combination [69,82–84]. A detailed technical description of all hardware and software components is provided in section 4.2. Ritonavir and Ritonavir formulations were used as model compounds.

3.1.1 General Model Design

The dissolution method was designed considering the following scaling factors, which were intended to be essential to describe a biphasic dissolution method:

1) Ration of surface to volume: $X = \frac{\text{aborption area}}{\text{aqueous volume}}$ Equation 11

2) Volume ration: $R_V = \frac{\text{volume organic phase}}{\text{volume aqueous phase}}$ Equation 12

3) Concentration of API

The BiPHa+ apparatus (Figure 9) contains four vessels: one blank and three sample vessels in a water bath at $37^\circ\text{C} \pm 0.5^\circ\text{C}$. Each vessel has a cylindrical shape with a diameter of 5.0 cm and a plain bottom. The filling height of both phases is 2.55 cm. The overall height of the cylindrical vessels is 10.0 cm. Due to its geometrical shape, the normalized interface area (X) can be adjusted by changing the aqueous volume (Equation 11). An unstirred water layer within the aqueous phase must be avoided [70]. Therefore, adequate mixing was achieved by triangle magnetic stirrers, which enable a turbulent movement of the water in order to uniformly disperse the ritonavir-containing ASD sample. The stirring rate was set to 160 rpm, making sure no funnel was formed at the interface between the aqueous and organic phase. ASD samples were put in sinkers (mesh size 1 mm) directly above the stirrer (Figure 9). Adjusting the pH and covering 1-decanol was conducted fully automated by a liquid dispensing system (precision: $\pm 10 \mu\text{L}$). Representative for the sample vessels, the pH-value during dissolution testing was controlled by a pH – electrode (Semi-mikro VWR Collection VWR Chemicals, Darmstadt, Germany) in the blank vessel. An Agilent 8454 diode array UV spectrophotometer (Agilent Technologies, Waldbronn, Germany) was used to quantify the drug substance in the aqueous and the organic layer. A Labview® application was developed which controls automated liquid dispensing

including pH adjustment as well as UV-Vis detection and subsequent data processing of recorded spectra.

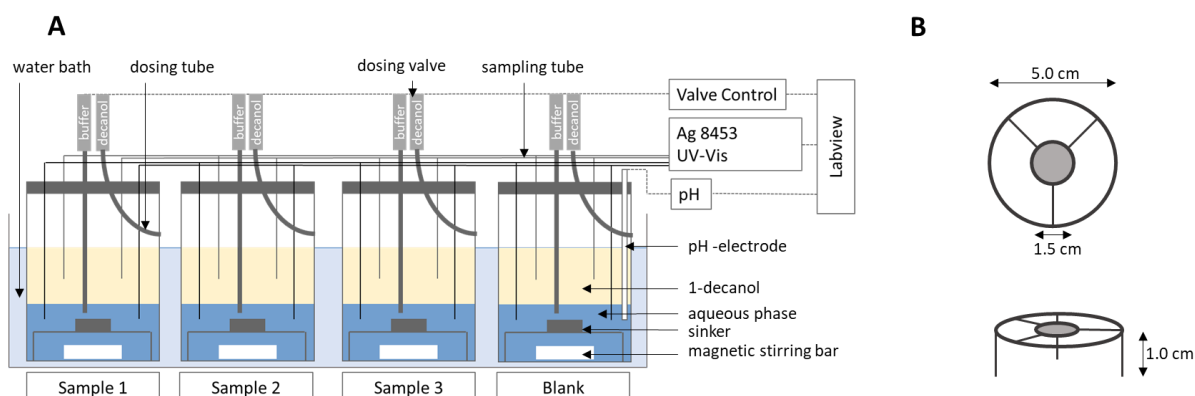


Figure 9: The BiPHA+ apparatus: (A) biphasic dissolution setup; (B) dimensions of sinkers.

3.1.2 Quantification and Scattering Correction

Drug concentrations were determined every 3 minutes by measuring the entire UV-Vis spectra in the range of 200 – 1200 nm in both layers for two reasons:

- In the aqueous phase: to perform scattering correction caused by precipitation or LLPS of supersaturated solutions, formulation ingredients or medium effects,
- In the organic phase: to correct for an overlap of the absorption with partitioned excipient spectra.

The implemented processing methods for correcting scattering and overlapping effects in the developed Labview® application were mean values over range, mono-exponential fit, and n^{th} derivatives (Figure 10).

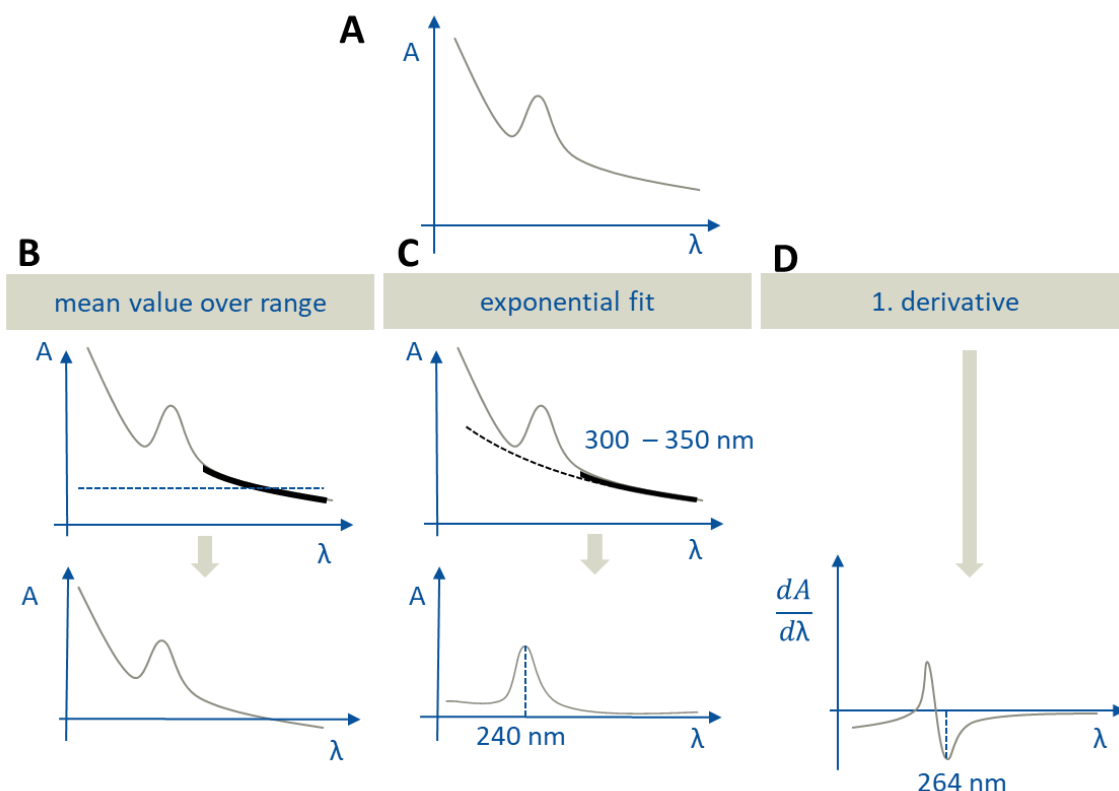


Figure 10: Different options to correct scattering in UV-Vis spectra: **(A)** Uncorrected spectrum; **(B)** Mean value over range, black bold range: mean value calculation (at the top) and the corrected spectrum (at the bottom); **(C)** Exponential fit, black bold range from 300 – 350 nm: fitting function range (at the top). Ritonavir is quantified at 240 nm using the corrected spectrum (at the bottom); **(D)** First derivative and the inflection point at 264 nm, where ritonavir is quantified (at the bottom).

Mean value over range was used to correct a simple offset of the spectra. The mean absorption value over a selected wavelength range is subtracted from the origin spectra. Correcting a spectrum by a mono-exponential fit (absorption $(\lambda) = a \cdot e^{-k\lambda}$) describes the scattering phenomena most accurately. The processing by derivatives is very helpful in order to evaluate overlapping spectra. Additional advantages of derivatives are the loss of the intercept and a lower degree of error caused by scattering (Owen, 2000). For the correction of the spectra in the aqueous phase the mono-exponential fit was applied and in the organic phase the first derivative was formed.

The ritonavir concentration in the aqueous layer was quantified at 240 nm (pH > 5.5) and 245 nm (pH = 1.0), correcting the related spectra using the mono-exponential fit function. To determine the fitting function, the range of 300 – 350 nm (black bold line) was selected and the resulting function was subtracted from the original spectra. Ritonavir was determined in the 1-decanol layer based on the first derivative. The

derived spectrum was subsequently evaluated at 264 nm to exclude overlapping with spectra of formulation excipients or components of the dissolution media.

3.1.3 Buffer Design

For the described method an in situ pH-shift from pH 1.0 to 5.5 and afterwards stepwise (increment: 0.25 pH) to 6.8 was employed mimicking the human gastrointestinal passage [37]. A suitable buffer composition or the proposed mini-scale method should have the following properties:

- a) highly concentrated in order to minimize volume changes,
- b) equal buffer capacities between pH = 5.5 and 6.8 [85,86],
- c) comparable osmolarity and buffer capacity to *in vivo* [85].

To meet these requirements, the development of a buffer concentrate was based on McIlvaine buffer [87], as a physiological carbonate buffer was not suitable for the online dissolution test due to carbon dioxide gas development. McIlvaine buffer solutions are mixtures of a phosphate and a citrate buffer system, which facilitates comparable in vivo buffer capacities, because pK_a-values of citrate/ phosphate buffer are similar to the pK_a-values in vivo in the entire range of physiological pH-values (Table 1). Thus, we regarded citrate and phosphate as biosimilar buffer components. Therefore, it was possible to design a dynamic pH-profile, which is described in literature [37,88].

Table 2: Overview of pKa values comparing McIlvaine-buffer and physiological conditions [86,88,89].

Component	McIlvaine		carbonate	Human	
	citrate	phosphate		phosphate	org. acid
pKa		2.2		2.2	
	3.1		3.5		
	4.8				≈5
	6.4		6.4		
		7.2		7.2	
	12.2		10.3	12.2	

Three steps have been taken to develop a buffer composition with comparable buffer capacities at pH = 5.5 and pH = 6.8. : (1) optimisation of molar ratio between citrate and phosphate to reach consistent buffer capacities between pH 5.5 and 6.8 [88], (2) maximization of buffer concentration to minimize its volume and (3) optimization of the buffer capacity and osmolarity to human data.

In the first step, a pH-profile was generated by adding increments of 1 ml of different ratios of potassium phosphate and potassium citrate concentrate (molar

$K_3PO_4/K_3C_6H_5O_7$ ratios are between 0.2/0.3 and 0.05/0.4) to 50 ml 0.1 N HCl (Figure 11A). The generated pH-profile provides information about the buffer capacity. The slopes of titration profiles at pH 5.5 and 6.8 were assumed as surrogate parameters for the buffer capacity. If the slopes at pH 5.5 and 6.8 are comparable with each other, the buffer capacity will also remain equal (Figure 11A, B).

In the second step, the adjusted buffers were titrated by 0.1 M NaOH and 0.1 M HCl to verify the buffer capacity at pH = 5.5 and 6.8. The slopes of the received titration profile represented the buffer capacity. A molar ratio between phosphate (0.15M K_3PO_4) and citrate (0.35M $K_3C_6H_5O_7$) of 0.429 was found to be the optimum resulting in equal buffer capacities at pH = 5.5 and 6.8 during the intestinal phase of the dissolution experiment. Higher concentrated citrate and phosphate with the same molar ratio resulted in the same buffer capacity by adding less volume. The final concentrations of both buffer salts were 0.225 M for potassium citrate and 0.525 M for tri-potassium phosphate. Higher concentrations were not possible because of solubility limitations.

In the last step, buffer capacity and added volume were optimized. Different amounts of sodium hydroxide were added to the concentrate to decrease both buffer capacities and the required addition volume to achieve pH 5.5 or 6.8 (Figure 11C). The buffer capacities can be described by an exponential fit (Figure 11C), so that the desired composition can be calculated. With the optimized buffer concentrate it is feasible to generate aqueous media of various pH with biorelevant buffer capacity and osmolarity [90], and can further be used to simulate an altered gastric stomach by adjusting the pH to 4.5 (Table 3). The proposed buffer compositions are shown in Table 3.

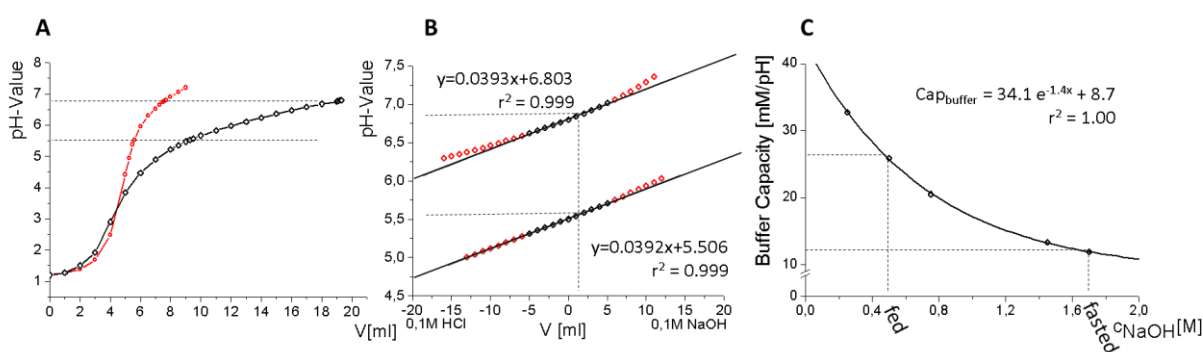


Figure 11: (A) pH Profile of 50 ml 0.1 N HCl by adding potassium-citrate and tri-potassium-phosphate; red line represents different buffer capacities, and black line represents similar buffer capacities between pH 5.5 – 6.8. Buffer capacities are similar if the slope of the titration curves at pH = 5.5 and 6.8 are similar, which is the case for the black coloured curve; (B) Titration profile of adjusted buffer at 5.5 and 6.8 to determine the buffer capacity at these levels. The adjusted buffers were either titrated by using 0.1 M NaOH or HCl. The slopes represent the buffer capacity at pH = 5.5 and pH = 6.8 (black line); (C) Optimization of buffer capacity by adding sodium hydroxide to the concentrate to reach fasted and fed conditions at pH = 6.8.

Results and Discussion

Table 3: Proposed buffer concentrate composition in the fasted for a dynamic pH-profile comparing to biorelevant media and necessary volumes of buffer concentrate to a 0.1 M HCl.

Composition		$dV_{\text{pH}5.5}$ [ml]	$dV_{\text{pH}6.8}$ [ml]	Capacity [mM/pH]	Osmolarity [mosmol/L]
K-Citrate	0.525 M				
K-Phosphate	0.225 M	2.12	2.54	11.9	245-257
NaOH	1.7 M				
FaSSIF-V1				12	270
FaSSIF-V2				10	180
K-Citrate	0.525M				
K-Phosphate	0.225M	3.90	5.80	25.9	455-608
NaOH	0.5M				
FeSSIF				76	635
FeSSIF-V2				25	390

3.1.4 Addition of Bile Salts

To generate an in-situ biorelevant aqueous medium for the fasted state, it was necessary to add biorelevant surfactants, namely sodium-taurocholate and lecithin. In the present study, the concentrations of sodium-taurocholate and lecithin were kept at the same level as for FaSSIF or FaSSIF-V2 [88,90]. Both surfactants, sodium-taurocholate (272.3 mg) and lecithin (97.5 mg in FaSSIF or 26.0 mg in FaSSIF-V2) were solubilized in 1.100 μL demineralized water. The biorelevant media formed in situ, by adding 333 μL surfactant concentrate to the aqueous medium (Table 1). Three media were investigated in the present study:

- 1) Bi-FaSSIF: pH-gradient with surfactant concentration of FaSSIF,
- 2) Bi-FaSSIF-V2: pH-gradient with surfactant concentration of FaSSIF-V2
- 3) Buffer: pH-gradient without biorelevant surfactant.

3.1.5 Selection of Organic Medium

In many studies, 1-octanol is used for generating distribution- or absorption-sink conditions [65,73,91] due to its physiochemical properties and its common use in logP determination. However, 1-octanol displays two major drawbacks for the use in our BiPHa+ model: (1) the high solubility of octanol in water (0.5 g/L), and (2) the bad

odour reducing personal compliance. In contrast, the odourless 1-decanol exhibits a water solubility of only 0.04 g/L [92]. Thus, decreased interaction between the organic solvent and the formulation in the aqueous medium could be expected. No evaporation is expected because of the high boiling point of 230°C.

3.1.6 Experiment Sequence

Prior to start of the experiments both phases, 1-decanol and the acidic aqueous phase, were saturated with each other. The selection of transition time and pH-profile were guided by Koziolok et al. [37]. During the first thirty minutes the formulation disintegrated / dispersed in 50 ml of 0.1N HCl. Subsequently, 333 μ L surfactant concentrate was added to generate Bi-FaSSIF of Bi-FaSSIF-V2. In the case of the plain buffer medium, no surfactant was added. Immediately after adding the surfactants, the pH was shifted to 5.5 by adding the buffer concentrate. The aqueous layer was covered by 1-decanol within 30 seconds after the pH shift. At 90 minutes the pH was further increased stepwise to pH 6.8. In contrast to the reported colon arrival time of 270 min, the overall test duration was 390 minutes to enable a comparison to previously published data [68].

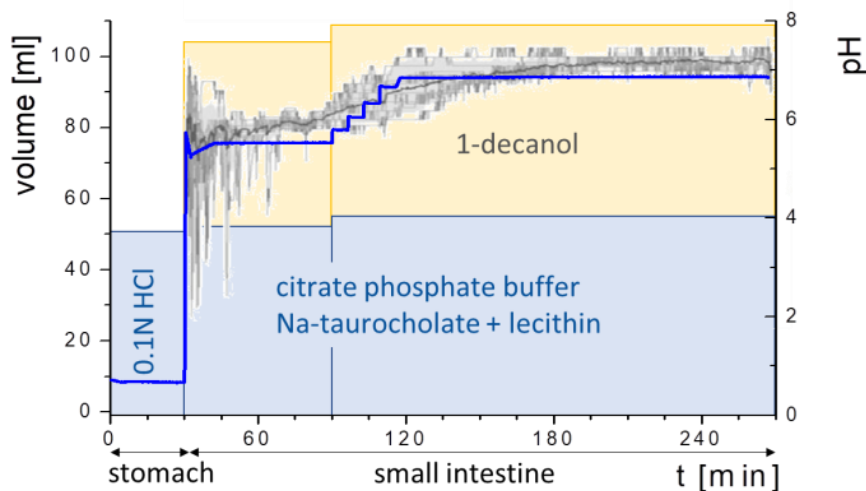


Figure 12: Dissolution procedure: (1) formulation disperses for 30 min in 0.1 M hydrochloric acid; (2) addition of surfactant concentrate after 30 min, buffer concentrate to reach pH 5.5, and overlaying of the aqueous phase with 50 ml of 1-decanol; (3) stepwise pH-adjustment at 90 min to reach pH 6.8. The grey line in the background represented measured human gastrointestinal pH-profile [37].

3.1.7 Hydrodynamic Assessment

In both cases, the dissolution vessel showed optimal hydrodynamics under the assessed mixing conditions, which is visualized by the distribution of glitter particles (Figure 13). Neither an unstirred water layer nor a funnel was formed. This can be explained by the turbulent movement of the water in both vessels caused by the triangular stir bar or the paddle. Due to the high mixing performance achieved with glitter, no unstirred water layer was expected for the ritonavir-containing droplets (precipitates) and dissolved ritonavir, which is crucial to achieve homogeneous and comparable partitioning processes.

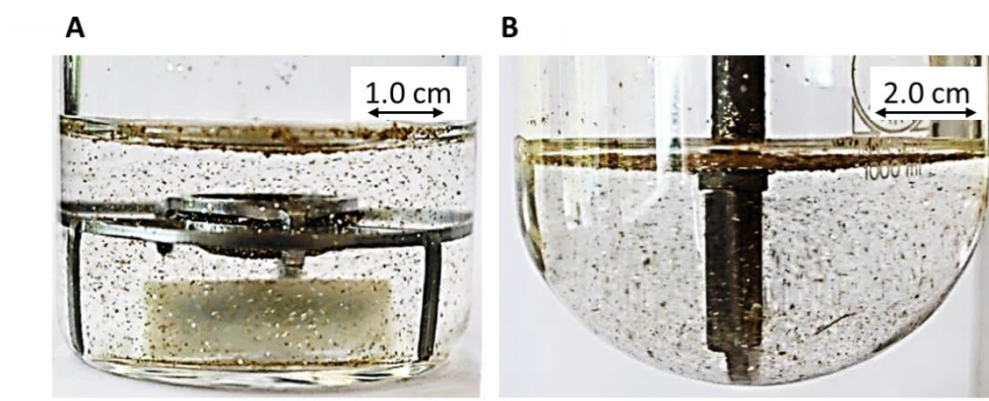


Figure 13: Hydrodynamics in (A) BiPha+ apparatus (50 ml at 160 rpm), and (B) USP II apparatus (200 ml at 60 rpm)

3.1.8 Physicochemical Characteristics of Ritonavir

The physicochemical characterisation of ritonavir is given in Table 4:

Table 4: Physicochemical characterisation of ritonavir pKa values, solubility (s), and LogP

Parameter	Value
pKa 1	1.9
pKa 2	2.5
s (0.1N HCl) [$\mu\text{g}/\text{ml}$]	382.8
s (6.8N Buffer) [$\mu\text{g}/\text{ml}$]	0.96
s (FaSSIF-V2) [$\mu\text{g}/\text{ml}$]	4.3
LLPS [$\mu\text{g}/\text{ml}$]	40 [68]
s (1-decanol) [mg/ml]	23.9
Log P	4.3 [93]

3.1.9 Comparison of BiPHA+ Assay with Established USP II/IV Biphasic Methods

The different ritonavir concentration-time profiles using Bi-FaSSIF, Bi-FaSSIF-V2 and plain buffer are shown in Figure 14. These three fasted state media including pH-change were compared to the results of Xu et al. [68], where ritonavir drug products were tested in 41 ml gastric fluid and subsequently diluted with FaSSIF-V2. No quantification of the drug during the first 30 minutes was performed. In the present study, the amount of ritonavir was quantified during the entire experiment in both layers. In the gastric stage approx. 75% of the drug was released into the aqueous phase after 30 min for all three investigated media (Figure 14) demonstrating reliable hydrodynamic conditions. Subsequent to the gastric period, buffer and surfactant were added. At intestinal dissolution stage the dissolution rapidly decreased due to the lower solubility of ritonavir at pH 5.5. Results from the BiPHA+ test containing biorelevant surfactant and the method of Xu et al. [68] showed a comparable concentration range in the aqueous phase. At 50 minutes a supersaturation peak of 10% (50 µg/ml) occurred in all setups containing biorelevant surfactant, which is probably the result of the ongoing dissolution process of the remaining ritonavir-containing ASD. Subsequently to this peak value, the concentration slowly decreased to 3% in Bi-FaSSIF-V2, 5% in Bi-FaSSIF-V1, 2% in plain buffer medium, and 2% in the method of Xu et al. [68] (HPLC determination) at the end of the experiment. Very slight supersaturation was observed in the plain buffer setup and the concentration remained at the same level of 2% (Figure 14D). The Bi-FaSSIF-V2 experiment was additionally evaluated by HPLC. Ritonavir concentration measured by HPLC were thereby comparable with results from online UV measurements, and in agreement with values reported by Xu et al. [68] (Table 5). A one-way ANOVA was performed to evaluate the statistical significance on a difference between the two analysing methods. A significance level of $\alpha = 0.05$ was chosen. A p-value of 0.87 was the result, which indicates that the quantification method did not influence the resulting concentration. Consequently, the implemented online UV quantification with scattering-correction for the BiPHA+ method provided reliable results.

Table 5: Comparing mean dissolution endpoint concentrations and standard deviation (n = 3) of ritonavir concentration after 6 hours under Bi-FaSSIF-V2 conditions.

	UV-Vis	HPLC	Xu et al. [30]
Organic layer	58.1% ± 1.5%	57.6% ± 5.1%	60 % ± 9.1%
Aqueous Layer	3.0% ± 0.3%	2.1% ± 0.4%	~2.0% (SD not available)

The dissolution experiment in Bi-FaSSIF-V2 (Figure 6A) and Bi-FaSSIF-V1 (Figure 6C) resulted in similar sigmoidal ritonavir concentration profiles for the organic phase as the one reported by Xu et al. [68] (Figure 6B). The partitioning of ritonavir was at a lower level in the early intestinal stage. During the course of dissolution, the partition rates into the organic phase increased. The inflection points occurred at earlier time points with increasing surfactant concentration in the dissolution medium. Furthermore, the slopes at these points increased with higher surfactant concentration. Hence, the partitioning rate of ritonavir into the organic phase increased. A plateau at 60% drug concentration was reached in all three dissolution media. In contrast, the ritonavir concentration in the organic phase by using plain buffer without biorelevant surfactants steadily increased without any change of the overall low partitioning rate and reached a maximum ritonavir concentration of only 19% at the endpoint of the dissolution experiment.

The drug concentration profile of the 1-decanol phase demonstrated its function as absorption compartment. The partitioning of ritonavir into the organic layer was much more pronounced in biorelevant medium, whereas without bile salts and lecithin the redissolution and partitioning rate into the organic layer were dramatically reduced. Interestingly, the amount of dissolved ritonavir in the aqueous phase was nearly the same in all cases. This observation supported the hypothesis from Taylor et al. [21], that API-rich nano droplets from liquid-liquid phase separation rapidly equilibrate with the dissolved drug in the aqueous medium. The nanodroplets serve as a reservoir, and enable the replenishment of dissolved API, that partitioned into the organic phase [21]. The formation of ritonavir-nanodroplets in biorelevant media from a ritonavir-ASD is also reported by Xu et al. [68]. Therefore, the process of redissolution of the API from the nanodroplets is of great importance for the performance of amorphous solid dispersions and is further described in section 3.3.

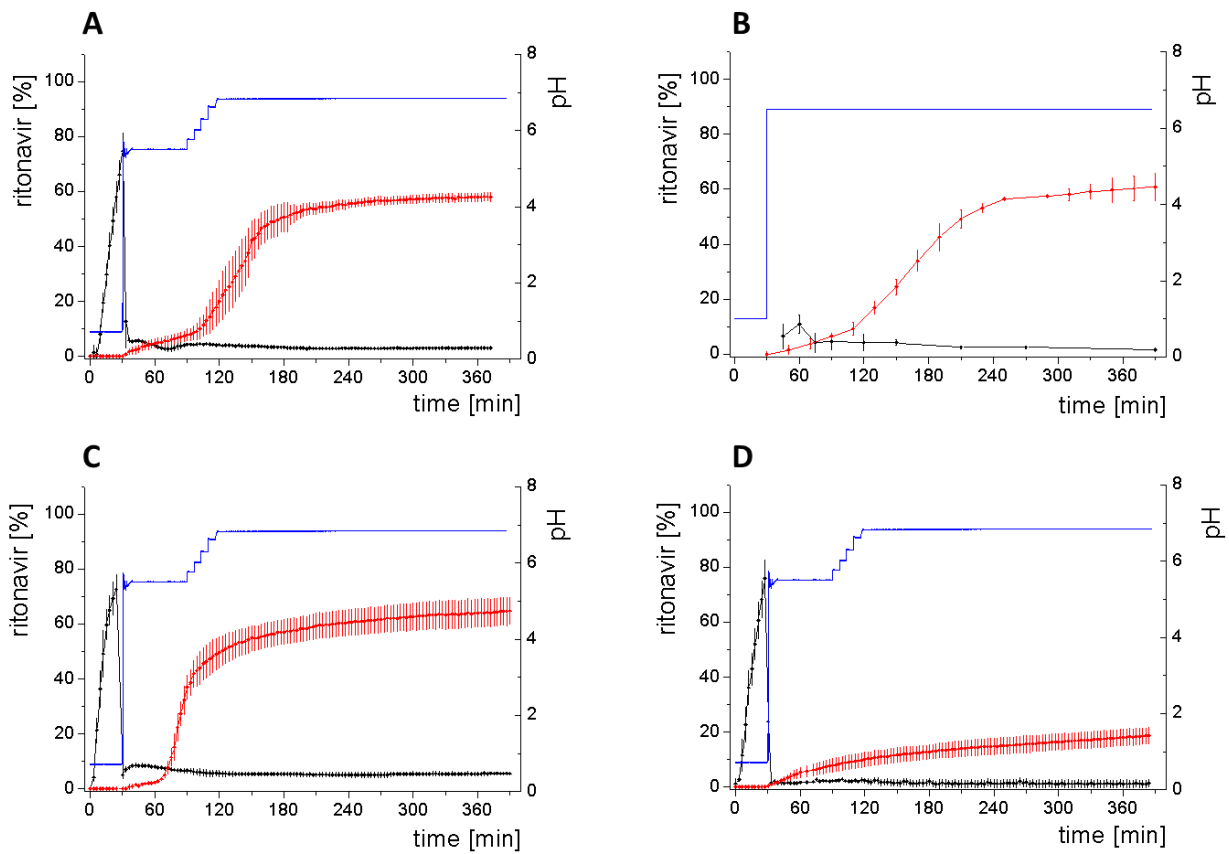


Figure 14: Biphasic dissolution experiments in (A) Bi-FaSSIF-V2 medium (BiPha+), (B) FaSSIF-V2 [68], (C) Bi-FaSSIF-V1 medium (BiPha+), (D) Buffer without surfactant (BiPha+); API concentration in the 1-decanol layer (red line, mean value and standard deviation); dissolved ritonavir in the aqueous medium (black line, mean value and standard deviation); pH values (blue line). All experiments were done in triplicate ($n = 3$). Investigation of organic / aqueous interfaces with regard on its impact on partitioning rate

3.2 Investigation of Organic / Aqueous Interfaces with Regard on Its Impact on Partitioning Rate

For a drug substance, distribution from the aqueous into the organic the phase in biphasic assay, such as the BiPHa+ assay, a passage of the dissolved drug molecules is obligatory. The interface potentially has a major influence on the distribution step. Based on this consideration, the interfacial properties might be influenced by formulation excipients and surfactants present in the aqueous phase of the BiPHa+ assay. To ensure that the partitioning of the drug is not discriminated by the interfacial properties, but by the formulation excipients, various surfactants, formulation excipients and FaSSiF-V2 compositions were firstly investigated with respect to the interfacial tension. Second, partitioning rates of dissolved dipyrindamole using different formulation excipient quantities were investigated to exclude a potential influence of the interface tension.

3.2.1 Interface Assessment

To investigate the properties of the aqueous phase / 1-decanol interface, measurements of interfacial tension for various polymer / surfactant mixtures in the aqueous phase were performed. Since very low interfacial tensions are expected at the interface, the spinning drop method was used for the determinations of the interface tension. The densities of water ($\rho=0.993 \text{ g/cm}^3$) and 1-decanol ($\rho=0.822 \text{ g/cm}^3$) required for this purpose, were determined using an oscillating U-tube at 37°C.

In a first step, the influence of surfactants of various HLB values at the interface tension was investigated in the presence of Soluplus® as a surface-active polymer that influences the interface. A concentration of 3 mg/ml Soluplus® was assessed with regard to the resulting interface tension in the presence of various surfactants at critical micelle forming concentration (Figure 15). Soluplus® as a hydrophilic polymer was selected for the initial investigations because it remains mostly in the aqueous phase, which was verified UV-metrically. The CMCs of the surfactants were determined on the water / air surface (Table 6).

Results and Discussion

Table 6: Critical micelle forming concentration (CMC), the respective interface tension and HLB-value of different surfactants.

Surfactant	CMC [mg/ml]	Surface tension at CMC [mN/m]	HLB-value
SDS	2.53	38	40
Poloxamer 407	3.83	43	22
Brij 35	0.14	45	17
Tween 20	0.13	47	17
Tween 85	0.32	46	11
Brij 30	0.27	28	9.7
Tween 80	0.24	47	15

Figure 15 summarizes the measured surface tension of the individual substances, as well as the respective mixtures at the water/decanol interface. The interfacial tension of pure water/1-decanol is 9.4 mN/m. In the presence of surface-active substances, the interfacial tension is always decreased. As the HLB value of individual surfactants increases, the resulting surface tension decreases. In the case of very lipophilic surfactants in combination with Soluplus[®], the interfacial tension is similar to that of pure Soluplus[®]. For rather hydrophilic surfactants (increased HLB) in combination with Soluplus[®], the interface tension is between those of the two individual components. Based on these results, lipophilic surfactants (Brij L4 and Tween 85) are likely to distribute into the organic phase: This suggests that the mixture has the interface tension of Soluplus[®] and the individual surfactants have higher interfacial tensions, which is probably caused by a surfactant concentration falling below the CMC. Hydrophilic surfactants remain in the aqueous phase and therefore, along with Soluplus[®], result in a mixed interfacial tension. Soluplus[®] in combination with FaSSIF-V2 results in a significantly reduced interfacial tension than that of the respective individual components.

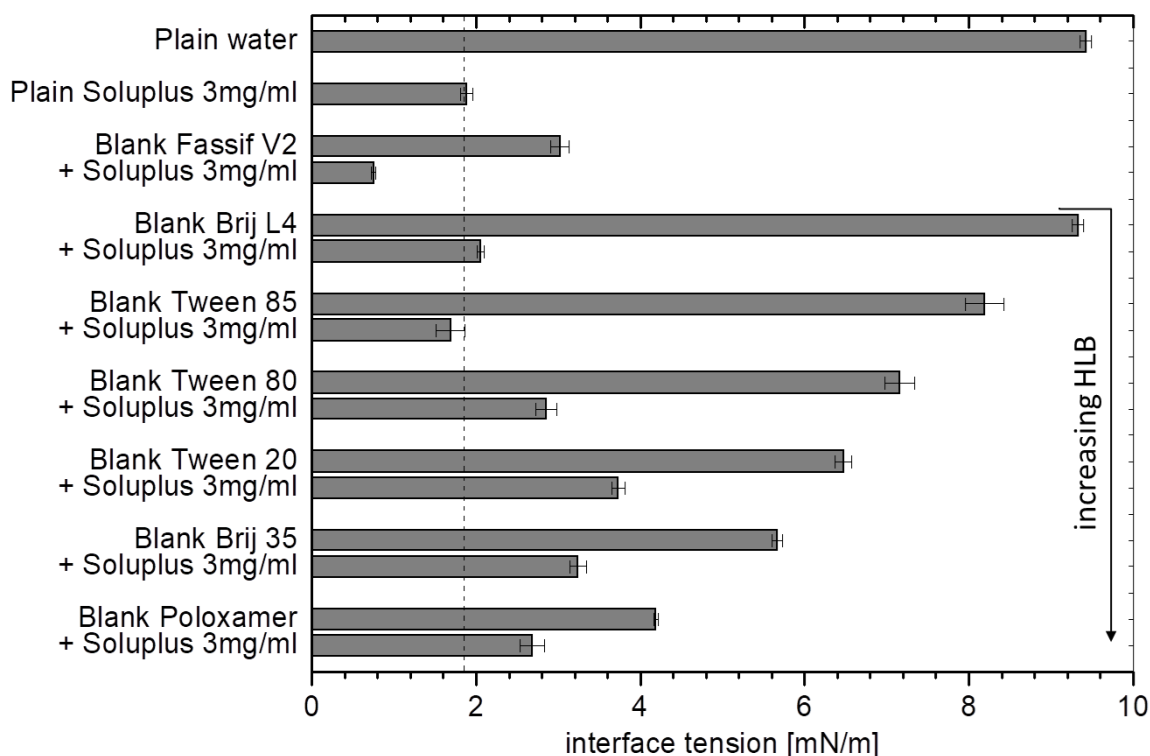


Figure 15: Interface tension of 1-decanole / water interface by using different surfactant at the critical micelle forming concentration in the aqueous phase (The CMC was measured at the surface water/ air). The same solutions are measured with additionally three mg/ml Soluplus®. Dotted line represents the interface tension for the plain Soluplus® solution.

Based on these results from Figure 15 and the fact that the BiPha+ assay is performed using FaSSIF-V2 medium, further investigations of the FaSSIF-V2/decanol interface were conducted. For this purpose, the interfacial tension of various polymer concentrations was measured (Figure 16). In addition, the influence of SDS, being a highly surface-active surfactant with a high HLB, was investigated at the CMC on the FaSSIF-V2/polymer solutions as no partitioning of SDS in the organic phase was expected (Figure 16). An interfacial tension approximately equal to that of pure SDS was found in almost all mixtures as soon as SDS was added (concentrated at the level of the CMC). Therefore, SDS at this concentration would be suitable to obtain a normalization of the interfacial tension. However, it should be mentioned that SDS is very highly concentrated for this application. For a potential application in the BiPha+ assay, the interface would exhibit comparable properties with different formulation components, but the high SDS concentration would have a significant influence on the dissolution process of a formulation. One noticeable finding was that Kollidon® VA 64 provided very low interfacial tension in FaSSIF-V2 medium regardless of its concentration. Soluplus® and methylcellulose resulted in rather variable interfacial tensions both individually and in combination with SDS. In general, once surfactant or polymer was added to FaSSIF-V2, the interfacial tension variations were in a very

small range between 1.8 and 0.4 mN/m and thus a large influence on the partitioning rate seems to be unlikely [84].

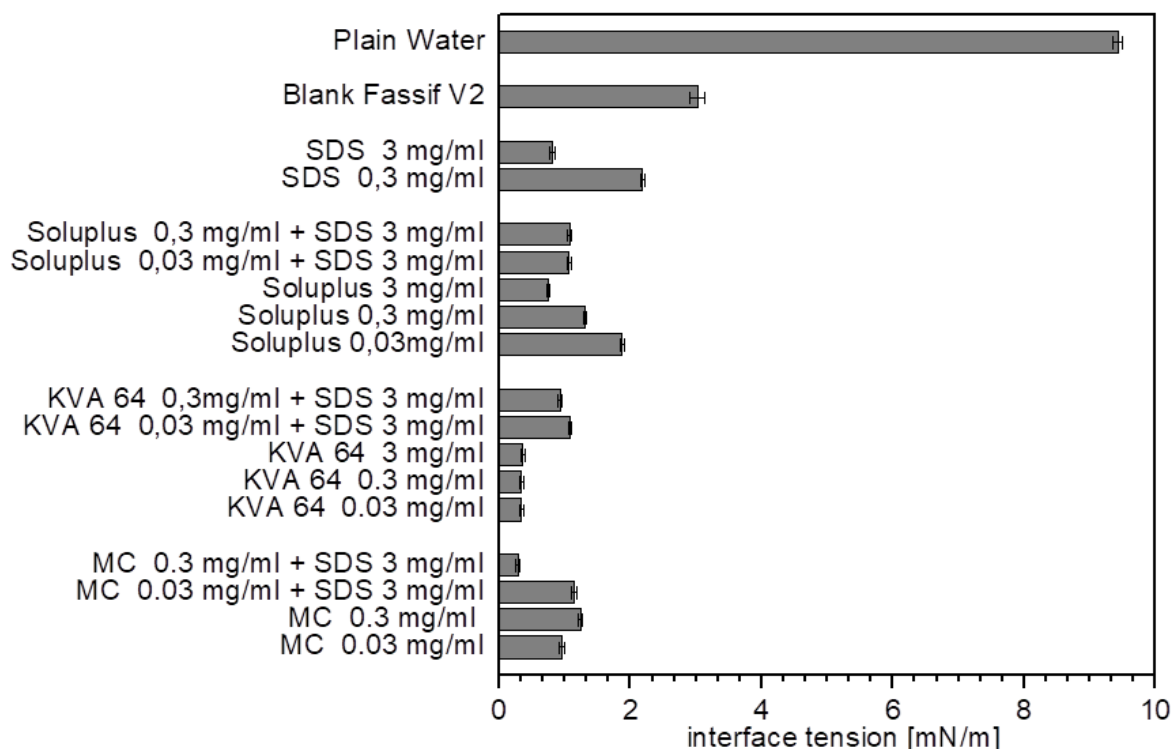


Figure 16: Interface tension of 1-decanole / water interface by using different polymer concentrations in the FaSSIF-V2 phase. Each mixture was additionally investigated by adding SDS at the CMC level.

To investigate the influence of interfacial properties on the partitioning rate in the presence of excipients, the Soluplus® system in combination with small amounts of Kollidon® VA 64 was initially investigated in terms of interfacial properties and in section 3.2.2 in terms of partitioning rate of dissolved dipyrindamole. Kollidon® VA 64 was chosen as the interface tension normalizing agent because it produces very low and constant interfacial tension ($\sigma = 0.4 \text{ mN/m}$) independent of its concentration without Soluplus® (Figure 16). Soluplus® was chosen as a polymer because of its surface-active properties, potentially influencing the partitioning rate and it remains largely in the aqueous phase, to simulate a formulation component. The concentration-dependent interfacial tension of pure Soluplus® in FaSSIF-V2 decreased from 1.8 mN/m to 0.8 mN/m at concentrations corresponding to 750 - 7.5 mg per 250 ml (Figure 17). The Kollidon® VA 64 concentration was tried to be minimized from 0.3 mg/ml to 0.003 mg/ml. As soon as Kollidon® VA 64 was added to Soluplus®, the interfacial tensions were in the range of 0.8 mN/m to 0.3 mN/m. Consequently, it was shown that the use of Kollidon® VA 64 has a normalizing effect on the interface at very small amounts even in the presence of the surface-active excipient Soluplus®.

Another advantage of Kollidon® VA 64 is that this small concentration range has likely a negligible influence on the formulation dissolution. Since the interfacial tension in the mixture of Kollidon VA 64 and Soluplus® in FaSSIF-V2 was in a narrow range between 0.8 and 0.4 mN/m, this system is expected to have an influence on the partitioning rate by a change in Soluplus® concentration but not by the interface properties, since the interface has similar properties over different concentrations (Figure 17).

In general, these results show that once polymers or surfactants are additionally contained in FaSSIF-V2 medium the interfacial properties are very similar to each other (1.8 mN/m to 0.3 mN/m).

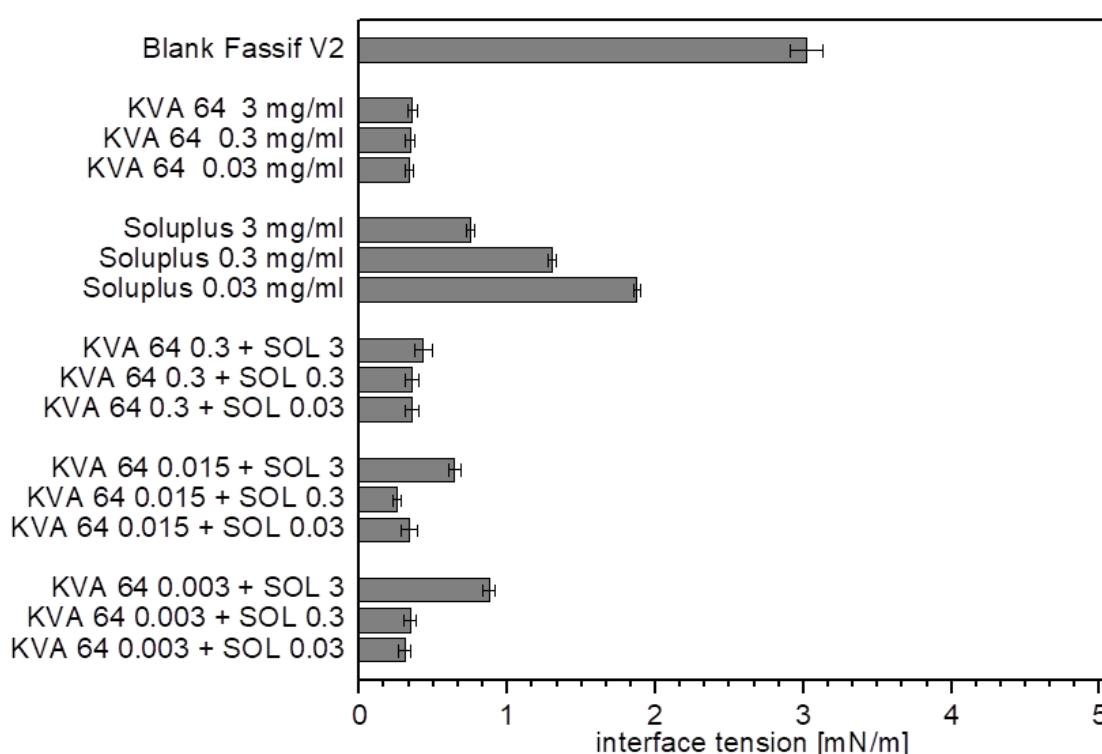


Figure 17: Interface tension of 1-decanole / FaSSIF-V2 interface by using Soluplus® as example excipient and Kollidon® VA 64 (KVA 64) as interface normalizing agent.

3.2.2 Influence of Interface Tension to Partitioning Rate

The objective of this section of the study was to evaluate the influence of Soluplus® in different concentrations simulating a formulation component on the distribution rate k_a of dissolved dipyrindamole into the organic phase and to verify a possible interfacial effect on the distribution rate by performing partitioning studies in the BiPha+ assay based on an experimental design (section 4.4.2). If the partitioning rate was discriminated by the interface tension, the partitioning rate would stay on the same level. The polymer Kollidon® VA 64 was used in concentrations of 0.031 to

Results and Discussion

0.003 mg/ml for the stabilization of the FaSSIF-V2 / 1-decanol interface. In this range the surface tension was almost identical at 0.8 mN/m to 0.3 mN/m. Soluplus[®] was investigated in the concentration range from 3.0 to 0.031 mg/ml. Slightly increased interface tensions can be measured at a high Soluplus[®] concentration of 3 mg/ml and at Kollidon[®] VA 64 concentrations of 0.003 mg/ml and 0.015 mg/ml (Figure 17). First order kinetics was assumed for the determination of the distribution rate constants. The BiPHA+ distribution studies were evaluated using statistical design of experiments (DOE) described in section 4.4.2. The determined rate constants are presented in Table 7. The determined rate constants are 0.0011 min⁻¹ and 0.0168 min⁻¹.

Table 7: Rate constants k_a of the distribution of dipyrnidamole into the organic phase at different Soluplus[®] / Kollidon[®] VA64 ratios in FaSSIF-V2 media.

Kollidon [®] VA64 [mg/ml]	Soluplus [®] [mg/ml]	k_a [1/min]
0.003	0.031	0.0146
0.017	1.52	0.0025
0.017	2.57	0.0022
0.027	1.52	0.0031
0.017	0.46	0.0130
0.003	3.00	0.0012
0.031	3.00	0.0011
0.0071	1.52	0.0014
0.017	1.52	0.0026
0.031	0.031	0.0168

Based on the evaluation of the DOE, only the Soluplus[®] concentration had a significant parameter influencing the distribution rate. The ANOVA of the model is shown in Table 7. The resulting Response Surface Area showed the quadratic correlation of the Soluplus[®] concentration but no influence of the Kollidon[®] VA 64 concentration on the partitioning rate (Figure 18). As the concentration of Soluplus[®] in the aqueous phase increased, the partitioning rate of dissolved dipyrnidamole decreased quadratically. Since the surface tension stayed at the same level at different Kollidon[®] VA 64 concentrations and at 3 mg/ml Soluplus[®], but the distribution rates remained constant (Table 7), the interfacial properties had no significant influence on the distribution rate (Figure 18). The decreasing partitioning rate with increasing Soluplus[®] concentration can be explained by the fact that dissolved dipyrnidamole was probably entrapped in the polymer micelles of Soluplus[®] [94]. The dipyrnidamole must therefore diffuse from the micelles into the aqueous phase and from there distribute into the organic phase. At lower Soluplus[®] concentrations, more dipyrnidamole was freely dissolved and can therefore distribute more rapidly into the organic phase.

Results and Discussion

In summary, the BipHa+ assay was performed using FaSSiF-V2 medium demonstrating that the aqueous phase discriminated for the formulation components (Soluplus®) and not for the surface tension. No effect on the distribution rate could be measured at slightly changing interfacial tensions. A normalization of interface tension can be generated by adding very small amounts of Kollidon® VA64, without affecting the formulation dissolution characteristics.

Table 8: ANOVA table: source: parameter; sum of squares: sum of the squared differences between the overall average and the amount of; df: degrees of freedom; Mean Square: variance; F Value: test for comparing the mean square to the residual mean square; p-value: probability of seeing the observed F-value

Source	Sum of Squares	df	Mean Square	F-value	p-value	
Model	0.0003	2	0.0002	103.97	< 0.0001	significant
B-Soluplus®	0.0003	1	0.0003	163.78	< 0.0001	
B ²	0.0001	1	0.0001	44.15	0.0003	
Residual	0.0000	7	1,65E-03			
Lack of Fit	0.0000	6	1,92E-03	384.41	0.0390	significant
Pure Error	5.00E-06	1	5,00E-06			
Cor Total	0.0004	9				

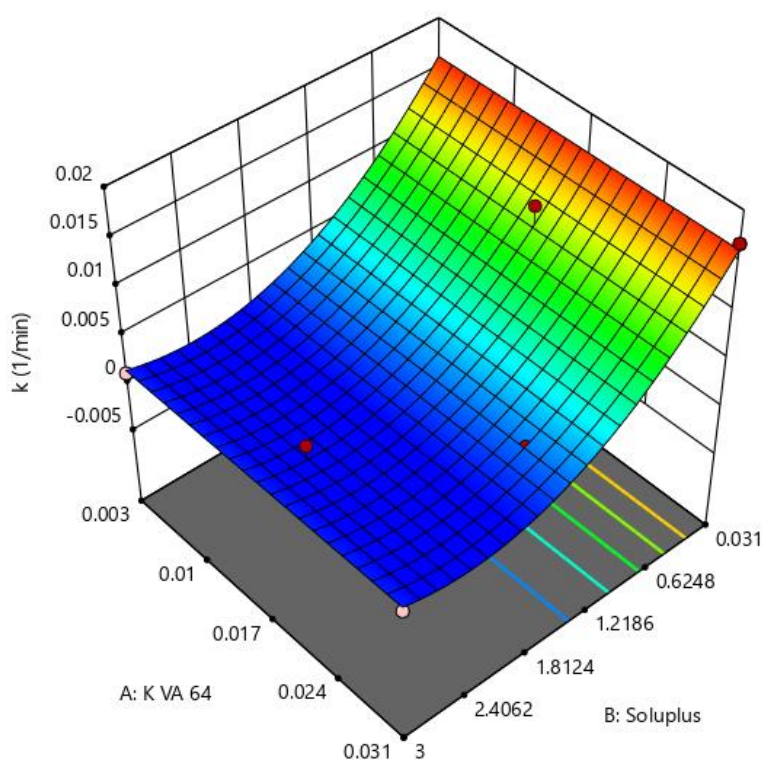


Figure 18: Response Surface Area of partitioning rate (k) as function of Kollidon® VA64 (K VA 64) and Soluplus® concentration.

3.3 Modelling of Biorelevant Kinetics for a Ritonavir Hot-Melt Extruded Amorphous Solid Dispersion

As reported in section 3.1.9, the dissolution of a ritonavir containing amorphous solid dispersion in biorelevant media (Bi-FaSSIF-V1 / V2) resulted in a sigmoidal partitioning profile into the organic phase, whereas the ritonavir concentration by using plain buffer without surfactants steadily increased without any change of the slow partitioning rate. For a better kinetic description and explanation of resulting organic concentration time profiles, the kinetic model of Locher et al. [81] for crystalline BCS II APIs was advanced towards an ASD by introducing additional phase separation processes in the aqueous phase as described in the following section.

3.3.1 Physical Explanations of the Complex *in vitro* Dissolution Kinetics for Ritonavir

The kinetic profile obtained from of the BiPHA+ dissolution experiment can be divided into three different stages as illustrated in Figure 19:

(1) Gastric stage - The ritonavir-containing ASD was tested for 30 min at pH 1.0 without the 1-decanol absorption layer. Upon contact with the dissolution medium the ritonavir-ASD disperses, API and excipients dissolve simultaneously [51], and a solution is generated in our experiments 80%. Dispersing of the ASD and dissolution of ritonavir are assumed as one irreversible step. Furthermore, it can be assumed that drug and polymer dissolve simultaneously for the given ritonavir-ASD at a drug load of 15% as demonstrated by Indulkar et al. [51].

(2) Early intestinal stage - After covering the aqueous layer with 1-decanol and changing the pH from 1.0 to 5.5, a 2-compartment model for the simulated early intestine was applied (Figure 19). Liquid-liquid phase separation (LLPS) supposedly occurs from the solution, when crystallization is slow [95] and the amorphous solubility of the API is exceeded leading to the formation of nanosized API-rich nano-droplets [68,96]. In the present kinetic model the formation of the nano-droplets refers to the generation of the an increased nano-droplet particle size as shown in Figure 20 and Figure 19. The ritonavir-rich nano-droplets provide a reservoir replenishing dissolved ritonavir that irreversibly partitioned into the organic layer [21,68,97,98].

(3) Late intestinal stage - At the timepoint, where the partitioning of ritonavir into the organic phase substantially increases, the re-dissolution rate of ritonavir from the nano-droplets into the aqueous phase increases, while the particle size of the small nanoparticles decreases [99–101]. Furthermore, the particle size reduction can be

further driven by Ostwald ripening of the nano-droplets [99] as also reported for nano-emulsions, which exhibit a typical size of 20 to 200 nm [102]. This is in the same size range (approx. 60 nm) as reported in a previous study [95,99]. The resulting dispersion formed in buffered aqueous medium contained particles at a mean diameter of approx. 60 nm in a monomodal particle size distribution [99]. Briefly, during the thermodynamically driven process of Ostwald ripening molecules on the surface of energetically unfavourable small particles (e.g. the API molecules from the nano-droplets) tend to detach from the particles and diffuse into the solution as free molecules generating a supersaturated solution. At the stage, where supersaturation is achieved, the free molecules have the tendency to condense on the surface of larger particles, or in our case, larger nano-droplets. Therefore, the smaller nano-droplets continue to shrink, while larger nano-droplets continue to grow as illustrated in Figure 20. While ritonavir is continuously removed by partitioning into the organic phase, the size of small nano-droplet decreases until they disappear. The continuously shrinking nano-droplets are described by forming small nano-droplets in the kinetic model (Figure 19). It is assumed that large nano-droplets and small nano-droplets lead to different kinetic properties in terms of the ritonavir dissolution from the nano-droplets due to their difference in particle size.

Because the surface energy has a great impact on the re-dissolution rate, the re-dissolution rate and change in particle size distribution is further increased in the biorelevant media [99,100]. For this reason, the partitioning of ritonavir into the organic layer was much more pronounced in biorelevant medium leading to a sigmoidal concentration time curve (Figure 22A-C), whereas re-dissolution and partitioning into the organic layer are dramatically reduced without bile salts and lecithin (Figure 22D). Remaining larger nano-droplets can merge by coalescence, as most likely they are not stable in the surfactant-free buffer medium. Consequently, the particle size distribution of the droplets can move further towards particle sizes in the lower micrometer scale during the course of the dissolution experiment [95,99,103].

The concentration of ritonavir in 1-decanol reaches a plateau at about 120 min. in Bi-FaSSIF-V2 (Figure 22A), 270 min. in FaSSIF-V2 (Figure 22B), and 180 min. in Bi-FaSSIF (Figure 22C) indicating a reduced concentration of free ritonavir in the aqueous medium. The presence of mainly very large nano-droplets or even coalesced droplets led to only very limited ritonavir dissolution into the aqueous medium. In the surfactant-free buffer medium these very large particles permitted only very slow ritonavir dissolution resulting in turn in an overall very low partition rate into the organic layer (Figure 22D).

Results and Discussion

Based on the assumptions provided above, five compartments (M) and six related rate constants (k) were introduced in the model to describe the concentration-time profiles kinetically. Each compartment was assigned to certain rate constants, which were negative, when the described process decreased the amount of ritonavir in the corresponding compartment:

- (1) M_{form} : the undissolved ritonavir-ASD formulation,
- (2) M_{diss} : dissolved ritonavir in the aqueous phase,
- (3) M_{IND} : ritonavir-rich nano-droplets,
- (4) M_{sND} : small, shrunken ritonavir-rich nano-droplets,
- (5) M_{part} : dissolved ritonavir in the organic phase.

Further details are given in Figure 19 and Table 9.

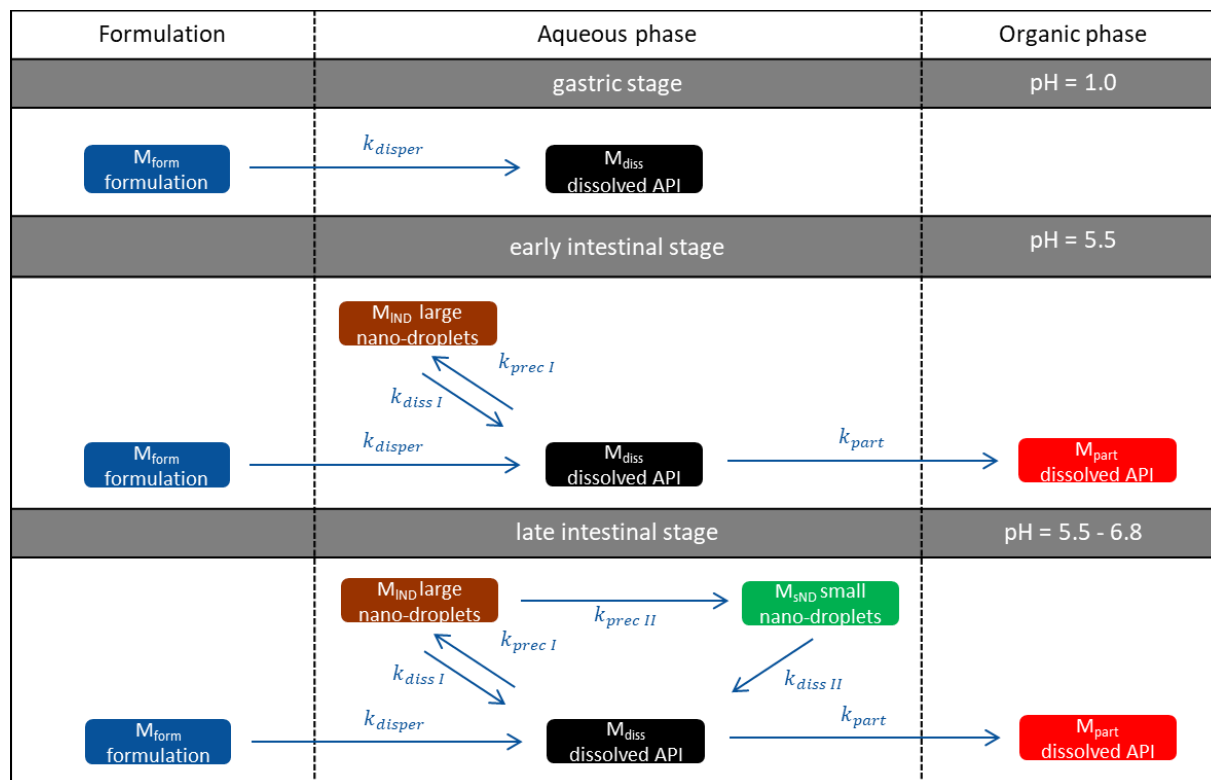


Figure 19: Schematic illustration of the five-compartment model to describe the proposed kinetic processes occurring in the BiPHA+ dissolution from dispersing of the ritonavir-ASD formulation to ritonavir partitioning into the organic (1-decanol) layer.

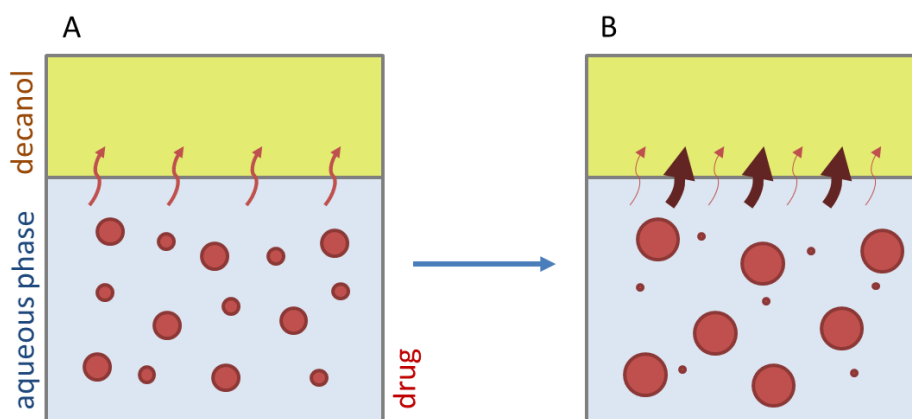


Figure 20: Schematic biphasic dissolution behavior of a ritonavir ASD: (A) In the course of the dissolution process, different sizes of nano-droplets (red dots) are formed via LLPS. Dissolved ritonavir partitions into the organic layer (red arrows). (B) After a while, larger and smaller ritonavir nano-droplets are generated because of Ostwald ripening, re-dissolution and partitioning. A higher re-dissolution rate of ritonavir from the small nano-droplets results in an increased partitioning rate (red bold arrows). In contrast, a lower re-dissolution rate of ritonavir from large nano-droplets ends up in a decreased partitioning rate (narrow red arrows).

3.3.2 Light Scattering Measurement as an Indicator of the Dynamic Behaviour of Small Nano-Droplets

Changing nano-droplets properties could be also deduced from scattering (Figure 21) as undissolved particles cause light scattering, which results in turbidity. In the UV - Vis spectrum, this effect was evidenced by an exponential trend of the baseline of the UV-spectrum, which increases with smaller wavelengths. Hence, the scattering extent related turbidity throughout the experiment correlated with generation, growth or dissolution of particles like e.g. nano-droplets.

As the aqueous phase was constantly pumped through a 1 μm cannula full-flow filter, particles of $> 1 \mu\text{m}$ could not account for the scattering in the flow through cuvette (Figure 1). Starting at wavelength of $> 300 \text{ nm}$, the UV-Vis spectrum results solely from light scattering as no absorbance of ritonavir is present. The extent of scattering was measured as turbidity values between wavelengths of 400 and 1000 nm (in 100 nm steps) during the entire experimental period. Consequently, when turbidity increased or decreased, it had to be related to LLPS, dissolution of nano-droplets or a change in particle size.

The scattering profile of the plain buffer medium showed turbidity only during the gastric phase (Figure 21B). Later the turbidity of the buffer medium (M3) rapidly decreased and remained at a low level which indicated a fast-increasing particle size, because large undissolved ritonavir particles could not pass the filter anymore (Figure

21B). As a result, the partitioning of ritonavir from the plain buffer medium in the organic phase was slow.

In contrast, the scattering profile of the Bi-FaSSIF-V2 medium was highly dynamic (Figure 21A). The generally higher level of scattering in the Bi-FaSSIF-V2 was additionally affected by the Bi-FaSSIF-V2 ingredients. After shifting the pH to 5.5, scattering rapidly increased because LLPS of ritonavir into nano-droplets likely occurred. The decrease of scattering in Bi-FaSSIF-V2 started intensively before the partitioning rate increased. The decrease in turbidity resulted on the one hand from the fact that the large nano-droplets no longer passed the filter and on the other hand from the dissolution and Ostwald ripening of the small nano-droplets. The subsequent increased partitioning rate of ritonavir could be explained by an increased dissolution rate of shrunken small nano-droplets which is represented in the kinetic model with the transformation of large nano-droplet (M_{IND}) into small nano-droplets (M_{sND}).

In summary, monitoring of scattering data is an easy and effective method to qualitatively measure the extent and kinetics of LLPS, particle size modification and re-dissolution of nano-droplets, which at the same time confirm the validity of our kinetic model.

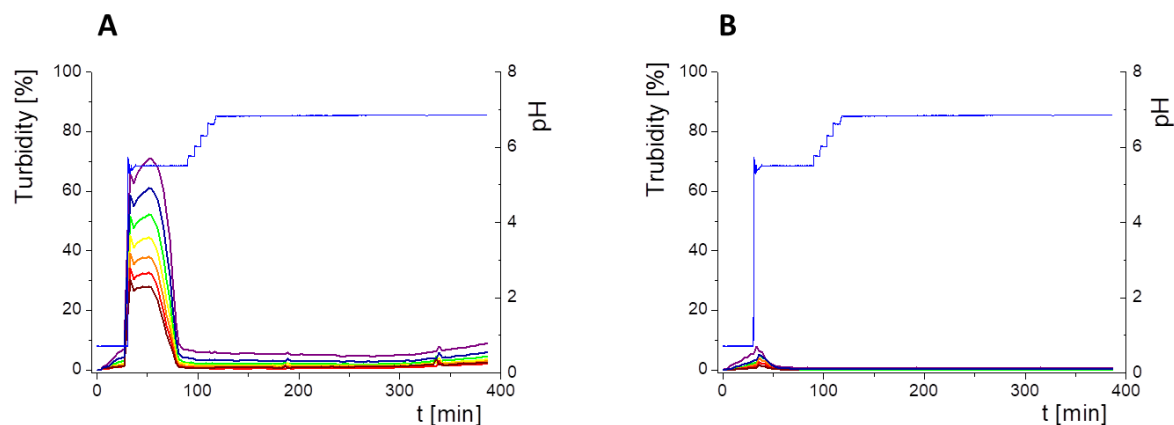


Figure 21 Turbidity in % ($1 - \frac{\text{light intensity of sample}}{\text{light intensity of blank}}$) in the course of the experiment caused by light scattering of particles smaller than $1 \mu\text{m}$ measured at various wavelengths; (A) is the scattering profile in Bi-FaSSIF-V2 medium; (B) represents the scattering profile in the surfactant free buffer medium. The colours of each turbidity profile resemble the colour in the electromagnetic spectrum: purple 400 nm, blue 500 nm, green 600 nm, yellow 700 nm, orange 800 nm, red 900 nm, dark-red 1000 nm

3.3.3 *In silico* Model Fitting of Ritonavir *in vitro* Dissolution and Partitioning Kinetics

The differential equations as well as the corresponding graphs describing the *in vitro* dissolution and partitioning kinetics are represented in Table 9. The iterative fittings of M_{diss} (Equation 14, Equation 15, Equation 18) and M_{part} (Equation 17, Equation 21) were compared with the amount of ritonavir in the aqueous and the organic medium. The amount of M_{form} (Equation 13), M_{IND} (Equation 16, Equation 19) and M_{SND} (Equation 20) directly resulted from the calculation. The rate constants (Table 10) and kinetic profile (Figure 22) from the experiments in three different dissolution media were calculated, accordingly. Figure 22 illustrates the kinetic profiles of the five compartments fitted with regard to the dissolved ritonavir (A1-C1). Figure 9 A2-C2 represents the mass balance of the unresolved ritonavir fractions. For this purpose, the measured undissolved ritonavir fractions (black line) were compared with the calculated undissolved fractions (grey area). The calculated undissolved ritonavir includes ritonavir in the formulation (M_{form}), small and large nano-droplets (M_{INM} , M_{SND}).

The process of dissolution started in the gastric medium within the first 30 minutes with dispersing of the ritonavir-ASD formulation (Equation 4) immediately followed by the dissolution of the ritonavir. The dispersing of the ritonavir- ASD formulation and the ritonavir dissolution from the compartment M_{form} was described by a first order kinetic with k_{diss} as rate constant (Equation 13, 5). Dispersion and dissolution from the ritonavir-ASD were assumed to be identical [51], because the API was molecularly dissolved in the polymer in contrast to the case of crystalline API described by Locher et al. [81]. If the polymer dissolves, the drug will also dissolve immediately. Approx. 75% of the ritonavir was dissolved at the end of the gastric stage (Figure 22).

During the early intestinal stage, the ritonavir-ASD was further dispersed. Because of the strongly pH-dependant solubility of ritonavir, the formation of the ritonavir-rich nano-droplets (M_{IND}) occurred directly after pH-adjustment (Table 9). The organic absorption layer was added 30 seconds after pH-change to 5.5. The compartment of dissolved ritonavir (M_{diss}) was complemented with that of the ritonavir-rich nanodroplets (M_{IND}) and the ritonavir absorption compartment (M_{part}) of 1-decanol (Equation 15 - Equation 17). The partitioning of dissolved ritonavir into the organic phase, (M_{part}) occurred irreversibly by first order kinetic. In the case of Bi-FaSSIF-V1 and Bi-FaSSIF-V2 the kinetic model in the early intestinal stage comprises a four-compartment model that accurately describes the experimental data between 30 and 80 min (Bi-FaSSIF-V1) as well as between 30 and 65 min (Bi-FaSSIF-V2), respectively. After these periods the partitioning rate strongly increased, leading to a sigmoidal

distribution profile (Figure 14 and 8). On the other hand, the absence of a sigmoidal partitioning profile in surfactant-free buffer medium confirmed the early intestinal model for the whole experimental period (Figure 22C).

Ritonavir-ASD dispersion and dissolution into the compartment M_{diss} as well as the partitioning process of ritonavir into the organic phase (M_{part}) were assumed to be irreversible. In contrast, re-dissolution of ritonavir from large nano-droplets (M_{IND}) into the compartment M_{diss} was considered as reversible. Furthermore, the model was able to describe the remaining ritonavir in the formulation compartment (M_{form}) after changing the pH from 1.0 to 5.5, and further to 6.8, which is described by a first order dissolution model, because the polymer dissolved pH-independently and the polymer matrix properties controlled the dissolution. This means that the active ingredient dissolves independently of the outer environment, but depending on the polymer [51].

The generation of the ritonavir-rich nano-droplets (M_{IND}) and the dissolution of the ritonavir into M_{diss} are limited by the residual dissolved ritonavir at the end of the experiment which is expressed by the term $(\text{sat} - M_{\text{diss}})$ and $(M_{\text{diss}} - \text{sat})$ (Equation 15, Equation 16). *Sat* values represent the measured ritonavir concentration in the aqueous phase at the end of the test [81]. Supersaturation followed by the formation of ritonavir-rich nano-droplets (M_{IND}) occurred at concentrations of freely dissolved ritonavir of higher than *sat*. The scaling factor was negative for the dissolution equation and positive for the precipitation equation (Equation 7).

In the late intestinal stage, all rate constants and model descriptions from early intestinal stage remained unchanged in further calculations (Table 10). The model was extended by a conversion process of ritonavir-rich nano-droplets generated from liquid-liquid phase separation (LLPS) during precipitation of dissolved ritonavir (M_{IND}) into smaller ritonavir-rich nano-droplets (M_{sND}) in Bi-FaSSIF and Bi-FaSSIF-V2, and described the changing re-dissolution and subsequently partitioning rate (Equation 19, Equation 20). The presence of smaller nano-droplets (M_{sND}) can physically explain the enhanced dissolution rate, which became the new rate limiting step (Table 10). Neither a direct formation of large nano-droplets in the M_{IND} compartment from small nano-droplets (M_{sND}) nor precipitation from dissolved ritonavir into small nano-droplets (M_{sND}) occurred (Equation 19, Equation 20). The expressions $(\text{max} - M_{\text{IND}})$ and $(M_{\text{IND}} - \text{max})$ (Equation 19, Equation 20) were introduced to scale the extent of the larger nanodroplets (M_{IND}), which underwent particle size reduction and contributed to partitioned ritonavir (see 3.5.1). *Max* values represented the amount of large particles ($> 1 \mu\text{m}$), which were not able to transform in smaller particles. The scaling factor is negative for the M_{IND} equation and positive for the M_{sND} equation. Thus, the

amount of M_{IND} decreased and the amount of M_{sND} increased. *Max* values were result of the model fitting: *max* = 32% in Bi-FaSSIF-V1 and *max* = 35% in Bi-FaSSIF-V2.

The partitioning of ritonavir into the organic phase (M_{part}) was described by a second order kinetic model (Equation 21). A second order model described the partitioning into the organic phase, which depended on the amount of dissolved ritonavir in the aqueous phase (M_{diss}) as well as the amount of ritonavir-rich nano-droplets (M_{sND}). This assumption took two considerations into account: (1) the fast re-dissolution rate of small nano-droplets (M_{sND}), and (2) the plateau in the organic phase at the end of the experiment (Figure 22). A plateau was reached, when the amount of small nano-droplets (M_{sND}) decreased. The larger nano-droplets in the M_{IND} compartment dissolved very slowly and did not substantially contribute to the partitioning of ritonavir in the organic phase (M_{part}). The extent and rate of plateau formation depends on the lecithin/taurocholate ratio [104].

The obtained rate-constants from the simulation results are listed in Table 10. The models matched very well with the experimental data (Figure 22). In all simulations, the same dispersion / dissolution rate (k_{disper}) constant was determined during the first 30 minutes in the gastric part.

Immediately after shifting the pH to 5.5 and covering the aqueous layer with 1-decanol, LLPS occurs from the solution leading to the formation of nanosized API-rich nano-droplets (M_{IND}). The rate of redissolution of ritonavir from these nano-droplets (M_{IND}) was very slow ($k_{prec1} = 0.009 \text{ min}^{-1}$) and represented the rate limiting step in all three tested dissolution media. Dispersing of the formulation, formation of API-rich nano-droplets, and re-dissolution had the same rate constants in all experiments. Consequently, they were hardly influenced by the dissolution medium (Table 10).

The Bi-FaSSIF and the Bi-FaSSIF-V2 dissolution medium lead to the same partitioning rate ($k_{part} = 0.015 \text{ min}^{-1}$) during the period of 30 to 80 min and 30 to 65 min, respectively. In this period no transformation into small nano-droplets (M_{sND}) occurred.

In contrast, the calculated partitioning rate in the plain buffer ($k_{part} = 0.023 \text{ min}^{-1}$) during the early intestinal time period starting at 30 min was little faster (Table 10) resulting in an increased onset of dissolved ritonavir in the organic phase (Figure 22). The difference in the kinetics can be explained by the presence of surfactants in the two biorelevant media, which could lead to a higher affinity of the API in the aqueous phase, and potentially influence the 1-decanol/buffer interface [84].

The nano-droplet properties in the plain buffer medium did not change until the end of the experiment.

Ritonavir-rich nano-droplets (M_{IND}) started to convert into small nano-droplets (M_{SND}) at 65 min (Bi-FaSSIF) and 80 min (Bi-FaSSIF-V2), which demonstrated faster dissolution rates. During dissolution, decreased nano-droplet size leads to an increased solubility with time and a shorter total dissolution time. Consequently, the generated small nano-droplets (M_{SND}) displayed different kinetics for the ritonavir dissolution compared to larger nano-droplets (M_{IND}), especially in the presence of surfactants (Figure 22A, B). Higher surfactant concentrations potentially resulted in a higher wettability of the nano-droplets, resulting in a faster shrinking of small nano-droplets, and a faster re-dissolution rate of the ritonavir from the small nano-droplets (M_{SND}) [100,102]. The re-dissolution rate (k_{dissII}) constant increased to 0.04 min^{-1} and 0.05 min^{-1} respectively and became the new rate limiting step (Table 10). It is important to emphasize that the partitioning (k_{part}) rate also increased to 0.45 min^{-1} and 0.55 min^{-1} . This leads to the conclusion that the kinetic stability of small nano-droplets (M_{SND}) strongly decreased caused by an increased surface energy [99,100], which led to a faster re-dissolution and partitioning process. The decreased kinetic stability was expressed in the kinetic model by a second order partitioning model dependent on the amount of small nano-droplets (M_{SND}) and the dissolved ritonavir concentration (M_{diss}).

In sum, the present kinetic modeling was able to describe the dissolution and partitioning of ritonavir in the BiPHa+ dissolution test on the basis of the dispersion and dissolution behavior of a ritonavir-ASD via API-rich nano-droplets generated by LLPS. The model considered the impact of nano-droplet size on ritonavir dissolution and partitioning as well. Furthermore, the model was able to quantify the amount of growing (M_{IND}) and shrinking (M_{SND}) particles by the Ostwald ripening. The described mechanism provides an additional aspect of the reservoir effect of API-rich nano-droplets by LLPS, which in turn can explain the potential of ASDs to increase the dissolution rate of the incorporated API and to enhance its bioavailability.

Results and Discussion

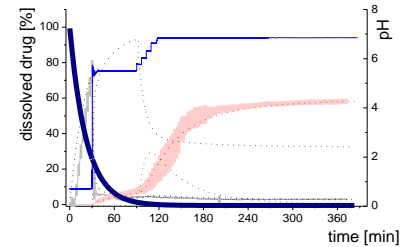
Table 9: Schematic representation of the differential equations to describe the proposed kinetic processes in the five-compartment model occurring in the BiPHA+ dissolution of a ritonavir-containing ASD (ritonavir-ASD) from initial formulation dispersion to final ritonavir partitioning into the organic layer (1-decanol).

Gastric Stage – Model for dispersing of the formulation and dissolution of ritonavir at pH = 1.0

M_{form}: undissolved ritonavir in the **ritonavir-ASD** formulation

$$\frac{dM_{form}}{dt} = -k_{disper} \cdot M_{form} \quad \text{- Simultaneous dispersing of the formulation and dissolution of ritonavir}$$

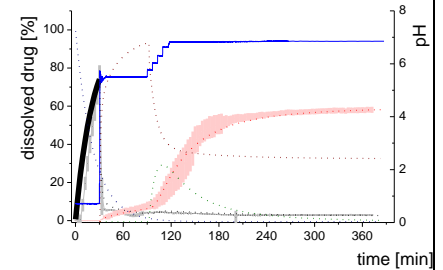
Equation 13



M_{diss}: dissolved ritonavir in the aqueous phase

$$\frac{dM_{diss}}{dt} = +k_{disper} \cdot M_{form} \quad \text{+ Simultaneous formulation dispersion and dissolution of ritonavir}$$

Equation 14



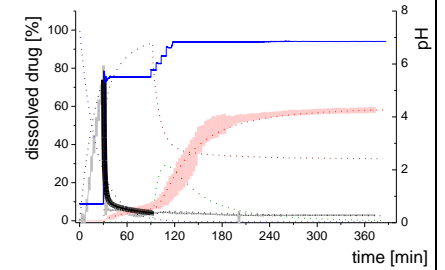
Early intestinal stage – Simple precipitation-absorption model after initial pH-shift to 5.5

M_{diss}: dissolved ritonavir in the aqueous phase–

$$\frac{dM_{diss}}{dt} = \begin{aligned} &+ k_{disper} \cdot M_{form} \\ &- k_{precI} \cdot M_{diss} \cdot (M_{diss} - sat) \\ &+ k_{diss} \cdot M_{IND} \cdot (sat - M_{diss}) \\ &- k_a \cdot M_{diss} \end{aligned}$$

Equation 15

- + Simultaneous dispersion and dissolution
- Precipitation of ritonavir as ritonavir-rich nano-droplets (normalized by saturation solubility)
- + Re-dissolution of ritonavir-rich nano-droplets (normalized by saturation solubility)
- Absorption of ritonavir by organic phase

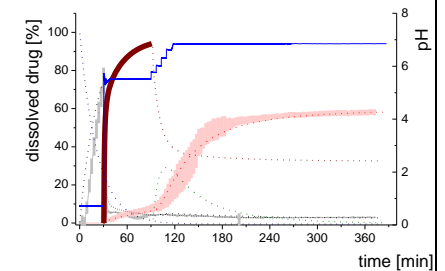


M_{IND}: Large nano-droplets in the aqueous phase

$$\frac{dM_{IND}}{dt} = \begin{aligned} &+ k_{precI} \cdot M_{diss} \cdot (M_{diss} - sat) \\ &- k_{dissI} \cdot M_{IND} \cdot (sat - M_{diss}) \end{aligned}$$

Equation 16

- + Precipitation of dissolved ritonavir as ritonavir-rich nano-droplets
- Re-dissolution of ritonavir-rich nano-droplets

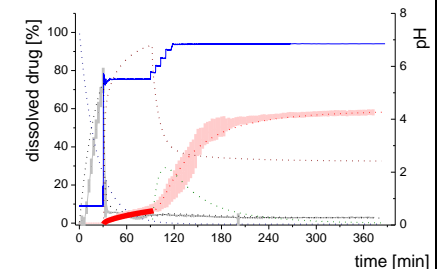


M_{part}: Compartment: dissolved ritonavir in the 1-decanol phase

$$\frac{dM_{part}}{dt} = +k_{part} \cdot M_{diss}$$

Equation 17

- + Absorption of dissolved ritonavir by the organic phase



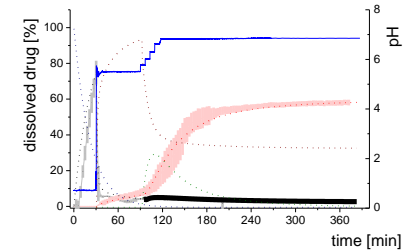
Late intestinal stage – Precipitation-absorption model including a nano-droplet transformation after a stepwise pH-shift to 6.8

M_{diss}: dissolved ritonavir in the aqueous phase

$$\frac{dM_{diss}}{dt} = +k_{disper} \cdot M_{form} - k_{precI} \cdot M_{diss} \cdot (M_{diss} - sat) + k_{dissI} \cdot M_{IND} \cdot (sat - M_{diss}) + k_{dissII} \cdot M_{SND} - k_{part} \cdot M_{diss} \cdot (M_{SND})$$

Equation 18

- + Simultaneous formulation dispersion and dissolution of ritonavir
- Precipitation of dissolved ritonavir as ritonavir-rich nano-droplets
- + Re-dissolution of ritonavir-rich nano-droplets
- + Re-dissolution of small ritonavir-rich nano-droplets
- Absorption of dissolved ritonavir by the organic phase

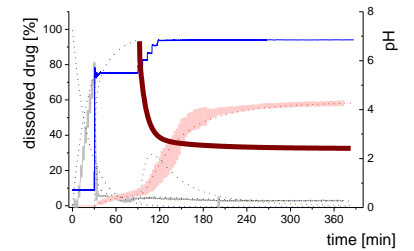


M_{IND}: Large nano-droplets in the aqueous phase

$$\frac{dM_{IND}}{dt} = +k_{precI} \cdot M_{piss} \cdot (M_{diss} - sat) - k_{dissI} \cdot M_{IND} \cdot (sat - M_{diss}) - k_{precII} \cdot M_{IND} \cdot (M_{IND} - max)$$

Equation 19

- + Precipitation of dissolved ritonavir as ritonavir-rich nano-droplets
- Re-dissolution of ritonavir-rich nano-droplets
- Transformation of large nano-droplets into small ritonavir-rich nano-droplets (normalization to the amount of large nano-droplets)

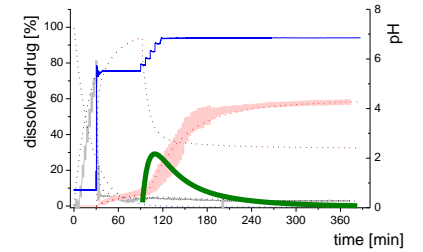


M_{SND} : Small nano-droplets in the aqueous phase

$$\frac{dM_{prec II}}{dt} = +k_{prec II} \cdot M_{IND} \cdot (M_{IND} - max) - k_{diss II} \cdot M_{SND}$$

Equation 20

+ Transformation of ritonavir-rich nano-droplets into small nano-droplets (normalization to the amount of large nano-droplets)
 - Faster re-dissolution of small ritonavir-rich nano-droplets

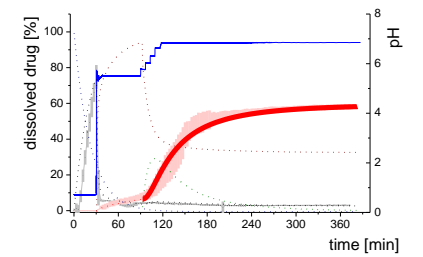


M_{part} : dissolved ritonavir in the 1-decanol phase

$$\frac{dM_{part}}{dt} = +k_{part} \cdot M_{diss} \cdot (M_{SND})$$

Equation 21

+ ritonavir partitioning into the organic layer during transformation process



Results and Discussion

Table 10: Estimated rate constants of three BiPHA+ settings. Bold values characterise the rate limiting steps.

Typ	Bi-FaSSIF-V2			Bi-FaSSIF			Buffer	
	0	30	80	0	30	65	0	30
$k_{\text{disper}} [\text{min}^{-1}]$	0.045	0.045	0.045	0.045	0.045	0.045	0.045	0.045
$k_{\text{dis1}} [\text{min}^{-1}]$		0.009	0.009		0.009	0.009		0.009
$k_{\text{prec1}} [\text{min}^{-1}]$		2.0	2.0		2.0	2.0		2.0
$k_{\text{dis2}} [\text{min}^{-1}]$			0.04			0.05		
$k_{\text{prec2}} [\text{min}^{-1}]$			0.6			0.70		
$k_{\text{part}} [\text{min}^{-1}]$		0.015	0.45		0.015	0.55		0.023
sat		3% (12 µg/ml)	3% (12 µg/ml)		5% (20 µg/ml)	5% (20 µg/ml)		2-5% (10 µg/ml)
max			35%			32%		

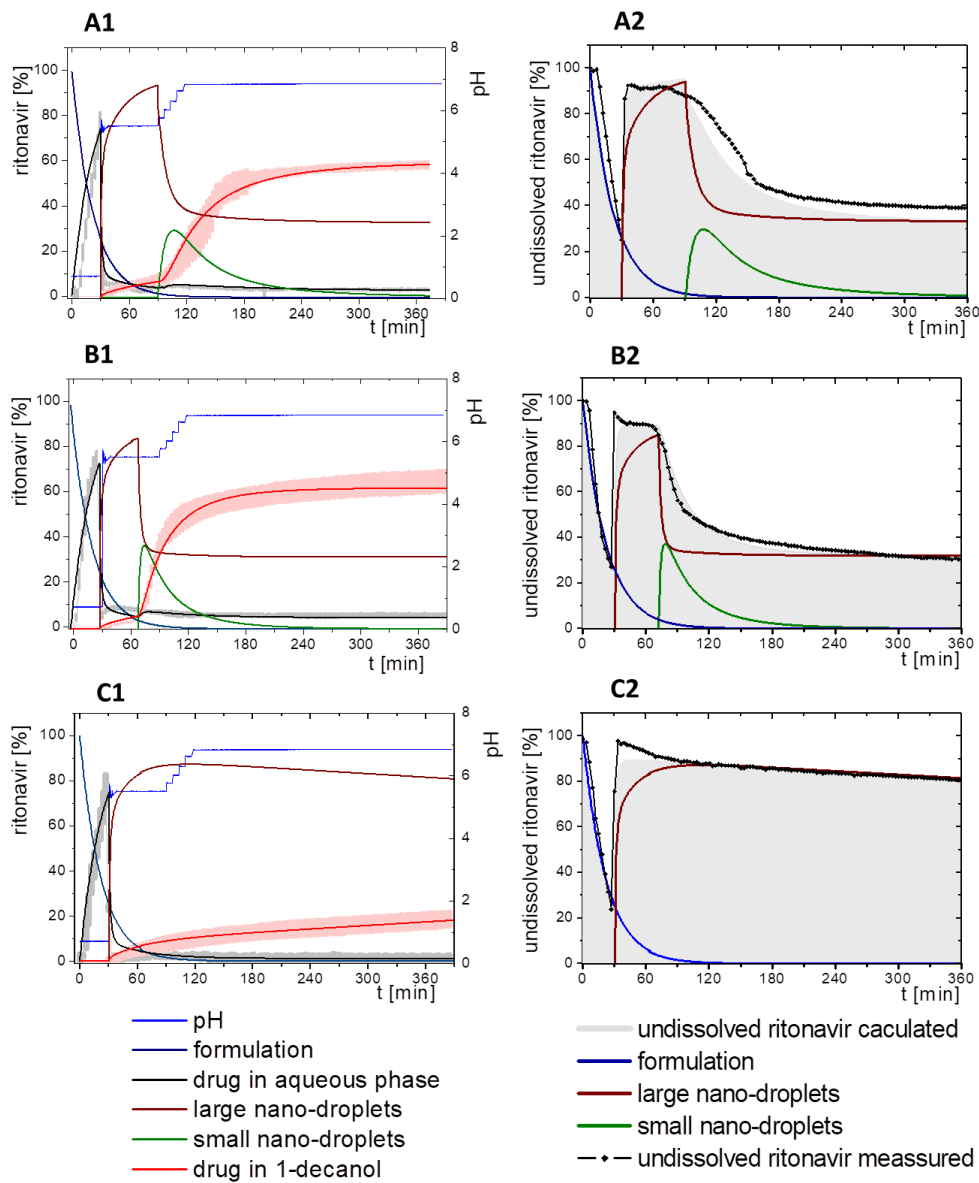


Figure 22: Model fit of four or five compartments compared to the experimental data (**A1-C1**) and mass balance of undissolved ritonavir portions (**A2-C2**). (**A1**) in Bi-FaSSIF-V2 including small nano-droplets (green line), (**B1**) in Bi-FaSSIF-V1 including small nano-droplets (green line), (**C1**) in surfactant-free buffer medium without a nano-droplet transformation. (**A2**) in Bi-FaSSIF-V2 including small nano-droplets (green line), (**B2**) Bi-FaSSIF-V1 including small nano-droplets (green line), (**C2**) in surfactant-free buffer medium without a nano-droplet transformation.

3.4 BiPHa+ Biphasec Dissolution Assay to assess *in vivo* Performance for poorly Soluble Drugs in six commercial enabling Formulations

This part of the work intended to confirm the *in vivo* relevance of the BiPHa+ biphasec dissolution assay using a single set of assay parameters. Herein, we evaluated six commercial drug products formulated by various enabling formulation principles (Table 11) under fasted conditions using the BiPHa+ assay. The *in vitro* partitioning profiles in the organic phase were compared with human pharmacokinetic data obtained from literature. In the first part, a meaningful *in vitro* dose of the formulations was assessed by determining the maximum drug concentration in the artificial absorption sink during dissolution (organic 1-decanol layer, $C_{dec,max}$). Then, the maximum concentration of the partitioned drug in the organic layer was correlated with the *in vivo* fraction absorbed, which was derived from published human pharmacokinetic data. Based on the *in vitro* kinetics of the BiPHa+ experiments, human *in vivo* plasma profiles were predicted using convolutional modelling approach. Subsequently, the calculated pharmacokinetic profiles were compared with *in vivo* performance of the studied drug products to assess the predictive power of the BiPHa+ assay.

Table 11: Investigated drug products: Drug substance, trade name, highest dose strength on market, and enabling formulation type. A dose strength of 10 mg was used for further biorelevance investigations (marked in bold); BCS related *in vitro* doses based on highest dose strength divided by 250 ml are marked in italic.

Drug substance	Trade name (Dose strength)	Formulation type	Investigated <i>in vitro</i> dose		
			[mg]	[mg/ml]	[μ mol]
Aprepitant	Emend® (125 mg)	Nanocrystal (Capsule, Pellets)	5	0.1	9.4
			10	0.2	18.7
			25	0.5	46.4
Celecoxib	Celebrex® (200 mg, 54 mg)	Microcrystal (Capsule, Powder)	5	0.1	13.1
			10	0.2	26.2
			40	0.8	104.8
Fenofibrate	Lipidil® (200 mg)	Microcrystal (Capsule, Powder)	5	0.1	13.9
			10	0.2	27.8
			40	0.4	111.1
Itraconazole	Sempera 7® (100 mg)	ASD (Capsule, Pellets)	5	0.1	7.1
			10	0.2	14.2
			20	0.4*	28.3
Nimodipine	Nimotop® (30 mg)	ASD (Tablet)	5	0.1	11.9
			10	0.2	23.9
			20	0.4	47.8
Ritonavir	Norvir® (100 mg)	ASD (Tablet)	5	0.1	6.9
			10	0.2	13.9
			20	0.4	27.7

3.4.1 Drug Properties

The neat drugs were characterized in terms of their LogP and pKa as well as aqueous solubility at gastric and intestinal pH (Table 12).

Celecoxib exhibits no physiological relevant pKa-value and fenofibrate represents a neutral drug. pKa-values of the weak bases aprepitant, itraconazole, nimodipine and ritonavir are in the range of 1.9 to 3.8. Log P values were in the range of 3.5 to 5.4 (Table 12)

The solubility was investigated in 0.1 M hydrochloric acid, phosphate buffer 6.8 and Bi-FaSSIF-V2 [14]. Itraconazole, ritonavir and aprepitant exhibit pH-dependent solubility. The solubility of celecoxib, aprepitant, nimodipine and ritonavir showed sensitivity to sodium-taurocholate and lecithin (Bi-FaSSIF-V2 medium) compared to the surfactant-free dissolution media. For celecoxib, fenofibrate and nimodipine the differences in solubility in diverse media is minor.

To ensure 10-fold sink conditions during the BiPha+ dissolution experiments, the solubility of the drugs in 1-decanol should be above 8.0 mg/ml (Table 12). Except from itraconazole and aprepitant, the solubility of all other drugs was higher than 8.0 mg/ml. Itraconazole showed a solubility of 1.23 mg/ml in 1-decanol. Therefore, the volume of 1-decanol was adjusted to 100 ml to ensure a 5-fold sink. The solubility of aprepitant in 1-decanol was 4.2 mg/ml, which was assumed to be sufficient to ensure sink conditions (Table 12).

The absolute oral bioavailability was taken from literature (section 4.6.2, Table 13). The fraction absorbed (fa) and bioavailability for nimodipine are different, because 90 % of the absorbed nimodipine is metabolized by first pass, which leads to a distinctly lower bioavailability [105].

Results and Discussion

Table 12: Physicochemical characterization of 6 investigated drugs: pKa values, solubility (S); LogP; bioavailability (F) and fraction absorbed (fa) and quantification wavelength (spectra processing method)

Parameter	Aprepitant	Celecoxib	Fenofibrate	Itraconazole	Nimodipine	Ritonavir
pKa	2.8	10.7 (acid)	N/A ¹⁾	3.8	2.6	1.9 2.5
S (0.1N HCl) [$\mu\text{g/ml}$]	62.0	2.67	0.62	6.1	3.21	382.8
S (6.8N Buffer) [$\mu\text{g/ml}$]	1.39	1.76	1.08	0.88	2.90	0.96
S (FaSSIF-V2) [$\mu\text{g/ml}$]	14.0	4.52	1.03	0.60	5.18	4.30
S (1-decanol) [mg/ml]	4.3	>8.0	>8.0	1.2	>8.0	>8.0
LogP	4.8	3.7	5.4	5.4	3.5	4.4
Bioavailability (F)	0.59 [106]	0.39 [107]	0.46 [83,108,109]	0.16 [110,111]	0.035 [25, 26]	0.75 [68]
Fraction absorbed (fa)	0.59 [106]	0.39 [107]	0.46 [83,108,109]	0.16 [110,111]	0.35 [25, 26]	0.75 [68]
Wavelength (in aqueous phase) [nm]	283 (1. der ²⁾)	285 (1. der ²⁾)	270 (exp ³⁾)	278 (1. der ²⁾)	366 (exp ³⁾)	240 (exp ³⁾)
Wavelength (in 1-decanol) [nm]	280 (1. der ²⁾)	268 (off ⁴⁾)	270 (off ⁴⁾)	290 (1. der ²⁾)	366 (off ⁴⁾)	263 (1. der ²⁾)

¹⁾N/A: not applicable; ²⁾ 1.der: first derivative; ³⁾exp: exponential correction; ⁴⁾off: offset

3.4.2 Dose Assessment

Each drug product was investigated at predetermined *in vitro* doses (5 mg, 10 mg and a BCS class dependent dose, Table 11) by comparing the highest drug concentration in the organic layer ($C_{\text{dec,max}}$) with the corresponding human fraction absorbed *in vivo* (fa[%], Figure 23). Fraction absorbed represents the percentage, which is absorbed from the intestine without considering first pass metabolism. As some experiments resulted in small partitioned drug quantities in the organic phase for some formulations (Figure 23), we empirically selected next to the BCS dependent quantity two *in vitro* doses, smaller, namely 5 mg and 10 mg. We assumed a higher relative partitioned drug quantity (relative $C_{\text{dec,max}}$) in the organic absorption sink layer by decreasing the *in vitro* dose. The rationale for the *in vitro* dose selected is based on the following considerations: The organic phase (absorption sink) pulls dissolved drug molecules out of the aqueous phase. Since only dissolved drug substance is able to partition into the organic phase, a minimum aqueous solubility of undissolved drug particles, dispersed in the aqueous phase (crystals, precipitated particles (amorphous or crystalline), LLPS, colloids), is essential. The undissolved drug particles form the reservoir for the molecularly dissolved

drug substance to be distributed into the organic phase. The extent of the reservoir is linked to the *in vitro* dose used in the biphasic assay. Moreover, Locher et al. 2016 proved a dissolved drug concentration dependent mass transfer [81]. Additionally, mass transfer is a function of interfacial area (aqueous/organic), hydrodynamics and the extent of sink in the organic phase [71]. Now, it is important to balance drug reservoir (in vitro dose) and mass transfer. It was hence anticipated that an optimal *in vitro* dose would result in distribution kinetics optimally matching *in vivo* absorption kinetics and consequently assessed experimentally.

The investigated *in vitro* doses of each formulation (μmol and mg) were plotted against the relative and molar partitioned quantity (% and μmol) to directly assess the biorelevance of each $C_{\text{dec,max}}$ in the organic layer (Figure 23).

Aprepitant (Emend[®], nanocrystal)

The drug product Emend[®] contains the active aprepitant as nanocrystals. By increasing the *in vitro* dose in the BiPHA+ dissolution test from 5 mg (9.4 μmol) to 25mg (46.8 μmol), relative $C_{\text{dec,max}}$ in the organic layer decreased from 85 % (7.8 μmol) to 18 % (9.5 μmol) respectively. The decrease was more pronounced in the dose range of 10 mg to 25 mg resulting in a relative $C_{\text{dec,max}}$ ranging from 60 % (7.8 μmol) to 18 % (8.42 μmol), compared to 5 and 10 mg (85 % - 60 %). $C_{\text{dec,max}}$ at 10 mg was in good agreement to the fraction absorbed *in vivo* of approx. 59 % (Figure 23A).

Celecoxib (Celebrex[®], microcrystal)

In the case of the micronized celecoxib formulation, the highest relative $C_{\text{dec,max}}$ value (41 %) was achieved at a dose of 10 mg (26.2 μmol), which was comparable to the fraction absorbed *in vivo*. At 5 mg (13.1 μmol) celecoxib the relative $C_{\text{dec,max}}$ value was 32 % (4.2 μmol). A lower relative amount of celecoxib (5 %) partitioned into the organic layer at the BCS dependent *in vitro* dose of 40 mg (Figure 23B).

Fenofibrate (Lipidil 200[®], microcrystals)

Lipidil[®] is a micronized formulation in order to enhance dissolution rate. Approximately 45 % (6.2 – 13.0 μmol) of fenofibrate partitioned at an investigated *in vitro* dose of 5 mg (13.9 μmol) and 10 mg (27.8 μmol) into the organic layer, which was similar to the observed fraction absorbed *in vivo*. At a high investigated microcrystalline fenofibrate quantity of 40 mg (111.1 μmol), $C_{\text{dec,max}}$ value decreases to 10 % (10.4 μmol) (Figure 23C).

Itraconazole (Sempera[®], ASD)

The enabling formulation of itraconazole is a HPMC-based amorphous solid dispersion, coated on pellets. Itraconazole partitioned up to 17 % (1.3 – 2.4 μmol) in the case of the 5 mg (7.1 μmol) and 10 mg (14.2 μmol) investigated *in vitro* dose into the organic phase. 9 % (2.6 μmol) of the 20 mg (28.3 μmol) itraconazole dose partitions in the organic phase. The *in vivo* fraction absorbed of the same formulation in the fasted state is 16 % (Figure 23D).

Nimodipine (Nimotop[®], ASD)

Nimotop[®] is a first generation ASD based on polyethylene-glycol. $C_{\text{dec,max}}$ values of 5 mg (11.9 μmol), 10 mg (23.9 μmol) and 20 mg (47.8 μmol) nimodipine-ASD were in a range of 38 to 50 % (5.7 – 20.1 μmol), which was higher compared to 35 % *in vivo* fraction absorbed (Figure 5E).

Ritonavir (Norvir[®], ASD)

The Norvir[®] drug product contains ritonavir as an amorphous solid dispersion consisting of a polymer/surfactant matrix. All investigated *in vitro* doses provided a relative $C_{\text{dec,max}}$ of 70 to 80 % (equal to 5.5 – 18.6 μmol) in the organic layer, which was in accordance with the *in vivo* fraction absorbed of 76 % (Figure 23F).

The drug products with crystalline drug substance, namely Emend[®] (nanocrystals), Celebrex[®] (microcrystals) and Lipidil 200 (microcrystals) showed similar *in vitro* behavior: an increase of the *in vitro* dose in the dissolution experiment led to decreased values for relative $C_{\text{dec,max}}$ in the organic layer. This behavior can be explained by the developability classification system [7,8] applied to the BiPha+ assay. Dissolution of the crystalline drug at a dose level range of 15-25 μmol was mainly dissolution rate limited (IIa) leading to a similar relative $C_{\text{dec,max}}$ in the organic layer. At the higher BCS class dependent dose levels as displayed in Figure 23, drug dissolution became mainly solubility limited (IIb) leading to lower $C_{\text{dec,max}}$ values. As a result, the BiPha+ assay was not able to discriminate the rate limiting step of dissolution at drug levels higher than 30 μmol , because the drug flux was limited by its solubility.

Ritonavir, itraconazole and nimodipine formulated as an ASD reached a rather comparable and slighter decreasing relative $C_{\text{dec,max}}$ values in the 1-decanol layer over the tested drug levels. This could be explained by the fact that the drugs were presented in their amorphous form causing the partitioning into the organic layer did not only depend on solubility and dissolution rate, but also on a complex interplay of dissolution, precipitation, re-dissolution as described previously [21,68,112].

$C_{dec,max}$ values obtained at an *in vitro* dose of 10 mg for all investigated drugs demonstrated the highest accordance to the values for the fraction absorbed *in vivo*. Based on these results, we propose an *in vitro* dose of 10 mg (equal to approx. 15–25 μmol) as a standard for our assay to determine bio-comparable partitioning profiles for *in vivo* doses in the range of 30–200 mg. This demonstrates that the presented BiPHA+ assay could generate discriminatory partitioning results, because dissolution or re-dissolution of drug substance has been proven to be the rate limiting step.

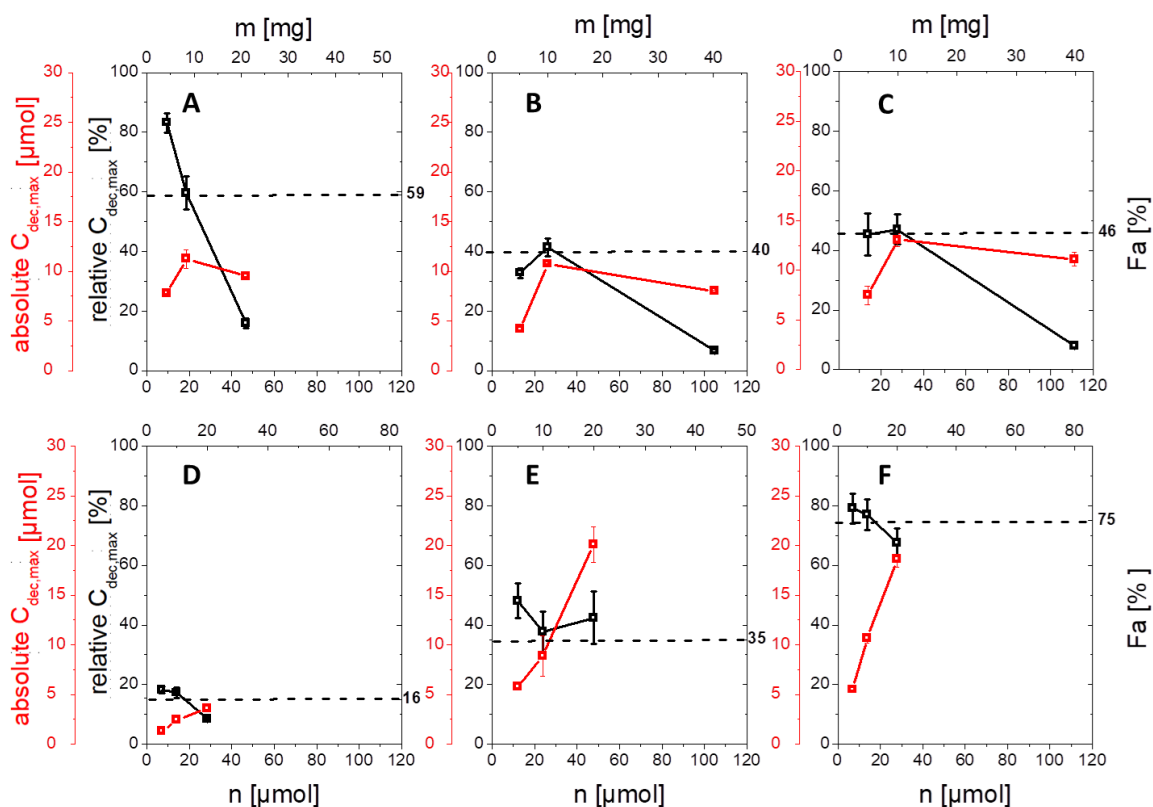


Figure 23: Relative C_{max} (%) and absolute C_{max} (μmol) values of the organic partitioning profiles with different drug contents (mg or μmol) investigated in the BiPHA+ assay after 4.5 hours: (A) aprepitant; (B) celecoxib; (C) fenofibrate; (D) itraconazole; (E) nimodipine; (F) ritonavir; dotted black line represents the *in vivo* oral fraction absorbed (%)

3.4.3 Drug Product Evaluation Using BiPHA+ Dissolution Assay

The six different market drug products formulated through different enabling principles were investigated under the same biorelevant biphasic dissolution setting mimicking fasted state conditions with a concentration of 10 mg in 50 ml aqueous phase (Figure 24). The equivalent molar quantities are given in Table 11.

Aprepitant (Emend[®], nanocrystals)

In the aqueous phase the nanocrystal formulation provided an aprepitant dissolution of up to 15 % in the gastric stage. The quantification of aprepitant within the intestinal stage became challenging, as pronounced scattering occurred from nano-sized particles in combination with Bi-FaSSiF-V2 surfactant (Figure 24A). Consequently, the quantification in the aqueous phase was probably overestimated leading to the curved shape of the aqueous concentration time profile. The partitioning rate into the organic layer represented a zero-order kinetic after a short phase of a faster onset caused by the pH-dependent solubility. As evident from a $C_{dec,max}$ of 60 %, the dissolution of nanocrystals was very efficient.

Celecoxib (Celebrex[®], microcrystals)

The microcrystal formulation of the neutral drug celecoxib provided drug dissolution in the gastric stage of up to 18 % (Figure 24B). In the early intestinal stage (pH 5.5, Bi-FaSSiF-V2) additional drug dissolved up to 22% after 30 min in the aqueous phase. The initially higher partitioning rate into the organic layer was attributed to the higher concentration of the drug in the aqueous phase within the time span of 30 - 80 min. During the late intestinal phase, starting at 80 min, the aqueous concentration of celecoxib remained at a constant level of 8%, and thus, results in a constant partitioning rate.

Fenofibrate (Lipidil[®], microcrystals)

Micronized fenofibrate reached approx. 3 % dissolved drug during the gastric stage (Figure 24C). After a short period of supersaturation between 30 min and 60 min, the drug concentration remained at 2 % in the aqueous phase. The organic partitioning profile was similar to a first order kinetics and after 90 min a slightly increasing plateau was reached with a $C_{dec,max}$ value of 45 %.

Itraconazole (Sempera[®], ASD)

The HPMC-based ASD of itraconazole enabled supersaturation of the drug in the aqueous gastric stage up to 60 % (Figure 24D). After the shift from gastric conditions to small intestine conditions, itraconazole precipitated resulting in approx. 17 % remaining dissolved drug at minute 30. The short period of supersaturation in the early intestinal stage (30 - 60 min) was mainly responsible for the partitioned amount of itraconazole in the organic layer. After the supersaturation period (30 - 60 min), the precipitated drug was apparently no longer able to re-dissolve (60 - 270 min), which resulted in no further increase of the partitioned itraconazole (Figure 24D).

Nimodipine (Nimotop[®], ASD)

In the case of the Nimotop[®] drug product (Figure 24E), nimodipine dissolved from the PEG-based ASD and reached a maximum concentration in the aqueous phase of 5 % within the first 15 min of the gastric stage. Precipitation occurred in the gastric stage during minutes 15 and 30. Even after a change to the intestinal stage, the nimodipine concentration did not exceed 5 % in the aqueous phase until the end of the dissolution experiment after 270 min. The organic partitioning profile followed a square root-t (\sqrt{t}) kinetic. The relatively high $C_{des,max}$ in the organic phase was probably achieved by a high but decreasing re-dissolution rate of the precipitated drug.

Ritonavir (Norvir[®], ASD)

Ritonavir exhibited a pronounced pH-dependent solubility. The ASD formulation provided drug dissolution in the aqueous phase of up to 75 % within the first 30 min at gastric conditions. After the change to intestinal conditions (pH 5.5, FaSSIF-V2), the amount of dissolved ritonavir drops to 3 %, and remained at this level until reaching the end of the dissolution experiment at 270 min. The drug concentration profile in the organic layer had a sigmoidal shape with a plateau at approx. 75 % (Figure 24F).

After description of the results of the BiPha+ dissolution experiments for each drug product, the following paragraphs discuss the results with respect to specific drug and formulation properties.

Crystalline formulations

Aprepitant, celecoxib and fenofibrate dissolved slowly in the gastric medium up to a concentration of less than 20 %, because the drugs are formulated using their crystalline forms. The partitioning profile of the three crystalline drugs aprepitant, fenofibrate and celecoxib followed a zero-order partitioning kinetic, because the drugs continuously dissolved from the crystalline particles released by the formulation, and only drug specific solubility effects driven by pH and bile-salts influenced the extent of drug dissolution (Figure 24A-C). Although the partitioning of the nano-sized aprepitant crystals was the fastest, conclusions on the influence of the crystal particle size were difficult to make, as the solubility of the respective drugs in the various media were different. The initial high and fast partitioning of fenofibrate could be explained by the high LogP and initially increased dissolution of fenofibrate in the early intestinal stage compared to aprepitant and celecoxib. The plateau was attributed to the low remaining solubility and re-dissolution rate. The partitioning profile of celecoxib was directly attributed to the dissolved amount of drug in the aqueous phase. The partitioning rate decreased with

decreasing aqueous concentration. A higher drug concentration than the saturation solubility was likely caused by enhanced dissolution of celecoxib in the presence of the surfactants and lipids in the biorelevant intestinal medium [113].

Amorphous solid dispersion

The drug dissolution mechanisms of the ASD-based formulations, responsible for the drug partitioning in the organic layer, were different (Figure 24D-F). Supersaturation, which was indeed responsible for an increase of the partitioning rate [114], was only observed in the case of itraconazole (Figure 24E). The partitioning of nimodipine and ritonavir was mainly driven by the ability of the precipitated drug to re-dissolve (Figure 24D, F) [68,115]. The ability of nimodipine to re-dissolve, which was characterized by the organic partitioning profile, decreased over time. Initially, nimodipine amorphously precipitated and then, started to crystallize moderately fast leading in a decreased re-dissolution and subsequent partitioning [116]. The partitioning profile of the ritonavir formulation resulted in a sigmoidal shape. This was caused by a dynamic behaviour of the drug-rich nano-droplets. The rather small particles underwent particle size reduction by re-dissolution. A plateau was reached as soon as all small drug-rich nano-droplets were dissolved [112].

Neutral drugs

As pH-dependent solubility did not apply for neutral drugs, surfactant mediated solubility enhancement could be observed even more pronounced for celecoxib and fenofibrate in combination with the biorelevant surfactant from Bi-FaSSiF-V2. In our biphasic assay this surfactant sensitivity resulted in initially higher partitioning rates of celecoxib and fenofibrate into the organic phase related to dissolved / solubilized drug (Figure 24B, C). Celecoxib showed chaser properties, whereby the micronized formulation supersaturated, i.e. next to undissolved crystalline celecoxib a supersaturated solution were present. Despite crystalline celecoxib was present, the supersaturated amorphous solubility remains, because the precipitated celecoxib slowly recrystallized [117]. Fenofibrate was more soluble in the presence of bile salts contained in Bi-FaSSiF-V2 compared to simple aqueous media [118]. Therefore, fenofibrate quickly dissolved immediately after generation of the Bi-FaSSiF-V2 medium leading in a high partitioning rate at the beginning of the intestinal phase. However, the amount of dissolved drug quickly dropped back to the level of the crystalline solubility. The slow dissolution rate of the crystalline drug resulted in a plateau of the concentration time profile in the organic phase

pH-dependent soluble drugs

The expected pH-dependent solubility of the weak base aprepitant is barely noticeable (Figure 24A). Consequently, the particle size reduction approach of the crystalline aprepitant was the main reason for the increased dissolution and in turn the high partitioning rate. However, the solubility of the weak bases ritonavir and itraconazole was strongly pH –dependent: The dissolved amount of both drugs dropped remarkably after entering the early intestinal stage at elevated pH. At the solubility maximum at pH 1, itraconazole initially supersaturated followed by precipitation over a period of 30 min. The generated supersaturation was mainly responsible for itraconazole partitioning in the organic layer. Once the crystalline solubility was re-established, itraconazole had no further tendency to re-dissolve. In contrast, ritonavir formed nano-droplets generated by liquid-liquid phase separation resulting in a constant aqueous concentration, and a highly increased partitioning rate [112].

Although nimodipine has a measured pKs value of 2.6, it precipitated already during the gastric phase (pH = 1.0). The change of partitioning rate was mainly driven by the properties of the amorphously precipitated nimodipine [116]. This can be seen by the fact that the dissolved nimodipine concentration remained on the same level and partitioning rate changed.

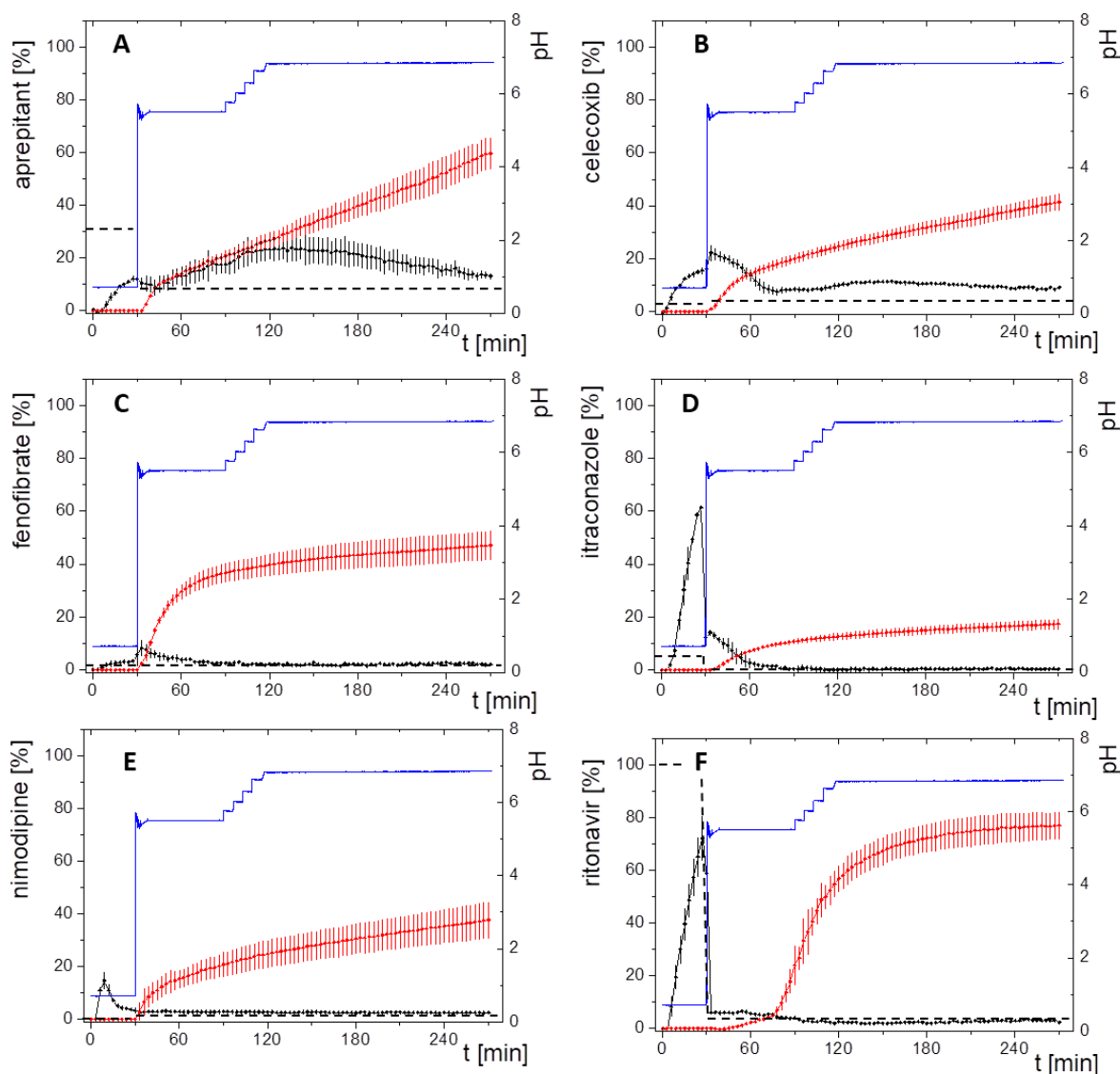


Figure 24: Biphasic dissolution profiles at 10 mg *in vitro* dose for (A) aprepitant; (B) celecoxib, (C) fenofibrate (D) itraconazole; (E) nimodipine; (F) ritonavir. Drug concentration in the aqueous layer (black line), and in the organic layer (red line); pH in the aqueous layer during dissolution test (blue line); crystalline drug solubility in the aqueous layer (black dotted line)

3.4.4 Pharmacokinetics and Compartment Analysis of *in vivo* Data

As described in section 4.6.2, distribution (λ_1) and elimination (k_e) were calculated from *in vivo* data (Table 13) by a two-compartment model (Figure 25), due to the high LogP values of the investigated drugs [31]. The high lipophilicity results in high protein binding distribution into tissue [31]. Since aprepitant has a more complex elimination profile, it was pragmatically described by a one-compartment model [119].

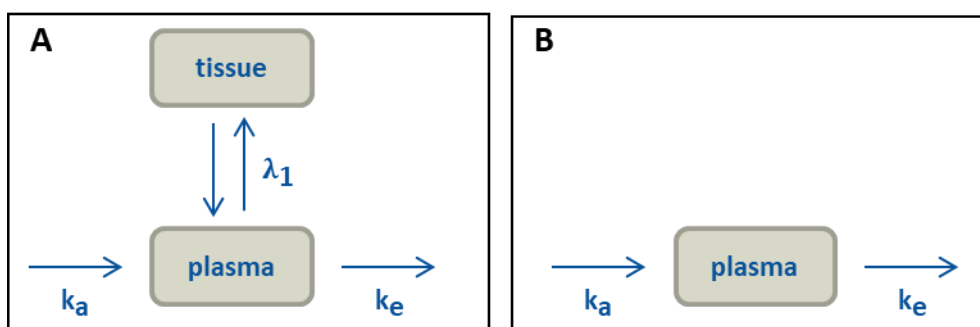


Figure 25: Pharmacokinetic models: (A) two-compartment model, (B) simplified model for aprepitant.

The pharmacokinetic constants were calculated using the residual method based on literature data (Table 14). The estimated absorption rate constant (k_{a1}) of the drugs aprepitant, celecoxib, itraconazole and ritonavir were quite comparable between 1.1 h^{-1} and 1.6 h^{-1} . In case of fenofibrate, the *in vivo* absorption was a two-step process: the absorption of the pro-drug and the subsequent metabolism into the active form fenofibric acid by esterases. For fenofibrate, there were two *in vivo* studies available applying 54 mg and 200 mg. The absorption rates strongly differ from each other (0.4 h^{-1} to 0.8 h^{-1}) dependent on the applied dose, which means C_{max} (maximum plasma concentration) also differs between 4 and 6 h (Figure 29). This observation likely relates to the transformation of fenofibrate into its active metabolite fenofibric acid contributing to the varying absorption rates of fenofibrate *in vivo* [120]. The determined absorption rate of nimodipine was very fast having a rate constant of 2.0 h^{-1} . However, a substantial part of the absorbed dose subsequently undergoes a high first-pass hepatic metabolism. As the metabolism rate of nimodipine is higher than the absorption rate, it could not be calculated based on the available data [33].

These findings demonstrated the applicability of the compartment model combined with the residual method to get a meaningful estimate of the absorption rate by a first order kinetic. However, some limitations occur in the case of extensive metabolism.

Table 13: Bioavailability (F, considering first-pass) and fraction absorbed (f_a , without first pass) reported in the literature.

Parameter	Aprepitant	Celecoxib	Fenofibrate	Itraconazole	Nimodipine	Ritonavir
Bioavailability (F)	0.59 [106]	0.39 [107]	0.46 [83,108,109]	0.16 [110,111]	0.035 [25, 26]	0.75 [68]
Fraction absorbed (f_a)	0.59 [106]	0.39 [107]	0.46 [83,108,109]	0.16 [110,111]	0.35 [25, 26]	0.75 [68]

Table 14: Calculated pharmacokinetic rate constants of the *in vivo* human plasma profile: k_{a1} (absorption rate), k_{a2} (absorption rate of the small 54 mg fenofibrate dose), λ_1 (distribution rate), k_e (elimination rate)

Rate constant	Aprepitant	Celecoxib	Fenofibrate	Itraconazole	Nimodipine	Ritonavir
k_{a1} [h^{-1}]	1.050	1.150	0.400 ¹⁾	1.580	2.040	1.496
k_{a2} [h^{-1}]	N/A	N/A	0.799 ²⁾	N/A	N/A	N/A
λ_1 [h^{-1}]	N/A	0.088	0.099	0.0931	0.481	0.123
k_e [h^{-1}]	0.0421	0.070	0.0319	0.0352	0.351	0.112

N/A: not applicable; ¹⁾ calculated by a 200 mg dose, ²⁾ calculated by a 54 mg dose

3.4.5 IVIVR: Compare Drug Partitioning during Dissolution and *in vivo* Absorption

Because the absolute bioavailability values were comparable to the end-concentrations of the organic layer $C_{max,dec}$ (Figure 23), a level A IVIVR was established based on the obtained *in vivo* absorption data and the results of the BiPHA+ dissolution test. Fenofibrate was excluded for the IVIVR for its high variability of the absorption rates (Table 14) of the two available *in vivo* studies [83,121]. Two cases were considered to assess the correlation between *in vitro* drug partitioning into the organic layer and the fraction absorbed *in vivo*:

In the first case, a regular level A IVIVR was calculated based on the Levy plot to commonly simulate the time-scaling between *in vitro* dissolution and *in vivo* absorption data (Figure 26A, B). The correlation of the Levy plot for all model drugs resulted in a regression coefficient of 0.91. Most single time values were within the 95 % confidence interval (Figure 26A). The resulting fractions absorbed were plotted against the drug concentration in the organic layer obtained during the *in vitro* dissolution, which led to a regression coefficient of 0.98 (Figure 26B). However, correlation values of ritonavir were outside the 95 % prediction limits (Figure 26B), due to the sigmoidal partitioning profile *in vitro* (Figure 24E). All IVIVR data points are sigmoidal distributed except those for ritonavir. This is caused by rapid initial partitioning rates compared to the calculated first order absorption profiles, which is reflected on the IVIVR plot by data points placed below the regression line within the first 20% *in vitro* partitioned drug (Figure 26B). Then, the partitioning rates decrease and the IVIVR data points distribute above the regression line. A profound interpretation of this finding is hardly possible, since the true *in vivo* absorption is not known.

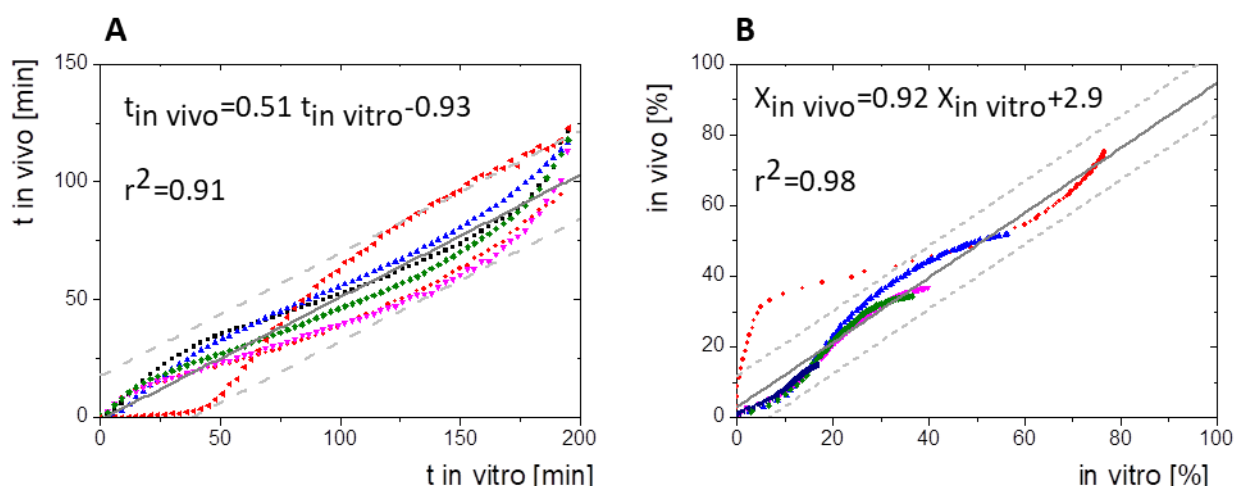


Figure 26: (A) Levy Plot/ time-scaling, (B) IVIVC of the five model drugs both including confidence interval 95 % (grey dashed lines), aprepitant (blue symbols), celecoxib (pink symbols), itraconazole (dark blue symbols), nimodipine (green symbols), red: ritonavir (red symbols)

In the second assessment, a direct comparison between *in vivo* absorption and *in vitro* partitioning profiles was performed (Figure 27). In consideration of the absolute bioavailability, the calculated first order absorption profiles were compared to the *in vitro* partitioning profiles. Both the directly measured (grey line) and the time-scaled (blue line, Levy plot) *in vitro* partitioning profiles are given in Figure 27. Levy plots are generally implemented, when rate constants of drug absorption and *in vitro* dissolution are different [122]. However, in our cases the rate constants of the BiPHA+ assay were similar with the *in vivo* constants. Thus, the partitioning profiles without time-scaling (grey lines, Figure 27) matched better with the calculated *in vivo* fraction absorbed compared to the time scaled partitioning profiles (blue lines, Figure 27). Independent on the time-scaling, the end value of the partitioned drug in the organic phase matched very well with the fraction absorbed (Figure 27), which is an additional indicator of the biorelevance of the BiPHA+ assay independent whether time-scaling was employed or not (Figure 27).

Consequently, the biphasic dissolution assay was likely able to characterize the drug absorption *in vivo* of all analyzed drugs. Overall, the partitioned amount of the investigated poorly soluble drugs was equivalent to the maximum amount of passively absorbed drug fraction *in vivo*.

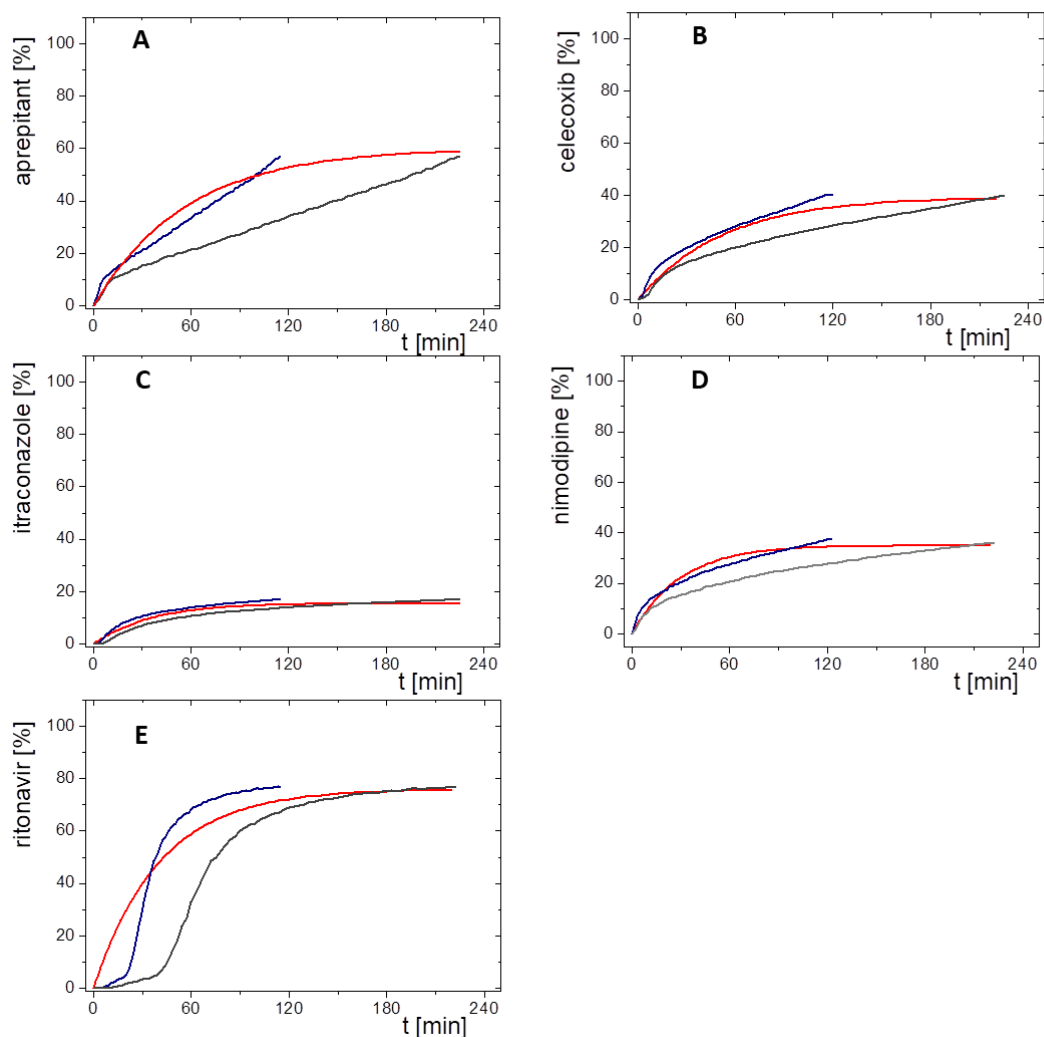


Figure 27: Comparisons of *in vivo* absorption profiles and *in vitro* partitioning profiles for (A) aprepitant; (B) celecoxib, (C) itraconazole; (D) nimodipine; (E) ritonavir; red line: fraction absorbed time profile *in vivo*; blue line: organic partitioning profiles corrected by Levy plot; grey line: organic partitioning

3.4.6 *In vivo* Prediction from Biphasic *In vitro* Data and Prediction Error

The information on distribution and elimination obtained from the compartmental models (derived from the published *in vivo* data) was combined with the corresponding partitioning profile obtained from the BiPha+ dissolution experiment to calculate the plasma concentration time profiles *in vivo* (Equation 28) for all six model drugs. Figure 28 shows the predicted *in vivo* plasma concentration-time profiles without (grey line) and with (blue line) time-scaling (Levy plot). For fenofibrate the same time scaling factor was applied as for the other formulations to enable a direct comparison. The calculated pharmacokinetic profiles are compared to the observed plasma concentrations (Figure 28). Fenofibrate was separately evaluated in Figure 29 since the *in vivo* absorption

between is significantly different. Pharmacokinetic parameters and prediction errors of observed and predicted plasma concentration time profiles are given in Table 15.

Aprepitant (Emend[®], nanocrystals)

In case of aprepitant, the applied one compartment model was in good agreement with the observed *in vivo* data (Figure 28A). By using the concentration-time profile from dissolution (organic layer) without time-scaling as absorption profile, a C_{\max} of 0.89 $\mu\text{g/ml}$ was calculated to be reached at 3.9 h (t_{\max}), which is in a good agreement with the reported t_{\max} *in vivo* (4.1 h) as a result of the zero-order dissolution kinetics *in vitro*. On the other hand, the use of the time scaled *in vitro* dissolution profile led to a similar C_{\max} value of (0.93 $\mu\text{g/ml}$) but an essentially lower t_{\max} (2.0 h) (Figure 28A).

Celecoxib (Celebrex[®], microcrystals)

After an initial increased partitioning rate, celecoxib partitioned with a zero-order kinetic in the dissolution experiment. This partitioning profile was used as basis for the absorption kinetic and led to the tip shape of the mathematically predicted pharmacokinetics (Figure 28B). T_{\max} of the predicted time scaled profile (1.9 h) was closer to the observed *in vivo* data (2.0 h) than the t_{\max} calculated without time-scaling (3.8 h). Overall, the predicted AUC was in good agreement with the reported AUC value for celecoxib (Table 15). The absolute fraction absorbed was estimated to be in the range of 40% by applying the present IVVC model in absence of human plasma concentration data after intravenous dosing.

Itraconazole (Sempera[®], ASD)

The tip shape of the itraconazole plasma profile and the predicted profiles (Figure 28C) were the result of the fast absorption *in vivo* (Figure 27C). Compared to the absorption profiles *in vivo* the partitioning profiles *in vitro* had similar shapes (Figure 27C), and demonstrated the high accuracy of the predicted plasma concentration-time profiles (Figure 28C). Both concentration-time predictions, with and without time-scaling, were only slightly different to the *in vivo* observed data (Table 15).

Nimodipine (Nimotop[®], ASD)

The predicted plasma concentration-time profile of the nimodipine drug product showed the highest prediction error in C_{\max} of 33.3 % and 49.9 % (Table 15). Due to the high extent of first-pass [123] and the high elimination rate, describing pharmacokinetics accurately was difficult. In fact, enzyme saturation occurs *in vivo* [123], which was of course not covered by the applied two-compartmental models (Figure 28D). As the

absorption rate is slower than the metabolizing rate, determining a metabolizing rate by *in vivo* plasma data was not possible. The only option to consider the metabolism in this case would be using the bioavailability ($F = 3.5\%$) in the prediction derived from the *in vivo* fraction absorbed ($f_a = 35\%$). Due to the short elimination half-life period, the partitioning profile strongly influences the shape of the pharmacokinetic prediction profile (Figure 28D).

Ritonavir (Norvir[®], ASD)

The *in vivo* performance of ritonavir could be very precisely predicted (Figure 28E). The sigmoidal shape of the *in vitro* dissolution profile led to a lag-time in the predicted profiles (Figure 24E). Due to the faster partitioning rate of the in time-scaled prediction, C_{max} ($0.63 \mu\text{g/ml}$) was overestimated and the not time scaled ($0.53 \mu\text{g/ml}$) was slightly overestimated (Table 15).

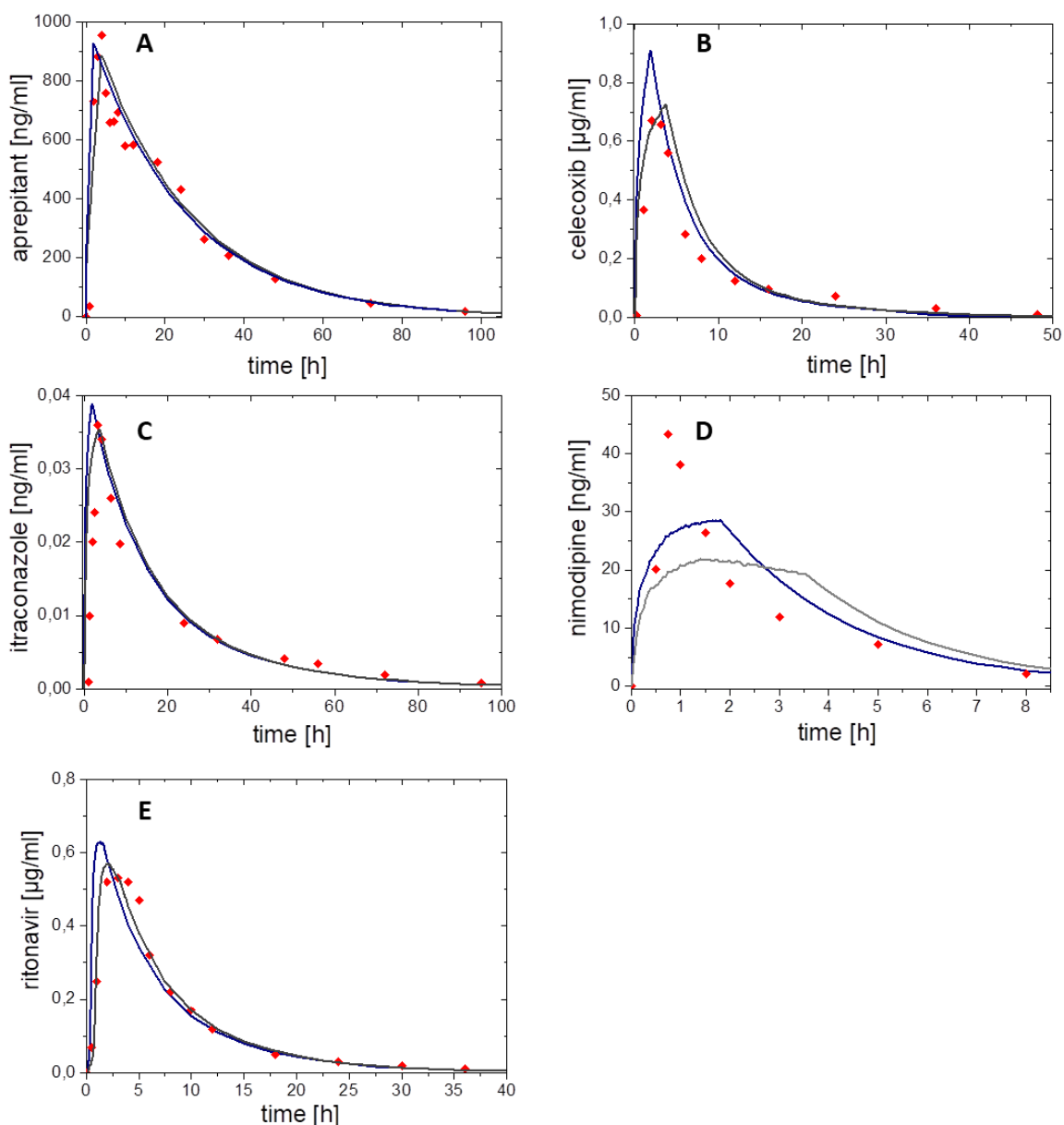


Figure 28: Plasma concentration time profiles for (A) aprepitant, (B) celecoxib, (C) itraconazole, (D) nimodipine, and (E) ritonavir. Modelled *in vivo* profile with time scale correction (blue line); Modelled profile without time scale correction (grey line); Plasma concentration-time profiles from humans (red dots).

Fenofibrate (Lipidil[®], microcrystals)

Fenofibrate as a prodrug is activated by a metabolic transformation into fenofibric acid [120]. Consequently, the actual absorption rate cannot be meaningfully calculated directly from the *in vivo* plasma concentration time data based on compartmental models. As the established Levy plot was considered to be a general factor, which might be drug independent, the pharmacokinetic predictions were performed by both the time scaled

and not time scaled approach. Hence, this additional metabolism step by tissue and plasma esterase led to an observed t_{\max} of 6.3 h for the 200 mg dose strength and t_{\max} of 4.0 h for the 54 mg dose strengths *in vivo* (Figure 29). This was likely caused by the slow activation rate, which became, with an increasing administered dose, the rate-limiting step of the absorption, because the activation is likely a saturable process. Consequently, the deviation of the predicted plasma concentration time profiles of the 200 mg dose strength was more pronounced with regard to the absorption period of the first six hours (Figure 29A) than the 54 mg dose strengths (Figure 29B). The higher and earlier predicted C_{\max} of the 200 mg dose was due to the fact that based on convolution approach no saturation step of fenofibrate activation was considered. According to this argumentation, the high agreement of the 54 mg dose prediction with the observed *in vivo* data can also be explained because potential enzyme saturation plays a minor role. The activation of fenofibrate to fenofibric acid was faster compared to the 200 mg dose and therefore results in a high consistency with the *in vivo* data (Figure 29B). The *in vivo* observed C_{\max} value of the 54 mg dose matched the theoretically calculated. The prediction error for AUC and t_{\max} agreed with the *in vivo* observed data for the smaller dose strength, whereas the higher dose strength results in a high agreement to observed AUC values but not for C_{\max} and t_{\max} (Table 15).

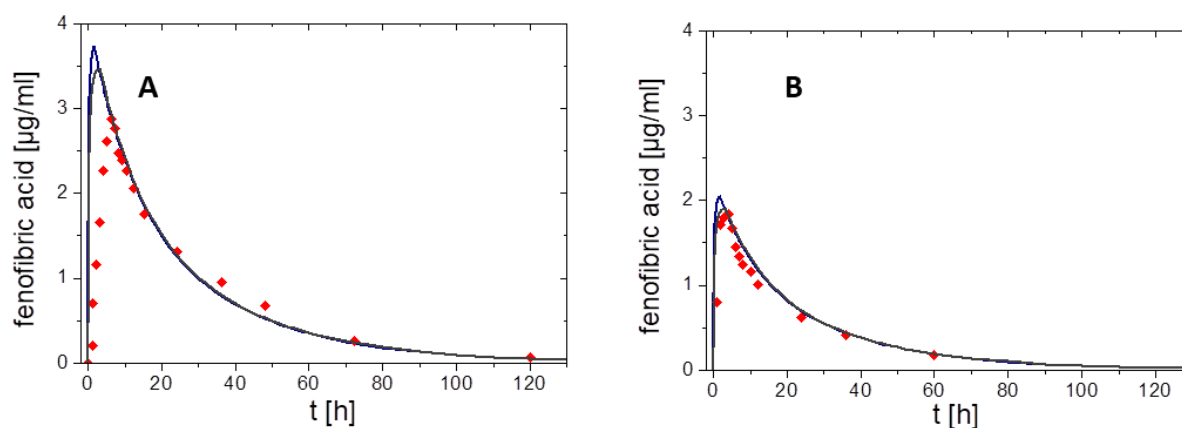


Figure 29: Plasma concentration time profiles for (A) fenofibrate 200 mg and (B) fenofibrate 54 mg as activated metabolite fenofibric acid. Predicted *in vivo* plasma concentration time profile with time scale correction (blue line); Predicted profile without time scale correction (grey line); Plasma concentration time profiles from humans (red dots).

Finally, based on the modelling results, prediction errors for AUC and C_{\max} were calculated and assessed based on the guidance from EMA and FDA [74,124]. In addition, the deviations of t_{\max} were determined as absolute values in hours. The results are displayed in Table 15, and summarized as follows:

- The average prediction error of AUC (including both fenofibrate doses) of time scaled corrected and not corrected partitioning profiles was (-)1.7 %, which confirmed the accuracy of the prediction. Furthermore, the prediction error for the AUC of single drug plasma concentration time profile was in the required acceptance range of 15 % of the EMA guideline [125].
- The average mean prediction error was (-)10.6 % for C_{\max} based on time scaled plasma concentration time profile, and (+)2.5 % without time-scaling.
- The mean deviation of t_{\max} of the predicted plasma concentration time profiles from the available pharmacokinetic data reported in literature is between -2.2 h for the time scaled and -0.3 h for the not scaled predictions. All t_{\max} values do not deviate more than -4.6 h to +1.8 h.

Results and Discussion

Table 15: Prediction errors for AUC, C_{max} and t_{max} based on FDA and EMA guidance [74,124] comparing time-scaled (Levy) dissolution profile and those without time-scaling.

Drug product	Origin of absorption kinetic	AUC [µg/ml·h]	Error AUC [%]	C_{max} [µg/ml]	Error C_{max} [%]	t_{max} [h]	Error t_{max} [h]
Aprepitant	<i>in vivo</i>	22.5		0.95		4.1	
	<i>in vitro</i> (Levy) <i>in vitro</i>	20.7	+8.0	0.93 0.89	+2.1 +6.3	2.0 3.9	-2.1 -0.2
Celecoxib	<i>in vivo</i>	5.96		0.67		2.0	
	<i>in vitro</i> (Levy) <i>in vitro</i>	5.80	+2.7	0.91 0.73	-35.8 +8.9	1.9 3.8	-0.1 +1.8
Fenofibrate (200 mg)	<i>in vivo</i>	88.2		2.90		6.3	
	<i>in vitro</i> (Levy) <i>in vitro</i>	89.7	-1.7	3.74 3.47	-28.9 -19.7	1.7 3.4	-4.6 -2.9
Fenofibrate (54 mg)	<i>in vivo</i>	39.0		1.8		4.0	
	<i>in vitro</i> (Levy) <i>in vitro</i>	49.2	-11.3	2.1 1.9	-16.7 -5.5	1.7 3.2	2.3 0.8
Itraconazole	<i>in vivo</i>	0.700		0.036		3.0	
	<i>in vitro</i> (Levy) <i>in vitro</i>	0.723	-3.0	0.039 0.035	-8.3 +2.8	1.9 3.8	-1.1 +0.8
Nimodipine	<i>in vivo</i>	0.104		0.043		0.8	
	<i>in vitro</i> (Levy) <i>in vitro</i>	0.112	-7.7	0.029 0.022	+32.5 +48.9	1.7 1.4	+0.9 +0.6
Ritonavir	<i>in vivo</i>	4.73		0.53		3	
	<i>in vitro</i> (Levy) <i>in vitro</i>	4.66	+1.5	0.63 0.56	-18.9 -5.7	1.4 2.1	-1.6 -0.9

In sum, the BiPHa+ assay delivered meaningful, *in vivo* relevant partitioning profiles of various poorly soluble drugs and their corresponding enabling formulation. First, a level A IVIVR was successfully established for all drugs and formulations, providing an accurate estimate of the absolute fraction absorbed based on *in vitro* data. It was found that the maximum drug concentration in the organic phase obtained from an *in vitro* dose of ten milligrams in 50 ml aqueous media, which is equivalent to a 15 – 25 µmol for each of the respective drug, led to the highest congruency with the fraction absorbed *in vivo*.

Second, the *in vivo* performance was successfully predicted based on compartmental models in combination with a convolution approach. Deviations from the observed *in vivo* data can be explained by metabolic pathway of the respective drug. A time-scaling step might be not essential, because the Levy plot just minimizes deviations of the *in vitro* partitioning profile from the first order absorption kinetic *in vivo* and both, fraction absorbed (f_a) and the highest partitioned drug quantities ($C_{dec,max}$) were in the same range at 4.5 h (the end of BiPHa+ assay).

Third, the prediction errors of predicted plasma concentration time profiles were in good agreement with EMA and FDA IVIVC guidelines. The higher prediction errors of C_{\max} compared to AUC are due to the mathematical prediction of plasma concentration time profiles, and related to specific drug pharmacokinetic properties, such as the strong first-pass effect and hepatic metabolism. In this case physiological based pharmacokinetic modelling would be appropriate to predict plasma concentration time profiles based on *in vitro* data.

3.5 Implementation of biphasic Dissolution Profiles in PBPK Models

The pharmacokinetic prediction approach described in section 3.4 is limited because an *in vitro* / *in vivo* relationship is needed, which in turn requires clinical PK data of the formulations *in vivo*. In addition, the prediction accuracies were lower for drugs undergoing high metabolism [126]. Therefore, a method was developed to integrate the *in vitro* data of the BiPHA+ assay into the *in silico* tools PK-Sim® and GastroPlus®. Still even this approach required available *in vivo* PK studies administering the drug intravenously or as an oral solution in order to establish an elimination / distribution pharmacokinetic model. In a second step the pharmacokinetics for the formulation studied in BiPHA+ were prediction based on the basic PBPK model mentioned above. This kind of applying PBPK modelling is called biopharmaceutical *in vitro in vivo* extrapolation (IVIVE) [127].

3.5.1 Principals of Model Building and Evaluation

PBPK models of the six different formulations of poorly soluble drugs (section 3.4) were developed by PK-Sim® 7.3 and GastroPlus® 9.6 using mean pharmacokinetic data of human subjects from clinical trials. In a first step physicochemical parameters of the drug and physiological parameters were implemented into the model. Subsequently, absorption and / or elimination models were developed. Finally, a pharmacokinetic prediction of each enabling formulation was calculated based on the biphasic partitioning profiles obtained by the BiPHA+ assay and compared to reported plasma concentration time data.

The physicochemical properties of the six model substances tested were implemented in the PBPK tools (Table 12). The intestinal permeability of the drugs were calculated using the PK-Sim® prediction (Equation 22) based on logP values instead of logMA values as recommended from Thelen et al., where MW_{eff} (>300 g/mol) is the molecular weight and MA is the membrane affinity [128].

$$P_{eff} = 265.8 \cdot MW_{eff}^{-4.500} \cdot MA \approx 265.8 \cdot MW_{eff}^{-4.500} \cdot 10^{logP} \quad \text{Equation 22}$$

To develop the PBPK models, parameter optimisation step of distribution, elimination or metabolism were performed with respect to the *in vivo* pharmacokinetic data to ensure model accuracy. If a drug undergoes CYP metabolism, the respective CYP enzymes were also considered in the identification procedure. Typically, elimination models are developed by plasma profiles of intravenously administered solutions. Thereon, absorption models were implemented by pharmacokinetic profiles of orally administered drug solutions. However, in the case of drugs having low solubilities, intravenous plasma

concentration data are often barely available. Therefore, most of the PBPK models calculated in this study were implemented by oral liquids (Figure 30). Depending on the available data, parameter identification was conducted based on reported data. Nimodipine and aprepitant models were developed by intravenous data (Figure 30). Itraconazole model development was stepwise established using intravenous and oral liquid *in vivo* data (Figure 30). In the case of celecoxib, fenofibrate and ritonavir, only oral liquid data were available (Figure 30). The predictive accuracy of the PBPK modelling was evaluated using mean literature data.

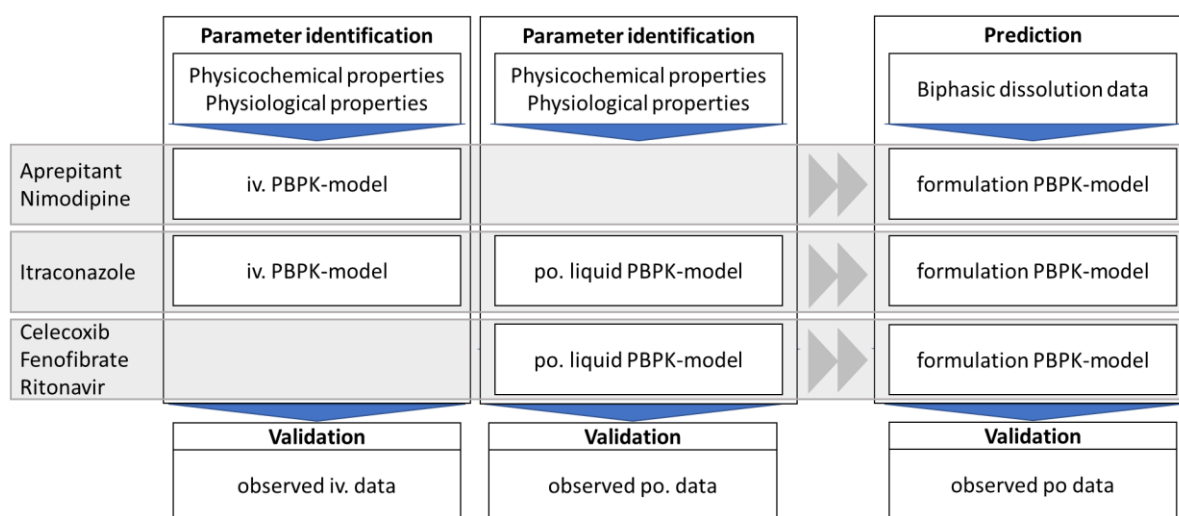


Figure 30: Workflow of PBPK-model development and prediction of different drugs and their validation with observed plasma concentration time profiles.

Basically, there are two methods to implement biphasic dissolution data into PBPK software:

(1) The organic partitioning profile was regarded as controlled release dissolution profile, which represents a novel approach in the present work (Figure 31). The dissolution of undissolved poorly soluble drug was assumed equivalent to drug release from a controlled release formulation of a highly soluble drug. Both, the controlled drug release and the dissolution of a poorly soluble drug, represent the rate limiting step of absorption. The partitioning into the organic layer of a poorly soluble drug was assumed to be equivalent to drug dissolution of a highly soluble drug, which are kinetically faster and therefore characterize the rate limiting steps (Figure 31). The partitioning rate of the drug is assumed to be comparable to *in vivo* absorption (section 3.4).

(2) DDDPlus (*in silico* simulation of biphasic dissolution assay), which is an add-on tool of Gastro plus, allows developing a mechanistic precipitation – dissolution model, which

can be integrated in a GastroPlus® PBPK model. The mechanistic model parameters were gained based on the biphasic dissolution data. However, the complex dissolution behaviours of enabling formulations are not entirely covered by this add-on tool. Additionally, PK-Sim® does not provide any mechanistic implementation for biphasic dissolution data.

Depending on the formulation approach, the dissolution and re-dissolution mechanism differs. For example in the case of the ASD formulation, drug and polymer dissolve simultaneously [51]. Micro- or nanosized formulations improve the dissolution rate by particle size reduction and surface enlargement. Depending on the drug and formulation properties, precipitation could occur. Thus, dissolution rate can differ from precipitated drug and formulated drug. Sometimes, the precipitate undergoes a transformation and change in dissolution behaviour [112]. However, the biphasic dissolution assay covers these (re-)dissolution processes indirectly by the partitioning profile.

Regarding these considerations and the fact that the currently available PBPK software provide the possibility to implement modified release dissolution profiles, the PBPK predictions were carried out by implementing the biphasic dissolution results as controlled release concentration time profiles into the previously develop distribution / elimination models.

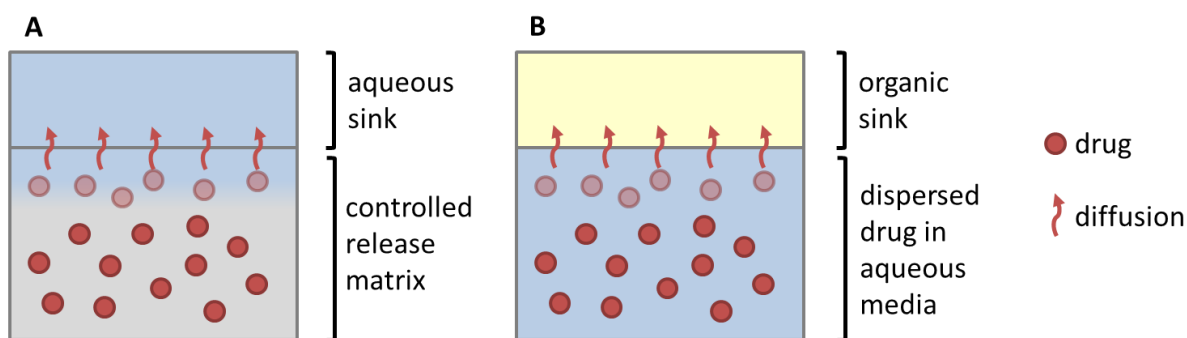


Figure 31: Comparison of (A) controlled release matrix dissolution and (B) partitioning behaviour of enabling formulation in the biphasic dissolution assay. The rate limiting steps represents either (A) drug release from a modified release matrix or (B) dissolution of a poorly soluble drug in an aqueous media. (modified Wagner [55])

3.5.2 Model Building

Prior to the implementation of the BiPHa+ results, the elimination/distribution PBPK models and subsequent oral absorption PBPK models were built based on literature data as described in section 4.7.2.

In a first step the elimination/distribution PBPK models were developed using the PK-Sim[®] and GastroPlus[®] software (Figure 32, Figure 33). The investigated drugs were generally poorly soluble. Consequently, an intravenous formulation was available for half of the drug substances. Thus, only oral solutions for these model drugs were used for the implementation of the elimination/distribution models. If an oral liquid was used for direct development of absorption/elimination models, the predicted permeability values of Table 12 were taken. All models were optimized using average pharmacokinetic data. In the following the results of model buildings are summarized. Figure 32A and Figure 33A show the *in silico* and *in vivo* observed data linearly and logarithmically plotted. The permeability values are provided in Table 16:

Aprepitant was administered as a 2 h infusion. The distribution/ elimination models described the observed data, even C_{max} values, very accurately in both modelling software (Figure 32A, Figure 33A). Especially the PK-Sim[®] model described visually the observed values very accurately (Figure 32A). During the elimination period in the GastroPlus[®] model after 10 h, the plasma concentration decreased rapidly. After that, the elimination rate decreased until the modelled values after 30 hours were higher than the *in vivo* data (Figure 33A).

The second model substance, which was intravenously applied as a bolus injection was nimodipine. Only 10% of nimodipine can be detected in the venous blood, because of its high CYP3A4 first-pass metabolism (Figure 32D, Figure 33D). Thus, CYP3A4 metabolism was implemented for the intravenous PBPK model to enhance model accuracy. The predicted and optimized pharmacokinetic profile from GastroPlus[®] displayed a higher accuracy during elimination (Figure 33D), whereas the PK-Sim[®] model resulted in a more decreased plasma concentration time profile compared to the observed data (Figure 32D).

No intravenous formulation has been developed for the pharmacokinetic assessment of celecoxib. Therefore, the model was established by an oral liquid. Both PBPK models matched the observed *in vivo* data with high accuracy (Figure 32B, Figure 33B). PK-Sim[®] predicted a changing slope of elimination / distribution at 5 h and 15 h, whereas one change of elimination/distribution slope was calculated in GastroPlus[®] at 5 h. C_{max} values were more accurately determined by PK-Sim[®].

The prodrug fenofibrate is activated by ester-hydrolysis. Thus, the plasma concentration time profile was detected as fenofibric acid. To ensure an accurate description of the oral solution pharmacokinetic, the model for fenofibric acid and fenofibrate were simultaneously developed [129]. Activation, distribution, and elimination were in good agreement with the observed data of the oral liquid formulation (Figure 32C, Figure 33C).

In the case of ritonavir, there was only a paediatric oral solution in moderate fed state available in literature to build the model. Elimination kinetics were well described in both PBPK models (Figure 32G, Figure 33G). To predict the *in vivo* performance of the oral marketed ASD, the model was adjusted from children to adult and from fed to fasted for the following implementation of BiPha+ data. Both *in silico* tools easily allow such a down scaling. Small deviations from the observed plasma profile occurred during the absorption period and after 30 h within the PK-Sim® prediction. (Figure 32G). Similar deviations were observed for the GastroPlus® simulation (Figure 33G). Both C_{max} values were calculated accurately.

Itraconazole was the only model substance, where intravenous and oral solution *in vivo* data were available. The elimination model of the cyclodextrin infusion was established including a CYP3A4 metabolism and enterohepatic circulation. The PK-Sim® and GastroPlus® optimized intravenous models described the pharmacokinetic profile with high accuracy (Figure 32E, Figure 33E). However, the elimination rate slowed down after 40 h in the PK-Sim® prediction. By extending the model with the oral solution, the elimination was slower than the observed elimination values (Figure 32F, Figure 33F). Nevertheless, C_{max} and t_{max} values were correctly calculated.

Table 16: Predicted permeability using PK-Sim®

Drug substance	Predicted permeability [cm/min]
Aprepitant	$1.67 \cdot 10^{-3}$
Celecoxib	$3.71 \cdot 10^{-3}$
Fenofibrate	$2.00 \cdot 10^{-2}$
Itraconazole	$8.13 \cdot 10^{-4}$
Nimodipine	$6.06 \cdot 10^{-4}$ ¹⁾
Ritonavir	$3.49 \cdot 10^{-5}$

¹⁾Taken from CaCo data and correlated using GastroPlus® [130]

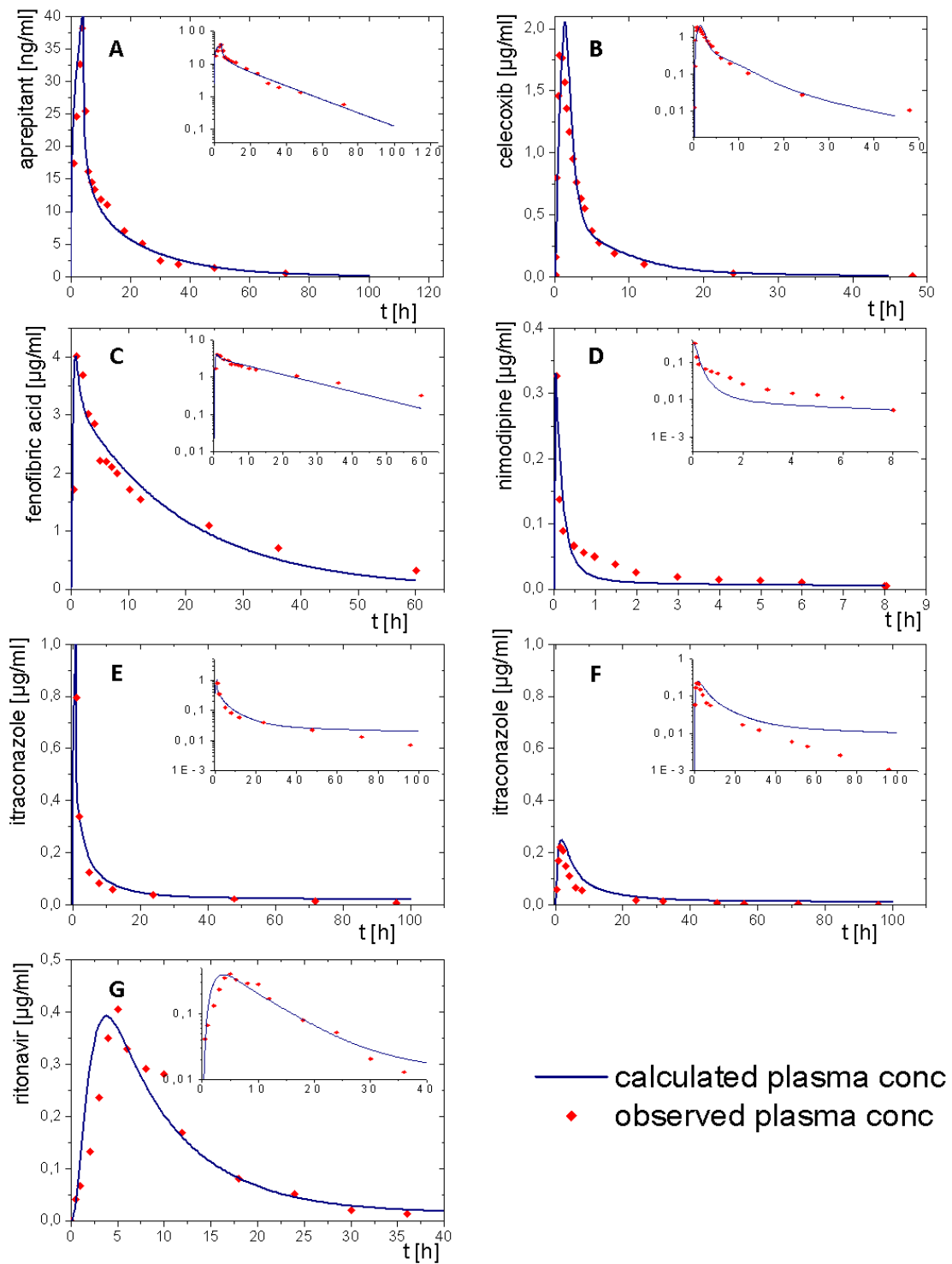


Figure 32: Simulated plasma concentration time profile using PK-Sim® (blue line) and observed pharmacokinetic data (red dots) linearly and logarithmically (small figures) plotted: (A) aprepitant after an 2 hour infusion (B) celecoxib following an oral solution (C) fenofibrate administered as oral liquid (D) nimodipine administered by a single injection (E) itraconazole after an cyclodextrin infusion (F) itraconazole orally administered as a liquid (G) ritonavir taken as oral solution.

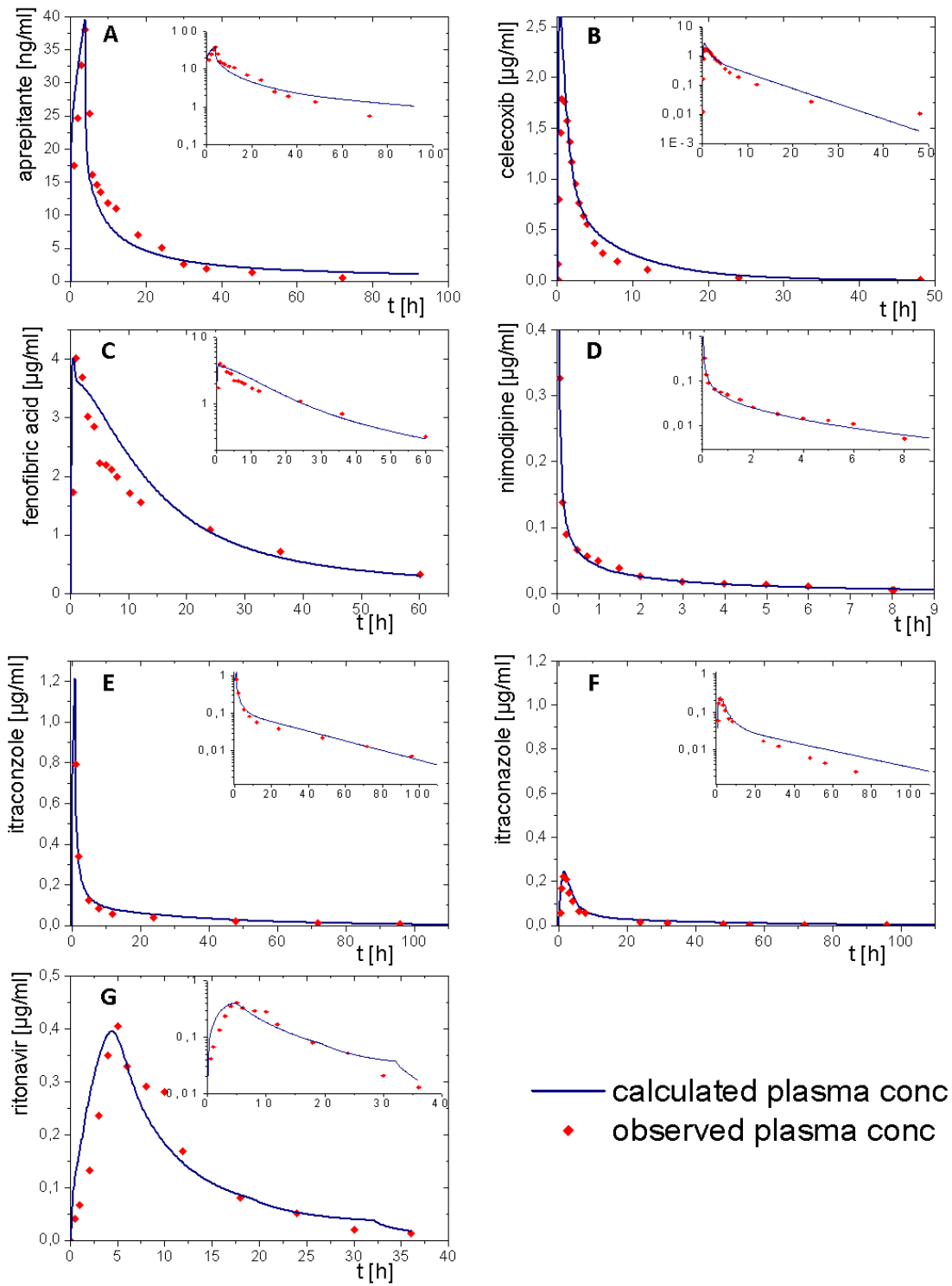


Figure 33: Simulated plasma concentration time profile using GastroPlus® (blue line) and observed pharmacokinetic data (red dots) linearly and logarithmically (small figures) plotted: (A) aprepitant after an 2 hour infusion (B) celecoxib following an oral solution (C) fenofibrate taken as oral liquid (D) nimodipine administered by a single injection (E) itraconazole after an cyclodextrin infusion (F) itraconazole orally administered as a liquid (G) ritonavir taken as oral solution.

3.5.3 IVIVE Using Organic Biphasic Partitioning Profiles

The PBPK elimination/distribution models, based on oral or intravenous solutions, of the six poorly soluble drugs were combined with the biphasic partitioning profiles from the organic phase and the predicted P_{eff} values (Table 12). The biphasic partitioning profiles were implemented similarly to controlled release dissolution profiles. Based on the *in vitro* BiPHA+ data and *in silico* elimination/distribution models, *in silico* pharmacokinetics were predicted by both GastroPlus® and PK-Sim® (Figure 34, Figure 35).

Aprepitant (Emend®, nanocrystals)

The nanosized formulation of aprepitant displayed a zero order partitioning profile after an initial higher partitioning rate in the organic phase up to a final concentration of approximately 60% (Figure 24). Plasma concentration time profiles combining *in vitro* and *in silico* data were predicted by PK-Sim® and GastroPlus® leading to accurately predicted C_{max} and t_{max} values (Figure 34A, Figure 35A). This highlighted the exactness of the absorption model. The observed pharmacokinetic data of aprepitant indicated an enterohepatic circulation between 10-30 h, which was additionally implemented into the PBPK models at first in the elimination/distribution and later on in the predicted model (Figure 34A, Figure 35A). Deviations of the PK-Sim® simulation from the observed pharmacokinetic data occurred (Figure 34A), because enterohepatic circulation in PK-Sim® just slows down elimination rate [131], The enterohepatic circulation model of GastroPlus® was able to predict the pharmacokinetic profile more accurately (Figure 35A).

Celecoxib (Celebrex®, microcrystals)

Celebrex was developed as a micronized formulation. A zero order absorption kinetic including an initial faster absorption rate was received by the biphasic assay (Figure 24). In particular, the absorption period of celecoxib, which was mainly driven by *in vitro* partitioning data, differed between PK-Sim® and GastroPlus® prediction. (Figure 34B, Figure 35B). Contrary, t_{max} and AUC were in good agreement to the clinical data. The course of elimination and distribution was matched by both models (Figure 34B, Figure 35B). Observed C_{max} value of 0.66 µg/ml was overestimated in PK-Sim® (0.83 µg/ml) and underestimated in GastroPlus® (0.50 µg/ml).

Fenofibrate (Lipidil®, microcrystals)

A first order and followed by a zero order absorption process was observed in the *in vitro* partitioning profile reaching a maximum at around 45% (Figure 24). Even though, a very fast absorption rate was expected. With regard to the high permeability (Table 12) and a

fast *in vitro* partitioning rate, t_{max} values were in a range of 4 h for the 54 mg dose strengths. Therefore, activation by ester-hydrolyses played an important role. Taking this activation step into account, the observed and predicted plasma concentration time profiles of fenofibric acid were very accurately matched by PK-Sim[®] as well as by GastroPlus[®] (Figure 34C, Figure 35C). C_{max} , predicted by PK-Sim[®] (1.59 $\mu\text{g/ml}$) and GastroPlus[®] (1.57 $\mu\text{g/ml}$), were slightly underestimated compared to an observed maximum *in vivo* plasma concentration of 1.89 $\mu\text{g/ml}$.

Regarding the 200 mg dose strengths, t_{max} values were in a range of 6 h. Considering the metabolic activation, the observed and predicted plasma concentration time profiles of fenofibric acid were very accurately matched by PK-Sim[®] and by GastroPlus[®] (Figure 34D, Figure 35D). C_{max} , predicted by PK-Sim[®] (2.59 $\mu\text{g/ml}$) and GastroPlus[®] (2.75 $\mu\text{g/ml}$), were slightly underestimated compared to the observed maximum *in vivo* plasma of 2.8 $\mu\text{g/ml}$ concentration.

Itraconazole (Sempera[®], ASD)

Itraconazole demonstrated an example for an IVIVE, which was stepwise developed from an intravenous administration to an oral liquid (Figure 32E-F, Figure 33E-F). The biphasic partitioning profile was implemented into the oral liquid PBPK model (Figure 24) to predict human pharmacokinetics. Observed *in vivo* C_{max} value of 36 ng/ml and predicted PK-Sim[®] and GastroPlus[®] values were almost identical. The predicted plasma concentration time profile of the PK-Sim[®] prediction in the first 10 hours matched the observed *in vivo* data. Looking at 10 hours, where the elimination is dominant, deviations from the observed *in vivo* profiles occurred. (Figure 34D). The same applies to GastroPlus[®], which predicted the plasma concentration to be slightly too low over the entire elimination period starting at 10 hours. (Figure 35D). However, both *in vivo* C_{max} and t_{max} values were in good agreement within both modelling predictions.

Nimodipine (Nimotop[®], ASD)

The formulation of nimodipine represents a first generation, propylene glycol based ASD, which resulted in a square root like partitioning profile (Figure 24). Nimodipine is a highly permeable drug which has limited bioavailability as a result of its high first-pass effect. Therefore, the use of PBPK modelling to predict *in vivo* pharmacokinetics based on the BiPha+ partitioning profiles is obligatory. The combination of PBPK modelling to describe the metabolism and the organic partitioning profile as absorption profile generated meaningful pharmacokinetic predictions. (Figure 34F, Figure 35F). The short elimination time and low bioavailability in the modelling were consistent with the observed plasma

data. Both *in silico* tools resulted in very good pharmacokinetic predictions, whereby the deviations for PK-Sim® were larger (Figure 34F).

Ritonavir (Norvir®, ASD)

A sigmoidal partitioning profile was acquired by evaluating the market ASD formulation of ritonavir in the BiPHa+ assay (Figure 24). The PBPK models were successfully scaled from fed state children to fasted state adults. GastroPlus® and PK-Sim® predicted the pharmacokinetic profile with a very high accuracy using the BiPHa+ partitioning profile. t_{\max} and C_{\max} agreed very precisely with the observed clinical data. (Figure 34G, Figure 35G).

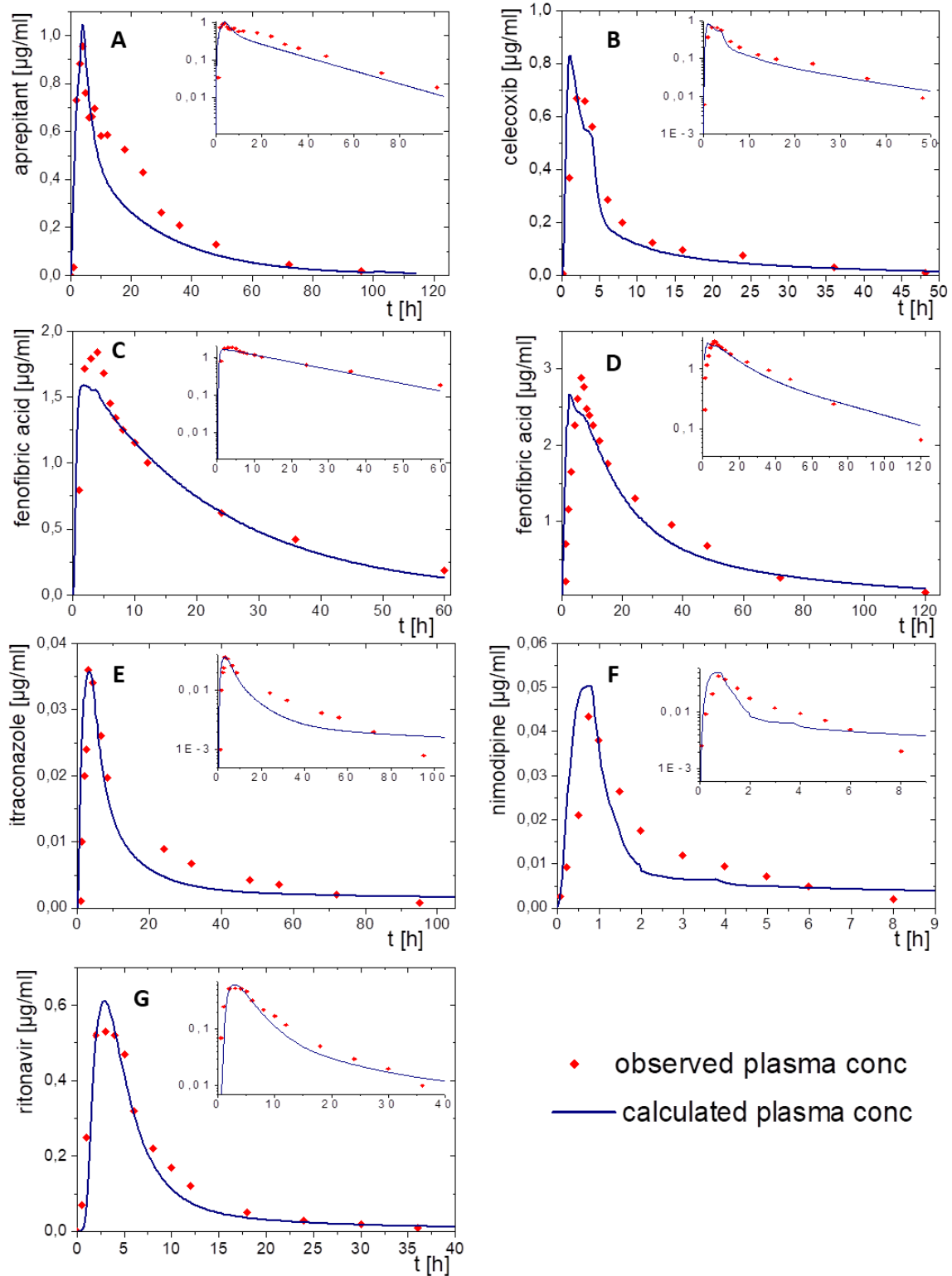


Figure 34: Simulated plasma concentration time profiles using PK-Sim® after oral administration (blue line) and observed clinical data (red dots) of market products linearly and logarithmically (small figures) plotted: (A) apreptitant (B) celecoxib (C) fenofibrate 54 mg dose (D) fenofibrate 200 mg (E) itraconazole (F) nimodipine (G) ritonavir.

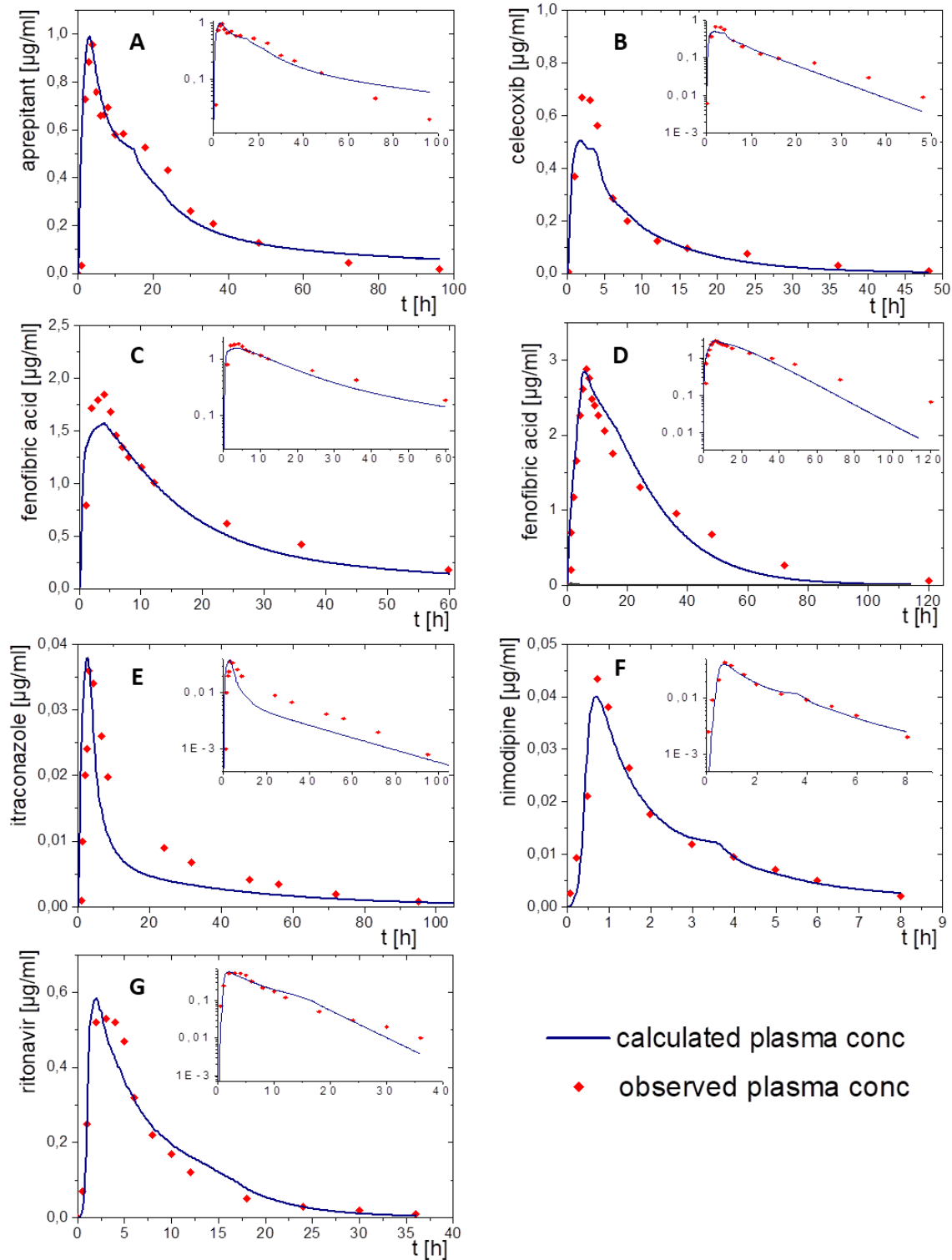


Figure 35: Simulated plasma concentration time profiles using GastroPlus® after oral administration (blue line) and observed clinical data (red dots) of market product linearly and logarithmically (small figures) plotted: (A) aprepitant (B) celecoxib (C) fenofibrate 54 mg dose (D) fenofibrate 200 mg (E) nimodipine (F) itraconazole (G) ritonavir.

3.5.4 Predictive Performance of PBPK Models

The developed elimination/distribution PBPK models were taken as basis for the prediction of the pharmacokinetic plasma profile of different market formulations using the BiPHA+ results. The predicted profiles were compared with observed *in vivo* plasma concentration time data. To validate the predictive performance, clinical *in vivo* AUC and C_{max} values and predicted AUC and C_{max} values were plotted (Figure 36). All PBPK-model predictions were within the twofold accordance boundary of the regulatory guidelines [132,133].

Figure 36 additionally presents the AUC and C_{max} values received from the pharmacokinetic predictions based on a compartmental model without any mechanistic implementation taken from section 3.4. The plasma concentration time profiles were calculated using a convolutional approach, where the single input function was the derivative of the biphasic dissolution data and the impulse response was a two compartmental model. Deviations between pharmacokinetic prediction and PBPK-modelling became obvious if a high degree of metabolism was present (e.g. nimodipine). The deviations between observed and predicted plasma concentration time profiles received from the nimodipine convolutional prediction were significantly decreased by the PBPK-models, because the high first pass effect was considered in the mechanistic PBPK model (Figure 28D, Figure 34F, Figure 35F), which led to a more accurate prediction (Figure 36). Sometimes, the PBPK-modelling reached similar prediction accuracies compared to the convolutional approach, but PBPK-modelling generates mechanistically understanding of the *in vivo* behaviour of drugs in terms of metabolic pathways.

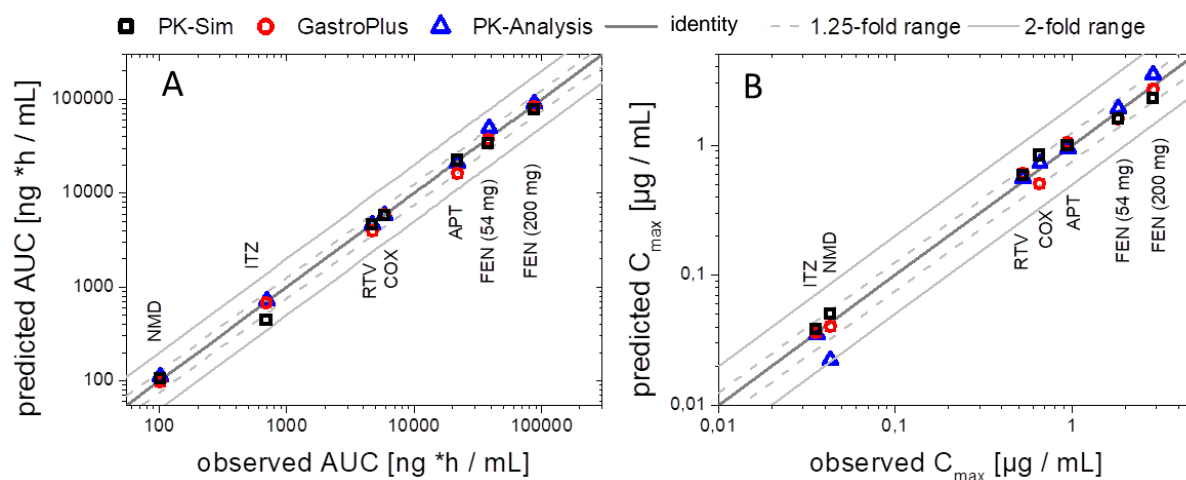


Figure 36: Verification of enabling formulation predictions by GastroPlus®, PK-Sim® and convolutional calculation (taken from section 3.4 without time scaling) including the biphasic partitioning profiles by comparing observed *in vivo* vs predicted values: (A) AUC values and (B) C_{max} values. The dark grey line represents the identical values of the observed and predicted value, the grey line the 2-fold deviation range and the grey dotted line the 1.25-fold deviation range.

3.5.5 Discussion

The general scope of this investigation was to get a rapid estimation and accurate prediction of the *in vivo* performance of enabling formulations using the BiPha+ assay in combination with *in silico* tools. Pharmacokinetic predictions were successfully performed by implementing the biphasic partitioning profiles in GastroPlus® and PK-Sim®. For this, the organic partitioning profiles were handled as controlled release dissolution profiles. Based on that assumption, the rate limiting step of absorption is intended to be dissolution in the case of poorly soluble drugs and not, as for freely soluble drugs, drug release from a (modified release) dosage form. This simplified approach enabled a rapid estimation and prediction of the *in vivo* performance with good accuracy as discussed in the following:

Because of the complex gastrointestinal dissolution behaviour of enabling formulation approaches, many dissolution models did not entirely cover all relevant processes which potentially take place [76]. The biphasic dissolution assay however, allowed a more dynamic characterisation of formulations by the additional partitioning step into an organic absorption sink [58,65]. Moreover, the rate-limiting and thermodynamically unfavoured (re-) dissolution process can be more meaningful characterized by the BiPha+ assay. Consequently, many biorelevant processes of the formulations were indirectly considered by implementing the *in vitro* partitioning profiles (refer to section 3.4.5) in the PBPK software and it was not necessary to develop a complex *in silico* dissolution/precipitation model, which is not for all software available. Additionally, at

the time when the present investigations were performed, DDDPlus (*in silico* simulation of biphasic dissolution assay) rather displayed a prototype tool that does not allow meaningful implementation.

A limitation of the presented approach was that the biphasic assay (section 3.1) was developed to simulate transition and absorption of the small intestine. Therefore, the BiPHa+ model only characterized absorption in early intestinal stages and does not consider absorption in later intestinal stages. This could be the reason for the mainly negative but small deviations of the predicted AUC values from the observed *in vivo* data (Figure 36).

A further objective of the study was to develop the simplest possible model using easily accessible input parameters. For this purpose, parameters were determined such as logP or *in vitro* solubility. Permeability (P_{eff}) values were calculated by PK-Sim[®] using logP values and were implemented in PK-Sim[®] and GastroPlus[®]. This was suitable for almost all investigated drugs, excluding nimodipine. A very early *in vivo* C_{max} value and high CaCo2 permeability of nimodipine suggest a very high *in vivo* permeability, which was confirmed by the good model description of pharmacokinetics [123,130]. Therefore, literature data for permeability of nimodipine was applied.

In general, the model development of the elimination/distribution model by parameter identification and implementation of the organic partitioning profiles led to an accurate description of the *in vivo* observed data. Plasma concentration time profiles for elimination/distribution models were successfully described in all cases (Figure 32, Figure 33). Intravenous data were available for aprepitant and nimodipine. Thus, only an elimination model was developed *in silico*. Celecoxib, fenofibrate and ritonavir were accurately described *in silico* based on absorption/elimination models. Itraconazole was the only example, where clinical data of an oral solution and an intravenous application were reported. Especially in this example, study to study variability became obvious: The identified elimination model based on intravenous data (Figure 32F, Figure 33F) led to deviations during the elimination period of the oral solution (Figure 32G, Figure 33G)

Implementing BiPHa+ partitioning profiles in PBPK modelling was demonstrated to be a suitable approach to predict *in vivo* performance of various enabling formulations. The consideration of an enterohepatic circulation or metabolism can enhance the predictive power of PBPK modelling compared to the convolutional approach of section 3.4 (Figure 36). Aprepitant probably underwent enterohepatic circulation, which was accurately predicted by GastroPlus[®] (Figure 35A), whereas the enterohepatic circulation (EHC) model in PK-Sim[®] just decreased elimination rate resulting in an insufficient prediction (Figure 34A). The EHC model applied for itraconazole did not entirely explain the slower

elimination after oral absorption of the drug substance from the ASD. (Figure 34E, Figure 35E). Activation of fenofibrate to fenofibric acid by plasma esterases was successfully implemented leading to high prediction accuracy for both dose strengths (Figure 34C/D, Figure 35C/D). The t_{\max} at 6.3 h reported *in vivo* was accurately predicted by the implemented saturable ester hydrolysis. GastroPlus[®] was able to calculate a t_{\max} which was closer on the observed *in vivo* t_{\max} compared to PK-Sim[®] for fenofibrate. Nimodipine represented an example for a highly permeable and highly metabolized drug which demonstrated approximately 3.5% bioavailability at 35% fraction absorbed. By implementing the extensive first pass metabolism, the pharmacokinetic of nimodipine was more accurately predicted in contrast to the simple convolutional/compartmental prediction approach reported in section 3.4.

As a conclusion, the BiPHa+ partitioning profiles were successfully assumed mechanistically to be treated as controlled release dissolution profiles to implement the partitioning profile in PBPK software (Figure 34, Figure 35). For the tested formulations this proved to be a meaningful approach to predict plasma concentration time profiles of a single dose of a certain enabling formulation, even if the gastrointestinal mechanisms of precipitation and (re-)dissolution is highly complex and metabolism or EHC take place. A limitation of the presented procedure is the un-scalability over various dose strengths as a connection between *in vitro* dose and *in vivo* applied dose was demonstrated to be in a range of 30 mg and 200 mg. However, the procedure demonstrated a rapid *in vitro/in silico* approach to predict *in vivo* pharmacokinetics of poorly soluble drugs resulting in high prediction accuracy of AUC and C_{\max} values (Figure 36). Moreover, the presented approach supported and improved the understanding of the potential *in vivo* pharmacokinetic of enabling formulations and in addition provided a valuable method to support formulation development especially in early stages.

3.6 Systematic Evaluation and *in vivo* Prediction of ABT-102 Drug Products by using the BiPHa+ Assay

In this section, the methodology developed and described in section 3.4 and 3.5 is applied to a specific example, which was an early stage formulation development project. The drug substance ABT-102 formulated as different ASDs (Table 17) was investigated *in vitro* by using the BiPHa+ assay (Section 4.8). These formulations were previously studied in beagle dogs *in vivo* (Section 4.8).

Table 17: Composition of ABT-102 amorphous solid dispersion

ASD composition (% wt.)	Form A	Form B	Form F	Form G
ABT-102	10	10	5	5
Copovidone	75	60	86.5	84
HPMC-AS	-	15	-	-
Poloxamer 188	12	12	6	8
Saccharose monopalmitate	3	3	1.5	2
Colloidal silicon dioxide	-	-	1	1

3.6.1 Assessing *in vivo* Relevance and Prediction Performance

To assess the *in vivo* relevance of the BiPHa+ data, an IVIVR was calculated based the observed oral *in vivo* data and *the in vitro* partitioning data (Figure 37). The prediction of *in vivo* performance was performed using *in vitro* data (BiPHa+ data, drug properties) and *in vivo* data (IV data). Two approaches were chosen (Figure 37):

(1) The convolution was calculated using the single impulse function (derivative of BiPHa+ partitioning data) and the single impulse response (compartment model of intravenous data, refer to section 4.6.3).

(2) A PBPK model prediction was established based on an intravenous PBPK model based on ABT-102 beagle dog *in vivo* data using PK-Sim® 7.3 and GastroPlus® 9.6. Physiochemical properties of the drug and physiological properties of an average dog were integrated. Subsequently, the elimination / distribution PBPK models were optimized based on observed mean intravenous data.

The following prediction was then performed using BiPHa+ partitioning data according to section 3.5.1.

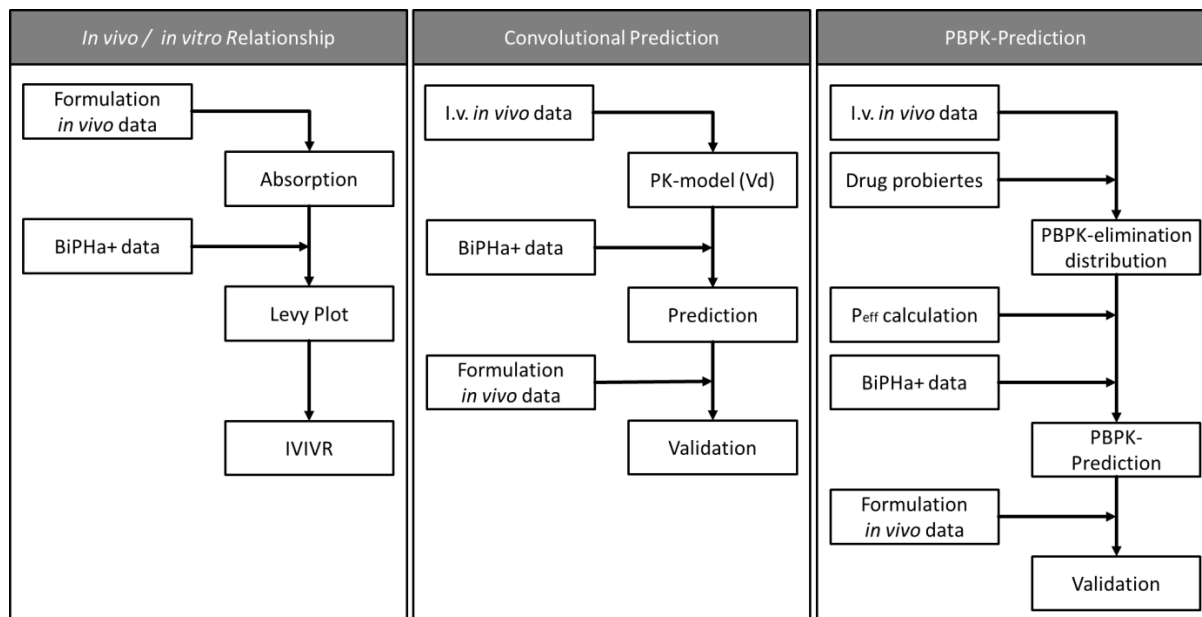


Figure 37: Workflow for biphasic dissolution data evaluation: *In vivo / in vitro* relationship, convolutional based prediction and PBPK – prediction-

3.6.2 ABT-102 Properties

ABT-102 did not have a physiologically relevant pKa value. Consequently, the poor ABT-102 solubilities in 0.1 N HCl of 1.40 µg/ml and in phosphate buffer of 0.37 µg/ml were in a similar range. No sensitivity to biorelevant surfactant was observed for the solubility in FaSSIF-V2 (0.40 µg/ml). The solubility in 1-decanol was higher than 1.0 mg/ml which ensured a more than tenfold sink in 50 ml decanol at an investigated *in vitro* dose of 5 mg in the BiPHA+ assay. LogP value of ABT-102 was 4.3, which indicated a high lipophilicity. Using the determined logP value, a permeability value of $1.16 \text{ E}^{-3} \text{ cm/min}$ was predicted by PK-Sim®. ABT-102 was quantified by first derivative at 285 nm in the 1-decanol layer to exclude an overlapping of spectra. The UV-metrically quantification in the aqueous media was performed by the absorption at 310 nm and was corrected by exponential fit to minimized scattering errors (Table 18).

Table 18: Physicochemical and physiological properties of ABT-102: solubility (S), LogP value, predicted intestinal permeability (P_{eff}), fraction unbound (F_u) and evaluation wavelength (λ)

Parameter	Value
S (0.1 N HCl)	1.40 $\mu\text{g/ml}$
S (buffer 6,8)	0.37 $\mu\text{g/ml}$
S (FaSSIF-V2)	0.40 $\mu\text{g/ml}$
S (1-decanol)	> 1.0 mg/ml
LogP	4.3
P_{eff}	$1.16 \text{ E}^{-3} \text{ cm/min}$
F_u	0.5%
λ (1-decanol)	285 nm (1 der.)
λ (aqueous phase)	310 nm (exp.)

3.6.3 Drug Product Evaluation by Using Biphasic Dissolution Assay

Form A

The first formulation Form A (Table 17) immediately supersaturated up to 10 % in the gastric stage at pH = 1.0 and precipitated within 15 min reaching a concentration level of 2-3%. No change in dissolved amount was observed at 30 minutes when pH increased to 5.5 and Bi-FaSSIF-V2 was formed. Subsequently, the concentration steadily decreased to a level of 1% in the intestine stage (Figure 38). After forming Bi-FaSSIF-V2 (see section 3.1), the aqueous layer was covered by 1-decanol allowing the drug to partition in the absorption sink medium. The initial partitioning rate (30 - 90 min) resembled a kinetic first order and subsequently became a zero order kinetic reaching a maximum concentration of 35% at the end of the experiment (Figure 38).

Form B

One percent ABT-102 of formulation Form B (Table 17) dissolved in the gastric aqueous stage during the first 30 minutes having an acid decreased solubility imparted by the formulation ingredient HPMC-AS (acidic polymer). After forming Bi-FaSSIF-V2 (pH 6.8) at 30 min, HPMC-AS became soluble and ABT-102 concentration slightly increased up to three percent in the aqueous layer. Subsequently, the aqueous concentration steadily decreased to one percent until the end of the experiment (Figure 38). The partitioning

process, starting at 30 minutes, demonstrated a zero order kinetic resulting in a final partitioned relative drug amount of 21% (Figure 38).

Form F

Form F had the half drug load of Form A (Table 17). For this, ABT-102 dissolved and supersaturated in gastric acid media pH-independently up to a level of ten percent and precipitated at 15 minutes with a dissolved drug quantity of 2 - 3 %. Reaching the intestinal stage at 30 minutes, the aqueous dissolved amount of ABT-102 was minimally influenced by bile salts and decreased slowly to one percent dissolved drug (Figure 38). Starting at 30 minutes, an absorption sink was generated by adding 1-decanol. ABT-102 started to partition between minute 30 and 60 likewise a kinetic zero order. After this period, the kinetic rate transformed in a slower kinetic zero order, resulting in a maximum concentration of 35% (Figure 38).

Form G

Form F and Form G contained the same drug content, but Form G had an increased surfactant quantity (Table 17). Form G supersaturated to a concentration of 10 % and precipitated within the first 15 minutes of the gastric stage resulting in a residual concentration of three percent at 30 minutes. During intestinal period (Bi-FaSSiF-V2) between 30 and 270 minutes, dissolved ABT-102 slowly decreased to one percent (Figure 38). After transforming the aqueous phase from gastric to intestinal stage at 30 minutes, 1-decanol was covered to enable partitioning in the organic phase. The partitioning kinetic can be divided in two periods of zero order kinetics including two different rate constants. During 30 and 60 minutes, the initial partitioning rate was faster compared to the second period between 60 and 270 minutes. The final concentration in the organic phase was 37% (Figure 38).

Discussion

The most effective *in vitro* formulations of ABT-102 with regard to the partitioning performance in the BiPHa+ assay were those based on copovidone (Form A, F and G) without pH-dependant soluble polymer (Form B). The analysis by the BiPHa+ assay indicated also high *in vivo* performance for Form A, F and G. These formulations supersaturated during dissolution. However, no stabilisation of supersaturation within the gastric period and beyond was achieved independent of surfactants and polymers. Formulation B was intended to inhibit dissolution during the gastric stage but the aim, supersaturation after pH-shift, was not observed. Consequently, the partitioning profiles of formulation A, F and G were similar to each other, whereas formulation B partitioned

as a kinetic zero order without a change in rate constant. In the course of dissolution and precipitation of formulation A, F and G, a fast dissolving precipitate species was generated [96], which was responsible for the rapidly partitioned ABT-102 [21] and subsequently contributed to the partitioned amount ABT-102. An increasing drug load (Form A vs. G, F) and a decreasing surfactant concentration (Form A, G vs. F) contribute to the yield of rapidly dissolving precipitate ($A > G > F$). In contrast, Form B did not supersaturate and consequently no rapid initial partitioned ABT-102 was observed. Regarding the partitioning rates starting at 90 minutes, ABT-102 partitioned with the following decreasing kinetic: $B > G > F > A$. The re-dissolution and subsequent the partitioning rate increased with a higher surfactant concentration (Table 17, HPMC was regarded as surfactant [134]). The combination of (re-) dissolution/precipitation and surfactant/polymer mixture played an important role towards the *in vitro* partitioning performance.

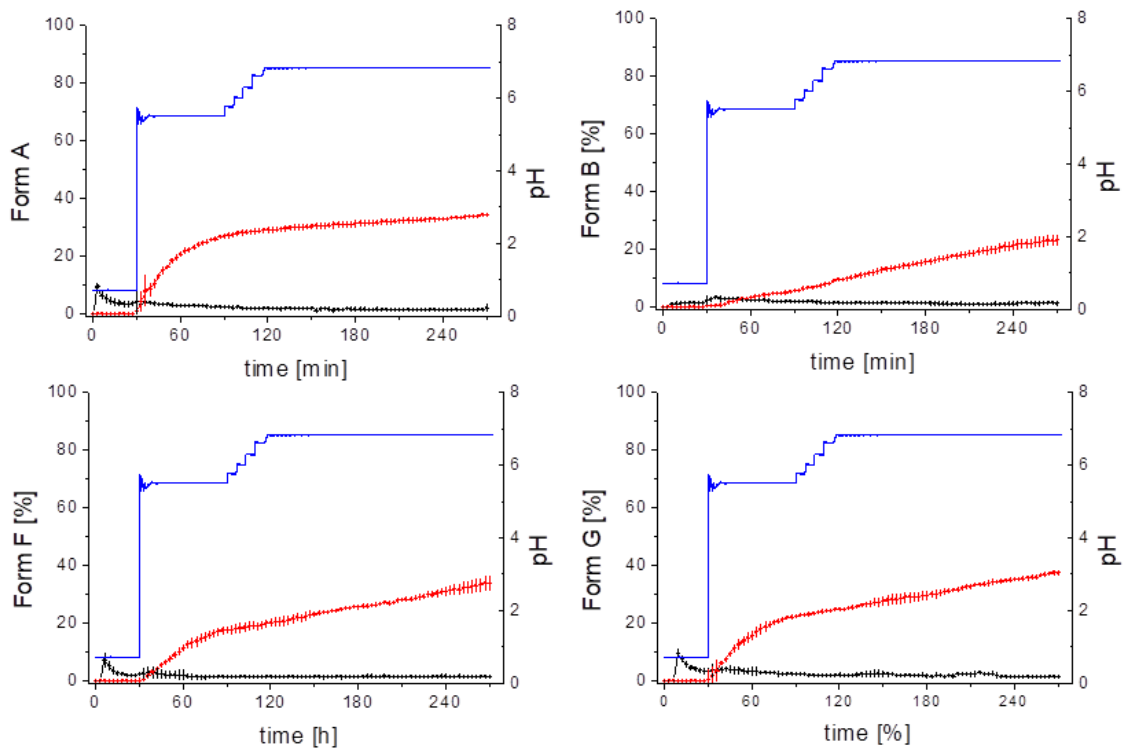


Figure 38: Biphasic dissolution results of ABT-102 Form A, B, F and G: aqueous dissolved concentration (black line), 1-decanol dissolved concentration (red line) and pH-value (blue line)

3.6.4 Compartment Analysis and IVIVR

In vivo absorption profiles were calculated based on observed *in vivo* pharmacokinetic data (Figure 41 to Figure 43) using the residual method. The absorption process was assumed as a first order kinetic and the distribution/elimination process as a second order kinetic as described in section 4.8.6. Form A had the highest absorption rate ($k_{AA} = 2.12 \text{ h}^{-1}$) followed by Form G ($k_{AG} = 1.42 \text{ h}^{-1}$), Form F ($k_{AF} = 1.14 \text{ h}^{-1}$) and finally Form B with the lowest absorption rate constant $k_{AB} = 0.75 \text{ h}^{-1}$. The maximum concentration ($C_{\text{dec,max}}$) of the organic partition profile was in a similar range to the absolute *in vivo* fraction absorbed (F_a), which is obligatory to establish a level A IVIVR (Table 19). The maximum values of the calculated *in vivo* absorption profiles were compared to $C_{\text{dec,max}}$ [122]. A Levy plot was calculated resulting in a time scaling factor 0.51 and a negligible small lag-time of two minutes (Figure 39). Finally *in vitro* partitioning profiles were directly correlated to the first order absorption profiles yielding in a correlation coefficient of $r^2 = 0.91$ and a slope close to one (Figure 39). The high degree of correlation accuracy confirmed a good correlation of the *in vivo* with the *in vitro* data. This result demonstrated the *in vivo* relevance of the *in vitro* partitioning profiles determined by the BiPHa+ assay. Moreover, the assay was successfully applied to beagle dog studies.

Table 19: Comparison of maximum concentration ($C_{\text{dec,max}}$) in the organic partitioning profile at the end of the experiment and absolute *in vivo* fraction absorbed (F_a)

Formulation	In vitro $C_{\text{dec,max}}$ [%]	In vivo F_a [%]
Form A	35	40
Form B	21	25
Form F	35	36
Form G	37	37

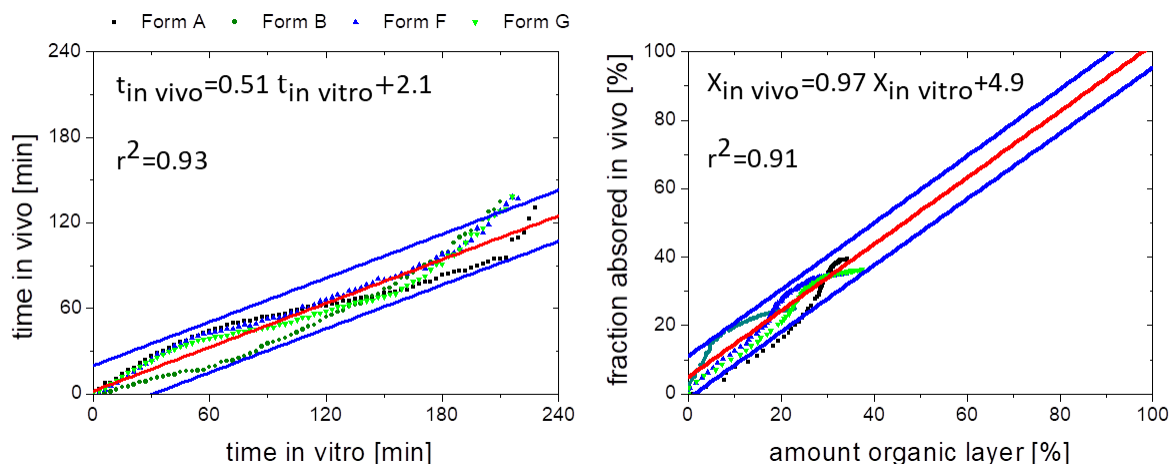


Figure 39: left: Levy plot (time scaling) and right: IVIVR of ABT-102 formulations (A, B, F and G); red line: correlation, blue line: 95 % prediction accuracy and equations of the correlation.

3.6.5 Elimination and Distribution Model of Compartment Analysis and PBPK Modelling

Based on intravenous pharmacokinetic *in vivo* data obtained from beagle dogs (Figure 40), elimination/distribution models were developed using a two-compartment model, PK-Sim® and GastroPlus®:

Rate constants of elimination ($k_e = 0.337 \text{ h}^{-1}$) and distribution ($\lambda_1 = 3.07 \text{ h}^{-1}$) were determined by residual method. The model was compared to *in vivo* observed plasma concentration time data (Figure 40A). The calculated pharmacokinetic profiles matched with the observed data. The initial calculated concentration at $t = 0 \text{ min}$ was $C_0 = 1.86 \text{ } \mu\text{g/ml}$ and resulted in a distribution volume of $V = 9.45 \text{ L}$.

PBPK models were developed in PK-Sim® and GastroPlus® based on the physiochemical drug properties and physiological parameter of an average beagle dog (section 3.6.2 and 4.8.5). The elimination rate of the PK-Sim® model changed at 6 h and became slower than the observed *in vivo* elimination data (Figure 40B). The GastroPlus® model demonstrated a high similarity to the *in vivo* data (Figure 40C).

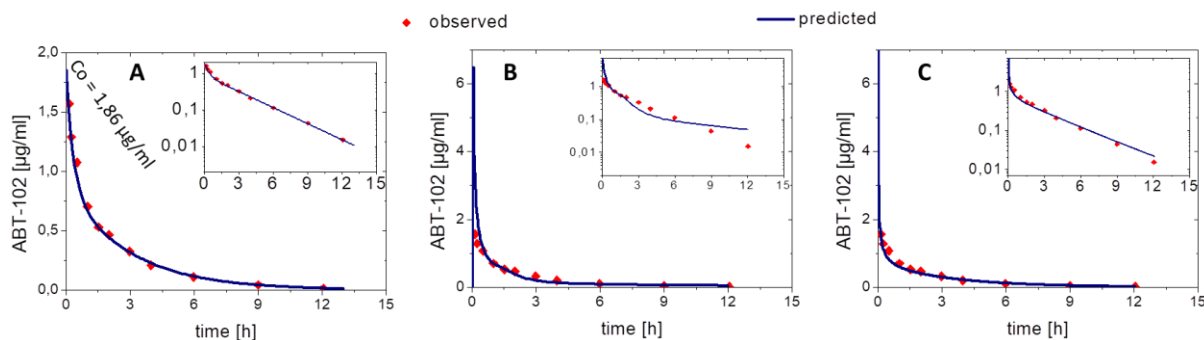


Figure 40: Elimination and distribution models and *in vivo* observed plasma concentration time profile: (A) two-compartment model, (B) PK-Sim[®] model and (C) GastroPlus[®] model. Small boxes show the (semi)logarithmic plasma concentration time profiles.

3.6.6 Predicting of the *in vivo* Performance by Convolution and PBPK Modelling

To predict the *in vivo* performance of Form A, B, F and G, partitioning profiles were combined with the intravenous compartment model or the intravenous PBPK models (Figure 41 - Figure 43). In a second step predicted versus observed AUC and C_{max} values were plotted (Figure 44) including an identity line, 1.25-fold and 2-fold deviation range according to WHO guideline [132,133].

Form A

The predicted t_{max} values of compartment model (1.5 h), PK-Sim[®] (2 h) and GastroPlus[®] (1h) of Form A matched with observed $t_{max} = 1.5$ h. C_{max} of convolutional model was overestimated (0.5 µg/ml) compared the observed $C_{max} = 0.38$ µg/ml, whereas PK-Sim[®] ($C_{max} = 0.31$ µg/ml) and GastroPlus[®] ($C_{max} = 0.35$ µg/ml) provided a smaller C_{max} . Starting at 2.5 h, concentration time profiles of compartment model and GastroPlus[®] described the observed elimination well (Figure 41 and Figure 43). PK-Sim[®] led to decreased concentration values during this period (Figure 42). The predicted AUC values resulted in the same tendency (Figure 44).

Form B

T_{max} of Form B, which was observed at 2.5 h, was predicted for later time points (Figure 41 - Figure 43): The highest modelled plasma concentrations were reached at 3 h (convolutional prediction), followed by 3.5 h (GastroPlus®) and finally 4 h (PK-Sim®). The predicted C_{max} values of the convolutional model (0.18 µg/ml), PK-Sim® (0.19 µg/ml) and GastroPlus® (0.17 µg/ml) of Form B were smaller compared to the observed C_{max} of 0.21 µg/ml (Figure 44). PK-Sim® modelled the plasma concentration in the period between 4 – 10 h too small (Figure 42). By comparing the predicted AUC values (0.97 – 1.07 µg h/ml) to the observed *in vivo* AUC (1.20 µg h/ml), the predictions underestimated AUC in all cases (Figure 44).

Form F

The observed t_{max} values of Form F (1.5 h) were in agreement to the predicted (1.0 h – 1.5 h). Observed plasma concentration values between 1 h and 3 h were in all simulations underestimated (Figure 41 - Figure 43). Consequently, C_{max} of convolutional model ($C_{max} = 0.33$ µg/ml), PK-Sim® ($C_{max} = 0.25$ µg/ml) and GastroPlus® ($C_{max} = 0.25$ µg/ml) were smaller compared to the *in vivo* data ($C_{max} = 0.37$ µg/ml). During the residual elimination period starting at 4 h, predicted and observed plasma profiles demonstrated high prediction accuracies in all cases (Figure 41 - Figure 43). Despite the underestimated C_{max} values, AUC values were accurately estimated (Figure 44).

Form G

GastroPlus® and PK-Sim® modelled T_{max} (1.0 h – 1.5 h) and C_{max} (0.29 – 0.30 µg/ml) of Form G with a high accuracy compared to the reference t_{max} (1.5 h) and C_{max} (0.30 µg/ml), whereas the convolutional modelling approach overestimated C_{max} (0.41 µg/ml). T_{max} (1.5 h) was in agreement to the *in vivo* data (1.0 h – 1.5 h). Elimination rate of the observed Form G plasma concentration time profile starting at 5 h was in all simulations underestimated. These observations led to smaller PBPK-modelling AUC values (1.59 – 1.61 µg h/ml) compared to the *in vivo* profile AUC (1.8 µg h/ml). An overestimation of AUC (2.04 µg h/ml) based on the compartment model was observed.

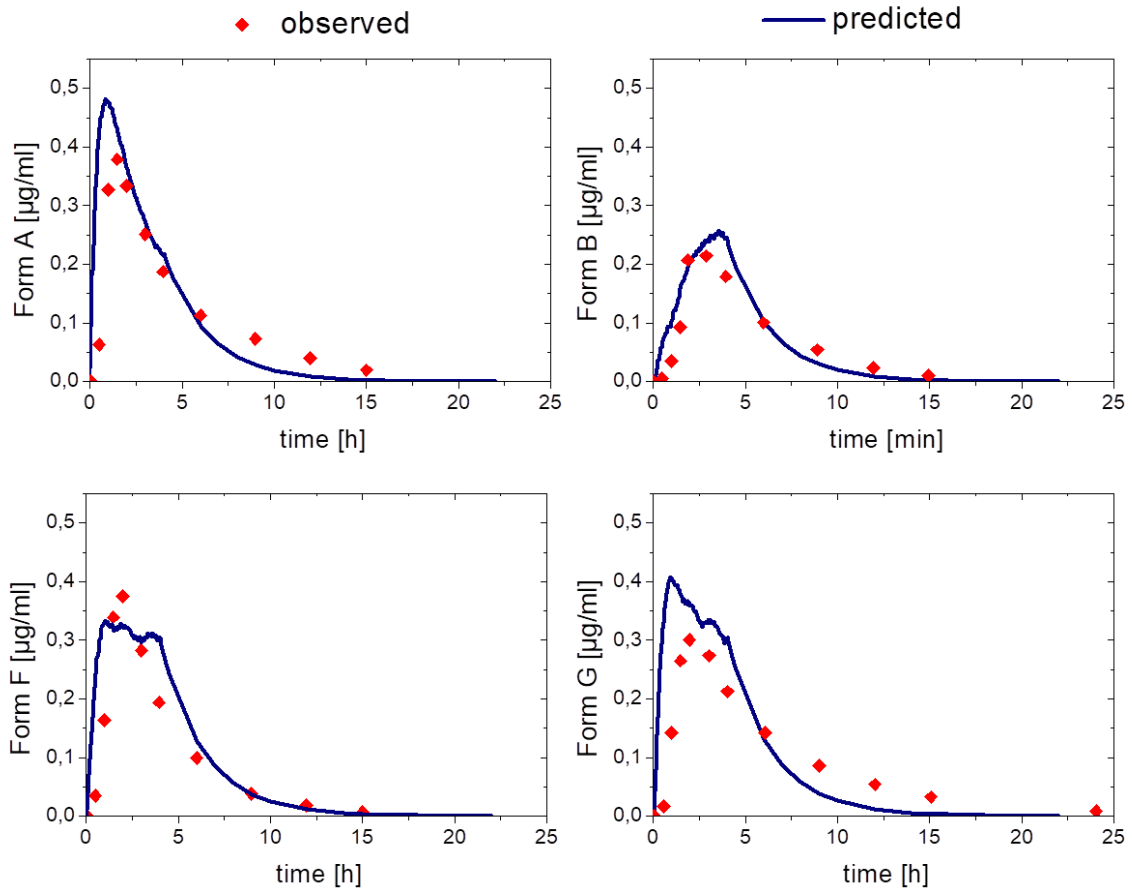


Figure 41: Prediction of ABT-102 plasma concentration time profile (blue line) based on convolutional prediction compared to the observed *in vivo* dog data (red dots).

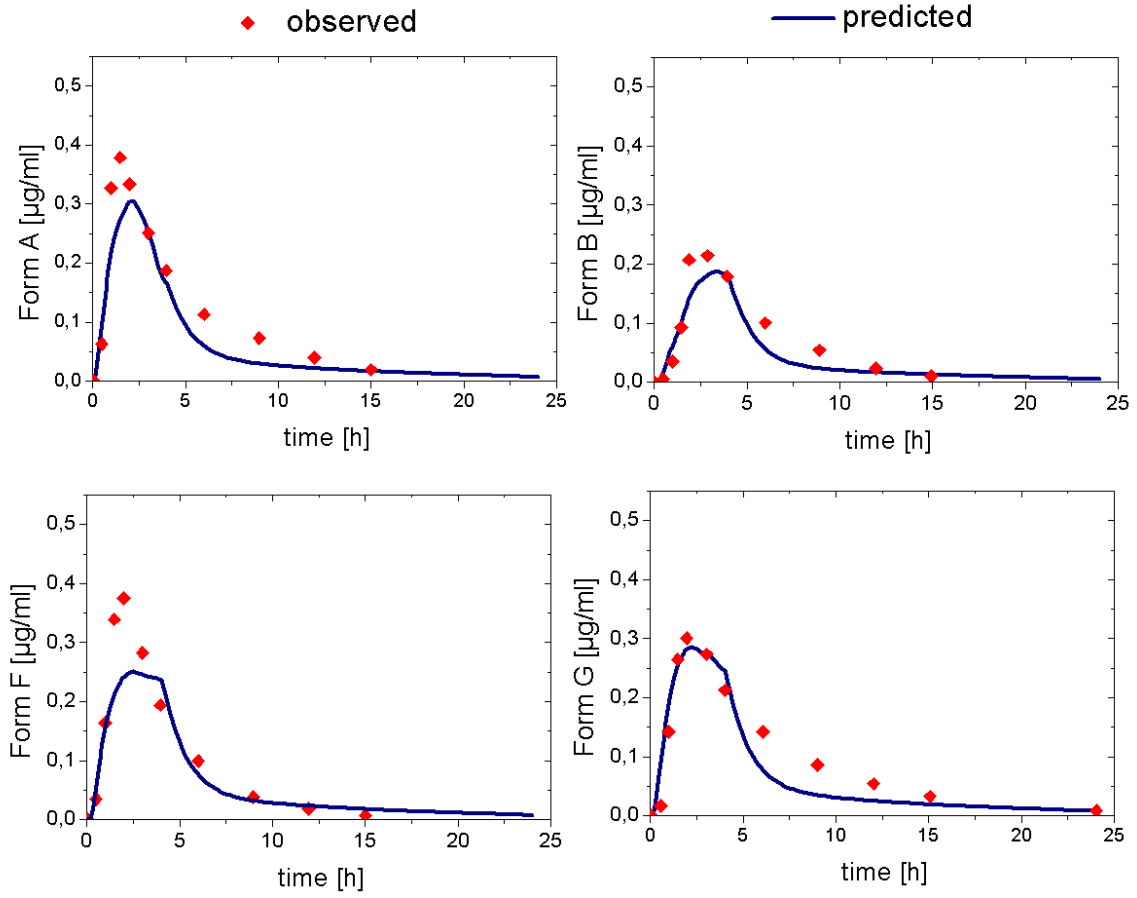


Figure 42: Prediction of ABT-102 plasma concentration time profile (blue line) based on PK-Sim® modelling compared to the observed *in vivo* dog data (red dots).

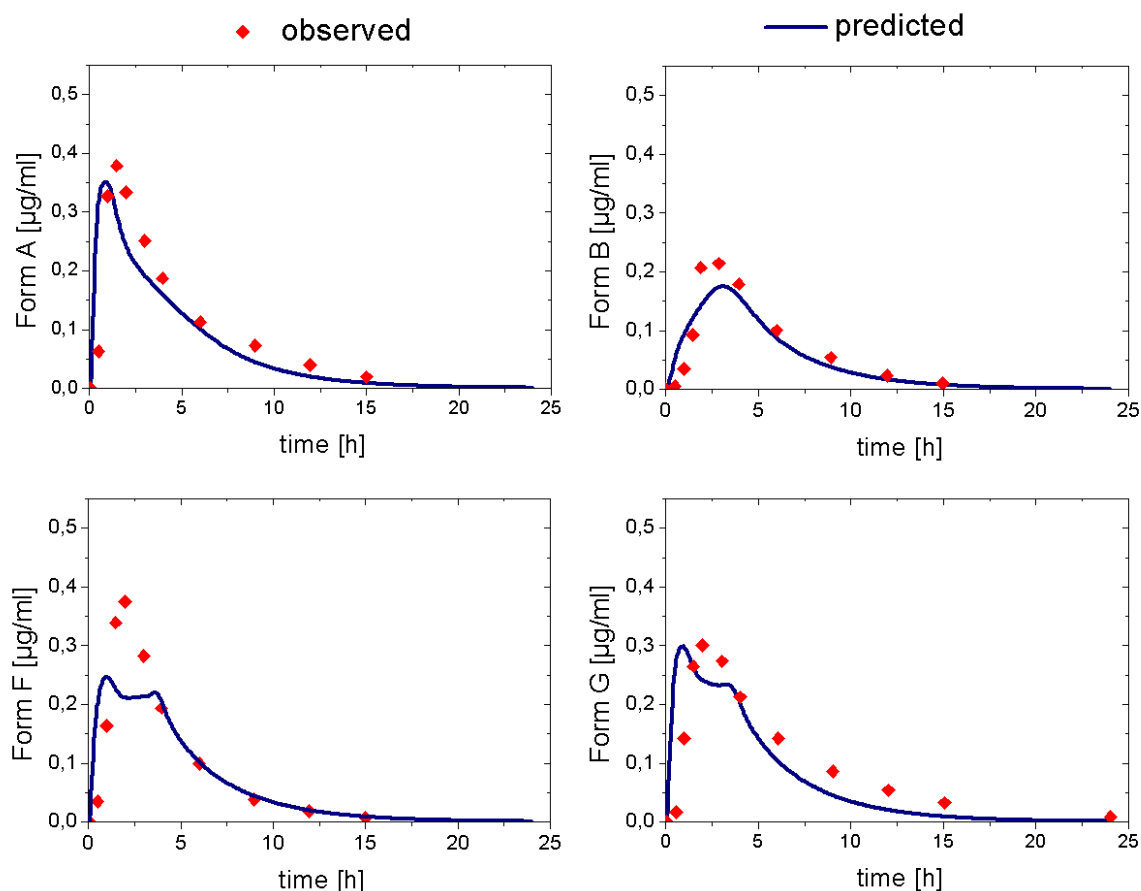


Figure 43: Prediction of ABT-102 plasma concentration time profile (blue line) based on GastroPlus® modelling compared to the observed *in vivo* dog data (red dots).

To assess the prediction accuracy, observed vs predicted C_{\max} and AUC were plotted including the identity line, the 1.25 - fold and 2.0 - fold deviation range (Figure 44).

All predicted AUC values were within the 1.25 – fold deviation range. The AUC prediction by convolutional approach resulted was overestimated for Form A, F and G, whereas the AUC of Form G was underestimated. PBPK – predictions led to smaller AUC values for all formulations compared to the observed *in vivo* data (Figure 44).

Predicted C_{\max} values demonstrated higher variability compared to the observed C_{\max} . Regarding the convolutional predictions, C_{\max} of Form A and F were outside the 1.25 – fold deviation range but inside the 2.0 –fold deviation range. In relation to C_{\max} predicted by both PBPK-software, Form G was outside the lower 1.25 – deviation range. The other C_{\max} values were within the 1.25 – fold deviation range (Figure 44).

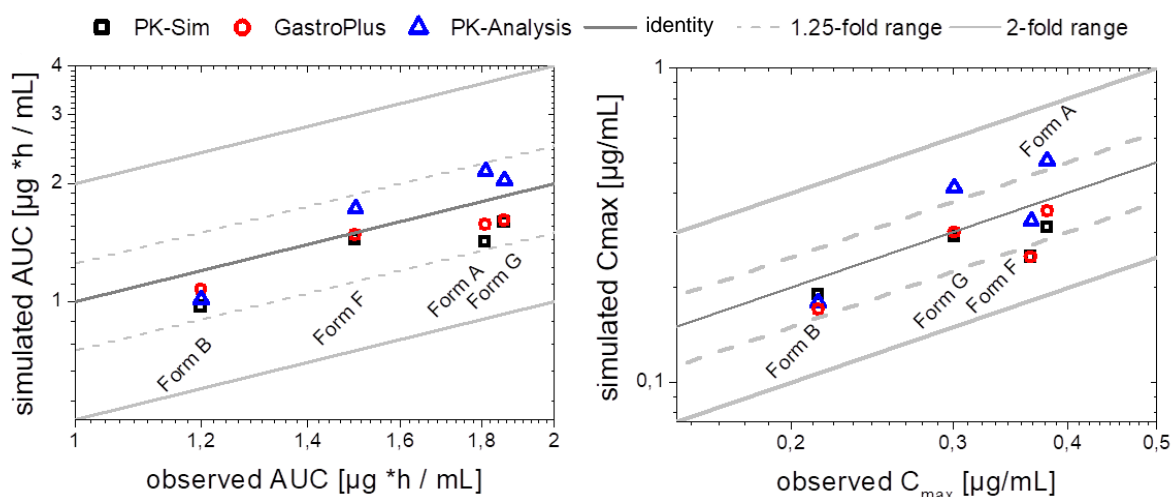


Figure 44: predicted vs. observed AUC and C_{max} values with identity line, 1.25 - fold and 2-fold range for PK-Sim[®], GastroPlus[®] and PK-Analysis (convolutional) predictions.

Discussion

The prediction of *in vivo* performance based on the biphasic partitioning profile led to meaningful, predictive results. Partitioning profiles of the BiPha+ assays were discriminatory towards the increased *in vivo* performance of Form B compared to Form A, F and G (Table 19). Consequently, the maximum concentration and the absolute fraction absorbed were in similar ranges of all tested formulations.

Form F predictions (Figure 41 - Figure 43) were the examples, which demonstrated some deviations from the observed data in the area of the C_{max} value. The deviations were caused by the shape of the partitioning profile and the high observed C_{max} value. Nevertheless, AUC values were accurately predicted.

Form A, F and G did slightly differ in their initial partitioning rate between 30-90 min and the subsequent partitioning rate starting at 90 min (Figure 41 - Figure 43). These slight differences resulted in distinct variations of C_{max} in the predicted plasma concentration time profiles. The sensitivity of a changing partitioning rate was pronounced in the convolutional predictions, because the partitioning profile was directly implemented into the predictions. PBPK predictions considered the permeability (P_{eff}) of ABT-102 through the gastrointestinal membrane and the gastrointestinal passage, which decreased the sensitivity to a change in the partitioning rate and therefore, led to a decreasing absorption rate. For this reason, C_{max} values and AUC values of PBPK models were smaller compared to the convolutional predictions.

Especially the convolutional prediction approaches represented an easy-to-handle method to get a rapid estimate of plasma concentration time profiles to assess the

performance of a certain formulation. In this context it has to be mentioned that this approach is suitable only for drugs having a minor metabolism. This is caused by the fact that no mechanistic detail is considered for the convolutional approach.

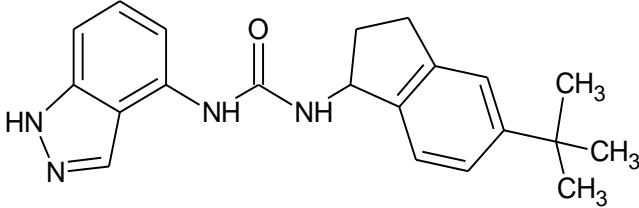
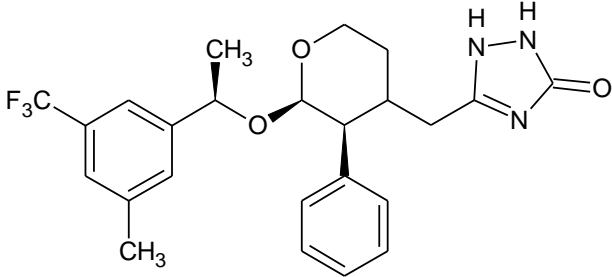
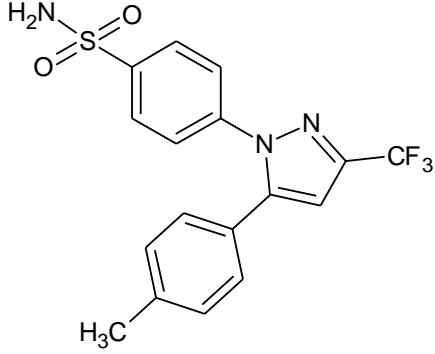
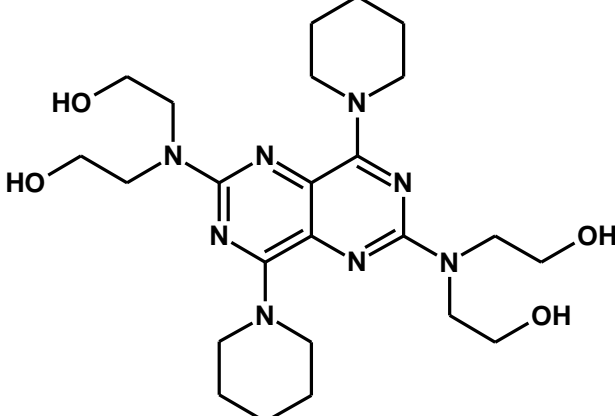
Overall, the described pharmacokinetic prediction methods, PBPK modelling and convolutional predictions, resulted in highly meaningful results with regard to the *in vivo* data. For this reason, the biphasic partitioning profile of the BiPHa+ assay demonstrated a remarkable predictive power to evaluated different enabling formulations of poorly soluble drugs in beagle dogs.

4 Material and Methods

4.1 Materials

4.1.1 Drug Substances

Table 20: Drug Substances

Drug Substance	Chemical Structure
ABT-102	
Aprepitant	
Celecoxib	
Dipyridamol	

Drug Substance	Chemical Structure
Fenofibrate	
Itraconazole	
Nimodipine	
Ritonavir	

4.2 BiPha+ Setup

The BiPha+ represents a fully automated biphasic dissolution assay, which consists of four main components:

- (1) Pneumatic Dosing system: Figure 45 and Figure 46
- (2) Dissolution: Figure 45 and Figure 46
- (3) Sampling: Figure 45 and Figure 46
- (4) Labview® Application: Figure 49

The hardware and interfaces are described in section 4.2.1. The hardware components are either controlled by a Labview® application developed in the course of the present work or have internal control loops. A detailed description of the Labview® software is provided in section 4.2.2. A detailed development and explanation of the experimental parameters are given in section 3.1 and section 4.3.

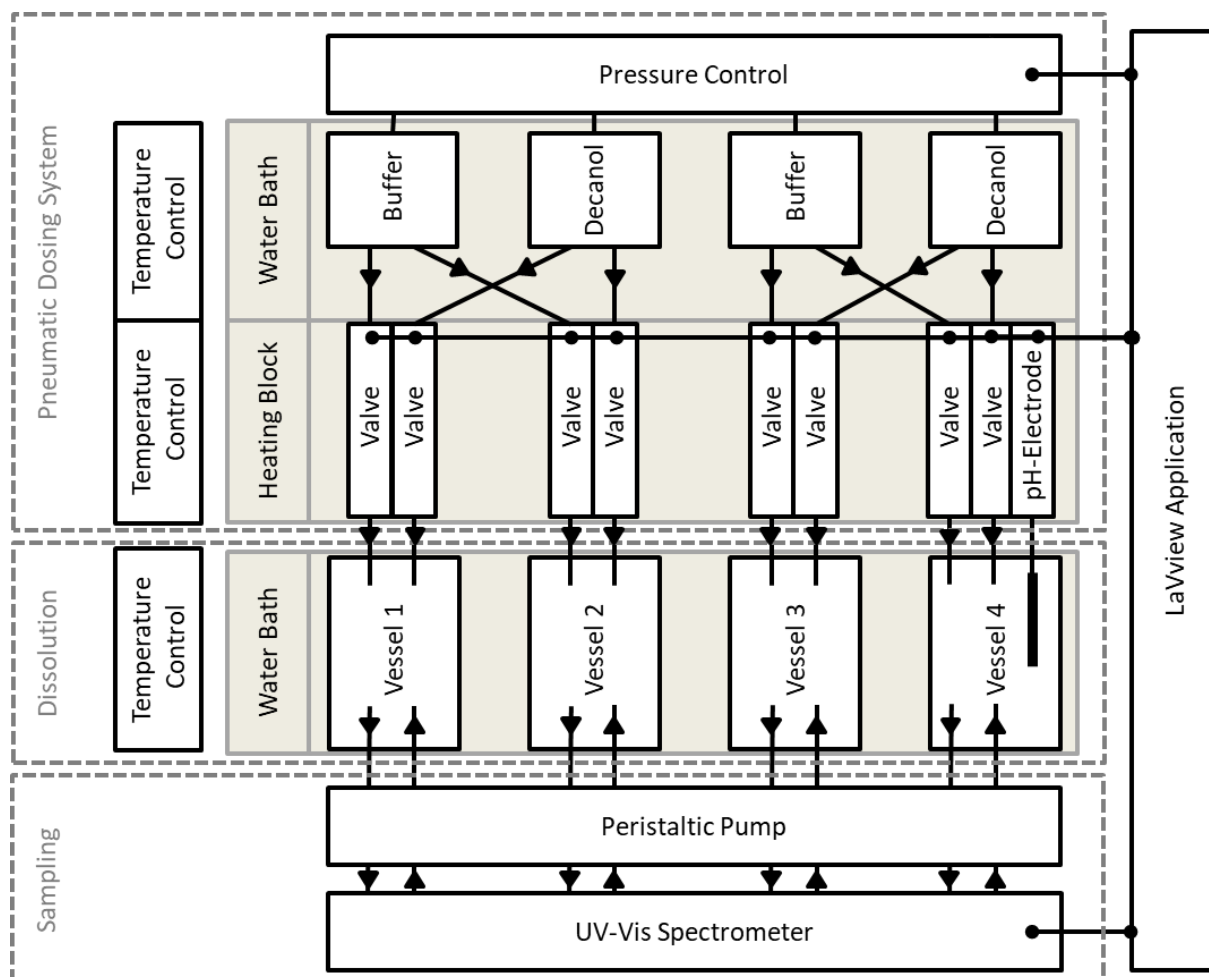


Figure 45: Schematic illustration of the BiPha+ setup containing of temperature controlled pneumatic dosing system, dissolution vessel in water bath and sampling system using a UV-Vis spectroscope. UV-Vis spectroscope and the pneumatic dosing system are controlled by the Labview® application.

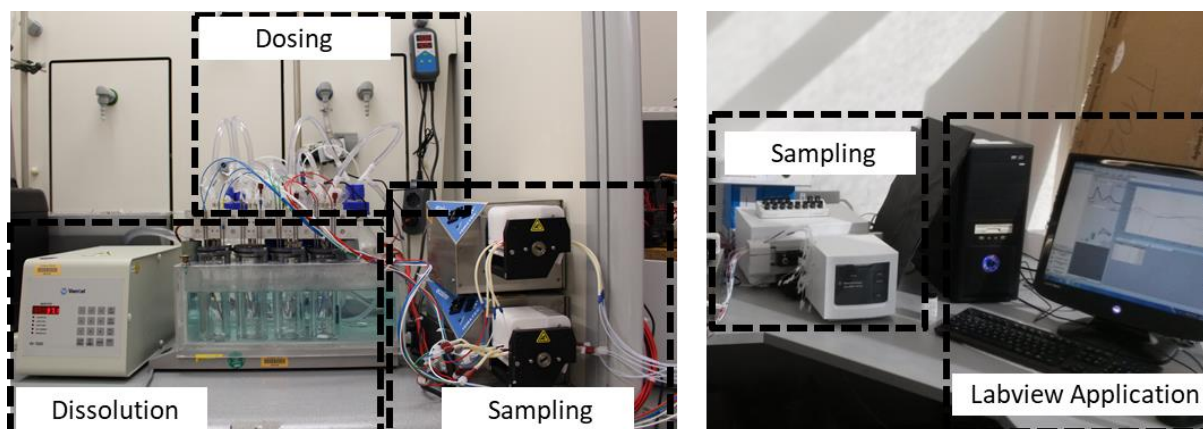


Figure 46: Picture of BiPHa+ apparatus: Pneumatic dosing system, dissolution vessels and water bath, sampling via two peristaltic pumps and an Agilent UV-Vis spectrometer; Labview® application

4.2.1 BiPHa+ Hardware

Pneumatic Dosing System

The adjustment and measurement of the pH as well as the dosing of decanol during the experiment is performed with a pneumatic dosing unit (Figure 47). Since the viscosity of the liquids and thus the dispensed quantity is strongly dependent on the temperature, the complete dispensing unit was temperature controlled at 37°C. All components that are not specified with a brand name were built in the workshops of the pharmaceutical, chemical and physical institute of the university Bonn. The solenoid valves (dosing head VTOE, Festo AG & Co. KG, Esslingen, Germany) are made of chemically resistant polyetheretherketone (PEEK) and are temperature-controlled by an aluminium heating block. The solenoid valves are controlled by the Labview® application via a digital NI USB-6000 interface (National Instruments Corporation, Austin, USA; Figure 48). The dosing tubes for the buffer or the decanol dispensing are sheathed with a water tube heater. The pressure for the pneumatic dosing is kept constant at about 0.7 bar overpressure via a compressed air control unit (proportional pressure control valve VEAB, Festo AG & Co. KG, Esslingen, Germany). The compressed air is connected to pairs of two pressure-resistant 250 ml (buffer) and 1000 ml (decanol) Duran® pressure plus bottles (Schott AG, Mainz, Germany; Figure 45). The Dissolution vessels and the Duran bottles are permanently tempered in a water bath at 37°C. For correct pH adjustment, a pH electrode (VWR micro Electrode, VWR International GmbH, Darmstadt, Germany) is connected to the Labview® application in the blank vessel via the DrDAQ interface (PSE Priggen Special Electronics, Steinfurt, Germany; Figure 48).

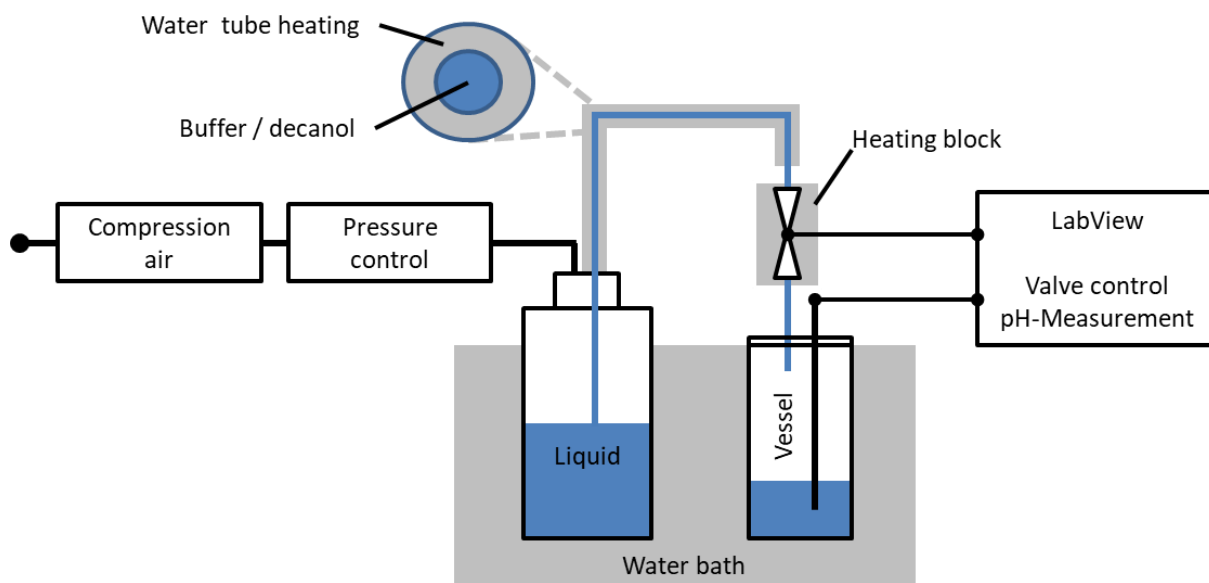


Figure 47: Pneumatic dosing system

Dissolution

A detail description of dissolution vessels, sinkers and stirring configuration is provided in section 3.1.1 and Figure 9.

Sampling

Samples are permanently circulated by peristaltic pumps (Ecoline VC-MS/CA8-6, Cole-Parmer GmbH, Wertheim, Germany) and quantified by an UV-Vis spectrometer (Ag 8453, Agilent Technologies Deutschland GmbH, Waldbronn, Germany). To reduce possible particles from the aqueous phase in the flow-through cuvettes of the spectrometer, 1 μm full-flow filters were used. The Agilent 8453 is controlled with the Labview® application via an Ethernet interface (Figure 48).

Interfaces

The Labview® application is connected to hardware components is based on three interfaces (Figure 48). The software contains drivers for the interfaces. The interfaces of the respective component convert the commands into electronic signals (Pneumatic dosing system, Agilent 8454) or electronic measuring into measured values (pH-electrode, Agilent 8454).

An overview of the interfaces is given in Figure 48. The locations of the individual drivers in the software are marked in grey in the figures of section 4.2.2.

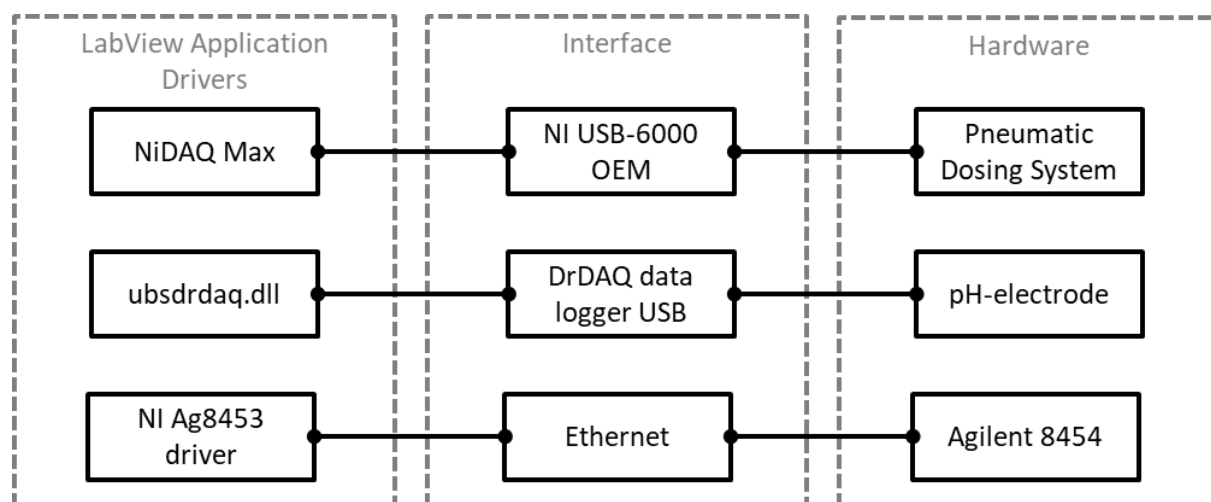


Figure 48: Hardware / Software interfaces

4.2.2 BiPha+ Labview® Application

The application was developed on the basis of Labview® 2016 (National Instruments Corporation, Austin, USA). The Labview® application can be divided into five sub-programs: Initialize, System Settings, Run Dissolution, Processing and Save Samples (Figure 49). The sub-programs are interconnected and share information with each other. Initialize, System Settings and Run Dissolution depend to each other, i.e. to perform a dissolution experiment, the system must first be initialized, then the settings for the experiment and the zero calibration of the cuvettes (System Settings) must be made, and then the dissolution experiment can be run with the appropriate parameters. The sub-programs Processing and Save Samples are linked to each other. These are used to process the analytical raw data and then to export the results in a text file.

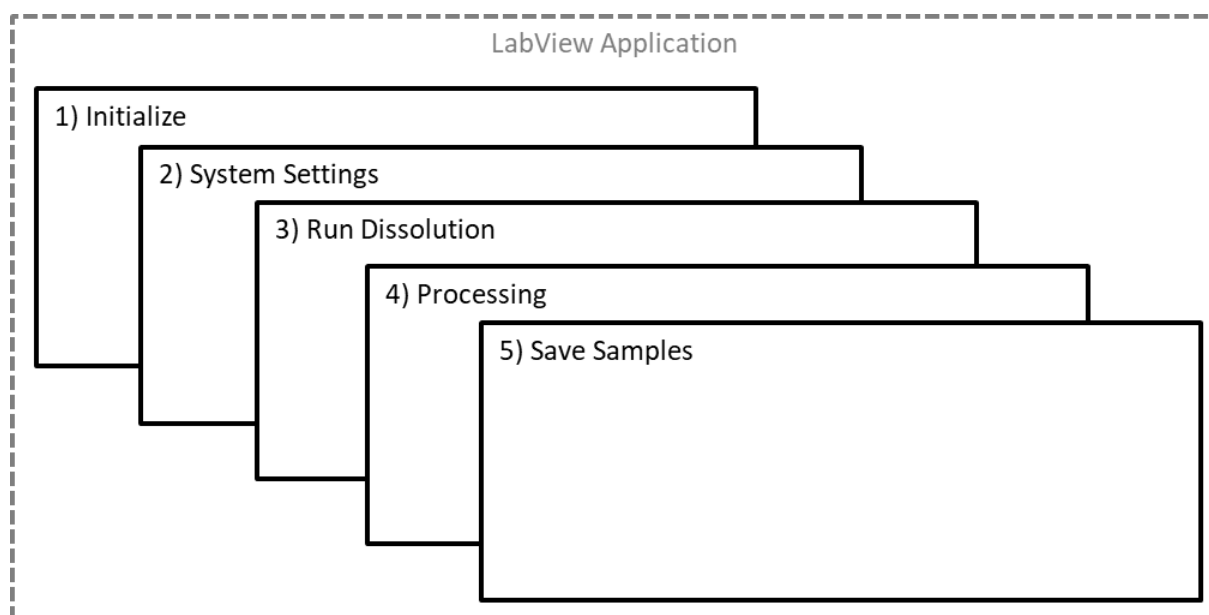


Figure 49: Five sub-programs of the BiPHA+ Labview® application

Initialize

The initialization establishes a connection between the Labview® application and the UV-Vis spectrometer (Agilent 8453) via the NI Ag8453 driver. In addition, all adjustable parameters are read out and transferred to the software (Figure 50). A successful connection is displayed in the software by a green signal. The system parameters are passed to the subsequent programs System settings and Run Dissolution.

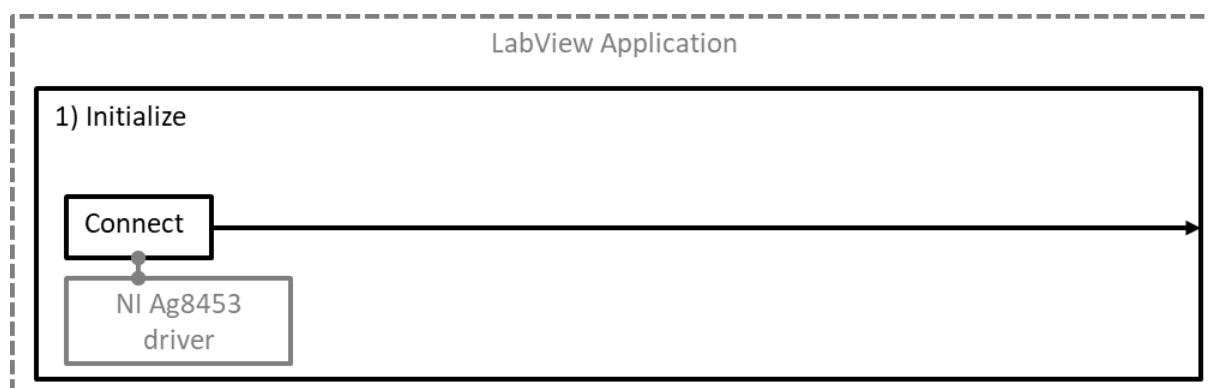


Figure 50: Sub: Initialize

System Settings

After successful initialization, settings on the Agilent 8453 and the calibration of the valves can be configured by the System Settings (Figure 51). For a zero cell, blanking the cuvettes must be performed before each dissolution experiment, which is also integrated in the sub System Settings. All other settings are stored in the system and can

be flexibly adjusted if necessary. The calibration of the valves can be made in this sub-program. The settings of the Agilent 8453 (e.g. wave lengths or shutter mode), the blanks and the calibration of the valves are automatically passed to Run Dissolution.

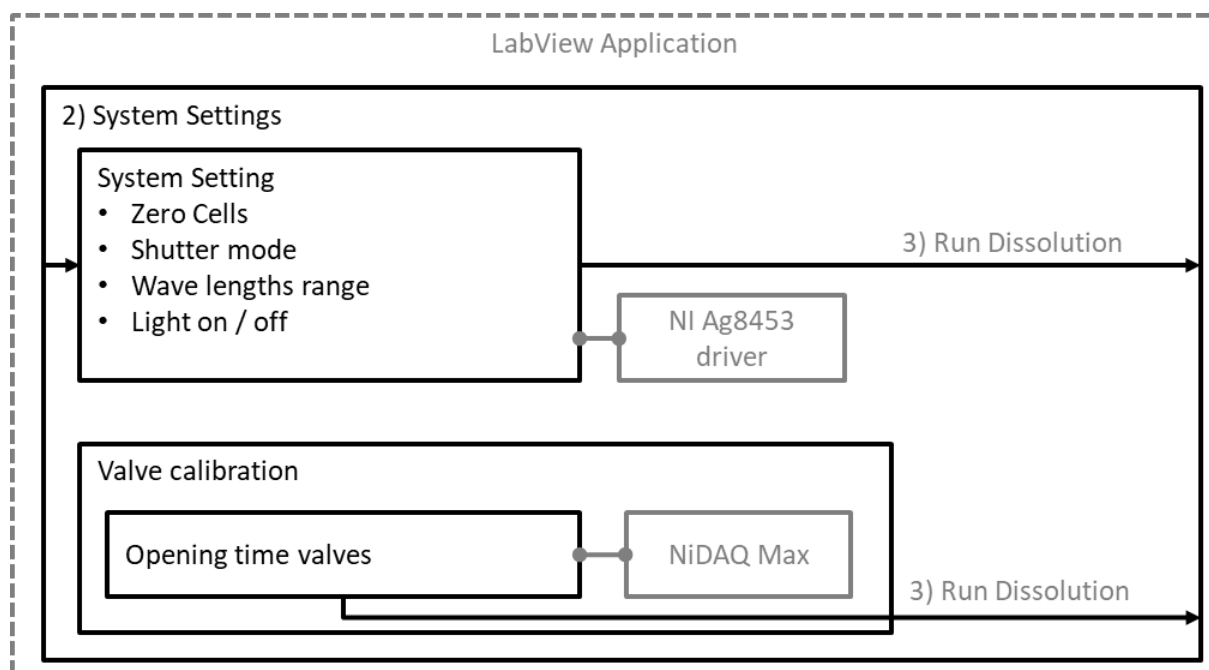


Figure 51: Sub: System Settings

Run Dissolution

To start a dissolution run (Figure 52), the initialization and the zero cells spectra must be available in advance. The zero cells spectra are automatically loaded into the Run Dissolution sub-program prior to the start of the experiment, as soon as they have been measured. The zero cell spectra are stored for each cuvette and allocated accordingly for each measurement. The multicell port has 8 cuvette positions. Position one represents the blank of the aqueous phase and position five represents the blank of the organic phase. In order to compensate for potential fluctuations in the course of the experiment, a blank is recorded for each measure cycle. Position 2 - 4 and 6 - 8 represent the samples cells of the aqueous and organic phase. The measuring sequence is identical for the aqueous and organic phase: Setting the cell position for blank and blank spectra recording, cell position for sample cuvettes and sample spectra recording, the measured blank is applied to each sample of one measurement cycle. The interval time between the individual measuring cycles can be set flexibly. In the present work, an interval of three minutes was applied. The spectra are saved as a binary file on the hard drive after each measurement cycle and the last measured spectra are displayed on the software screen. To save RAM, binary data was used whenever possible. A pH electrode

permanently measures the pH value in the blank vessel in parallel to the spectra recording. The pH adjustment is performed according to a predefined time schedule in a control loop with the measured pH value. At the end of an experiment, the measured pH values are saved as a final binary file on the hard drive.

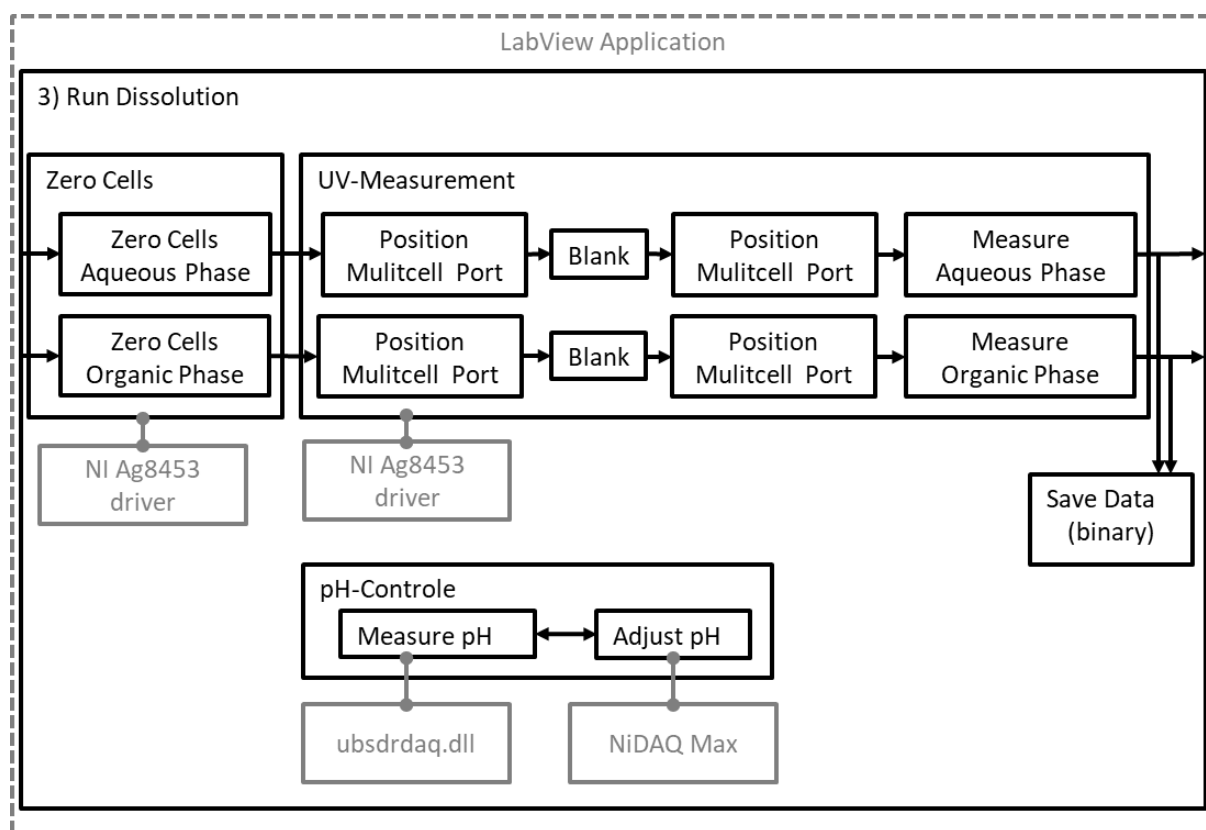


Figure 52: Sub Run Dissolution

Processing

The spectra measured during the dissolution experiment are stored as binary files on the hard drive and can be uploaded and processed after completion of an experiment (Figure 53). The spectra are processed using different mathematical algorithms to determine the actual concentration of dissolved active ingredient in the aqueous and organic phase. A detailed description of the spectra corrections can be found in section 3.1.2. It is possible to use several correction methods at the same time. After mathematical processing, the spectra are displayed visually on the software screen in order to check the meaningfulness of the processing. From the processed spectra, the data of a corresponding wavelength is extracted and output as a binary file. The data processing steps are applicable to both organic and aqueous phase files.

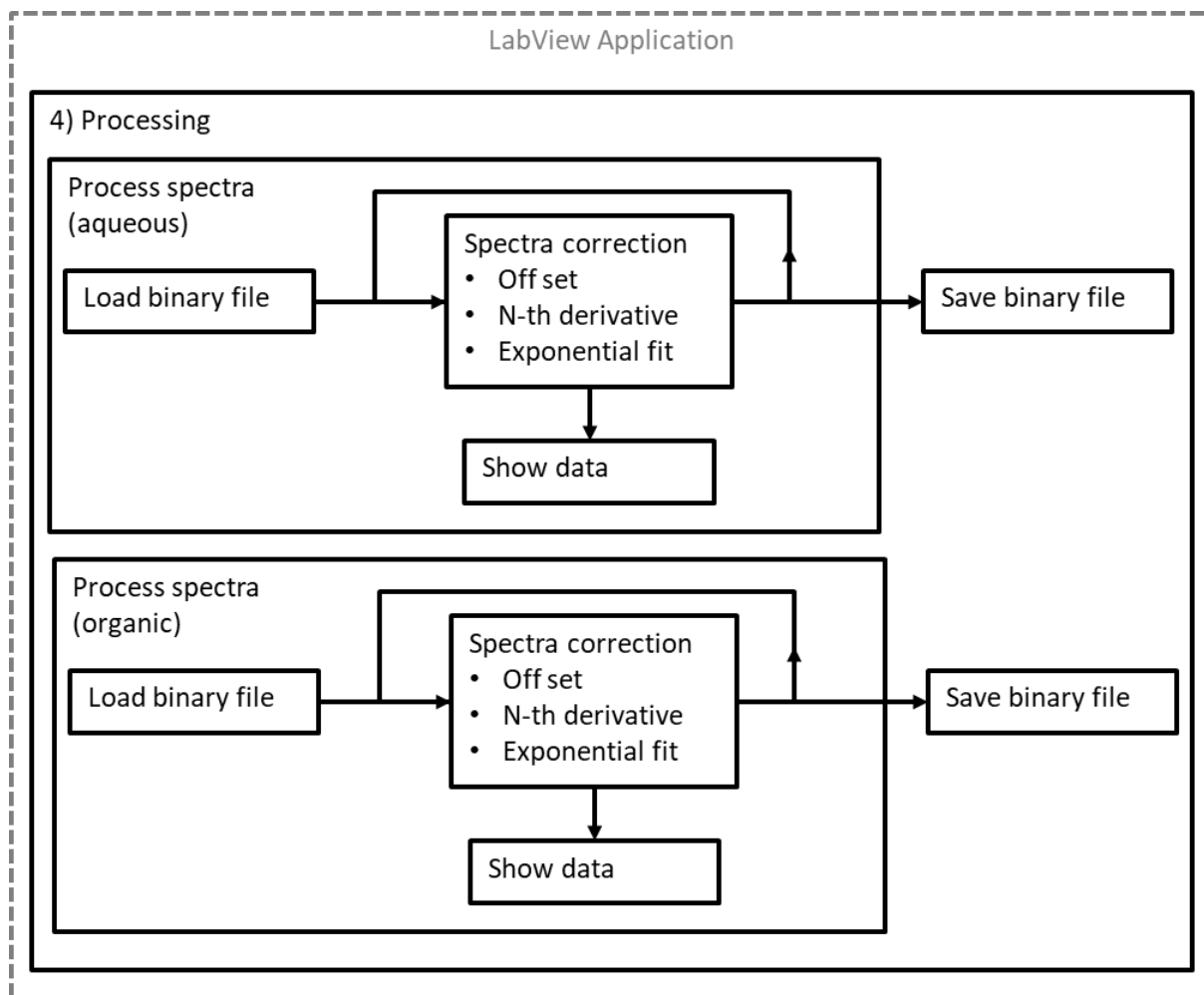


Figure 53: Sub Processing

Save Samples

Since the spectra are processed as a binary file, various reformatting steps are performed to save the file as a text file on the hard drive (Figure 54). The results text file includes the following: processing method, wavelength, sample quantity (*in vitro* dose), single and averaged absorbance values, single and averaged relative dissolved drug amount with respect to the used *in vitro* dose.

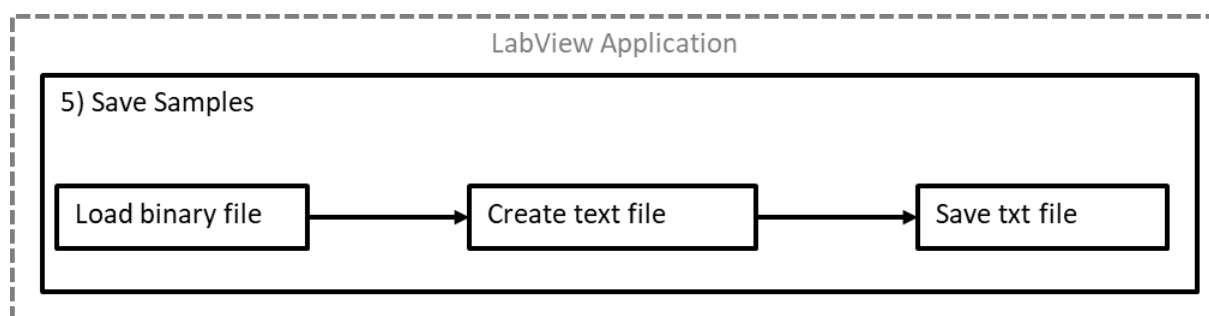


Figure 54: Sub Save Samples

4.3 Rational Design of the Biphasic Dissolution Setup (BiPha+)

4.3.1 Hydrodynamic assessment

Hydrodynamic influences drug dissolution and precipitation as well as partitioning in the organic layer [70,71,83]. Therefore, sufficient mixing is of vital importance to avoid and as worst-case precipitated particles. Photographic images were taken to illustrate the hydrodynamic in the dissolution vessel (Canon EOS 700D SLR at 1/320 s exposure unstirred water layer. Both described biphasic dissolution setups were assessed regarding their hydrodynamic [70]. The volumes of the aqueous phase and the mixing speed were set to 160 rpm for our method, while Xu et al. used 60 rpm for an USP II/ USP IV combination [68]. To visualize the velocity of the water, glitter powder (density 1.33 g/cm [135] was used

4.3.2 HPLC Method of Ritonavir

A HPLC-method was established to verify the dissolved amount of ritonavir in comparison to UV-spectrophotometric determination. A Waters DAD-Array with a reversed phase column (Phenomenex Inertial ODS-3 150x4.6 mm, 5 μ m) was used at 35°C. The mobile phase contained 40% methanol, 40% acetonitrile and 20% demineralized water. The quantification was performed in triplicates. All samples from the aqueous phase were filtered immediately after withdrawing the samples through a 0.45 μ m cellulose-acetate syringe filter. The filters were pre-saturated by 10 ml of the aqueous phase to exclude adsorption of ritonavir to the membrane. After Filtration, 5 μ L of the samples were directly injected. The measurement was performed at 240 nm and at a retention time of 7.0 minutes.

4.3.3 Equilibrium Solubility of Ritonavir

The equilibrium solubility was determined using the shaking flask method for both the aqueous and the organic medium. The aqueous medium was adjusted to pH 1.0 and 6.8.

For FaSSIF-V2 sodium taurocholate and lecithin were added as mentioned above. Ritonavir was added in excess. The flasks were shaken at $37^{\circ} \pm 0.5^{\circ}\text{C}$ for three days. All samples were analysed as described in HPLC method (section 2.2).

4.3.4 pKa Determination of Ritonavir

All pKa values were determined UV-spectrophotometrically using a Sirius T3 apparatus. The pKa values were identified, where a maximum change of UV-spectra was detected between pH 1.0 to 13.0. The titration was performed at room temperature in a 0.15 M potassium chloride / methanol mixture (ratios of 5/5, 4/6, 3/7). About 1 mg of ritonavir was used for each titration [136].

4.3.5 Comparison of the BiPha+ Assay with Established USP II/IV Biphasic Methods

A general purpose of the present study was to combine the advantages of a small scale one vessel method as a useful tool in formulation screening [67,72,81] and the proven biorelevance of the USP II and USP model [69,82–84]. All experiments were conducted in triplicate. Dissolution behaviour was studied using three different aqueous buffer media, namely Bi-FaSSIF (M1), Bi-FaSSIF-V2 (M2), and plain buffer without surfactant (M3). The relative absorption area (A_{rel}) was adjusted to a value of 0.4. The volume ratio (R_V) of the aqueous and organic medium was kept at 1 similar to most of the published models [65]. The target concentration of the aqueous phase was calculated based on the biopharmaceutical classification system as the ratio of the highest ritonavir dose of 100 mg [137] and 250 ml, resulting in 0.4 mg/ml.

The reference biphasic dissolution test for the present study basically consists of a combination of an USP apparatus II and IV [68,83,138]. Initially, the ritonavir drug product disintegrates / dissolves in 41 ml SGF (pH = 1.6) in the flow-through cell (USP apparatus IV) at 5 ml/min for 30 minutes in a closed loop (Xu et al., 2017). Later the closed loop is coupled with the USP II including 200 ml of FaSSIF-V2 and 200 ml of octanol. Both phases were saturated with each other before the experiment starts. The biphasic dissolution test runs for 6 h. The quantification in the organic layer was conducted by UV-Vis measurement using the 2nd derivative, excluding interferences from formulation excipients or dissolution medium. Aqueous samples were quantified by HPLC after centrifugation [68]. The published data were extracted using Engauge Digitizer 10.9.

A comparison of the dissolution test setup for the BiPha+ and the USP apparatus II/IV biphasic setup is given in Table 21. The BiPha+ setup was parameterized to keep the surface-volume ratio (A/V), the volume-volume ratio (V/V), and the ritonavir concentration in the aqueous phase (C_{BCS}) similar.

Table 21: Dissolution setup parameters and comparison

	BiPha+	USP II/IV biphasic method [68]
Radius	2.5cm	5.0cm
$\frac{A_{\text{interface}}}{V_{\text{aqueous}}}$	$\frac{20\text{cm}^2}{50\text{cm}^3} = 0.4\text{cm}^{-1}$	$\frac{80\text{cm}^2}{240\text{cm}^3} = 0.33\text{cm}^{-1}$
$\frac{V_{\text{organic}}}{V_{\text{aqueous}}}$	$\frac{50\text{cm}^3}{50\text{cm}^3} = 1$	$\frac{200\text{cm}^3}{241\text{cm}^3} = 0,8$
C_{BCS}	$1.0 \times C_{\text{BCS}} = 0,4 \frac{\text{mg}}{\text{ml}}$	$1.0 \times C_{\text{BCS}} = 0,4 \frac{\text{mg}}{\text{ml}}$
Mixing	Magnetic stirrer	Paddle
(Biphasic) Vessel	Cylindric vessel	USP II vessel

4.4 Investigation of Organic / Aqueous Interfaces with Regard on Its Impact on Partitioning Rate

4.4.1 Interface Assessment (Spinning Drop)

The method is based on the optical contour evaluation of a drop of immiscible light and heavy liquids placed in a rotating capillary. By this method very low interfacial tensions $< 10\text{mN/m}$ can be determined. The spinning drop experiments performed in this work were conducted with a SpinningDrop Video Tensiometer SVT 20N (Dataphysics, Filderstadt, Germany) at the Institute of Technical Thermodynamics Karlsruhe Institute of Technology. The experiments are carried out in the temperature-controlled measuring cells, in our case at $37\text{ }^\circ\text{C}$. The pre-saturated samples were tempered in a water bath at $37\text{ }^\circ\text{C}$ for 3 days before being measured to achieve thermodynamic equilibrium. Approximately 1 mL of the heavy aqueous phase is placed in the capillary of the tensiometer. Then a drop of the lighter 1-decanol phase is created by a syringe. By a fast rotation of the capillary around its longitudinal axis, the phase with the higher density is pressed between the capillary wall and the drop having the lower density. This results in a cylindrical deformation of the 1-decanol and thus an increase in the interfacial area of the droplet, which is counteracted by the interface tension. Based on the drop shape, the interface tension can be calculated from (Equation 23). The contours of the cylindrical drop can be determined automatically via the microscope cam.

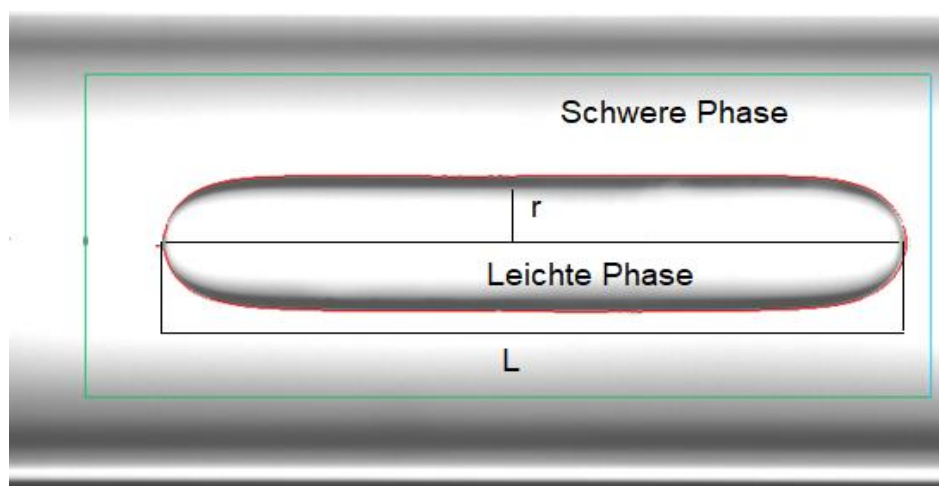


Figure 55: Spinning drop of aqueous phase and 1-decanole

The interface tension is calculated by the following dependence:

$$\sigma = \frac{\Delta\rho\omega^2r^3}{4} \quad \text{Equation 23}$$

The radius r of the cylindrical drop is the parameter to be measured, $\Delta\rho$ is the density difference between the aqueous and organic phases, ω is the angular velocity. The

angular velocity is set by the rotational frequency of the capillary. The experiments were performed at various rotation speeds in range 3500-6000 rpm.

4.4.2 Influence of Interface Tension to Partitioning Rate

Partitioning Rate Evaluation

The dissolution experiments were performed in biorelevant medium FaSSIF-V2 at pH= 6.8 and, with the rotation speed 160 rpm over the entire period of 220 minutes. The drug substance dipyridamole is a weak base and therefore slightly soluble at pH = 6.8. For this reason, the amount of dipyridamole added to the aqueous phase was selected to prevent precipitation. By the fact that dipyridamole is present as a dissolved species is obligatory since the test system should be kept as simple as possible and consequently the distribution rate can be clearly characterized. The dipyridamole concentration is 15 µg/ml in the solution, which is much smaller compared to the saturation solubility [139]. For this purpose, 22.5 mg of the substance was dissolved in 1 ml of methanol. Then 100 µl of the dipyridamole solution was added to 50 ml of aqueous phase. The experiment was performed as described in section 4.2 without pH shift.

The dipyridamole concentration was quantified both in the aqueous phase and in the 1-decanol phase. The partitioning rates in the organic phase correspond to a first order kinetic. The partitioning rate of dC/dt is directly proportional to the concentration C_0 and k_a (Equation 27). By integration, Equation 28 is obtained. The rate constant k_a is achieved by a linear regression of the logarithmized concentration time profiles (Equation 29).

$$\frac{dC}{dt} = k_a C_0 \quad \text{Equation 24}$$

$$C(t) = C_0 e^{-k_a t} \quad \text{Equation 25}$$

$$\ln C(t) = \ln C_0 - k_a t \quad \text{Equation 26}$$

Design of Experiments

Design-Expert® 12 was used to design and evaluate the dissolution experiments. First the experimental space was defined for influencing factors, Kollidon® VA 64 and Soluplus® concentrations, as well as the number of stages per factor (Table 22). The interface tension of the experiments was not used as input parameter since it reflects the resultant of influencing factors. The Soluplus® concentration was chosen to correspond to about 750 - 7.5 mg per 250 ml. Kollidon® VA 64 concentration was chosen to cover the

upper range of concentrations studied (0.3 mg/ml - 0.003mg/ml), according to the results of section 3.2.1. A full factorial design by combining all possible factor level, are processed in a randomized pure sequence. In the experiment, a central-composite design with inner star-points and with an additional central point was selected. The central point tests the assumption of linear behaviour of the factors between the low level and the high level. The inner star points described the design space more accurately but allow less precise predictions. A one-factor analysis of variance ANOVA was used to test the influence of the independent factors on the dependent factor k_a . Based in the results a response surface area was established for the visualisation of the results.

Table 22: Input factors of the experimental design

Factor	Name	Lower limit (-1)	Upper limit (+1)
A	Kollidon® VA 64	0.003 mg/ml	0.031 mg/ml
B	Soluplus®	0.031 mg/ml	3.0 mg/ml

4.5 Modelling of Biorelevant Kinetics for a Ritonavir Hot-Melt Extruded Amorphous Solid Dispersion

4.5.1 Development of an Advanced Kinetic Model

A kinetic model was established guided by the work of Locher et al. [81]. It is based on ordinary differential equations (ODE), which describes the fraction of dissolved drug in both phases resulting from the disintegration of the ritonavir-containing ASD, API dissolution, and partitioning into the organic phase. These ODEs were numerically solved by the Runge-Kutta approximation method. The ODEs were iteratively calculated by a self-programmed Labview[®] application. To describe and explain the concentration-time profiles resulting from BiPHA+ experiments appropriately, the kinetic model was advanced by introducing additional phase separation processes in the aqueous phase: (1) the formation of API-rich nanodroplets via liquid-liquid phase separation (LLPS) as described by Xu et al. [68] for the same ritonavir-ASD, and (2) the process of transformation of the nanosized droplets to smaller particles, whereas the API remained amorphous [95]. Further details are given in section 3.2.

4.6 BiPha+ Biphasic Dissolution Assay to Assess *in vivo* Performance for Poorly Soluble Drugs in Six Commercial Enabling Formulations

4.6.1 Dose Assessment

The effect of the formulation quantity (*in vitro* dose) was investigated regarding the obtained partitioning profiles in the organic layer. Three formulation quantities were selected referring to an *in vitro* dose of 5 mg, 10 mg and a BCS class dependent quantity (section 3.4.2). To calculate the BCS dependent quantity, the highest dose on the market was divided by 250 ml and multiplied with 50 ml [112,115]. The *in vivo* fractions absorbed for each drug were obtained from literature and compared to the maximum concentration at the end of the experiment ($C_{dec, max}$) from the 5 mg, 10 mg, and the BCS-class dependent quantity (section 3.4.2). Fraction absorbed (f_a) is the absorbed quantity without considering metabolic pathways. Bioavailability (F) considers metabolism during absorption. A high degree of biorelevance is assumed, when $C_{dec, max}$ values of the organic phase are comparable with the *in vivo* fractions absorbed [68,69].

4.6.2 Pharmacokinetics and Compartment Analysis of *in vivo* Data

All pharmacokinetic profiles were evaluated using an oral two-compartment model (Figure 25A). Given that the LogP values of the evaluated drugs were higher than 3 (Table 12), a two-compartment model was applied to accurately describe the *in vivo* behaviour, which includes a distribution step of the drug in a peripheral compartment. [33,140].

The sub-processes of the two-compartment model, absorption ($C(t)_{absorption}$), distribution ($A \cdot C(t)_{distribution}$), and elimination ($B \cdot C(t)_{elimination}$), were assumed to show first order kinetics (Equation 27). The kinetic rate constants of all drugs were obtained by the residual method [31,33]. For this, the observed plasma profile data were linearized by calculating the logarithm of plasma concentration over time (Figure 56A). At first, the first order elimination functions ($B \cdot C(t)_{elimination}$) were calculated and subtracted from the observed plasma data. Then, the obtained data points were used to calculate the first order distribution function ($A \cdot C(t)_{distribution}$). Factor A and B were the intercept of the determined elimination and distribution functions and could be interpreted as scaling factor towards the absorption function ($C(t)_{absorption}$). For all calculations, distribution was assumed to be slower than absorption. Therefore, absorption was calculated by subtracting distribution and elimination function from the plasma data. The absorption rate constants of $C(t)_{absorption}$ were estimated from the logarithm of the residual concentration values.

In addition, the fraction absorbed (f_a) was needed to assess the biorelevance of the partitioning profiles (section 4.6.1). A high degree of biorelevance was assumed if $C_{dec, max}$ values of the organic phase and fraction absorbed values were equivalent [68,69].

All calculated absorption profiles were assumed to show first order kinetic without knowing the real *in vivo* kinetic [31,33]. However, this calculation method is useful to get an idea about the amount and kinetic of the absorption process *in vivo*.

$$C(t) = C(t)_{absorption} - A \cdot C(t)_{distribution} - B \cdot C(t)_{elimination} \quad \text{Equation 27}$$

Aprepitant (Emend[®], nanocrystal)

The oral pharmacokinetics of the market formulation was assessed in two clinical studies by Majumdar et al. From the first study the absolute bioavailability of 59 % has been reported based on the data obtained from 20 volunteers under fasted conditions [106]. The second study provides the pharmacokinetics based on the data obtained from 21 volunteers, assuming a one-compartment model [119]. Analysis of the study was performed by the residual method analysis of the fasted state plasma profile (Figure 25B), because of the inhomogeneous elimination period (10 h – 40 h) of aprepitant. The inhomogeneous elimination is apparent by the slower elimination rate between 10 and 20 hours compared to the later increased elimination rate (Figure 28A).

Celecoxib (Celebrex[®], microcrystal)

The plasma profiles reported by Paulson et al. [107] were utilized for the pharmacokinetic evaluations of the two-compartment model in the present work (Figure 25A). It should be noted that the absolute bioavailability of celecoxib in human has not been determined, since no intravenous formulation of the drug has been developed and tested so far [141]. In the study by Paulson et al., the absolute bioavailability of micronized celecoxib of approximately 40 % was obtained from a study in poor metabolizing beagle dogs under fasting conditions [107]. In this case, minimal first pass effects were expected, and the fraction absorbed was assumed to be the maximum amount of passive absorbable drug, which was correlated to the results of the biphasic dissolution model.

Fenofibrate (Lipidil[®], microcrystals)

The pharmacokinetic data of fenofibrate were obtained from Xu et al. [83] for the 200 mg dose and from Fei et al. [121] for the 54 mg does strength. The absolute bioavailability of a fenofibrate nanocrystal suspension has been reported to be about

70 %, which is considered to be equal to the solid nanocrystal formulation [83,108,109]. The fraction absorbed (46 %) of the micronized formulation was indirectly calculated using the relative bioavailability compared to the nanocrystal formulation under fasting conditions [83]. As fenofibrate represents a prodrug activated by ester hydrolysis, the plasma concentration was determined based on its active form fenofibric acid [129]. As the saturable process of activation by ester cannot be covered by compartmental models a simple two-compartment model was selected to describe the plasma profile (Figure 25A).

Itraconazole (Sempera[®], ASD)

Brone et al. investigated the plasma profile of 100 mg itraconazole in healthy male volunteers [142]. The absolute bioavailability of the oral solution was examined at fasted state [111]. The relative bioavailability for capsule and solution were compared to calculate the oral absolute bioavailability of the capsule formulation [110]. The absolute bioavailability was reported to be 16 %. A two-compartment model was assumed to evaluate pharmacokinetics (Figure 25A).

Nimodipine (Nimotop[®], ASD)

The pharmacokinetic data were taken from Blardi et al. [105]. Nimodipine undergoes a strong first-pass effect and hepatic metabolism of about 85 % – 95 % resulting in a low bioavailability of 3.5 % when taken under fasted condition [105]. Without first-pass, the real fraction absorbed could be around 35 % based on a mean metabolizing value of 90 % [123]. Because of the very fast metabolism (much faster than absorption), the metabolic rate can only be calculated imprecisely with the residual method and is not relevant for the kinetic of the absorption [33]. Consequently, pharmacokinetic was evaluated based on a two-compartmental model (Figure 25A).

Ritonavir (Norvir[®], ASD)

Klein et al. investigated the pharmacokinetic of 100 mg Norvir[®] in 27 healthy human subjects [143]. Xu et al. established a Level A IVIVC with different ritonavir drug products including a fraction absorbed of 60-80 % [68]. They suggested a direct correlation between the maximum fraction absorbed and the maximum partitioned drug, in this case approx. 75 % [112]. A two-compartment model was applied to calculate the rate constants (Figure 25A).

4.6.3 Verification of *in vivo* Relevance and Predictive Power

The biphasic partitioning profiles of the five model drugs were assessed with respect to their *in vivo* relevance. A level A IVIVR was calculated, partitioning and absorption profiles were directly compared and prediction errors were calculated comparing the predicted and observed plasma concentration time profiles. As many mathematical methods were performed, we illustrated the methods applied for *in vitro* and *in vivo* data treatment in Table 23.

As described in section 2.5, two-compartment models were applied in order to gain the *in vivo* fraction absorbed versus time profiles (Figure 56). The rate constants of absorption, distribution and elimination were calculated by the residual method [31,33] using data obtained from the literature (Figure 56A, C). The first order absorption model was selected, because the deconvolution approach leads sometimes to a limited number of data points (drug concentration-time values) in the *in vivo* absorption period which can be respectively correlated to *in vitro* data [31,33].

In a first step, the calculated *in vivo* absorption profiles and the *in vitro* partitioning profiles (drug concentration over time in the organic layer) were used to calculate a level A IVIVC [80,144] as follows:

- (1) A Levy-plot (normalization of time scale) was established for all five formulations to estimate a general time-scaling factor between *in vitro* and *in vivo* data [122].
- (2) The first order *in vivo* absorption time profiles were correlated to the *in vitro* partitioning profiles (section 3.5.1).

In a second step, the drug concentration-time profiles of the organic layer were compared to those obtained by absorption *in vivo* in the same figure (section 3.5.1).

For an assessment of the BiPHA+ data compared to the *in vivo* pharmacokinetic, retro-IVIVCs (single stage [124]) were calculated based on a convolutional approach, where $C_{\delta}(t)$ is the impulse response and $I_Q(t)$ are the arbitrary impulses which can be interpreted as the amount of released / absorbed drug [145]. The predicted plasma concentration time profiles are the sum of all unit impulse responses ($C(t)$ vs. t , Equation 2). Each impulse $I_Q(t-t_n)$ decreases following the single impulse function. The single impulse function represents the two-compartmental models including the distribution and elimination function. We deliberately used the single input function calculated from the *in vivo* data of the oral formulations, because we aimed to avoid the influence of study to study variabilities. The arbitrary impulses $I_Q(t)$ are calculated by determining the *in vitro* partitioning rate every three minutes where the concentration in the organic

layer was measured (Figure 56). The *in vivo* estimated gastric emptying of 30 min [37] was considered in the BiPHA+ assay by a pH shift from 1.0 to 5.5. We applied the time shift approach, i.e. only data where distribution into the organic phase were considered, in analogy with the methodology used in other research studies, which do not consider these 30 min lag-time for calculating IVIVR or pharmacokinetic prediction [67,68,83].

$$C(t) = I_Q(t) * C_\delta(t)$$

$$= \sum I_Q(t - t_n) - A \cdot C(t - t_n)_{distribution} - B \cdot C(t - t_n)_{elimination}$$

Equation 28

To assess the prediction accuracy of the calculated pharmacokinetic profiles based on retrospective IVIVC, prediction errors (PE) according to EMA and FDA guidelines [74,124] of AUC (area under the curve of plasma profile), C_{max} (maximum plasma concentration), and t_{max} (time point with maximum plasma concentration) were calculated. All calculations were performed using EXCEL 2016 (Microsoft, Redmond, USA).

$$PE [\%] = \frac{\text{Observed value} - \text{Predicted value}}{\text{Observed value}}$$

Equation 29

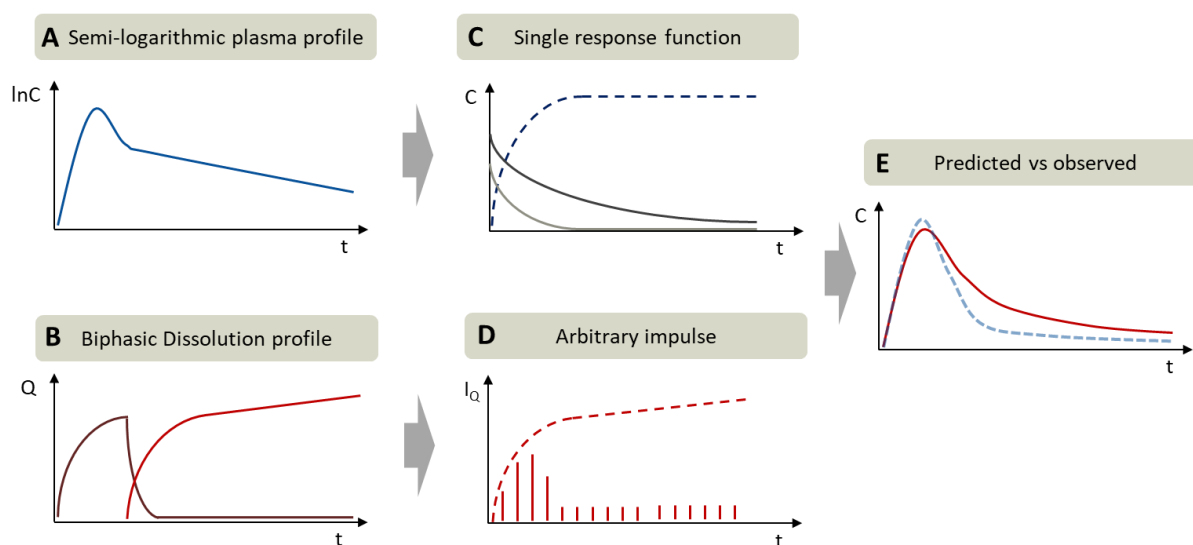


Figure 56: Exemplary procedure of pharmacokinetic parametrization by residual method (curve stripping) and *in vivo* prediction assessment: (A) logarithmic plasma concentration-time profile; (B) biphasic dissolution profile: aqueous phase (purple) and organic phase (red); (C) first order absorption (dark blue) and the determined single impulse functions: distribution (light grey), elimination (dark grey) received by residual method; (D) Arbitrary impulses (I_Q) calculated by *in vitro* partitioning rate on each time point (red stripes), (E) comparison of predicted plasma profile (red) vs. observed plasma profile (blue)

Material and Methods

Table 23: Overview of the methods applied for *in vitro* and *in vivo* data treatment. Each method comprises of one or more operations as well as the required input and output data.

Method	Operation	Input	Output
Compartmental analysis	Residual Method (Compartmental analysis)	<i>In vivo</i> pharmacokinetic data	Absorption rate constant (profile)
			Distribution rate constant (profile)
			Elimination rate constant (profile)
<i>In vitro/ in vivo</i> relationship	(1) Levy plot	<i>In vitro</i> partitioning profile (without time-scaling)	Time-scaling
	(2) Fraction absorbed vs. partitioned drug plot (IVIVR)	Absorption rate constant (profile) <i>In vitro</i> partitioning profile (with time-scaling) Absorption rate constant	IVIVR
Comparisons of <i>in vivo</i> absorption profiles and <i>in vitro</i> partitioning profile	n/a*	<i>In vitro</i> partitioning profile (with and without time scaling) Absorption rate constant (profile)	n/a*
Pharmacokinetic prediction	(1) Derivation of partitioning curve	<i>In vitro</i> partitioning profile (with and without time-scaling)	Arbitrary impulses
	(2) Residual Method (Compartmental analysis)	<i>In vivo</i> pharmacokinetic data	Single impulse response (Distribution rate constant & Elimination rate constant)
	(3) Convolution	Single impulse response Arbitrary impulses	Predicted pharmacokinetic
	(4) Prediction accuracy	Predicted pharmacokinetic <i>In vivo</i> pharmacokinetic data	Prediction errors

* not applicable

4.7 Implementation of Biphasic Dissolution Profiles in PBPK Models

4.7.1 Methods

Models were developed as described in section 3.5.1. As the model development was novel in terms of the methodology, the workflows are presented in the result section. All physicochemical properties were taken from section 3.4.1. The *in vitro* data are taken from section 3.4.3.

4.7.2 Drug Dossiers for Developing PBPK Models

The clinical *in vivo* pharmacokinetics and the metabolic properties of each investigated drug are summarized in the following section.

Aprepitant (Emend[®], nanocrystal)

The highly lipophilic drug exhibits a high plasma protein binding of > 98 % and undergoes enterohepatic circulation [146]. Based on literature data, the absolute oral bioavailability was reported to be approximately 60 %. In the same study of Majumdar et al., 20 volunteers received 2 mg aprepitant intravenously [146]. The final oral market formulation was administered with 227 ml water [106].

Celecoxib (Celebrex[®], microcrystal)

The estimated plasma protein binding of celecoxib is higher than 97 % [147]. Celecoxib is mainly metabolized by CYP 2C9 [147]. No absolute oral bioavailability has been investigated in humans. However the absolute oral bioavailability was investigated in poor metabolizing beagle dogs in the fasted state [148]. Pal et al. investigated an oral solution in human under fasted conditions [149]. Celebrex *in vivo* pharmacokinetic data were also taken from literature [148]. Celebrex was administered in the fasted state with 210 ml water [148].

Fenofibrate (Lipidil[®], microcrystals)

Fenofibrate is a highly permeable prodrug which is activated by ester hydrolysis [129]. No fenofibrate is detectable in the plasma just its active form fenofibric acid [120]. Fenofibric acid is highly bounded on plasma proteins (>99%) [129]. The absolute oral bioavailability of fenofibrate 46 % was indirectly calculated by a nano-formulation as described in literature. The nano-formulation is compared to a micronized formulation [83,108,109]. Fei et al. compared the oral plasma profile of micronized fenofibrate and an oral solution [121]. The pharmacokinetic data of fenofibrate were obtained from Xu et al. [83] for the 200 mg dose and from Fei et al. [121] for the 54 mg does strength.

Itraconazole (Sempera[®], ASD)

The plasma protein binding of itraconazole is reported with 99.8%. Itraconazole undergoes a CYP 3A4 metabolism [142]. Additionally, itraconazole underwent enterohepatic circulation [150]. A oral solution was investigated to determine the absolute oral bioavailability in the fasted state [111]. Thus, absolute bioavailability of the capsule formulation (15.6%) was estimated by comparing the relative bioavailability of liquid and capsule formulation [110]. Itraconazole was intravenously administered as a β -cyclodextrin solution [151]. Both, the oral solution and the HPMC-based formulation were investigated under fasted conditions in two studies of Barone et al [142,152]. The capsule formulation was administered with 200 ml of water.

Nimodipine (Nimotop[®], ASD)

Nimodipine C_{max} -values were rapidly detected within 1 h, which indicates a high permeability. However the predicted permeability value of 8.08 E-5 cm/min was very low [123]. Therefore, the permeability from CaCo-assay (6.06 E-4 cm/min) was used to calculate the *in vivo* value by GastroPlus[®] correlation [130]. Blardi et al. investigated an i.v. formulation and the marketed product in a clinical study [105]. No study with an oral solution has been conducted. Additionally, nimodipine is extensively metabolized by Cyp-3A4 liver enzymes, which explains the small 3.5% oral bioavailability. Approximately 90% of the absorbed drug is metabolically inactivated during the first liver passage [105]. Thus, the fraction absorbed of nimodipine is in a range of 35%, which is in accordance to *in vitro* biphasic dissolution data (Figure 24).

Ritonavir (Norvir[®], ASD)

CYP 3A4 is the most important metabolizing enzyme of ritonavir [137]. Fraction absorbed in a range of 60-80 % was reported in literature [83]. under The study of the oral liquid formulation in children was conducted by Salem et al. moderate fat conditions [153]. The solubility of ritonavir in FeSSIF-V2 is 18.5 μ g/ml [68], which was necessary because a scaling from fasted to fed state was performed for the predictions (section3.4). The oral pharmacokinetic profile of the ASD marked product was investigated by administering 100 mg ritonavir after a 10 hour fasting period [143].

4.8 Systematic evaluation and *in vivo* prediction of ABT-102 drug products by using the biphasic dissolution model

4.8.1 Materials

ABT-102, copovidone, hydroxypropyl methylcellulose acetate / palmitate (HPMCAS), poloxamer 188, saccharose monopalmitate and colloidal silicon dioxide were obtained from AbbVie Deutschland GmbH.

Hard gelatin capsules size 4 and 00 (Capsula GmbH, Ratingen, Germany) were used for *in vitro* and *in vivo* studies. The buffer concentrate was made of tri-potassium phosphate (Alfa Aesar, Kandel, Germany), tri-potassium citrate (Carl Roth, Karlsruhe, Germany) and sodium hydroxide (VWR Chemicals, Darmstadt, Germany). Sodium-taurocholate, lecithin and 1-decanol were ordered from Alfa Aesar (Kandel, Germany). HPLC eluents consisted of methanol (VWR Chemicals, Darmstadt, Germany), and demineralized water (Merck Milli-Q, Darmstadt Germany).

4.8.2 Physicochemical Characterisation

LogP value was determined by a waters DAD-HPLC and a Lichrospher RP-18 5 µm 10x4 mm column using a water methanol gradient [154]. Based the determined logP value permeability was calculated by PK-Sim® [131].

Solubility in 6.8 phosphate buffer, Bi-FaSSIF-V2 (section 3.1) and 0.1 M hydrochloric acid was investigated using shaking flask method at 37°C. After 72 h shaking time, samples were centrifuge for 20 min at 4500 rpm. The supernatant was quantified by a diode array UV-Vis spectrometer (Agilent 8453, Waldbronn, Germany).

4.8.3 Extrudate Preparation

Compositions of extrudates are provided in Table 17. Prior to extrusion, all ingredients were mixed using a cutting mill (IKA M20, IKA-Werke GmbH & Co.KG, Staufen, Germany). Hot melt extrusion was performed using a bench scale extruder (Minilab II, Thermo Fischer Scientific, Karlsruhe, Germany) at a temperature of 142°C and screw speed of 75 rpm. The extrudates were milled using a cutting mill (IKA M20, IKA-Werke GmbH & Co.KG, Staufen, Germany). A particle sizes range of the milled extrudate of 250 to 1000 µm was used for the *in vivo in vitro* investigations. A 25 mg dose was selected for the *in vivo* investigation in beagle dogs and a dose of 5 mg was taken for the *in vitro* investigations. Subsequently, a mixture of 50 % milled extrudate and 50 % filling material (mannitol 99 % and 1 % colloidal silicon dioxide) was filled in hard gelatin capsules (size 00 for *in vivo*, size 4 for *in vitro* investigation) and was mixed after closing. The absence

of drug substance related crystallinity in the ASD was confirmed by polarized light microscopy (Model DMLM, Leica Microsystems, Wetzlar, Germany).

4.8.4 BiPha+ Assay

Extrudate powders were filled in hard gelatin capsules having an *in vitro* dose of five milligram ABT-102, which were investigated in the BiPha+ assay. Each formulation was tested in triplicates. The capsules were placed in a sinker above the stirrer. The experiments were performed according to section 4.3.

4.8.5 *In vivo* Study

ABT-102 was prepared as a solution in 10% DMSO in PEG-400 vehicle at a concentration of 20 $\mu\text{mol/kg}$ for intravenous investigation. A dose of 1.74 mg/kg ABT-102 intravenous solution was administered as a slow bolus in a cephalic vein to three beagle dogs (male/female). The dogs were fasted overnight prior to dosing. Mean weight of a dog was 10.5 kg.

For oral investigation each formulation (Form A, B, F and G) was tested in a group of six dogs at a dose of 25 mg/dog administered as capsule (size 00). Fasted dogs were pre-treated with histamine approximately 30 minutes prior to dosing. Food was provided to these dogs approximately 12 hours after dosing. In the non-fasted (fed) dogs, the dogs were fasted overnight, with food provided approximately 30 minutes prior to dosing. Bioavailability was separately investigated to pharmacokinetic assessment in the fasted state.

4.8.6 Compartment Analysis and IVIVR

A level A IVIVR was calculated based in observed *in vivo* data. The workflow is given in Figure 37. A two-compartment model was applied to calculate the pharmacokinetic rate constants of the orally administered formulations (Figure 57). Because of the high lipophilicity, the drug was assumed to distribute in peripheral compartments [33,140]. The two-compartment model describes absorption, distribution and elimination as a kinetic first order [31,33]. For the compartment model, the rate constants were calculated by residual method (section 4.6.2) from intravenous data to determine the rate constants λ_1 (distribution rate) and k_e (elimination rate). The calculated rate constants of elimination and distribution were used to calculate k_a (absorption rate) from the oral data. Besides that, it was necessary to know the absolute fraction absorbed *in vivo* to calculate a level A IVIVR based on the BiPha+ data. The absolute fraction absorbed has to be in a similar range of the end concentration of the *in vitro* partitioning profile [69,82].

In vivo fraction absorbed time profiles and *in vitro* partitioning profiles were used to calculate a level A IVIVR. In a first step a Levy Plot was fitted to generate a time scaling factor [80,144]. Based on the time scaling, the IVIVR was fitted to demonstrate the *in vivo* relevance of the *in vitro* partitioning profile (refer also to section 4.6.3).

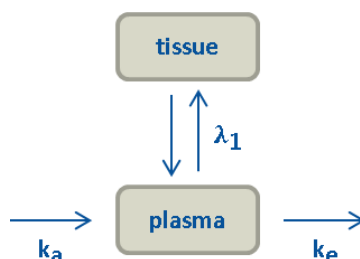


Figure 57: Assumed two compartment model: absorption rate constant (k_a), distribution rate constant (λ_1) and elimination rate constant (k_e)

4.8.7 Predicting of the *in vivo* Performance by Compartment Analysis

Intravenous data were evaluated by residual method to obtain the intravenous distribution (λ_1) and elimination (k_e) rate constants (Figure 37). Using the two-compartment description of the intravenous pharmacokinetic data, the initial concentration at $t = 0$ min was calculated. Considering the initial concentration and the administered dose, which depends on the weight of a dog (10.5 kg), the distribution volume (V_d) was calculated.

As described in section 4.6.3 the *in vivo* plasma concentration time profiles were calculated based on a convolution using the partitioning profiles gained by the BiPha+ model and the distribution / elimination model. A direct calculation of oral plasma concentration time profiles using biphasic partitioning profiles and the two-compartment model was possible because ABT-102 do not undergo high first pass metabolism [155]. The calculations were performed by Microsoft Excel (Microsoft, Redmond, USA). The predictive accuracy was validated to mean plasma concentration time profiles in beagle dog (Figure 37).

4.8.8 Predicting *in vivo* Performance by PBPK Modelling

A mean intravenous elimination / distribution PBPK model of ABT-102 in beagle dogs was developed using PK-Sim® 7.3 and GastroPlus® 9.6 (Figure 37). Physiochemical properties of the drug and physiological properties of an average dog were integrated. Subsequently, the elimination / distribution PBPK models were optimized based on observed mean intravenous data. A development of a absorption model from oral liquid formulation was not suitable, as the oral liquid most likely precipitates in the intestine [155,156].

The intravenous PBPK models were extended to an oral absorption model by implementing predicted permeability values and biphasic partitioning profiles of each formulation. Intestinal permeability (P_{eff}) was predicted by PK-Sim® and this value was also implemented in GastroPlus® [128]. The biphasic partitioning profiles were implemented likewise controlled release dissolution profiles (section 3.5.1). This is the cause by the following assumptions: the rate limiting step of absorption of a highly soluble drug (BCS 1) is drug release, which is pictured by the aqueous dissolution profile, whereas the rate limiting step of poorly soluble drug (BCS 2) is dissolution of the drug, which is pictured by the organic partitioning profile by the BiPHA+ assay (section 3.5.1). The predictive accuracy was assessed by mean *in vivo* concentration time profiles (Figure 37) and by plotting predicted versus observed C_{max} and AUC values.

5 Conclusion and Outlook

5.1 Conclusion

A fully automated, small scale, biphasic dissolution setup (BiPHA+) was developed which was characterized by the volume ratio of aqueous and organic phase, the ratio of absorption area to aqueous volume, as well as the concentration of ritonavir in the aqueous phase. UV - quantification in both layers was suitable to determine the drug concentration despite the appearance of scattering or overlapping spectra. One major advantage of the BiPHA+ apparatus was the automation of critical analytic parameters such as dispensing of liquids and pH adjustment. Bi-FaSSIF and Bi-FaSSIF-V2 and a biorelevant buffer system were developed to simulate the gastrointestinal transition *in vivo*. The control of hydrodynamics was realized by triangular magnetic stirrers creating a turbulent movement of the aqueous phase. This one vessel dissolution assay was able to generate comparable data to the biphasic method of Xu et al. [31] consisting of a combination of USP apparatus II and IV, which has already demonstrated *in vivo* relevance [31,34,38]. Two media Bi-FaSSIF and Bi-FaSSIF-V2 led to complex partitioning profiles of a ritonavir containing ASD, while the partitioning rate of the experiment in surfactant free medium was more homogeneous and reached a much lower level of distributed drug in the organic phase. Thus, constitution and re-dissolution were significantly influenced by biorelevant surfactants.

The interface between the organic and aqueous phases was a key factor in the assay. If the aqueous phase contained biorelevant surfactants and different formulation ingredients, the resulting interfacial tensions were generally at a similar level. One example demonstrated that the discriminatory properties of the assay were caused by the formulation components in the aqueous phase, rather than the organic / aqueous interface properties.

In order to get a deeper insight into the complex *in vitro* dissolution process of the ritonavir ASD measured dissolution in the BiPHA+ assay, a kinetic model was established including the transformation of nano-droplets, which was necessary to explain the sigmoidal distribution kinetics profile. The kinetic model described the dissolution process mathematically, and parametrized the processes of disintegration, dissolution, precipitation as nano-droplets, re-dissolution, and absorption into the organic layer *in vitro*. As a result, the re-dissolution step was discovered as the time limiting step in all cases. Ostwald ripening of nano-droplets is proposed as a new effect, which can possibly influence the drug dissolution from an ASD. Beside supersaturation, an improved re-

dissolution of precipitated drug substance also provides an essential contribution to enhanced drug dissolution from an ASDs.

The potential of the BiPHA+ assay to assess *in vivo* performance for poorly soluble drugs was investigated by six model drugs formulated by different enabling approaches (micro- and nanocrystals, amorphous solid dispersion). The mini-scale approach of the BiPHA+ test system required a down-scaling of the drug product *in vitro* dose. It was found that 15-25 μmol (10 mg) of drug was a suitable *in vitro* dose to reach a high *in vivo* predictive power for dose ranges of the tested drug products from 30 to 200 mg. The correlation indicated that in this dose range the *in vitro* concentration time profiles of the partitioned drugs in the organic layer actually behaved similar to the passively absorbed drug-amount *in vivo*. The *in vitro* concentration time profiles of the partitioned drugs in the organic layer (3.4.3) were successfully correlated with their *in vivo* fraction absorbed concentration time profiles, obtained from published human *in vivo* data. In most cases of the highly lipophilic drugs, a two-compartment model was suitable to predict the *in vivo* pharmacokinetics calculated on the basis of the *in vitro* partitioning profile by convolutional approach from various enabling formulations. Overall, the results indicate that the rationally developed BiPHA+ assay with pH-shift demonstrate a great biorelevance and predictive power. Establishing an IVIVR using the compartment prediction approach is a valuable tool to assess the biphasic model in terms of *in vivo* relevance, and to predict the influence of varying partitioning profiles to plasma profile. Consequently, the BiPHA+ assay is an *in vivo* relevant characterization tool for highly lipophilic and poorly soluble drugs presented in an enabling formulation.

An approach to implement biphasic dissolution data in the PBPK-software tools PK-Sim[®] and GastroPlus[®] was successfully developed. Six model drugs formulated through various enabling formulation approaches demonstrated high prediction accuracies for the *in silico* pharmacokinetic profiles compared to the observed clinical data. The organic partitioning profile was similarly interpreted to the drug release of modified release dosage forms. Therefore, the biphasic partitioning profiles gained by the BiPHA+ assay were implemented likewise modified release dissolution profiles in the PBPK software tools. This led to the advantage, that a deeper mechanistic understanding of precipitation or dissolution was not necessarily needed because these effects were covered by the organic partitioning profile. The models were developed based on easily accessible *in vitro* parameters such as partition coefficients (e.g. logP) and calculated permeability values without considering too much mechanistic details. Hence, a fast model development and pharmacokinetic prediction was feasible. To verify pharmacokinetic predictions, AUC and C_{max} values were correlated with observed *in vivo* data. In the case of a high metabolism, such as nimodipine (first-pass) or fenofibrate

(prodrug), PBPK-models were very helpful to describe these metabolic processes highly relevant. Coupling biphasic dissolution data with *in silico* tools provided meaningful results in terms of pharmacokinetic prediction relevant for early stage pharmaceutical development.

Finally an advanced screening approach for the prediction of the *in vivo* performance in dog of ABT-102 amorphous solid dispersions by using the BiPHa+ model was performed. For this, four amorphous solid dispersions of ABT-102 were investigated in the BiPHa+ assay simulating fasted conditions. In a first step, a level A IVIVR was established to demonstrate the biorelevance of the BiPHa+ model. The *in vivo* plasma concentration time profiles were successfully predicted based on the convolutional approach including compartment models in combination with the organic partitioning profiles. A second prediction method was applied based on PBPK modelling. The organic partitioning profiles were implemented in the same manner as modified release concentration time profiles in the PBPK software PK-Sim® and GastroPlus® leading to accurate *in vivo* plasma concentration time profile predictions. Both the level A IVIVR and the predictions, based on PBPK models and compartment models, demonstrated a high biorelevance for the BiPHa+ assay, which was proven as a powerful tool for formulation screening of poorly soluble drugs. The presented workflows based linked to the BiPHa+ assay can be applied as a potential screening tool to guide formulation selection in the turn of pharmaceutical development.

Overall the rationally developed BiPHa+ biphasic dissolution assay in combination with different prediction approaches demonstrate a remarkable predictive power for a meaningful assessment of various enabling formulation. Especially the identification of the *in vitro* dose was crucial and significantly improved the applicability of the assay. The BiPHa+ assay is potentially applicable from early stage formulation screening to formulation optimization, even if the final dose range is not known. By this, the assay and presented prediction approaches contribute to reduce development risks for preclinical and clinical studies. In addition, the number of animal experiments can potentially be reduced.

5.2 Outlook

The presented BiPHa+ assay has demonstrated high predictive power for many examples and presents a promising approach for the characterization of enabling formulations in terms of their *in vivo* performance. Based on the present work, the BiPHa+ model can be further developed and improved for either a wider range of applications or to generate in-depth mechanistic understanding of the dissolution process of particular formulations.

Moreover, it is possible to further down scale the model into a micro-scale screening technology platform, requiring very small amounts of drug substance while allowing for rapid and meaningful evaluation of prototype enabling formulation approaches.

The identification of the specific *in vitro* dose represents a crucial advance for the BiPHa+ assay and for biphasic assays in general. The successful dose finding indicates that there is may be a relationship between *in vitro* dose, *in vivo* fraction absorbed and the associated AUC. In this context, there is may be the potential to establish a link between the *in vivo* AUC and the *in vitro* data in a way that it is possible to estimate a scaling factor between the *in vitro* dose and the administered dose *in vivo*. Once this link is established, there is the potential to assess the linear dose/AUC proportional range based on *in vitro* data.

Generally, the biphasic assay approach sometimes struggles with flotation formulation and drug substance components at the aqueous/organic interface. An approach to design an absolutely robust system could be to filtrate or extract the dissolution medium by hollow fibre membranes. A membrane bundle is held in the medium. – The membrane bundle is used to filter the aqueous medium by negative pressure or the inside of the membranes is flushed with a suitable organic solvent. The all hollow fibre membranes bundle have a very large surface area together and simultaneously a pore size in the nano-meter range. This ensures that only dissolved drug substance is filtered or extracted by an organic solvent containing hollow fibre and thus the performance of the formulation can be assessed by removing dissolved drug out of the dissolution medium. In a secondary step, the dissolved drug can be collected or extracted by an acceptor compartment. Third, the advantages of such a hollow fibre set-up would be that this model could be integrated into a standard dissolution vessel and the flux limitation as described for biphasic assays could be eliminated by a possible flexibly adjustable filtration/extraction rate and a high surface area of the hollow fibre membrane.

In its future application, the BiPHa+ assay can contribute significantly to a deeper mechanistic understanding of the dissolution behaviour of different enabling formulation

by dynamic characterization of dissolution, precipitation and re-dissolution. Once the mechanisms for the increased solubility / bioavailability of a new drug substance are better understood, formulations can be developed more effectively in a way that either supersaturating systems are designed or rapidly re-dissolving precipitate creating formulations can be generated as described in section 3.3. Both mechanisms can contribute significantly to bioavailability, but depending on the active substance, not all formulation approaches are always possible. For example, different surfactant additives in an ASD could be used to control the properties of the precipitates that are formed, and thus optimize the potential *in vivo* performance in a targeted manner.

References

- [1] C.A. Lipinski, Drug-like properties and the causes of poor solubility and poor permeability, *J. Pharmacol. Toxicol. Methods.* 44 (2000) 235–249. [https://doi.org/10.1016/S1056-8719\(00\)00107-6](https://doi.org/10.1016/S1056-8719(00)00107-6).
- [2] C.A. Lipinski, F. Lombardo, B.W. Dominy, P.J. Feeney, Experimental and computational approaches to estimate solubility and permeability in drug discovery and development settings, *Adv. Drug Deliv. Rev.* 23 (1997) 3–25. [https://doi.org/10.1016/S0169-409X\(96\)00423-1](https://doi.org/10.1016/S0169-409X(96)00423-1).
- [3] Y. Kawabata, K. Wada, M. Nakatani, S. Yamada, S. Onoue, Formulation design for poorly water-soluble drugs based on biopharmaceutics classification system: Basic approaches and practical applications, *Int. J. Pharm.* 420 (2011) 1–10. <https://doi.org/10.1016/j.ijpharm.2011.08.032>.
- [4] H. Pham-The, T. Garrigues, M. Bermejo, I. González-Álvarez, M.C. Monteagudo, M.Á. Cabrera-Pérez, Provisional Classification and *in Silico* Study of Biopharmaceutical System Based on Caco-2 Cell Permeability and Dose Number, *Mol. Pharm.* 10 (2013) 2445–2461. <https://doi.org/10.1021/mp4000585>.
- [5] G.L. Amidon, H. Lennernäs, V.P. Shah, J.R. Crison, A Theoretical Basis for a Biopharmaceutic Drug Classification: The Correlation of *in Vitro* Drug Product Dissolution and *in Vivo* Bioavailability, *Pharm. Res.* 12 (1995) 413–420. <https://doi.org/10.1023/A:1016212804288>.
- [6] ICH Consensus Guideline, ICH M6 BIOPHARMACEUTICS CLASSIFICATION SYSTEM-BASED BIOWAIFERS, (2018). https://www.ich.org/fileadmin/Public_Web_Site/ICH_Products/Guidelines/Multidisciplinary/M9/M9EWG_DraftGuideline_Step2_2018_0606.pdf (accessed August 7, 2019).
- [7] J.M. Butler, J.B. Dressman, The Developability Classification System: Application of Biopharmaceutics Concepts to Formulation Development, *J. Pharm. Sci.* 99 (2010) 4940–4954. <https://doi.org/10.1002/jps.22217>.
- [8] J. Rosenberger, J. Butler, J. Dressman, A Refined Developability Classification System, *J. Pharm. Sci.* 107 (2018) 2020–2032. <https://doi.org/10.1016/j.xphs.2018.03.030>.
- [9] E. Rinaki, G. Valsami, P. Macheras, Quantitative Biopharmaceutics Classification System: The Central Role of Dose/Solubility Ratio, *Pharm. Res.* 20 (2003) 1917–1925. <https://doi.org/10.1023/B:PHAM.0000008037.57884.11>.
- [10] L.Z. Benet, The role of BCS (biopharmaceutics classification system) and BDDCS (biopharmaceutics drug disposition classification system) in drug development, *J. Pharm. Sci.* 102 (2013) 34–42. <https://doi.org/10.1002/jps.23359>.
- [11] Y. Tsume, D.M. Mudie, P. Langguth, G.E. Amidon, G.L. Amidon, The Biopharmaceutics Classification System: Subclasses for *in vivo* predictive dissolution (IPD) methodology and IVIVC, *Eur. J. Pharm. Sci.* 57 (2014) 152–163. <https://doi.org/10.1016/j.ejps.2014.01.009>.
- [12] K. Sugano, K. Terada, Rate- and Extent-Limiting Factors of Oral Drug Absorption: Theory and Applications, *J. Pharm. Sci.* 104 (2015) 2777–2788. <https://doi.org/10.1002/jps.24391>.

-
- [13] J. Rosenberger, J. Butler, U. Muenster, J. Dressman, Application of a Refined Developability Classification System, *J. Pharm. Sci.* 108 (2019) 1090–1100. <https://doi.org/10.1016/j.xphs.2018.10.044>.
- [14] N. Blagden, M. de Matas, P.T. Gavan, P. York, Crystal engineering of active pharmaceutical ingredients to improve solubility and dissolution rates, *Adv. Drug Deliv. Rev.* 59 (2007) 617–630. <https://doi.org/10.1016/j.addr.2007.05.011>.
- [15] A.T.M. Serajuddin, Salt formation to improve drug solubility, *Adv. Drug Deliv. Rev.* 59 (2007) 603–616. <https://doi.org/10.1016/j.addr.2007.05.010>.
- [16] M.-S. Jung, J.-S. Kim, M.-S. Kim, A. Alhalaweh, W. Cho, S.-J. Hwang, S.P. Velaga, Bioavailability of indomethacin-saccharin cocrystals, *J. Pharm. Pharmacol.* 62 (2010) 1560–1568. <https://doi.org/10.1111/j.2042-7158.2010.01189.x>.
- [17] K.T. Savjani, A.K. Gajjar, J.K. Savjani, Drug Solubility: Importance and Enhancement Techniques, *ISRN Pharm.* 2012 (2012) 1–10. <https://doi.org/10.5402/2012/195727>.
- [18] M. Mosharraf, C. Nyström, The effect of particle size and shape on the surface specific dissolution rate of micro-sized practically insoluble drugs, *Int. J. Pharm.* 122 (1995) 35–47. [https://doi.org/10.1016/0378-5173\(95\)00033-F](https://doi.org/10.1016/0378-5173(95)00033-F).
- [19] R.H. Müller, K. Peters, Nanosuspensions for the formulation of poorly soluble drugs: I. Preparation by a size-reduction technique, *Int. J. Pharm.* 160 (1998) 229–237. [https://doi.org/10.1016/S0378-5173\(97\)00311-6](https://doi.org/10.1016/S0378-5173(97)00311-6).
- [20] R. Shegokar, R.H. Müller, Nanocrystals: Industrially feasible multifunctional formulation technology for poorly soluble actives, *Int. J. Pharm.* 399 (2010) 129–139. <https://doi.org/10.1016/j.ijpharm.2010.07.044>.
- [21] L.S. Taylor, G.G.Z. Zhang, Physical chemistry of supersaturated solutions and implications for oral absorption, *Adv. Drug Deliv. Rev.* 101 (2016) 122–142. <https://doi.org/10.1016/j.addr.2016.03.006>.
- [22] T. Reintjes, Solubility Enhancement with BASF Pharma Polymers, 2011.
- [23] M. Rodriguez-Aller, D. Guillarme, J.-L. Veuthey, R. Gurny, Strategies for formulating and delivering poorly water-soluble drugs, *J. Drug Deliv. Sci. Technol.* 30 (2015) 342–351. <https://doi.org/10.1016/j.jddst.2015.05.009>.
- [24] R.G. Strickley, Solubilizing Excipients in Oral and Injectable Formulations, *Pharm. Res.* 21 (2004) 201–230. <https://doi.org/10.1023/B:PHAM.0000016235.32639.23>.
- [25] W. Xu, J. Riikonen, V.-P. Lehto, Mesoporous systems for poorly soluble drugs, *Int. J. Pharm.* 453 (2013) 181–197. <https://doi.org/10.1016/j.ijpharm.2012.09.008>.
- [26] T. Vasconcelos, B. Sarmiento, P. Costa, Solid dispersions as strategy to improve oral bioavailability of poor water soluble drugs, *Drug Discov. Today.* 12 (2007) 1068–1075. <https://doi.org/10.1016/j.drudis.2007.09.005>.
- [27] S. Kumar, S.K. Gupta, P.K. Sharma, Self-Emulsifying Drug Delivery Systems (SEDDS) for Oral Delivery of Lipid Based Formulations - A Review, (2012) 5.
- [28] R.H. Müller, K. Mäder, S. Gohla, Solid lipid nanoparticles (SLN) for controlled drug delivery – a review of the state of the art, *Eur. J. Pharm. Biopharm.* 50 (2000) 161–177. [https://doi.org/10.1016/S0939-6411\(00\)00087-4](https://doi.org/10.1016/S0939-6411(00)00087-4).

- [29] V.J. Stella, R.A. Rajewski, Cyclodextrins: Their Future in Drug Formulation and Delivery, *Pharm. Res.* 14 (1997) 556–567. <https://doi.org/10.1023/A:1012136608249>.
- [30] S.I.F. Badawy, M.A. Hussain, Microenvironmental pH Modulation in Solid Dosage Forms, *J. Pharm. Sci.* 96 (2007) 948–959. <https://doi.org/10.1002/jps.20932>.
- [31] P. Langguth, G. Fricker, H. Wunderli-Allenspach, *Biopharmazie*, John Wiley & Sons, 2012.
- [32] A. Langner, H.-H. Borchert, S. Pfeifer, W. Mehnert, *Biopharmazie: Pharmakokinetik - Bioverfügbarkeit - Biotransformation*; 98 Tab, Wiss. Verlag-Ges., 2011.
- [33] N. Gugeler, U. Klotz, *Einführung in die Pharmakokinetik: pharmakokinetische Grundkenntnisse, Prinzipien und ihre klinische Bedeutung, Terminologie und Tabellen pharmakokinetischer Daten, 2., neubearb. Aufl*, Govi-Verl, Eschborn, 2000.
- [34] M. Vertzoni, P. Augustijns, M. Grimm, M. Koziolk, G. Lemmens, N.J. Parrott, C. Pentafragka, C. Reppas, J. Rubbens, J. Van den Abeele, T. Vanuytsel, W. Weitschies, C.G. Wilson, Impact of regional differences along the gastrointestinal tract of healthy adults on oral drug absorption: An UNGAP review, *Eur. J. Pharm. Sci.* (2019) S0928098719301514. <https://doi.org/10.1016/j.ejps.2019.04.013>.
- [35] J. Van Den Abeele, J. Rubbens, J. Brouwers, P. Augustijns, The dynamic gastric environment and its impact on drug and formulation behaviour, *Eur. J. Pharm. Sci.* 96 (2017) 207–231. <https://doi.org/10.1016/j.ejps.2016.08.060>.
- [36] P.B. Pedersen, P. Vilman, D. Bar-Shalom, A. Müllertz, S. Baldursdottir, Characterization of fasted human gastric fluid for relevant rheological parameters and gastric lipase activities, *Eur. J. Pharm. Biopharm.* 85 (2013) 958–965. <https://doi.org/10.1016/j.ejpb.2013.05.007>.
- [37] M. Koziolk, M. Grimm, D. Becker, V. Iordanov, H. Zou, J. Shimizu, C. Wanke, G. Garbacz, W. Weitschies, Investigation of pH and Temperature Profiles in the GI Tract of Fasted Human Subjects Using the Intellicap® System, *J. Pharm. Sci.* 104 (2015) 2855–2863. <https://doi.org/10.1002/jps.24274>.
- [38] M. Koziolk, F. Schneider, M. Grimm, C. Modeß, A. Seekamp, T. Roustom, W. Siegmund, W. Weitschies, Intra-gastric pH and pressure profiles after intake of the high-caloric, high-fat meal as used for food effect studies, *J. Controlled Release.* 220 (2015) 71–78. <https://doi.org/10.1016/j.jconrel.2015.10.022>.
- [39] D.M. Mudie, K. Murray, C.L. Hoad, S.E. Pritchard, M.C. Garnett, G.L. Amidon, P.A. Gowland, R.C. Spiller, G.E. Amidon, L. Marciani, Quantification of Gastrointestinal Liquid Volumes and Distribution Following a 240 mL Dose of Water in the Fasted State, *Mol. Pharm.* 11 (2014) 3039–3047. <https://doi.org/10.1021/mp500210c>.
- [40] D. Riethorst, R. Mols, G. Duchateau, J. Tack, J. Brouwers, P. Augustijns, Characterization of Human Duodenal Fluids in Fasted and Fed State Conditions, *J. Pharm. Sci.* 105 (2016) 673–681. <https://doi.org/10.1002/jps.24603>.
- [41] L. Marciani, E.F. Cox, C.L. Hoad, S. Pritchard, J.J. Totman, S. Foley, A. Mistry, S. Evans, P.A. Gowland, R.C. Spiller, Postprandial Changes in Small Bowel Water Content

- in Healthy Subjects and Patients With Irritable Bowel Syndrome, *Gastroenterology*. 138 (2010) 469-477.e1. <https://doi.org/10.1053/j.gastro.2009.10.055>.
- [42] C. Pentafragka, M. Symillides, M. McAllister, J. Dressman, M. Vertzoni, C. Reppas, The impact of food intake on the luminal environment and performance of oral drug products with a view to in vitro and in silico simulations: a PEARRL review, *J. Pharm. Pharmacol.* 71 (2019) 557–580. <https://doi.org/10.1111/jphp.12999>.
- [43] M. Drozdik, D. Busch, J. Lapczuk, J. Müller, M. Ostrowski, M. Kurzawski, S. Oswald, Protein Abundance of Clinically Relevant Drug-Metabolizing Enzymes in the Human Liver and Intestine: A Comparative Analysis in Paired Tissue Specimens, *Clin. Pharmacol. Ther.* 104 (2018) 515–524. <https://doi.org/10.1002/cpt.967>.
- [44] A. Galetin, M. Gertz, J. Brian Houston, Contribution of Intestinal Cytochrome P450-Mediated Metabolism to Drug-Drug Inhibition and Induction Interactions, *Drug Metab. Pharmacokinet.* 25 (2010) 28–47. <https://doi.org/10.2133/dmpk.25.28>.
- [45] A. Mitra, F. Kesisoglou, M. Beauchamp, W. Zhu, F. Chiti, Y. Wu, Using Absorption Simulation and Gastric pH Modulated Dog Model for Formulation Development To Overcome Achlorhydria Effect, *Mol. Pharm.* 8 (2011) 2216–2223. <https://doi.org/10.1021/mp200062a>.
- [46] M. Koziolok, M. Grimm, T. Bollmann, K.J. Schäfer, S.M. Blattner, R. Lotz, G. Boeck, W. Weitschies, Characterization of the GI transit conditions in Beagle dogs with a telemetric motility capsule, *Eur. J. Pharm. Biopharm.* 136 (2019) 221–230. <https://doi.org/10.1016/j.ejpb.2019.01.026>.
- [47] H. Musther, A. Olivares-Morales, O.J.D. Hatley, B. Liu, A. Rostami Hodjegan, Animal versus human oral drug bioavailability: Do they correlate?, *Eur. J. Pharm. Sci.* 57 (2014) 280–291. <https://doi.org/10.1016/j.ejps.2013.08.018>.
- [48] H.A. Schiffter, *Pharmakokinetik - Modelle und Berechnungen: mit 25 Tabellen*, Wiss. Verlag-Ges., 2009.
- [49] R.C. Rowe, P.J. Sheskey, S.C. Owen, American Pharmacists Association, eds., *Handbook of pharmaceutical excipients: edited by Raymond C. Rowe, Paul J. Sheskey, Siân C. Owen, 5th ed*, Pharmaceutical Press ; American Pharmacists Association, London ; Greyslake, IL : Washington, DC, 2006.
- [50] S.T. Buckley, K.J. Frank, G. Fricker, M. Brandl, Biopharmaceutical classification of poorly soluble drugs with respect to “enabling formulations,” *Eur. J. Pharm. Sci.* 50 (2013) 8–16. <https://doi.org/10.1016/j.ejps.2013.04.002>.
- [51] A.S. Indulkar, X. Lou, G.G.Z. Zhang, L.S. Taylor, Insights into the Dissolution Mechanism of Ritonavir–Copovidone Amorphous Solid Dispersions: Importance of Congruent Release for Enhanced Performance, *Mol. Pharm.* 16 (2019) 1327–1339. <https://doi.org/10.1021/acs.molpharmaceut.8b01261>.
- [52] K.C. Johnson, Comparison of Methods for Predicting Dissolution and the Theoretical Implications of Particle-Size-Dependent Solubility, *J. Pharm. Sci.* 101 (2012) 681–689. <https://doi.org/10.1002/jps.22778>.
- [53] J. Brouwers, M.E. Brewster, P. Augustijns, Supersaturating Drug Delivery Systems: The Answer to Solubility-Limited Oral Bioavailability?, *J. Pharm. Sci.* 98 (2009) 2549–2572. <https://doi.org/10.1002/jps.21650>.

-
- [54] K.J. Frank, K.M. Rosenblatt, U. Westedt, P. Hölig, J. Rosenberg, M. Mägerlein, G. Fricker, M. Brandl, Amorphous solid dispersion enhances permeation of poorly soluble ABT-102: True supersaturation vs. apparent solubility enhancement, *Int. J. Pharm.* 437 (2012) 288–293. <https://doi.org/10.1016/j.ijpharm.2012.08.014>.
- [55] K.G. Wagner, Perorale Retardarzneiformen, *Pharmakon.* (2016) 107–116. <https://doi.org/10.1691/pn.20160013>.
- [56] C.K. Brown, H.P. Chokshi, B. Nickerson, R.A. Reed, B.R. Rohrs, P.A. Shah, Acceptable Analytical Practices for Dissolution Testing of Poorly Soluble Compounds, *Dissolution Technol.* 12 (2005) 6–12. <https://doi.org/10.14227/DT120405P6>.
- [57] H. Grady, D. Elder, G.K. Webster, Y. Mao, Y. Lin, T. Flanagan, J. Mann, A. Blanchard, M.J. Cohen, J. Lin, F. Kesisoglou, A. Hermans, A. Abend, L. Zhang, D. Curran, Industry's View on Using Quality Control, Biorelevant, and Clinically Relevant Dissolution Tests for Pharmaceutical Development, Registration, and Commercialization, *J. Pharm. Sci.* 107 (2018) 34–41. <https://doi.org/10.1016/j.xphs.2017.10.019>.
- [58] D.J. Phillips, S.R. Pygall, V.B. Cooper, J.C. Mann, Overcoming sink limitations in dissolution testing: a review of traditional methods and the potential utility of biphasic systems: Dissolution testing: biphasic systems, *J. Pharm. Pharmacol.* 64 (2012) 1549–1559. <https://doi.org/10.1111/j.2042-7158.2012.01523.x>.
- [59] USP 42 - NF 37 The United States Pharmacopeia and National Formulary 2019: Main Edition Plus Supplements 1 and 2, Deutscher Apotheker Verlag, 2018.
- [60] Europäisches Arzneibuch Digital, 9. Ausgabe, 1. Nachtrag: Amtliche deutsche Ausgabe (Ph. Eur. 9.1)., Deutscher Apotheker Verlag, 2018.
- [61] C. Markopoulos, C.J. Andreas, M. Vertzoni, J. Dressman, C. Reppas, In-vitro simulation of luminal conditions for evaluation of performance of oral drug products: Choosing the appropriate test media, *Eur. J. Pharm. Biopharm.* 93 (2015) 173–182. <https://doi.org/10.1016/j.ejpb.2015.03.009>.
- [62] M. Koziolk, G. Garbacz, M. Neumann, W. Weitschies, Simulating the Postprandial Stomach: Biorelevant Test Methods for the Estimation of Intragastric Drug Dissolution, *Mol. Pharm.* 10 (2013) 2211–2221. <https://doi.org/10.1021/mp300607e>.
- [63] Y. Shono, E. Jantratid, F. Kesisoglou, C. Reppas, J.B. Dressman, Forecasting in vivo oral absorption and food effect of micronized and nanosized aprepitant formulations in humans, *Eur. J. Pharm. Biopharm.* 76 (2010) 95–104. <https://doi.org/10.1016/j.ejpb.2010.05.009>.
- [64] J. Butler, B. Hens, M. Vertzoni, J. Brouwers, P. Berben, J. Dressman, C.J. Andreas, K.J. Schaefer, J. Mann, M. McAllister, M. Jamei, E. Kostewicz, F. Kesisoglou, P. Langguth, M. Minekus, A. Müllertz, R. Schilderink, M. Koziolk, P. Jedamzik, W. Weitschies, C. Reppas, P. Augustijns, In vitro models for the prediction of in vivo performance of oral dosage forms: Recent progress from partnership through the IMI OrBiTo collaboration, *Eur. J. Pharm. Biopharm.* 136 (2019) 70–83. <https://doi.org/10.1016/j.ejpb.2018.12.010>.

- [65] A. Pestieau, B. Evrard, In vitro biphasic dissolution tests and their suitability for establishing in vitro-in vivo correlations: A historical review, *Eur. J. Pharm. Sci.* 102 (2017) 203–219. <https://doi.org/10.1016/j.ejps.2017.03.019>.
- [66] E.S. Kostewicz, B. Abrahamsson, M. Brewster, J. Brouwers, J. Butler, S. Carlert, P.A. Dickinson, J. Dressman, R. Holm, S. Klein, J. Mann, M. McAllister, M. Minekus, U. Muenster, A. Müllertz, M. Verwei, M. Vertzoni, W. Weitschies, P. Augustijns, In vitro models for the prediction of in vivo performance of oral dosage forms, *Eur. J. Pharm. Sci.* 57 (2014) 342–366. <https://doi.org/10.1016/j.ejps.2013.08.024>.
- [67] K.J. Frank, K. Locher, D.E. Zecevic, J. Fleth, K.G. Wagner, In vivo predictive mini-scale dissolution for weak bases: Advantages of pH-shift in combination with an absorptive compartment, *Eur. J. Pharm. Sci.* 61 (2014) 32–39. <https://doi.org/10.1016/j.ejps.2013.12.015>.
- [68] H. Xu, S. Vela, Y. Shi, P. Marroum, P. Gao, In Vitro Characterization of Ritonavir Drug Products and Correlation to Human in Vivo Performance, *Mol. Pharm.* 14 (2017) 3801–3814. <https://doi.org/10.1021/acs.molpharmaceut.7b00552>.
- [69] A. Pestieau, S. Lebrun, B. Cahay, A. Brouwers, B. Streel, J.-M. Cardot, B. Evrard, Evaluation of different in vitro dissolution tests based on level A in vitro–in vivo correlations for fenofibrate self-emulsifying lipid-based formulations, *Eur. J. Pharm. Biopharm.* 112 (2017) 18–29. <https://doi.org/10.1016/j.ejpb.2016.10.030>.
- [70] K. Locher, J.M. Borghardt, H. Wachtel, K.J. Schaefer, K.G. Wagner, Mechanistic study on hydrodynamics in the mini-scale biphasic dissolution model and its influence on in vitro dissolution and partitioning, *Eur. J. Pharm. Sci.* 124 (2018) 328–338. <https://doi.org/10.1016/j.ejps.2018.09.005>.
- [71] D.M. Mudie, Y. Shi, H. Ping, P. Gao, G.L. Amidon, G.E. Amidon, Mechanistic analysis of solute transport in an in vitro physiological two-phase dissolution apparatus, *Biopharm. Drug Dispos.* 33 (2012) 378–402. <https://doi.org/10.1002/bdd.1803>.
- [72] U. Heigoldt, F. Sommer, R. Daniels, K.-G. Wagner, Predicting in vivo absorption behavior of oral modified release dosage forms containing pH-dependent poorly soluble drugs using a novel pH-adjusted biphasic in vitro dissolution test, *Eur. J. Pharm. Biopharm.* 76 (2010) 105–111. <https://doi.org/10.1016/j.ejpb.2010.05.006>.
- [73] J.S. Grundy, K.E. Anderson, J.A. Rogers, R.T. Foster, Studies on dissolution testing of the nifedipine gastrointestinal therapeutic system. I. Description of a two-phase in vitro dissolution test, *J. Controlled Release.* 48 (1997) 1–8. [https://doi.org/10.1016/S0168-3659\(97\)00064-3](https://doi.org/10.1016/S0168-3659(97)00064-3).
- [74] FDA, Guidance for Industry Extended Release Oral Dosage Forms: Development, Evaluation, and Application of In Vitro/In Vivo Correlations, (1997).
- [75] N. Kaur, A. Narang, A.K. Bansal, Use of biorelevant dissolution and PBPK modeling to predict oral drug absorption, *Eur. J. Pharm. Biopharm.* 129 (2018) 222–246. <https://doi.org/10.1016/j.ejpb.2018.05.024>.
- [76] E.S. Kostewicz, L. Aarons, M. Bergstrand, M.B. Bolger, A. Galetin, O. Hatley, M. Jamei, R. Lloyd, X. Pepin, A. Rostami-Hodjegan, E. Sjögren, C. Tannergren, D.B. Turner, C. Wagner, W. Weitschies, J. Dressman, PBPK models for the prediction of in

- vivo performance of oral dosage forms, *Eur. J. Pharm. Sci.* 57 (2014) 300–321. <https://doi.org/10.1016/j.ejps.2013.09.008>.
- [77] M. Berlin, A. Ruff, F. Kesisoglou, W. Xu, M.H. Wang, J.B. Dressman, Advances and challenges in PBPK modeling – Analysis of factors contributing to the oral absorption of atazanavir, a poorly soluble weak base, *Eur. J. Pharm. Biopharm.* 93 (2015) 267–280. <https://doi.org/10.1016/j.ejpb.2015.03.031>.
- [78] E. Sjögren, H. Thörn, C. Tannergren, In Silico Modeling of Gastrointestinal Drug Absorption: Predictive Performance of Three Physiologically Based Absorption Models, *Mol. Pharm.* 13 (2016) 1763–1778. <https://doi.org/10.1021/acs.molpharmaceut.5b00861>.
- [79] V. Rastogi, P. Yadav, N. Lal, P. Rastogi, B.K. Singh, N. Verma, A. Verma, Mathematical prediction of pharmacokinetic parameters-an in-vitro approach for investigating pharmaceutical products for IVIVC, *Future J. Pharm. Sci.* 4 (2018) 175–184. <https://doi.org/10.1016/j.fjps.2018.03.001>.
- [80] M.A. Nguyen, T. Flanagan, M. Brewster, F. Kesisoglou, S. Beato, J. Biewenga, J. Crison, R. Holm, R. Li, E. Mannaert, M. McAllister, M. Mueller-Zsigmondy, U. Muenster, K. Ojala, S. Page, A. Parr, S. Rossenu, P. Timmins, A. Van Peer, A. Vermeulen, P. Langguth, A survey on IVIVC/IVIVR development in the pharmaceutical industry – Past experience and current perspectives, *Eur. J. Pharm. Sci.* 102 (2017) 1–13. <https://doi.org/10.1016/j.ejps.2017.02.029>.
- [81] K. Locher, J.M. Borghardt, K.J. Frank, C. Kloft, K.G. Wagner, Evolution of a mini-scale biphasic dissolution model: Impact of model parameters on partitioning of dissolved API and modelling of in vivo-relevant kinetics, *Eur. J. Pharm. Biopharm.* 105 (2016) 166–175. <https://doi.org/10.1016/j.ejpb.2016.06.008>.
- [82] H. Xu, S. Krakow, Y. Shi, J. Rosenberg, P. Gao, In vitro characterization of ritonavir formulations and correlation to in vivo performance in dogs., *Eur. J. Pharm. Sci. Off. J. Eur. Fed. Pharm. Sci.* 115 (2018) 286–295. <https://doi.org/10.1016/j.ejps.2018.01.026>.
- [83] H. Xu, Y. Shi, S. Vela, P. Marroum, P. Gao, Developing Quantitative In Vitro – In Vivo Correlation for Fenofibrate Immediate-Release Formulations With the Biphasic Dissolution-Partition Test Method, *J. Pharm. Sci.* 107 (2018) 476–487. <https://doi.org/10.1016/j.xphs.2017.06.018>.
- [84] H. Xu, W. Wang, Y. Shi, P. Gao, Characterization of the Partition Rate of Ibuprofen Across the Water-Octanol Interface and the Influence of Common Pharmaceutical Excipients, *J. Pharm. Sci.* 108 (2019) 525–537. <https://doi.org/10.1016/j.xphs.2018.11.026>.
- [85] J.B. Dressman, G.L. Amidon, C. Reppas, V.P. Shah, Dissolution Testing as a Prognostic Tool for Oral Drug Absorption: Immediate Release Dosage Forms, *Pharm. Res.* 15 (1998) 11–22. <https://doi.org/10.1023/A:1011984216775>.
- [86] J.E. Boni, R.S. Brickl, J. Dressman, Is bicarbonate buffer suitable as a dissolution medium?, *J. Pharm. Pharmacol.* 59 (2007) 1375–1382. <https://doi.org/10.1211/jpp.59.10.0007>.

- [87] T.C. McIlvaine, A Buffer Solution for Colorimetric Comparison, *J. Biol. Chem.* 49 (1921) 183–186.
- [88] A. Fuchs, J.B. Dressman, Composition and Physicochemical Properties of Fasted-State Human Duodenal and Jejunal Fluid: A Critical Evaluation of the Available Data, *J. Pharm. Sci.* 103 (2014) 3398–3411. <https://doi.org/10.1002/jps.24183>.
- [89] H.M. Bloch, J.R. Thornton, K.W. Heaton, Effects of fasting on the composition of gallbladder bile., *Gut.* 21 (1980) 1087–1089. <https://doi.org/10.1136/gut.21.12.1087>.
- [90] M. Marques, Dissolution Media Simulating Fasted and Fed States, *Dissolution Technol.* 11 (2004) 16–16. <https://doi.org/10.14227/DT110204P16>.
- [91] R.N. Smith, C. Hansch, M.M. Ames, Selection of a reference partitioning system for drug design work, *J. Pharm. Sci.* 64 (1975) 599–606. <https://doi.org/10.1002/jps.2600640405>.
- [92] K. Kinoshita, H. Ishikawa, K. Shinoda, Solubility of Alcohols in Water Determined the Surface Tension Measurements, *Bull. Chem. Soc. Jpn.* 31 (1958) 1081–1082. <https://doi.org/10.1246/bcsj.31.1081>.
- [93] D. Law, E.A. Schmitt, K.C. Marsh, E.A. Everitt, W. Wang, J.J. Fort, S.L. Krill, Y. Qiu, Ritonavir–PEG 8000 Amorphous Solid Dispersions: In vitro and In vivo Evaluations, *J. Pharm. Sci.* 93 (2004) 563–570. <https://doi.org/10.1002/jps.10566>.
- [94] J.M.O. Pinto, A.F.C. Rengifo, C. Mendes, A.F. Leão, A.L. Parize, H.K. Stulzer, Understanding the interaction between Soluplus® and biorelevant media components, *Colloids Surf. B Biointerfaces.* 187 (2020) 110673. <https://doi.org/10.1016/j.colsurfb.2019.110673>.
- [95] Y. Sun, A. Deac, G.G.Z. Zhang, Assessing Physical Stability of Colloidal Dispersions Using a Turbiscan Optical Analyzer, *Mol. Pharm.* 16 (2019) 877–885. <https://doi.org/10.1021/acs.molpharmaceut.8b01194>.
- [96] K.J. Frank, U. Westedt, K.M. Rosenblatt, P. Hölig, J. Rosenberg, M. Mägerlein, G. Fricker, M. Brandl, The amorphous solid dispersion of the poorly soluble ABT-102 forms nano/microparticulate structures in aqueous medium: impact on solubility, *Int. J. Nanomedicine.* 7 (2012) 5757–5768. <https://doi.org/10.2147/IJN.S36571>.
- [97] G.A. Ilevbare, L.S. Taylor, Liquid–Liquid Phase Separation in Highly Supersaturated Aqueous Solutions of Poorly Water-Soluble Drugs: Implications for Solubility Enhancing Formulations, *Cryst. Growth Des.* 13 (2013) 1497–1509. <https://doi.org/10.1021/cg301679h>.
- [98] E. Deneau, G. Steele, An In-Line Study of Oiling Out and Crystallization, *Org. Process Res. Dev.* 9 (2005) 943–950. <https://doi.org/10.1021/op050107c>.
- [99] I. Tho, B. Liepold, J. Rosenberg, M. Maegerlein, M. Brandl, G. Fricker, Formation of nano/micro-dispersions with improved dissolution properties upon dispersion of ritonavir melt extrudate in aqueous media, *Eur. J. Pharm. Sci.* 40 (2010) 25–32. <https://doi.org/10.1016/j.ejps.2010.02.003>.
- [100] D.R. Ely, R. Edwin García, M. Thommes, Ostwald–Freundlich diffusion-limited dissolution kinetics of nanoparticles, *Powder Technol.* 257 (2014) 120–123. <https://doi.org/10.1016/j.powtec.2014.01.095>.

- [101] Tharwat F. Tadros, *Nanodispersions*, De Gruyter Graduate, Berlin, Germany, 2016. <https://www.degruyter.com/downloadpdf/books/9783110290349/9783110290349-fm/9783110290349-fm.pdf> (accessed April 24, 2019).
- [102] C. Solans, P. Izquierdo, J. Nolla, N. Azemar, M. Garciacelma, *Nano-emulsions*, *Curr. Opin. Colloid Interface Sci.* 10 (2005) 102–110. <https://doi.org/10.1016/j.cocis.2005.06.004>.
- [103] O. Hirlak, S. Dieluweit, R. Merkel, K.G. Wagner, *Polymer-mediated drug supersaturation – A spotlight on the interplay between phase-separated amorphous drug colloids and dissolved molecules*, *J. Colloid Interface Sci.* 603 (2021) 370–379. <https://doi.org/10.1016/j.jcis.2021.06.089>.
- [104] G. Pahomi, G. Corlan, R. Sandulovici, *Study of the influence of bile salts and lecithin on distribution of ketoconazole between plasma and methylene chloride*, *Farmacia.* 60 (2012) 13.
- [105] P. Bardi, *Nimodipine: Drug pharmacokinetics and plasma adenosine levels in patients affected by cerebral ischemia*, *Clin. Pharmacol. Ther.* 72 (2002) 556–561. <https://doi.org/10.1067/mcp.2002.128127>.
- [106] A.K. Majumdar, L. Howard, M.R. Goldberg, L. Hickey, M. Constanzer, P.L. Rothenberg, T.M. Crumley, D. Panebianco, T.E. Bradstreet, A.J. Bergman, S.A. Waldman, H.E. Greenberg, K. Butler, A. Knops, I. De Lepeleire, N. Michiels, K.J. Petty, *Pharmacokinetics of Aprepitant After Single and Multiple Oral Doses in Healthy Volunteers*, *J. Clin. Pharmacol.* 46 (2006) 291–300. <https://doi.org/10.1177/0091270005283467>.
- [107] S.K. Paulson, M.B. Vaughn, S.M. Jessen, Y. Lawal, C.J. Gresk, B. Yan, T.J. Maziasz, C.S. Cook, A. Karim, *Pharmacokinetics of Celecoxib after Oral Administration in Dogs and Humans: Effect of Food and Site of Absorption*, *J. Pharmacol. Exp. Ther.* 297 (2001) 638–645.
- [108] T. Zhu, J.-C. Ansquer, M.T. Kelly, D.J. Sleep, R.S. Pradhan, *Comparison of the Gastrointestinal Absorption and Bioavailability of Fenofibrate and Fenofibric Acid in Humans*, *J. Clin. Pharmacol.* 50 (2010) 914–921. <https://doi.org/10.1177/0091270009354995>.
- [109] R. Sauron, M. Wilkins, V. Jessent, A. Dubois, C. Maillot, A. Weil, *Absence of a food effect with a 145 mg nanoparticle fenofibrate tablet formulation*, *Int. J. Clin. Pharmacol. Ther.* 44 (2006) 64–70. <https://doi.org/10.5414/CPP44064>.
- [110] SPORANOX® (itraconazole) Capsules, (n.d.). https://www.accessdata.fda.gov/drugsatfda_docs/label/2012/020083s048s049s050l.bl.pdf (accessed August 6, 2018).
- [111] SPORANOX® (itraconazole) Oral Solution, FDA, 2011. https://www.accessdata.fda.gov/drugsatfda_docs/label/2011/020657s025l.bl.pdf (accessed August 6, 2018).
- [112] A. Denninger, U. Westedt, J. Rosenberg, K.G. Wagner, *A Rational Design of a Biphasic Dissolution Setup—Modelling of Biorelevant Kinetics for a Ritonavir Hot-Melt Extruded Amorphous Solid Dispersion*, *Pharmaceutics.* 12 (2020) 237. <https://doi.org/10.3390/pharmaceutics12030237>.

- [113] M.M. Knopp, J.H. Nguyen, C. Becker, N.M. Francke, E.B. Jørgensen, P. Holm, R. Holm, H. Mu, T. Rades, P. Langguth, Influence of polymer molecular weight on in vitro dissolution behavior and in vivo performance of celecoxib:PVP amorphous solid dispersions, *Eur. J. Pharm. Biopharm.* 101 (2016) 145–151. <https://doi.org/10.1016/j.ejpb.2016.02.007>.
- [114] M. Van Speybroeck, R. Mols, R. Mellaerts, T.D. Thi, J.A. Martens, J.V. Humbeeck, P. Annaert, G.V. den Mooter, P. Augustijns, Combined use of ordered mesoporous silica and precipitation inhibitors for improved oral absorption of the poorly soluble weak base itraconazole, *Eur. J. Pharm. Biopharm.* 75 (2010) 354–365. <https://doi.org/10.1016/j.ejpb.2010.04.009>.
- [115] M. Monschke, K.G. Wagner, Amorphous solid dispersions of weak bases with pH-dependent soluble polymers to overcome limited bioavailability due to gastric pH variability – An in-vitro approach, *Int. J. Pharm.* 564 (2019) 162–170. <https://doi.org/10.1016/j.ijpharm.2019.04.034>.
- [116] S.A. Raina, B. Van Eerdenbrugh, D.E. Alonzo, H. Mo, G.G.Z. Zhang, Y. Gao, L.S. Taylor, Trends in the Precipitation and Crystallization Behavior of Supersaturated Aqueous Solutions of Poorly Water-Soluble Drugs Assessed Using Synchrotron Radiation, *J. Pharm. Sci.* 104 (2015) 1981–1992. <https://doi.org/10.1002/jps.24423>.
- [117] S. Rathi, R.B. Chavan, N.R. Shastri, Classification of the crystallization tendency of active pharmaceutical ingredients (APIs) and nutraceuticals based on their nucleation and crystal growth behaviour in solution state, *Drug Deliv. Transl. Res.* (2019). <https://doi.org/10.1007/s13346-019-00663-w>.
- [118] D. Sironi, J. Rosenberg, A. Bauer-Brandl, M. Brandl, Dynamic dissolution-/permeation-testing of nano- and microparticle formulations of fenofibrate, *Eur. J. Pharm. Sci.* 96 (2017) 20–27. <https://doi.org/10.1016/j.ejps.2016.09.001>.
- [119] Y. Shono, E. Jantratid, N. Janssen, F. Kesisoglou, Y. Mao, M. Vertzoni, C. Reppas, J.B. Dressman, Prediction of food effects on the absorption of celecoxib based on biorelevant dissolution testing coupled with physiologically based pharmacokinetic modeling, *Eur. J. Pharm. Biopharm.* 73 (2009) 107–114. <https://doi.org/10.1016/j.ejpb.2009.05.009>.
- [120] M.J. Chapman, Pharmacology of fenofibrate, *Am. J. Med.* 83 (1987) 21–25. [https://doi.org/10.1016/0002-9343\(87\)90867-9](https://doi.org/10.1016/0002-9343(87)90867-9).
- [121] Y. Fei, E.S. Kostewicz, M.-T. Sheu, J.B. Dressman, Analysis of the enhanced oral bioavailability of fenofibrate lipid formulations in fasted humans using an in vitro–in silico–in vivo approach, *Eur. J. Pharm. Biopharm.* 85 (2013) 1274–1284. <https://doi.org/10.1016/j.ejpb.2013.03.001>.
- [122] J.-M. Cardot, B.M. Davit, In vitro–In Vivo Correlations: Tricks and Traps, *AAPS J.* 14 (2012) 491–499. <https://doi.org/10.1208/s12248-012-9359-0>.
- [123] Bayer Vital GmbH Geschäftsbereich Pharma, Fachinformation: Nimotop®, 30 mg, Filmtabletten, (2014).
- [124] M. Simeoni, Guideline on the pharmacokinetic and clinical evaluation of modified release dosage forms (EMA/CPMP/EWP/280/96 Corr1), (2014) 46.

- [125] EMA, Guideline on the investigation of bioequivalence, (2010). https://www.ema.europa.eu/en/documents/scientific-guideline/guideline-investigation-bioequivalence-rev1_en.pdf (accessed August 29, 2019).
- [126] A. Denninger, U. Westedt, K.G. Wagner, Shared IVIVR for Five Commercial Enabling Formulations Using the BiPha+ Biphasic Dissolution Assay, *Pharmaceutics*. 13 (2021) 285. <https://doi.org/10.3390/pharmaceutics13020285>.
- [127] S.M. Pathak, K.J. Schaefer, M. Jamei, D.B. Turner, Biopharmaceutic IVIVE—Mechanistic Modeling of Single- and Two-Phase In Vitro Experiments to Obtain Drug-Specific Parameters for Incorporation Into PBPK Models, *J. Pharm. Sci.* (2018). <https://doi.org/10.1016/j.xphs.2018.11.034>.
- [128] K. Thelen, K. Coboeken, S. Willmann, R. Burghaus, J.B. Dressman, J. Lippert, Evolution of a detailed physiological model to simulate the gastrointestinal transit and absorption process in humans, Part 1: Oral solutions, *J. Pharm. Sci.* 100 (2011) 5324–5345. <https://doi.org/10.1002/jps.22726>.
- [129] D.B. Miller, J.D. Spence, Clinical Pharmacokinetics of Fibric Acid Derivatives (Fibrates);, *Clin. Pharmacokinet.* 34 (1998) 155–162. <https://doi.org/10.2165/00003088-199834020-00003>.
- [130] Agilent, 989-7668EN, (2007). <http://citeseerx.ist.psu.edu/viewdoc/download?doi=10.1.1.615.4436&rep=rep1&type=pdf> (accessed March 25, 2019).
- [131] Open Systems Pharmacology Suite Community, Open Systems Pharmacology Suite Manual, Version 7.0, 2017.
- [132] J.-F. Schlender, D. Teutonico, K. Coboeken, K. Schnizler, T. Eissing, S. Willmann, U. Jaehde, H. Stass, A Physiologically-Based Pharmacokinetic Model to Describe Ciprofloxacin Pharmacokinetics Over the Entire Span of Life, *Clin. Pharmacokinet.* 57 (2018) 1613–1634. <https://doi.org/10.1007/s40262-018-0661-6>.
- [133] K. Abduljalil, T. Cain, H. Humphries, A. Rostami-Hodjegan, Deciding on Success Criteria for Predictability of Pharmacokinetic Parameters from In Vitro Studies: An Analysis Based on In Vivo Observations, *Drug Metab. Dispos.* 42 (2014) 1478–1484. <https://doi.org/10.1124/dmd.114.058099>.
- [134] J. You, F. Cui, Y. Wang, Y. Yu, X. Li, Q. Li, The study of the emulsification efficiency of Aerosil and HPMCAS type and their ratio to stabilize emulsions of zedoary turmeric oil, *Colloids Surf. Physicochem. Eng. Asp.* 280 (2006) 76–80. <https://doi.org/10.1016/j.colsurfa.2006.01.034>.
- [135] W. McMahon, H.A. Birdsall, G.R. Johnson, C.T. Camilli, Degradation Studies of Polyethylene Terephthalate., *J. Chem. Eng. Data.* 4 (1959) 57–79. <https://doi.org/10.1021/je60001a009>.
- [136] D. Schönherr, U. Wollatz, D. Haznar-Garbacz, U. Hanke, K.J. Box, R. Taylor, R. Ruiz, S. Beato, D. Becker, W. Weitschies, Characterisation of selected active agents regarding pKa values, solubility concentrations and pH profiles by SiriusT3, *Eur. J. Pharm. Biopharm.* 92 (2015) 155–170. <https://doi.org/10.1016/j.ejpb.2015.02.028>.

- [137] AbbVie Ltd, Fachinformation Norvir 100mg Filmtablette, (2017). <https://www.fachinfo.de/pdf/012355#view=FitH&pagemode=none&toolbar=1&statubar=0&messages=0&navpanes=0> (accessed May 5, 2017).
- [138] Y. Shi, P. Gao, Y. Gong, H. Ping, Application of a Biphasic Test for Characterization of In Vitro Drug Release of Immediate Release Formulations of Celecoxib and Its Relevance to In Vivo Absorption, *Mol. Pharm.* 7 (2010) 1458–1465. <https://doi.org/10.1021/mp100114a>.
- [139] P. Sieger, Y. Cui, S. Scheuerer, pH-dependent solubility and permeability profiles: A useful tool for prediction of oral bioavailability, *Eur. J. Pharm. Sci.* 105 (2017) 82–90. <https://doi.org/10.1016/j.ejps.2017.04.016>.
- [140] B. Testa, P. Crivori, M. Reist, P.-A. Carrupt, The influence of lipophilicity on the pharmacokinetic behavior of drugs: Concepts and examples, (n.d.) 33.
- [141] M. Schwab, ed., CELEBREX® (celecoxib), *Encycl. Cancer.* (2016) 2609–2609. https://doi.org/10.1007/978-3-662-46875-3_100050.
- [142] J.A. Barone, J.G. Koh, R.H. Bierman, J.L. Colaizzi, K.A. Swanson, M.C. Gaffar, B.L. Moskovitz, W. Mechlinski, V.V. de Velde, Food interaction and steady-state pharmacokinetics of itraconazole capsules in healthy male volunteers., *Antimicrob. Agents Chemother.* 37 (1993) 778–784. <https://doi.org/10.1128/AAC.37.4.778>.
- [143] C. Klein, J. Ng, D. Kim, Y. Chui, W. Awni, J. Morris, T. Podsadecki, Y. Cui, B. Bernstein, The effect of food on ritonavir bioavailability following administration of ritonavir 100 mg film-coated tablet in healthy adult subjects, *J. Int. AIDS Soc.* 11 (2008) P247. <https://doi.org/10.1186/1758-2652-11-S1-P247>.
- [144] M. Ostrowski, T. Baczek, E. Wilkowska, The Influence of Averaging Procedure on the Accuracy of IVIVC Predictions: Immediate Release Dosage Form Case Study, *J. Pharm. Sci.* 99 (2010) 5040–5045. <https://doi.org/10.1002/jps.22209>.
- [145] P. Buchwald, Direct, differential-equation-based in-vitro–in-vivo correlation (IVIVC) method, *J. Pharm. Pharmacol.* 55 (2003) 495–504. <https://doi.org/10.1211/002235702847>.
- [146] MSD SHARP & DOHME GMBH, Fachinformation Emend, (n.d.). <https://www.msd.de/fileadmin/files/fachinformationen/emend.pdf> (accessed April 3, 2019).
- [147] Fachinfo CELEBREX® 100 mg/200 mg Hartkapseln, (2017) 8.
- [148] S.K. PAULSON, M.B. VAUGHN, S.M. JESSEN, Y. LAWAL, C.J. GRESK, B. YAN, T.J. MAZIASZ, C.S. COOK, A. KARIM, Pharmacokinetics of Celecoxib after Oral Administration in Dogs and Humans: Effect of Food and Site of Absorption, (n.d.) 8.
- [149] A. Pal, S. Shenoy, A. Gautam, S. Munjal, J. Niu, M. Gopalakrishnan, J. Gobburru, Pharmacokinetics of DFN-15, a Novel Oral Solution of Celecoxib, Versus Celecoxib 400-mg Capsules: A Randomized Crossover Study in Fasting Healthy Volunteers, *Clin. Drug Investig.* 37 (2017) 937–946. <https://doi.org/10.1007/s40261-017-0548-6>.
- [150] T. Grabowski, A. Świerczewska, B. Borucka, R. Sawicka, M. Sasinowska-Motyl, S.W. Gumulka, Chromatographic/Mass Spectrometric Method for the Estimation of Itraconazole and its Metabolite in Human Plasma, *Arzneimittelforschung.* 59 (2009) 422–428. <https://doi.org/10.1055/s-0031-1296418>.

- [151] S.M. Abdel-Rahman, R.F. Jacobs, J. Massarella, R.E. Kauffman, J.S. Bradley, H.C. Kimko, G.L. Kearns, K. Shalayda, C. Curtin, S.D. Maldonado, J.L. Blumer, Single-Dose Pharmacokinetics of Intravenous Itraconazole and Hydroxypropyl-β-Cyclodextrin in Infants, Children, and Adolescents, *Antimicrob. Agents Chemother.* 51 (2007) 2668–2673. <https://doi.org/10.1128/AAC.00297-07>.
- [152] J.A. Barone, J.L. Colaizzi, Food Interaction and Steady-State Pharmacokinetics of Itraconazole Oral Solution in Healthy Volunteers, 18 (1998) 7.
- [153] A.H. Salem, Y.-L. Chiu, J.M. Valdes, A.M. Nilius, C.E. Klein, A novel ritonavir paediatric powder formulation is bioequivalent to ritonavir oral solution with a similar food effect, *Antivir. Ther.* 20 (2015) 425–432. <https://doi.org/10.3851/IMP2932>.
- [154] S.F. Donovan, M.C. Pescatore, Method for measuring the logarithm of the octanol–water partition coefficient by using short octadecyl–poly(vinyl alcohol) high-performance liquid chromatography columns, *J. Chromatogr. A.* 952 (2002) 47–61. [https://doi.org/10.1016/S0021-9673\(02\)00064-X](https://doi.org/10.1016/S0021-9673(02)00064-X).
- [155] Othman Ahmed A., Nothaft Wolfram, Awni Walid M., Dutta Sandeep, Pharmacokinetics of the TRPV1 Antagonist ABT-102 in Healthy Human Volunteers: Population Analysis of Data From 3 Phase 1 Trials, *J. Clin. Pharmacol.* 52 (2013) 1028–1041. <https://doi.org/10.1177/0091270011407497>.
- [156] Othman Ahmed A., Cheskin Howard, Locke Charles, Nothaft Wolfram, Dutta Sandeep, A Phase 1 Study to Evaluate the Bioavailability and Food Effect of 2 Solid-Dispersion Formulations of the TRPV1 Antagonist ABT-102, Relative to the Oral Solution Formulation, in Healthy Human Volunteers, *Clin. Pharmacol. Drug Dev.* 1 (2013) 24–31. <https://doi.org/10.1177/2160763X11430860>.